Radiative Transfer in Low-Density, Low-Z Foam

by

Gregory A. Rochau

A dissertation submitted in partial fulfillment of

the requirements for the degree of

Doctor of Philosophy

(Nuclear Engineering and Engineering Physics)

at the

UNIVERSITY OF WISCONSIN - MADISON

2003

to my wife, Ellen,

who always reminds me that "It's just foam"

Abstract

Low-density CH_2 foams are utilized in z-pinch applications as a radiation pulse shaper for driving internal or external targets. In the dynamic hohlraum configuration, with an internally located Inertial Confinement Fusion (ICF) capsule, the pinch generated radiation must propagate through this foam before impacting the capsule. The foam is initially at a very low macroscopic density ($5 - 15mg/cm^3$), but is actually composed of a webbed structure of solid CH_2 separated by voids. It is not known how this structure affects either the radiation transport or the hydrodynamics in the foam.

For computational reasons, it is typically assumed that the dynamic hohlraum foam is a uniform high-density vapor. During the early stages of the pinch process, this CH_2 plasma is not in equilibrium with the penetrating, non-thermal radiation field. The additional energy in the radiation field is calculated to propagate in the region just below the carbon K-edge, and different atomic models predict significantly different absorption opacities in this region. Determining the proper computational methods and physical models for these foams requires experimental data of the radiative transfer characteristics for the radiation spectra of interest.

To address this issue, experiments have been fielded at Sandia National Laboratory's Z facility to investigate the radiative transfer process in $5mg/cm^3$ CH_2 foams. Absorption spectroscopy of aluminum and/or magnesium-fluoride tracers embedded in planar CH_2 samples are the primary diagnostic of the radiative transfer through the foam. An

extensive set of simulations are performed for each experiment to model the driving radiation spectra, the sample response, and the detailed spectroscopic absorption of the tracer elements. Through these simulations, a specific set of physical models and data tables are found to consistently reproduce the experimental data. This thesis provides a detailed description of the experiments and computational methods utilized to investigate the radiative transfer characteristics in these foams, along with a discussion about the implications for z-pinch driven ICF in the dynamic hohlraum configuration.

Acknowledgments

I would like to express my sincere appreciations to the many people who have provided their help and guidance in this work. They are far too numerous to name, and their support has been far too valuable to quantify. In particular, I would like to thank Prof. Greg Moses for his educational guidance, Dr. Jim Bailey for sharing his experimental expertise and overall knowledge of everything, Dr. Joe MacFarlane for the computational tools that made this work possible, Pat Lake for helping me 'turn the bolts,' and Dr. Ray Leeper and Dr. Tom Mehlhorn who always believed in me and provided the sizable budget that was required to carry out both the experiments and analysis contained in this thesis.

I would also like to express a special thanks to my family. My parents have always provided their unselfish support, and their guidance has been the pinnacle of my success. I strive to fill my father's shoes, and I am proud to have had the chance to walk in his footsteps. Finally, I bid a heartfelt and sincere thank you to my wife, Ellen. She has followed me where I needed to go and led me where I needed to grow. To her, I dedicate this work.

Funding provided by Sandia National Laboratories. Sandia is a multiprogram laboratory operated by Sandia Corporation, a Lockheed Martin Company, for the United States Department of Energy's National Nuclear Security Administration under Contract DE-AC04-94AL85000.

Contents

List of Figures

List of Tables

Thesis Guide

The primary goals of this thesis are to measure the dynamics of the radiative transfer process in low density CH_2 foam, and develop a computational method and suite of physical data tables to understand and model this process in the z-pinch environment at Sandia National Laboratory's Z facility. This has been identified as an important problem because of the application of low density CH_2 foam in the dynamic hohlraum driven Inertial Confinement Fusion (ICF) program at Sandia.

This thesis is written without any assumption on the reader's knowledge of ICF, z-pinches, or radiation transport. Therefore, Chapter 1 contains a number of lengthy sections on the introduction of these concepts. Section 1.1 is devoted to the general goals and requirements of ICF as a method for achieving controlled fusion in the laboratory, while §1.2 focuses on the physics behind the ICF implosion process. This discussion is aimed specifically at describing the importance of the radiation driver in ICF, and identifying the requirements of the radiation timing at the surface of an ICF capsule. Once these important details have been described for general ICF, §1.3 describes the basic concept of the z-pinch, a description of the Z facility at Sandia National Laboratory, and the dynamic hohlraum approach to ICF. These sections highlight the role of a low-density CH_2 foam in the dynamic hohlraum concept, and discuss the importance of understanding the transport of radiation in this foam in order to understand the radiation

field that drives an ICF capsule. Finally, §1.4 discusses the most common methods for calculating the transport of radiation in high-energy-density plasmas, and weighs the assumptions of each transport method in the context of their validity to different conditions of the plasma.

After defining the importance of the radiative transfer in CH_2 foam in Chapter 1, Chapter 2 moves on to describe published work that has special relevance to the problem at hand. Section 2.1 describes computational studies on the application of different radiation transport approximations to some simple analytic problems. The primary intent of this section is to provide a few examples where approximations can break down, and what effect that has on the calculated radiation transport. Section 2.2 summarizes work that has been published on the measurement of radiative transfer in other low-density foams. This section focuses on the methods that were used to make these measurements, and the assumptions that were required to model the data.

After setting the stage in Chapters 1 and 2, Chapter 3 describes the general experimental methods used in this thesis. Section 3.1 describes a set of calculations to explore the effects of different physical models on the calculated radiation transport in a CH_2 plasma under similar conditions as in the experiments. These calculations reveal the sensitivity of the transport solutions on the wide-range of choices available in the radiation-transport models. With these issues in mind, §3.2 describes the experimental method used to constrain the models, and describes the details of the spectroscopic tracer method that acts as the primary diagnostic of the radiative transfer. Then, §3.3 discusses the details of the experimental geometry on Sandia's Z facility, the diagnostics that are used to measure the observables in the experiments, and the spectral characteristics of the z-pinch source.

Chapter 4 is devoted to describing the computational methods employed in this thesis

for modeling the experiments. This chapter includes a detailed explanation of the computer codes that are used to model the experiments, with a focus on the physical models that are contained in each code. Because some of these codes contain a choice of physics models, or rely on uncertain input parameters, this chapter also investigates the sensitivity of the calculated solutions on the various uncertainties in the models. In addition, this chapter includes the description of a new code, SPECTROFIT, that was developed for this thesis. As discussed in §4.5, this code is utilized to provide an unbiased analysis of the experimental data to facilitate the comparison of this data to the computational models.

Since the experiment geometry presented in this thesis is relatively new, Chapter 5 describes two thin foil experiments intended to verify the computational methods in this geometry. These experiments have two primary goals. One goal is to test the atomic models of the tracer elements (aluminum and magnesium) in the spectral range that is relevant to the experiments. The other goal is to provide a level of confidence in the computational methods for simulating the radiation drive and the associated radiation-hydrodynamics in the absence of the foam material.

Finally, Chapter 6 describes three generations of experiments that were conducted to measure the radiative transfer in low-density CH_2 foam. This chapter focuses on both the details of the experiments, and the requirements on the computational models to reproduce the measurements. At the end of that chapter, §6.4 summarizes the foam experiments and contrasts a number of different computational models and data tables to the 'baseline' calculations that successfully reproduced the experimental measurements. §6.4.6 discusses the relevance of these experiments to the dynamic hohlraum ICF program, and provides possible directions for future work. Chapter 7 then summarizes the work performed for this thesis and the primary conclusions.

Chapter 1

Introduction

1.1 Inertial Confinement Fusion

Inertial confinement fusion (ICF) and magnetic confinement fusion (MCF) have historically received the majority of attention and funding in fusion energy research [1]. Each approach strives to create and confine a hot ($> 10keV$) deuterium-tritium plasma for time-scales long enough to create more energy through fusion reactions than was required to achieve confinement. In this case, the primary fusion reaction under consideration is:

$$^2H + {}^3H \rightarrow {}^4He(3.5MeV) + n(14.1MeV), \tag{1.1}$$

which has a peak reaction rate of $< \sigma v > \approx 9 \times 10^{-16} cm^3/s$ at an ion temperature of $\approx 60keV$ [2, 3].

In MCF, the confinement of a low-density ($10^{13} - 10^{14} cm^{-3}$) plasma is achieved through the application of a magnetic field in a near steady state. The relation typically applied to determine the approximate conditions of a MCF plasma required to

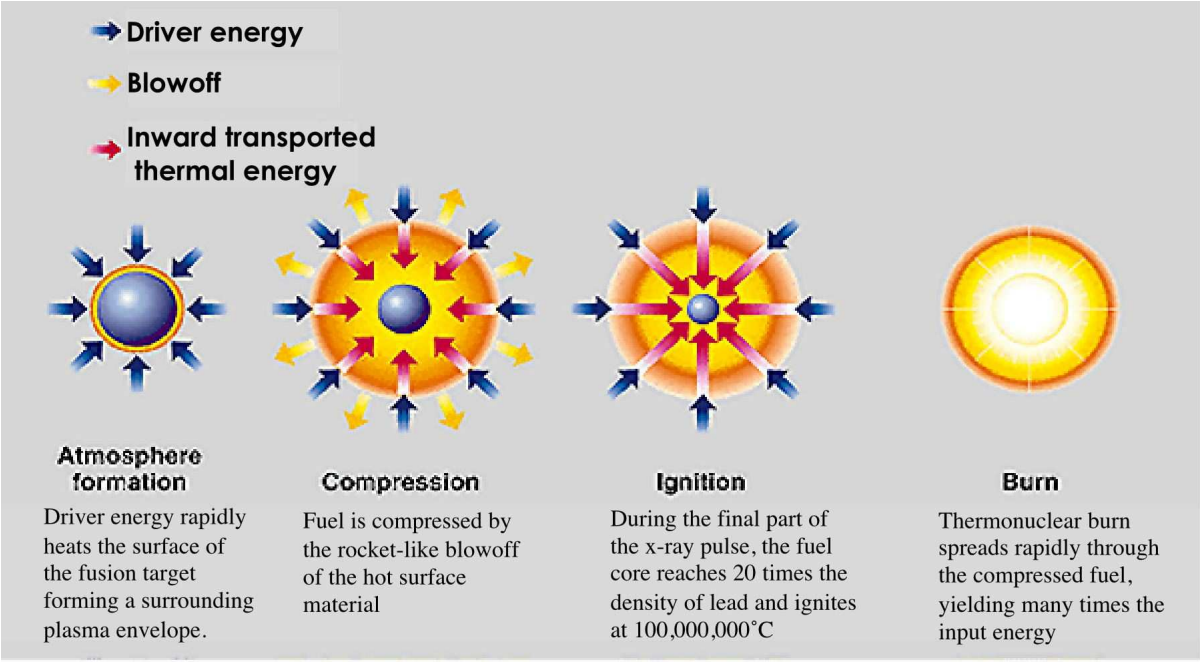

Figure 1.1: The inertial confinement fusion concept [9].

reach ignition is expressed through the Lawson criterion [4]:

$$n\tau > \frac{12\,T}{<\sigma v>(17.6MeV)}, \tag{1.2}$$

where n is the plasma density, τ is the confinement time, T is the plasma temperature (energy units), and $<\sigma v>$ is the fusion reaction cross section averaged over a Maxwellian velocity distribution. For a $10keV$ D-T plasma, then $<\sigma v> \approx 10^{-16}cm^3/s$ requiring that $n\tau > 10^{14}s/cm^3$, or that a $10^{14}cm^{-3}$ plasma must be confined for $\tau > 1s$.

In contrast to the MCF approach, ICF relies on the inertial energy of an imploding spherical capsule to confine and compress the D-T plasma [5–7]. Rather than heating the plasma in a near steady state, ICF would achieve ignition by isentropically compressing and shock heating the D-T fuel. Typically, an ignition scale ICF capsule is $\approx 1mm$ in radius with a $\approx 100\mu m$ thick outer ablator and an inner core of D-T gas surrounded by a thin layer of cryogenic solid D-T [8]. A schematic of the ICF process is shown

in Figure 1.1 [9]. The ablator is super-heated by intense laser, ion, or x-ray radiation causing it to quickly expand outward under its increased vapor pressure. Like a rocket, the exploding ablator pushes inward on the fuel thereby compressing it to peak final densities of $n \approx 10^{26} cm^{-3}$ and temperatures of $T > 10keV$. At the time of ignition, the fuel contains a central hot spot $\approx 50\mu m$ in radius surrounded by the bulk of the much colder D-T fuel. Fusion reactions begin in the hot spot and the charged fusion reaction products (alpha particles) deposit their energy in the surrounding fuel. This initiates a thermonuclear burn wave that consumes a fraction of the bulk D-T fuel and releases the majority of the fusion energy through the $14.1MeV$ neutrons.

According to the Lawson criterion, an ICF plasma at an average density of $10^{25} cm^{-3}$ only needs to achieve containment at $10keV$ for $\approx 1ns$. However, the derivation of the Lawson criterion relies on a classical energy balance in a plasma at steady-state. This criterion is not applicable for an inertially confined plasma. In this case, the capsule compression as expressed through the density-radius product, ρr, is a more appropriate figure of merit [10].

Since the fusion burn wave in an ICF capsule is propagated in large part by the α fusion reaction products, the hot-spot must be both dense and large enough to absorb most of these particles. As long as the α particles contain enough energy to heat the D-T to $\approx 10keV$ (ie. enough of the D-T has been fused), then the burn wave will be self-sustaining. Thus, the minimum ρr required for an ICF capsule to reach ignition is limited by either the burn-up required to sustain the fusion reactions, or the range of α particles in a hot D-T plasma (whichever dictates a larger ρr).

First, consider the minimum burn-up requirements for a D-T plasma to produce enough fusion energy to sustain a temperature of $\approx 10keV$. This can be found by an energy balance between the fuel burn-up and the energy required to to heat the D-T fuel

mass. The rate of thermonuclear reactions in the ICF fuel can be expressed by [10]:

$$\frac{dn}{dt} = N_D N_T < \sigma v >= \left(\frac{1}{2}N_0 - n\right)^2 < \sigma v >, \tag{1.3}$$

for n the number of reactions and N_0 the number density of the equimolar D-T fuel. Defining the fuel burn-up as $\phi = \frac{2n}{N_0}$, and assuming that the fusion cross section is approximately constant in time, then integrating Eq. 1.3 yields:

$$\phi = \frac{N_0 \tau < \sigma v >}{2 + N_0 \tau < \sigma v >}. \tag{1.4}$$

The burn time in ICF is limited by the disassembly of the capsule as it rebounds outward. This final expansion launches a rarefaction wave that propagates into the fuel at the speed of sound, c_s. Calculations indicate that the fusion reaction rate is extinguished by the time this rarefaction wave propagates $\approx 1/3$ of the way into the fuel [17]. Thus, setting $\tau = \frac{r}{3c_s}$ and writing N_0 as the D-T mass density, ρ, the burn-up can be expressed as:

$$\phi = \frac{\rho r < \sigma v >}{6c_s + \rho r < \sigma v >}. \tag{1.5}$$

This equation has been shown to compare well with full-scale radiation-hydrodynamics calculations of laser driven ICF capsules, and it provides a convenient rule of thumb for calculating the fraction of D-T fused during the implosion.

According to Eq. 1.1, the fusion of deuterium and tritium produces an energy of $17.56MeV$ per reaction, or about $3.4 \times 10^{11} J/g$ of fusion fuel in the form of neutrons and α particles. Assuming that the $14.1MeV$ neutrons escape without interacting, and that the alphas are completely absorbed, each fusion reaction deposits about $6.7 \times 10^{10} J/g$ in the surrounding fuel. For a D-T plasma in thermodynamic equilibrium (equivalent electron and ion temperatures), it requires $\approx 2.3 \times 10^9 J/g$ to heat the fuel up to $20keV$. Equating these then requires that the burn-up must be $> 3.4\%$ for ICF ignition (with a

self-sustaining burn wave). Therefore, Eq. 1.5 indicates that the the D-T hot-spot must be compressed to a $\rho r > 0.21 g/cm^2$ in order to sustain the temperatures required for efficient fusion.

However, the analysis above assumes that the α particles are completely absorbed. This is only true if the range of these particles is less than the size of the hot-spot. The α range in a D-T plasma at $10keV$ and $\approx 50 g/cm^3$ has been determined by Fraley et. al. [14] to be $\approx 0.3 g/cm^2$. Thus, the hot-spot must have a $\rho r > 0.3 g/cm^2$ in order to capture a large majority of the α particles. This is a more stringent requirement than that dictated by the burn-up, and is therefore the minimum hot-spot ρr required to achieve ignition.

Outside the hot-spot, the majority of the fusion fuel is much colder and more dense. How much colder and more dense it is depends on the efficiency of the implosion. That is, since a colder plasma can follow a lower isentrope, it requires less energy to compress a cold plasma then a very hot one. The lowest possible isentrope (ie. the highest compression efficiency), is that for a fermi-degenerate plasma [15]. Figure 1.2 shows the fermi-degenerate pressure of D-T as a function of density for both an ideal fermi fluid, and that given by the Sesame equation-of-state tables [25]. Also shown on this plot is the phase-space of an ICF hot-spot at $\approx 50 g/cm^3$ and $\approx 10keV$ ($P \approx 10^5 Mbar$) based on the criteria derived above. Assuming that the pressure in the main fuel is similar to that in the hot-spot, and that the main fuel is very nearly fermi-degenerate, then the main fuel density must be about 10 times higher than that in the hot-spot. Since the main fuel is at a slightly larger radius, this corresponds to a ρr of about $2 - 3 g/cm^2$ (or a $\rho \Delta r \approx 1 g/cm^2$ assuming a $10 \mu m$ fuel thickness). Additionally, the fermi energy of a fully-stripped D-T plasma at a density of $500 g/cc$ is about $800eV$. If the electrons in the plasma are going to behave as a fermi-degenerate fluid, the temperature of the main fuel

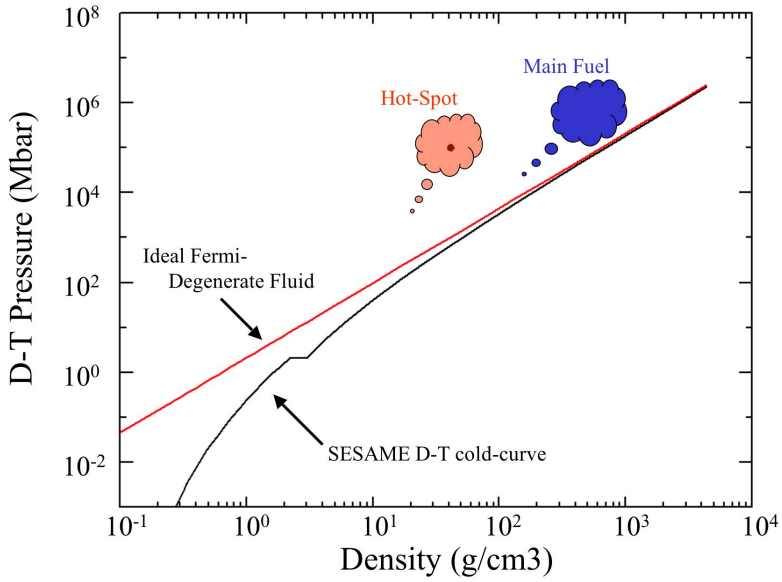

Figure 1.2: P-ρ phase-space plots for an ignition scale D-T ICF capsule. The hot-spot has a ρr of $\approx 0.3 g/cm^2$, and the main fuel is nearly fermi-degenerate.

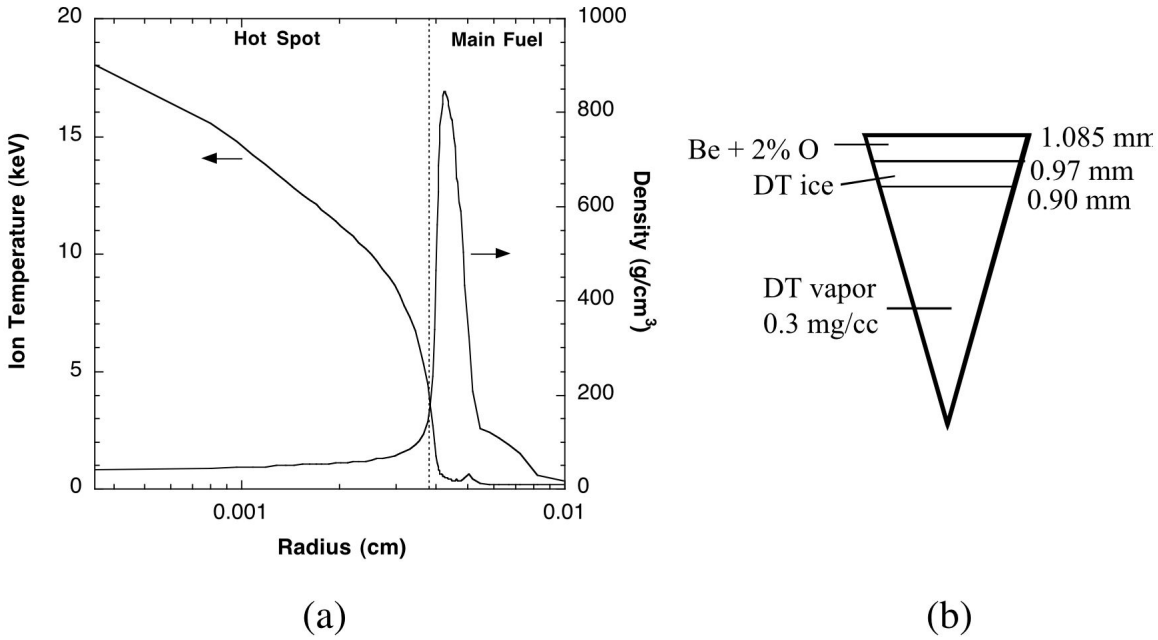

Figure 1.3: (a)BUCKY simulated plasma conditions at the time of peak compression for a NIF type ICF capsule with the radial build shown in (b).

must be much lower than the fermi energy.

Thus, at the time of ignition, an ICF capsule must contain a $10keV$ hot-spot with a ρr of about $0.3g/cm^2$ surrounded by a layer of D-T at a temperature $<< 1keV$ with a $\rho r \geq 2g/cm^2$. An example of the ICF fuel configuration around the time of ignition is shown in Figure 1.3(a). This calculation was conducted using the 1-D BUCKY [11] radiation- hydrodynamics code (see §4.2) for a National Ignition Facility (NIF) [12, 13] radiation drive history and the capsule design shown in Figure 1.3(b) [16]. The hot spot is $\approx 40\mu m$ in radius with a peak temperature of $\approx 17keV$ while the main fuel contains a peak density of $\approx 850g/cm^3$ $(2 \times 10^{26}cm^{-3})$ at a radius of $\approx 45\mu m$.

—

In order to achieve the ρr required for ignition, an ICF capsule must be irradiated by a high power source of radiation with a carefully tuned time history. In addition, this radiation field must contain a high degree of uniformity to avoid seeding hydrodynamic instabilities, which reduce the compression efficiency of the implosion process. Configurations that have been investigated to drive ICF capsules under these strict requirements are divided into two main categories; direct-drive and indirect-drive ICF.

Direct-drive ICF is the direct irradiation of an ICF capsule by laser, light-ion, or heavy-ion beams [18]. The driver energy is coupled to the capsule through inverse bremsstrahlung (for a laser driven system) or through charged particle collisions (in ion beam driven systems [20]). Electron conduction then transfers energy inward at the ablation front to drive the capsule implosion. A schematic of the direct-drive ICF concept is shown in Figure 1.4(a). This configuration has the benefit of a high drive efficiency, but can have a relatively low illumination symmetry due to the individual beam-spots on the capsule surface. For a discussion on direct-drive ICF, and the issues associated with beam-spot induced hydro instabilities, see S. Eliezer and H. Hora [19]. Laser driven

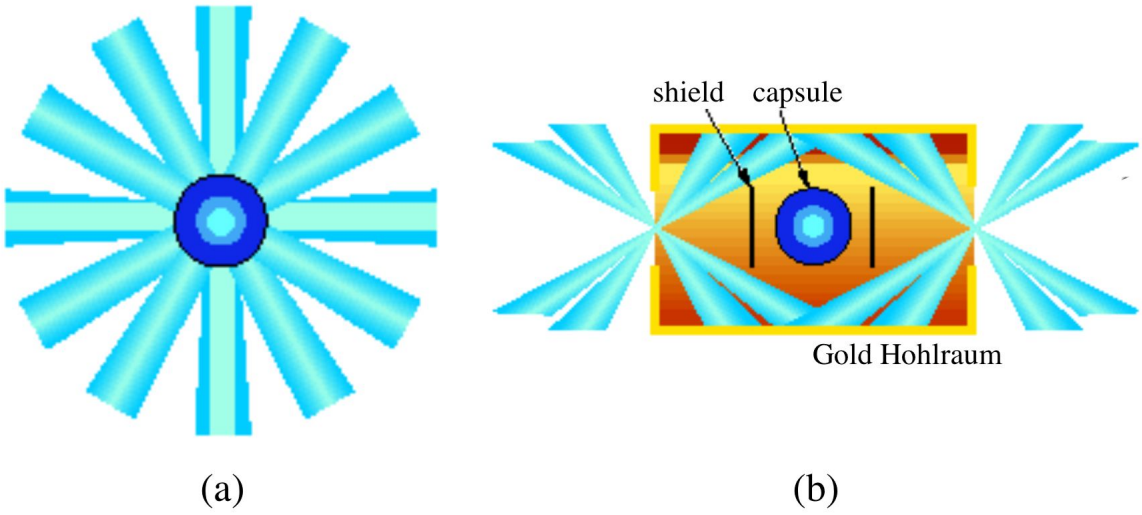

Figure 1.4: (a)In the direct-drive ICF concept, laser or ion beam radiation is incident directly on the capsule surface. (b)In the laser driven indirect-drive concept, laser beams are incident on the inside surface of the cylindrical hohlraum, which re-emits x-rays.

direct-drive is under serious investigation at both the University of Rochester OMEGA Neodymium glass laser and the Naval Research Facility (NRL) NIKE KrF Laser. Recent progress in laser beam smoothing [21] and foam layered capsule design for hydro smoothing [22] have shown promise for improved implosion stability.

Due to the initial difficulties in drive symmetry with direct-drive ICF, a large fraction of ICF research has historically been devoted to the indirect-drive approach. In this configuration, the ICF capsule is located at the center of a high-Z radiation case, or hohlraum. Laser or z-pinch radiation is directed onto the wall of the hohlraum, which re-emits a portion of the incident energy in the form of x-rays. These x-rays are then absorbed, thermalized, and re-emitted by other parts of the hohlraum wall thereby filling the cavity with a nearly uniform field of x-rays. The x-rays are then absorbed in the capsule ablator to drive the ICF implosion.

As an example, a schematic of the laser indirect-drive approach to ICF is shown in

Figure 1.4(b). The hohlraum is composed of a high-Z (usually gold) cylinder with two laser entrance holes (LEH) at either end. In the most recent ignition scale target designs for the NIF, the hohlraum is $\approx 10mm$ long with a case-to-capsule ratio of $R_{cc} \approx 3.5$ [23, 24], which implies a hohlraum radius of $\approx 3mm$. The laser beams enter through the LEH and illuminate the inside walls of the gold hohlraum. The high conversion efficiency of the hohlraum wall re-emits from $60\% - 70\%$ of the laser energy in the form of x-rays, which are thermalized by further absorption and re-emission within the cavity. Because the hohlraum surface area is ≈ 10 times that of the capsule surface area, only $10\%-15\%$ of the initial driver energy is available to implode the capsule. Thus, indirect-drive ICF has a lower driver efficiency than the direct-drive approach. However, the increased radiation symmetry on the capsule surface within the thermal radiation field has the promise of actually increasing the hydrodynamic stability, and therefore achieving a higher capsule compression.

1.2 ICF Implosion Physics

Regardless of the method, both direct and indirect drive ICF strive to one common goal: irradiate the surface of an ICF capsule with a properly tuned pulse of radiation to compress the capsule to a high enough ρr that more energy is generated through fusion than was required to heat the fuel. This section describes the basic capsule physics that dictate the pulse timing, and the stringent requirements on that timing in order to achieve the desired compression. Because this thesis is focused on the z-pinch driven approach to ICF (see §1.3.2), these driver requirements are discussed in the context of the indirect drive approach, where the capsule is driven by a pulse of x-rays.

Achieving the optimal ρr of an ICF capsule requires near isentropic compression of

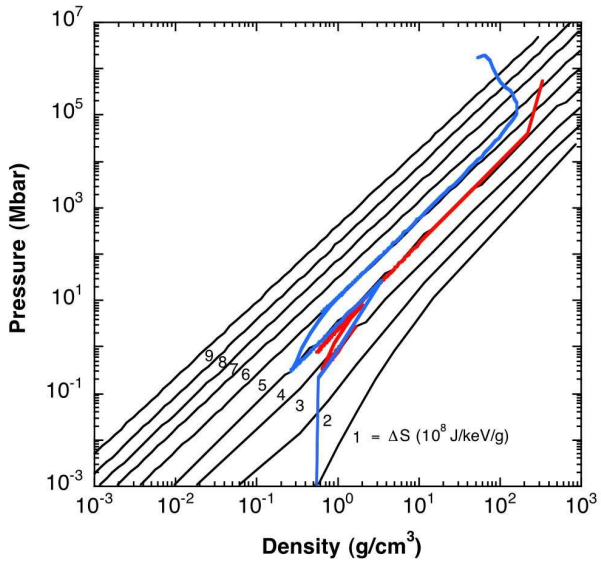

Figure 1.5: Isentropes (black) in pressure-density phase space for a DT plasma with an initial density of $0.25 g/cm^3$ and an initial temperature of $0.1 eV$. Also shown is the path in pressure-density space of the bulk DT fuel in a NIF type capsule for a well timed drive history (red) and a mistimed drive history (blue).

the DT fuel. The isentropes (lines of constant entropy) of a compressible fluid have the minimum possible slope in the pressure-density phase space. Thus, compressing the fuel along an isentrope requires the least amount of energy for any given increase in density. Figure 1.5 shows a number of isentropes for DT, each separated by a change in entropy of $10^8 J/keV/g$ as calculated from data in the Sesame equation of state tables [25]. For each change in entropy of $10^8 J/keV/g$, the pressure at any given density increases by a factor of about 2. This increase in pressure decreases the compressibility and therefore lowers the overall ρr of the capsule implosion. Thus, the characteristics of the drive history on an ICF capsule must be carefully tailored such that the main fuel implodes with the least possible change in entropy.

The characteristics of an isentropic capsule implosion were addressed in detail by R.E. Kidder through a series of papers in the mid 1970's [26–30]. He proposed an analytical

solution to the hydrodynamics equations for the isentropic compression of a spherical capsule. Assuming that the fluid is initially at rest in a state of uniform entropy, it can be shown that the capsule will implode isentropically under a time-dependent pressure boundary condition given by:

$$P(R,t) = P(R,0)\left[1 - \left(\frac{t}{t_c}\right)^2\right]^{-5/2}, \tag{1.6}$$

where $P(R,0)$ is the initial pressure at time $t = 0$ and t_c is the time of total collapse (the time when the capsule radius goes to zero). Thus, a driver must impart a pressure history on the DT fuel like that of Eq. 1.6 in order to achieve maximum compression. However, the assumption that the fuel is at an initial state of uniform entropy places a restriction on the initial radial pressure, density, and temperature profiles. These profiles correspond to:

$$P(r,0) = P(0,0)\left[1 + \beta\left(\frac{r}{R}\right)^2\right]^{5/2} \tag{1.7}$$

$$\rho(r,0) = \rho(0,0)\left[1 + \beta\left(\frac{r}{R}\right)^2\right]^{3/2} \tag{1.8}$$

$$T(r,0) = T(0,0)\left[1 + \beta\left(\frac{r}{R}\right)^2\right], \tag{1.9}$$

where β is a unit-less coefficient which depends on the total implosion time by:

$$\beta = \frac{1}{3}\left(\frac{\rho(0,0)}{\gamma P(0,0)}\right)\left(\frac{R}{t_c}\right)^2. \tag{1.10}$$

According to these equations, if the DT fuel initially has a uniform pressure, density, and temperature profile, then isentropic compression can only be achieved for 'slow' implosions ($\beta << 1$). For moderate ($\beta \approx 1$) to fast ($\beta >> 1$) implosions, the fuel conditions must have an unphysically strong dependence on radius. Therefore, a rapidly imploding ICF capsule with initially uniform fuel conditions cannot be isentropically compressed. However, if the ICF fuel can be rearranged into a thin spherical shell, then

Eq. 1.7-1.9 are approximately satisfied for very high β. This is one of the reasons why modern ICF capsule designs, such as that shown in Figure 1.3(b), have the bulk of the DT fuel mass in a thin layer just inside the ablator.

The analysis above depends on a tailored time-dependent pressure profile on the boundary of the ICF capsule. Clearly, it is not possible to apply such a profile directly. Instead, the capsule ablator is heated by a radiation field that is tailored to launch a series of shock waves which compress the fuel approximately like the pressure boundary condition given in Eq. 1.6. However, the strength of these shocks must be carefully tuned in order to minimize the increase from the initial state of entropy.

The change in entropy of a fluid under a strong shock is determined by the Hugoniot relations as discussed in the authoritative book by Zel'dovich and Raizer [31]. The Hugoniot relation for the specific energy, ϵ, on either side of a shock front can be written as:

$$\epsilon_1 - \epsilon_0 = \frac{1}{2}(P_1 + P_0)(V_0 - V_1), \tag{1.11}$$

where P is the plasma pressure, V is the specific volume $(1/\rho)$, and the subscripts 0 and 1 correspond to the conditions ahead and behind the shock front respectively. Assuming the hydrodynamics of the plasma motion to follow that of a perfect gas, and assuming constant specific heats, c_v and c_p, then the specific energy and the specific enthalpy can be written as:

$$\epsilon = c_v T = \frac{1}{\gamma - 1} PV; \qquad h = c_p T = \frac{\gamma}{\gamma - 1} PV, \tag{1.12}$$

where γ is the ratio of the specific heats . Solving these for the ratio of the specific volumes (i.e. the compression) and taking the strong shock limit where $P_1 >> P_0$, then the maximum compression attainable from a single shock in a DT gas ($\gamma \approx 5/3$) is:

$$\eta = \frac{\gamma + 1}{\gamma - 1} \approx 4. \tag{1.13}$$

This is not a sufficient compression to reach the final density of $10^{25} cm^{-3}$ required for ignition. In addition, assuming the entropy of a perfect gas with constant specific heats to be given by $S = c_v \ln [PV^\gamma]$, then the change in entropy across the shock front as determined by Eq. 1.12 is given by:

$$\Delta S = c_v \ln \left[\frac{P_1 V_1^\gamma}{P_0 V_0^\gamma} \right] = c_v \ln \left[\frac{P_1}{P_0} \left(\frac{(\gamma - 1)(P_1/P_0) + (\gamma + 1)}{(\gamma + 1)(P_1/P_0) + (\gamma - 1)} \right)^\gamma \right] \tag{1.14}$$

Thus, the stronger the shock, the higher the change in entropy. Eq. 1.13 and 1.14 indicate that, to achieve a high compression with a low change in entropy requires many weak shocks rather than one very strong one.

—

As an example of the drive conditions required to achieve the near isentropic compression of an indirect-drive, ignition scale ICF capsule, a few calculations have been conducted of the capsule performance for a NIF-type target. These calculations were carried out by the BUCKY 1-D radiation hydrodynamics code discussed in §4.2. Plotted in Figure 1.6 are two proposed radiation drive histories that may be achieved inside a hohlraum on the NIF. Each drive has a low-energy foot pulse at a temperature of $\approx 75eV$, a second pulse at $\approx 120eV$, and a final peak at $\approx 270eV$. The only difference between the two curves is a $1ns$ delay in the timing of the main pulse[a]. Using an ICF capsule with the radial build shown in Figure 1.3(b), the implosion dynamics were calculated in BUCKY with a complete rad-hydro model (including the thermonuclear burn of the capsule core) using each drive history as a radiation boundary condition on the capsule surface.

To visualize the hydrodynamics of the calculated implosions, mass contours (lagrangian zone boundaries) over the entire simulation time are shown in Figure 1.7(a) and (b) for the longer and shorter drive histories respectively. Each plot looks qualitatively

[a]The shorter drive pulse delivers $\approx 1\%$ less total energy to the capsule

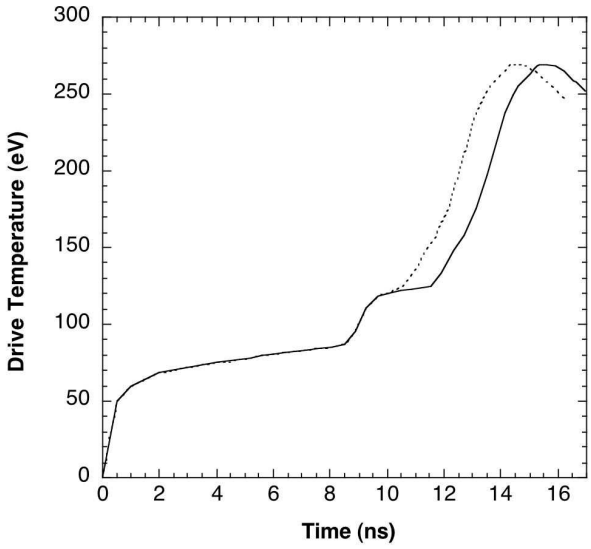

Figure 1.6: Radiation drive histories on the surface of an ICF capsule attainable inside an indirect drive hohlraum on the NIF. The two drives are identical with the exception of the main drive pulse which occurs $1ns$ earlier for the shorter total drive (dotted).

similar with a few minor differences. As expected, the longer drive history corresponds to a peak compression that occurs $\approx 1ns$ later than the shorter drive history. During this compression, the main fuel layer in Figure 1.7(a) remains at a lower total thickness than in the equivalent stage shown in Figure 1.7(b). In addition, at the time that the fuel begins its main compression, there is a much sharper curvature in the rate of implosion as shown in Figure 1.7(b) than that for the equivalent stage shown in Figure 1.7(a). This sharp curvature is due to a mistiming in the arrival of each shock within the fuel layer.

To better visualize this important feature of the implosion, a magnified view of the mass contours at the start of the peak implosion is shown in Figure 1.8(a) and Figure 1.8(b) again for the longer and shorter drive histories respectively. In Figure 1.8(a), the three main shocks pass through the bulk fuel in rapid succession leaving no room for the shocked fuel to decompress before the inertia of the imploding shell collapses it

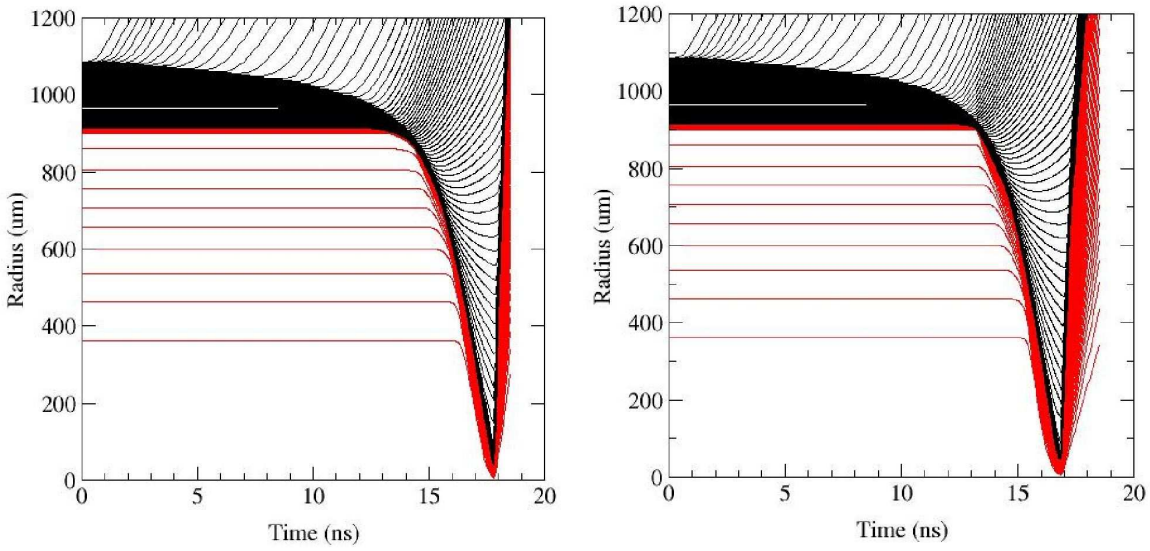

(a) **(b)**

Figure 1.7: BUCKY simulated mass contours (lagrangian zone boundaries) in the ablator (black) and the DT fuel (red) for the NIF type capsule shown in Figure 1.3(b). These calculations were conducted for the **(a)** longer drive history and the **(b)** shorter drive history in Figure 1.6.

(isentropically) to the axis. This results in a relatively smooth, rounded path as the fuel layer begins its implosion. The situation is quite different in Figure 1.8(b). In this case, the fastest moving shock overtakes the slower shocks before they can pass completely through the fuel layer. Because the main fuel has not been 'prepared' by the weaker shocks, this very strong shock leads to a high pressure ratio across the shock front that, according to Eq. 1.14, creates a large change in entropy. Thus, by the time the inertia of the imploding shell begins its isentropic compression of the fuel layer, the fuel is already along a higher isentrope. This results in lower compressibility and a correspondingly greater thickness in the fuel layer during the implosion.

The path of the bulk fuel layer in pressure-density phase space in comparison to the DT isentropes is shown for each simulation back on Figure 1.5. The bulk fuel starts at

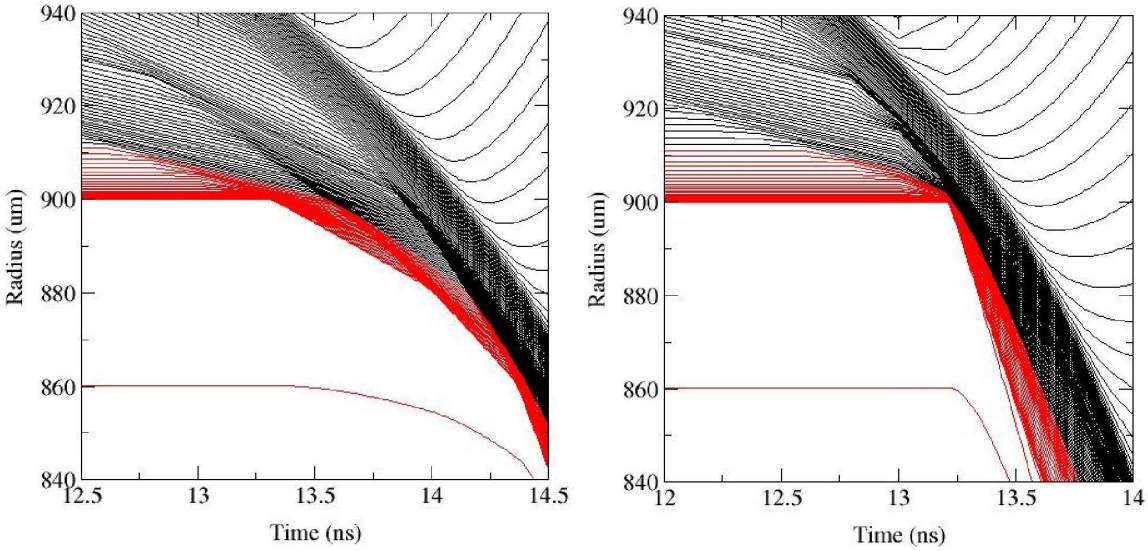

(a) **(b)**

Figure 1.8: BUCKY simulated mass contours (lagrangian zone boundaries) in the ablator (black) and the DT fuel (red) when the shocks pass through the bulk fuel. These calculations were conducted for the **(a)** longer drive history and the **(b)** shorter drive history in Figure 1.6.

a density of $0.25 g/cm^3$ and gains an entropy of $\approx 3 \times 10^8 J/keV/g$ as it is externally heated. As each successive shock passes through the fuel it suffers a quick compression, decompression, and a corresponding change in entropy. For the simulation with the later peak drive pulse, the shocks come in quick succession preventing the fuel from significantly decompressing before the start of the isentropic compression. In this case, the bulk fuel isentropically compresses along the $\Delta S \approx 4 \times 10^8 J/keV/g$ isentrope to a final (average) density of $\approx 300 g/cm^3$ and a peak ρr of $\approx 1.53 g/cm^2$. In contrast, the simulation with the earlier peak drive pulse gains an additional $10^8 J/keV/g$ of entropy because of the larger pressure ratio that occurs across the strong shock front in the under-shocked fuel layer. This causes the bulk fuel to isentropically compress along the the $\Delta S \approx 5 \times 10^8 J/keV/g$ isentrope therefore lowering the attainable compression. In

this case, the bulk fuel reaches an average density of $\approx 150 g/cm^3$ and a peak ρr of only $\approx 0.72 g/cm^2$.

Published results of similar NIF capsule designs calculated in LASNEX [32] show a very high sensitivity in the resulting fusion yield to uncertainties in the pulse timing. A sensitivity study by R.E. Olson [33] on an oxygen doped beryllium capsule design showed that it only required a $200ps$ mistiming in the radiation drive to reduce the overall capsule yield to $\approx 1/2$ of the optimal. Additionally, Kilkenny et.al. [34] report a factor of 10 drop in the fusion yield by a $500ps$ mistiming in the rise of the main radiation pulse. As a result of this sensitivity, the ignition plan for the NIF [34] requires that the shock timing (and therefore the radiation timing) be known to $\approx 100ps$ for a high confidence of successful ignition [35]. These requirements are the same for any indirect-drive approach where the ICF capsule absorbs $\approx 200kJ$ of driver energy, including that for z-pinch driven ICF.

1.3 Z-Pinch Driven ICF

1.3.1 The *'Fast'* Z-pinch

The classical z-pinch is a plasma physics phenomenon that was first investigated by J. Bennett [36] in 1934 and termed a "pinch" by L. Tonks [37] in 1937. The pinch mechanism, in its most basic form, is simple. A large voltage applied across either a neutral or partially ionized gas will break it down into a plasma of ions and electrons which conduct a strong axial current. The current flowing in this plasma induces an azimuthal magnetic field that in turn induces a $J \times B$ Lorentz force directed radially inward. This force causes the plasma to implode toward the axis thereby increasing the current density and further heating the plasma column. In the original studies of

z-pinch phenomenon, it was believed that a DT gas could be compressed in a z-pinch configuration to a sufficient density and temperature to reach fusion ignition conditions. The pinch theoretically reaches a state of equilibrium with the magnetic field (called the Bennett equilibrium) where it is confined in a hot, dense state for a time sufficient to satisfy the Lawson criterion. While minor efforts are still in effect to investigate this [38], it was discovered that the z-pinch configuration suffers from many debilitating magneto-hydrodynamic instabilities. Because the plasma is supported and compressed by a magnetic field, any axial variations in the plasma density will efficiently seed $m = 0$ (sausage) or $m = 1$ (kink) instabilities that disrupt the implosion. These effects are difficult to mitigate, and cause the pinch to prematurely disassemble. Thus, attempts to utilize the z-pinch as a magnetic confinement fusion approach were mostly abandoned.

A resurgence in the interest of z-pinches occurred in the 1980's with the progress of pulsed-power technology. Pulsed-power driven z-pinches differ from the classical MHD z-pinch in that very high, short duration currents drive the plasma column to the axis without ever reaching a state of equilibrium with the magnetic field [39]. The current pulse-width is comparable to the implosion time such that the z-pinch stagnates on the central axis just after the peak of the current drive, and disassembles as it rebounds. Figure 1.9 shows a schematic diagram of this 'fast' z-pinch process. In a simple 1-D model of a thin shelled plasma (or liner), the equation of motion for the imploding z-pinch can be written as:

$$m\frac{\partial^2 r}{\partial t^2} = -\frac{B(t)^2}{2\mu}(2\pi r l) = -\frac{\mu I(t)^2}{4\pi r}l, \tag{1.15}$$

where m is the plasma mass, l is the length of the z-pinch, μ is the magnetic permeability, $B(t)$ is the time-dependent magnetic field at the pinch surface, and $I(t)$ is the pinch current. As the liner implodes, the magnetic field energy is converted into kinetic energy,

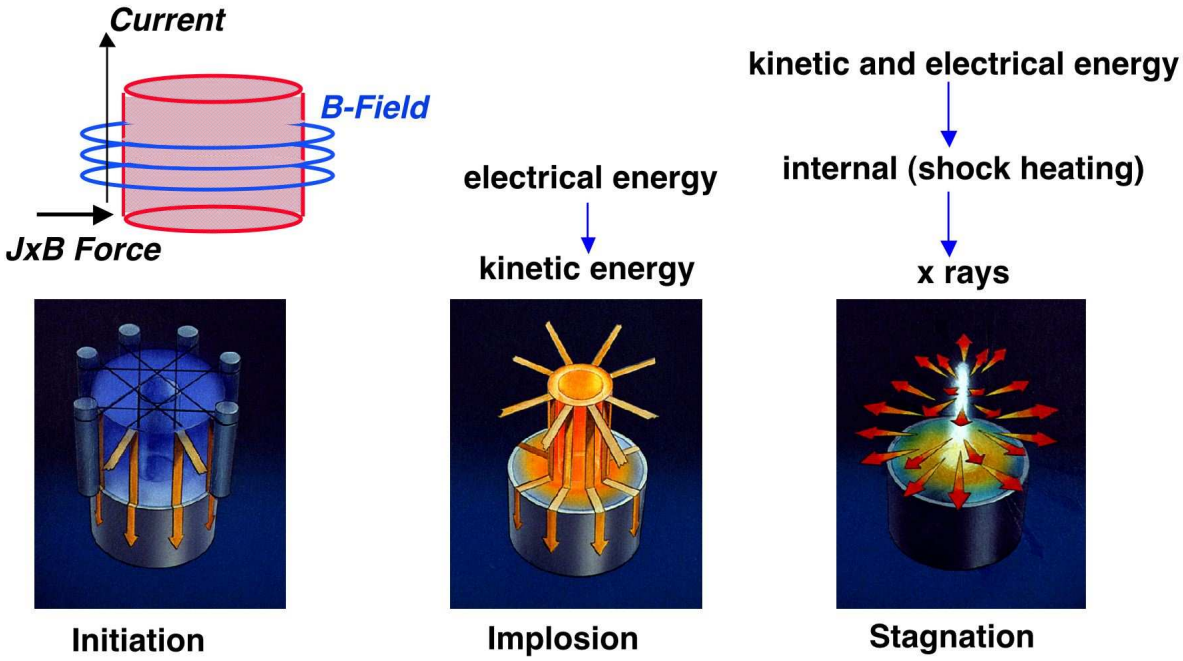

Figure 1.9: The 'fast' z-pinch concept.

W. Multiplying Eq. 1.15 by $\partial r/\partial t$ yields:

$$m\frac{\partial r}{\partial t}d\left(\frac{\partial r}{\partial t}\right) = -\frac{\mu}{4\pi}l\left[\frac{1}{r}\left(\frac{\partial r}{\partial t}\right)I(t)^2\right]dt. \tag{1.16}$$

Integrating the right-hand-side by parts, and noting that $W = 0.5m(\partial r/\partial t)^2$, then the equation for the kinetic energy of the imploding z-pinch can be written as:

$$W = \frac{\mu}{4\pi}l\int_0^t \frac{\partial I(t')^2}{\partial t'}\ln\left(\frac{r_0}{r}\right)dt', \tag{1.17}$$

for r_0 the initial z-pinch radius, and r the radius at time t. If the time-dependent current and radius profiles are known, then this equation can be integrated to determine the kinetic energy at time t. However, because the logarithm is a slowly varying function, then an approximate solution can be found by assuming a constant dependence on r. The integration in Eq. 1.17 is then trivial and yields the following expression for the

kinetic energy:

$$W \approx \frac{\mu}{4\pi} I(t)^2 \ln[C] l, \tag{1.18}$$

where C is the convergence, r_0/r, at time t. The kinetic energy density, w, at the time of pinch stagnation can then be written as:

$$w \approx \frac{\mu}{4\pi} I(t_p)^2 \frac{C^2 \ln(C)}{\pi r_0^2}, \tag{1.19}$$

for t_p the time of peak pinch current. Assuming that the current peaks at a value of $20MA$, the initial pinch radius is $1cm$, and that the convergence is ≈ 10, then the kinetic energy density of the z-pinch at stagnation is $w \approx 3 \times 10^7 J/cm^3$.

At the time of stagnation, a shock wave from the on-axis impact propagates through the plasma thereby converting a portion of the kinetic energy into thermal energy, which is radiated away in the form of x-rays. Assuming that the radiation is approximately black-body in nature, then the power balance for the plasma temperature, T_p, can be written as:

$$\sigma T_p^4 \approx \eta u w, \tag{1.20}$$

where η is the conversion efficiency from kinetic to thermal energy (determined by the shock hugoniot of the plasma), and u is the speed of the imploding liner. Relating u to W by $W = 0.5mu^2$, and substituting Eq. 1.19 in for w yields a final (approximate) expression for the temperature of the z-pinch:

$$T_p \approx \left[\left(\frac{\eta}{\sigma} \sqrt{\frac{\mu^3}{32\pi^5}} \right) \sqrt{\frac{l}{m}} \frac{C^2 \ln(C)^{3/2}}{r_0^2} I(t)^3 \right]^{1/4}. \tag{1.21}$$

Thus, for a z-pinch that is initially $1cm$ tall and $1cm$ in radius with a total mass of $3mg$, a $20MA$ peak current will produce a plasma temperature of $T_p \approx 215eV$ (assuming $\eta \approx 0.1$). This corresponds to a pinch luminosity of $\approx 220TW/cm^2$.

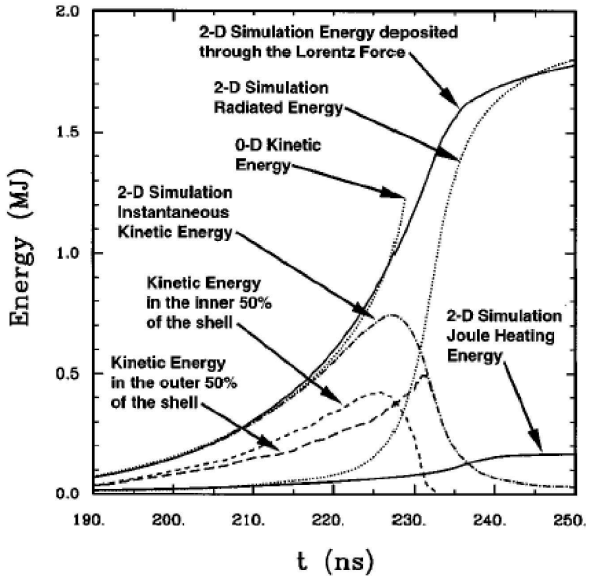

Figure 1.10: Example energy balance in a 2-D simulation of a 'fast' z-pinch [40].

The primary complication associated with 1-D models of the z-pinch dynamics is the lack of accounting for a 2-D instability structure. It is well known that fast z-pinches are Rayleigh-Taylor (R-T) unstable such that the growth of R-T bubbles and spikes can thicken the imploding liner. This has the effect of broadening the stagnation time creating a 2-D x-ray yield with a much lower peak and a much broader temporal profile than a 1-D calculation might predict. In Eq. 1.21, these 2-D effects are absorbed into the coefficient η, which must be determined by a detailed calculation of the liner thickness and the propagation of the shock at stagnation. Figure 1.10 shows the energy balance from a detailed 2-D calculation of a fast z-pinch [40]. Note that the primary source of energy deposition is through the Lorentz force, which goes directly into the kinetic energy of the imploding liner. It is also evident from Figure 1.10 that the outer 50% of the liner moves at a decreasing velocity with respect to the inner 50%, and reaches the axis $\approx 5ns$ later.

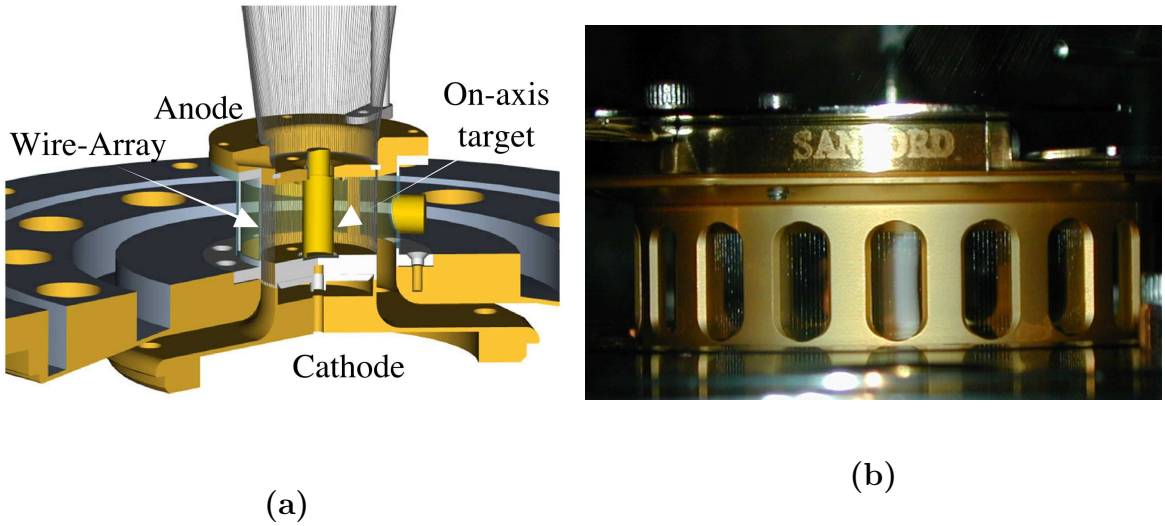

(a) **(b)**

Figure 1.11: **(a)**Schematic illustration of the Z machine diode. **(b)**Picture of a wire-array in the dynamic hohlraum configuration on Z.

1.3.2 The Dynamic Hohlraum

The simple analysis above demonstrates the relatively high radiation powers that can be achieved with a fast z-pinch. However, driving sufficiently high currents to create a $200eV$ plasma is not trivial, and a great deal of research has been conducted on the development of pulsed-power for this purpose. Sandia National Laboratories in Albuquerque, New Mexico has built a pulsed-power generator called the Z machine for conducting research in high power, fast z-pinches [41]. The Z machine typically drives a $100ns$ wide current pulse, peaked at $20MA$, through a z-pinch load that is $1-2cm$ tall and $1-2cm$ in radius. This load is generally constructed of an array of very thin tungsten wires that bridge the gap between the anode and the cathode of the Z machine diode. A schematic of the Z machine diode is shown in Figure 1.11(a), and a photograph of a typical wire array load is shown in Figure 1.11(b). Experimental studies of z-pinch performance on the Z machine have demonstrated x-ray powers up to $230TW$, and total x-ray yields up to $1.8MJ$.

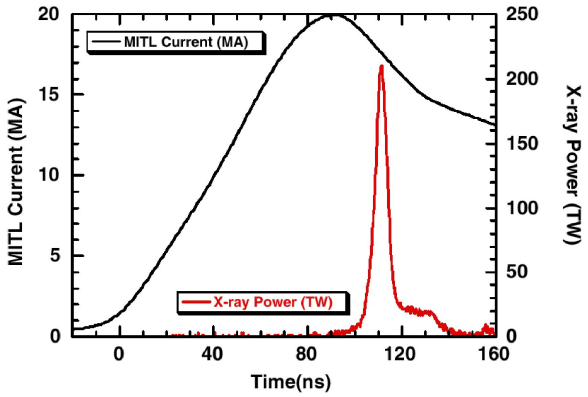

Figure 1.12: Z machine load current (black) and associated x-ray power profile (red) for a high-performance, single-array z-pinch with no internal load [42].

As an example, Figure 1.12 shows the current and x-ray power profile from a high-performance shot on the Z machine [42]. The current drive is $\approx 150ns$ long, peaking at a value of $20MA$, while the x-ray power profile occurs in a $\approx 5ns$ full-width-at-half-maximum (FWHM) pulse peaking at a value of $210TW$. This large amount of x-ray power available from a fast z-pinch on the Z machine can be used in a number of applications. These include x-ray effects experiments, material opacity and equation of state studies, basic plasma instability experiments, and inertial confinement fusion.

Of the many proposed approaches to achieve indirect-drive ICF with a fast z-pinch, the dynamic hohlraum is the most energy efficient [43]. That is, the dynamic hohlraum can deliver the most amount of energy to an ICF capsule for a given amount of input power. A schematic of the dynamic hohlraum configuration for driving an ICF capsule is shown in Figure 1.13 [44]. There are essentially three components; a tungsten wire-array(s), a foam 'converter', and the ICF capsule. As was discussed in §1.3.1, the main source of radiation from a fast z-pinch is the thermal emission associated with the shock-heating of the liner. Thus, when the z-pinch liner strikes the surface of the foam, a shock wave is launched in both the liner and foam, which radiates x-rays to the interior [45].

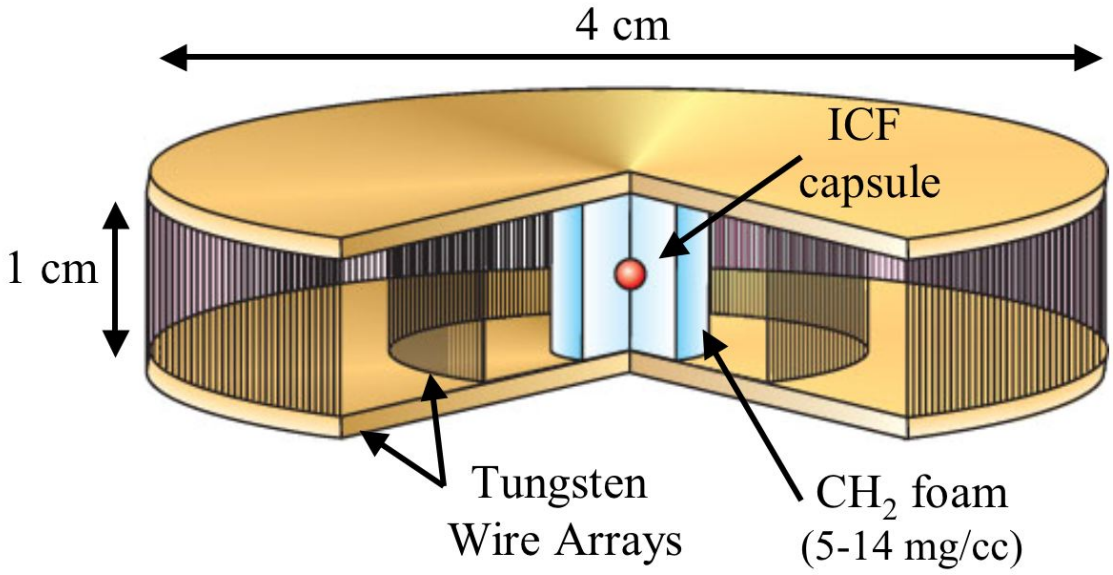

Figure 1.13: Schematic illustration of the dynamic hohlraum configuration for conducting indirect-drive ICF experiments using a fast z-pinch driver. [44]

Experiments indicate that the shock front propagating into the foam is the primary source of radiation in the dynamic hohlraum [46], and can reach emission temperatures greater than $600eV$ [47]. Assuming that the foam is optically thin to these x-rays, then the radiation will thermalize in the hohlraum, heat the ablator layer of the ICF capsule, and induce an indirect-drive type implosion. A schematic of the 'dynamic hohlraum phase' of the z-pinch implosion is shown in Figure 1.14. One point of special importance is that the radiation emitted by both the shock-front and the hohlraum 'wall' must propagate through the CH_2 foam before interacting with the capsule. It is therefore important to understand the transport of radiation in that foam medium in order to understand the radiation drive at the capsule surface.

Dynamic hohlraum arrangements on the Z machine typically utilize a $1-2cm$ tall,

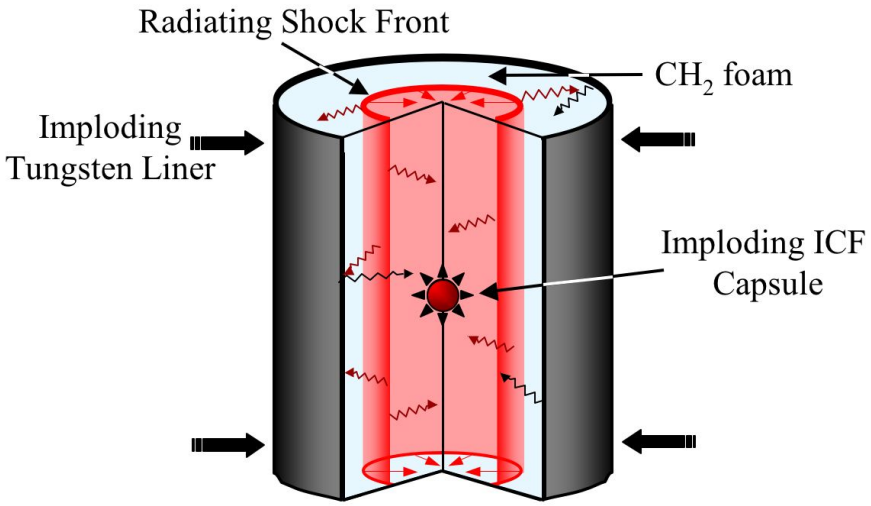

Figure 1.14: Schematic illustration of the dynamic hohlraum phase of the z-pinch implosion. The shock-front in the CH_2 foam is the primary source of radiation, which is absorbed and re-emitted by the Tungsten liner. After propagating to the center of the foam, the x-rays are absorbed in the ICF capsule ablator and induce an indirect-drive implosion.

$3-4mg$ nested wire array (a small diameter wire array within a larger diameter array), and a $5-14mg/cc$ CH_2 foam placed on the axis. The foam converter is between $2.5-5mm$ in radius with a $0.5-1mm$ radius ICF capsule at the center.

As an example, the dynamic hohlraum configuration and the experimental hohlraum temperature and shock radius for some typical experiments on the Z machine are shown in Figure 1.15(a) and (b) [46]. The z-pinch consists of a nested, $1.5cm$ long tungsten wire array containing 240 wires at an initial radius of $2cm$ and 120 wires at initial radius of $1cm$ with a $5mm$ radius, $5mg/cc$ CH_2 foam converter on axis. Also shown in Figure 1.15(b) is the capsule radius evolution on a shot with the same z-pinch and hohlraum geometry. The capsule had an initial radius of $1.05mm$, and contained a $12atm$ $D_2/0.075atm$ Ar gas fill. The figure indicates that the capsule is driven with a radiation temperature up to $\approx 135eV$ and reaches a maximum convergence ratio of ≈ 5. The shock arrives at the

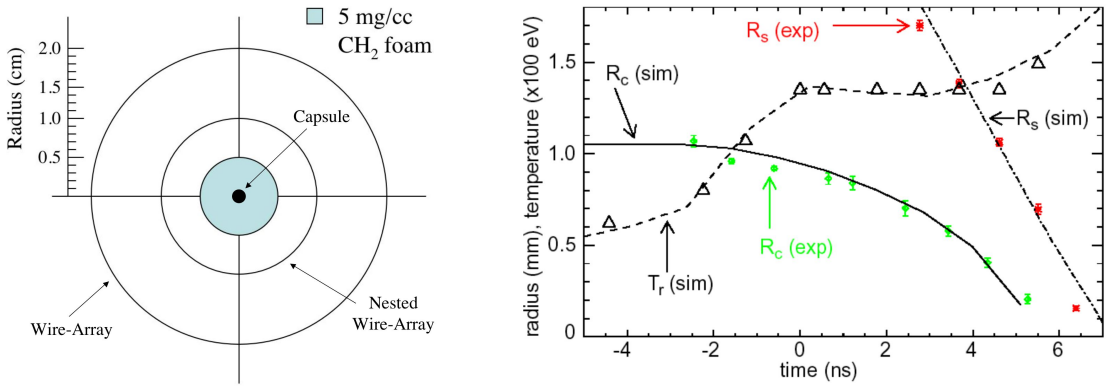

(a) **(b)**

Figure 1.15: (a) Diagram of the dynamic hohlraum geometry. **(b)** Experimental shock radius (red stars), capsule radius (green diamonds), and hohlraum temperature at the capsule location (black triangles) along with the simulated equivalents in a dynamic hohlraum on Z [46].

hohlraum axis $\approx 1ns$ after the peak of the capsule implosion, at which time the radiation temperature sharply increases under the final stagnation of the z-pinch plasma. In this particular experiment, calculations suggest that the core temperature of the capsule only reached $\approx 500eV$, and therefore did not produce any observable neutron or argon x-ray signals.

The most recent dynamic hohlraum experiments on Z utilize a $2.5cm$ radius, $14mg/cc$ CH_2 foam converter and a $1.2cm$ tall z-pinch. This geometry can drive a capsule with a hohlraum temperature up to $\approx 200eV$, and therefore has the possibility of compressing a capsule to higher temperatures and densities. Figure 1.16(a) and (b) show the argon emission spectrum and an image of the capsule self-emission near the time of peak compression in one of these experiments [48]. Comparisons between the argon emission spectrum and detailed calculations of the spectroscopic line transitions indicate that the capsule core reached a density of $1-2\times10^{23}cm^{-3}$ and a temperature of $\approx 1000eV$ [49]. The neutron production from similar shots was measured at $\approx 2\times10^{10}$, which is $10-30\%$

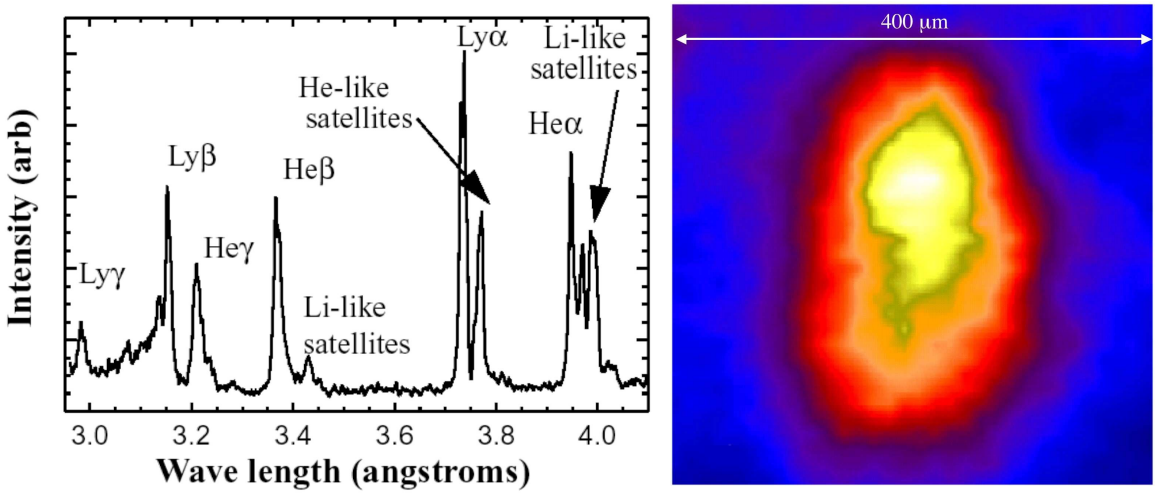

(a) **(b)**

Figure 1.16: **(a)** Argon emission spectrum and **(b)** a self-emission image of the capsule implosion near the time of peak compression in a dynamic hohlraum on the Z machine [48].

of the clean 1-D capsule simulation yield [48]. However, as evident from Figure 1.16(b), the capsule implosion suffers from a polar/equator asymmetry due to the closer proximity of the capsule equator to the encroaching shock front. This is one of the primary concerns surrounding the z-pinch driven dynamic hohlraum approach to ICF. As was discussed in §1.1, implosion symmetry is critical to achieving the ρr conditions required for an ignition level fusion yield.

The other issue of primary concern in the dynamic hohlraum is the overall pulse shape. As discussed in §1.2, obtaining the ρr required for successful ICF requires carefully tailored radiation drive profiles in order to compress the fuel along a low isentrope. In a z-pinch driven dynamic hohlraum, the radiation output can be tailored with shock converters or burn-through foils placed inside the radius of the imploding liner. If these are properly chosen, it will produce a radiation pulse at the capsule that launches shock-waves with the proper timing for a high ρr.

Tuning the profile will require an extensive collection of data regarding the effects of different converters and foils on the radiation drive, as well as a good understanding of the radiation propagation through the foam medium. The former can be accomplished with a large-scale parameter study on the Z machine. This thesis is a first attempt at addressing the latter.

1.4 Computational Radiation Transport

The last few sections of this thesis have been devoted to defining the requirements for successful ICF, as well as explaining the current state-of-the-art for achieving these requirements in a z-pinch driven dynamic hohlraum. As was discussed in detail in §1.2, one of the primary requirements is a well-understood, carefully timed radiation drive history on the capsule surface. The specific example in §1.2 demonstrated a $\approx 50\%$ drop in the calculated ρr of an ignition scale ICF capsule by a $< 1ns(\approx 5\%)$ mistiming in the main radiation pulse. This has serious implications for a z-pinch driven dynamic hohlraum. Namely, if there are inadequacies in the radiation transport model within the CH_2 foam converter, then capsules designed under the calculated drive profile may be irradiated by a very different drive history during the experiment. This would cause a diminished ρr and a correspondingly poor capsule performance.

It can be shown that the mean free path of some important frequencies in a $5mg/cc$ CH_2 plasma is on the order of the dynamic hohlraum radius over a significant portion of the hohlraum temperature rise (see §3.1). Under these conditions, radiation is neither free-streaming nor diffusing. This is a difficult regime in which to calculate the radiation transport, and one must pay careful attention to the assumptions made in computing the radiative transfer rates. To better understand the possible inadequacies associated with

the standard computational radiation transport methods in this regime, it is beneficial to look at these methods in detail while paying close attention to the assumptions made throughout their derivations.

—

The radiative transfer equation has been the subject of many papers and books in the open literature [50–52]. In its most simple form, the equation is the same for both neutrons and photons, and much of its rich history is owed to the nuclear energy community. However, there are distinct differences in the details of the transport equation for thermal x-rays within a high-temperature plasma than are typically considered for the transport of neutrons and gammas in a nuclear reactor. For this reason, the following discussion is taken from Mihalas [53] and Rybicki [54] for the transport of radiation in stellar atmospheres, which are qualitatively similar to that of a laboratory plasma under a high-temperature thermal radiation field.

The specific intensity, I, of a radiation stream propagating along a direction within a hot gas is determined by a conservation of flux. Requiring that the intensity of a ray from an infinitesimal volume element be equivalent to the incident intensity plus any emission and minus any absorption, then the space-, frequency-, angle-, and time-dependent intensity can be written as:

$$\begin{aligned}\frac{1}{c}\frac{\partial}{\partial t}I(\overrightarrow{r},\nu,\hat{\Omega},t)+\hat{\Omega}\cdot\nabla I(\overrightarrow{r},\nu,\hat{\Omega},t)+\chi(\overrightarrow{r},\nu,t)I(\overrightarrow{r},\nu,\hat{\Omega},t)\\ =\int_0^\infty\int_{4\pi}\sigma_s(\overrightarrow{r},\nu'\rightarrow\nu,\hat{\Omega}'\rightarrow\hat{\Omega},t)I(\overrightarrow{r},\nu',\hat{\Omega}',t)d\hat{\Omega}'d\nu'+S(\overrightarrow{r},\nu,\hat{\Omega},t),\end{aligned} \tag{1.22}$$

where the various variables and constants are defined as:

$$I(\overrightarrow{r},\nu,\hat{\Omega},t)=ch\nu f(\overrightarrow{r},\nu,\hat{\Omega},t)\hat{=}\text{ Specific photon intensity}$$

$$f(\overrightarrow{r},\nu,\hat{\Omega},t)\hat{=}\text{ Photon distribution function}$$

$$\chi(\overrightarrow{r},\nu,t) = \sigma_a(\overrightarrow{r},\nu,t) + \sigma_s(\overrightarrow{r},\nu,t) \hat{=} \text{ Total plasma opacity}$$

$$S(\overrightarrow{r},\nu,\hat{\Omega},t) \hat{=} \text{ Intensity contribution from external sources}$$

This is the form of the transport equation typically found in many textbooks. For completeness, however, Eq. 1.22 must be corrected for the quantum effects of stimulated emission and scattering (a substantial deviation from the neutron transport equation) [59]. Defining the induced emission and scattering term from the Einstein-Milne relations as $(c^2/2h\nu^3)I(\overrightarrow{r},\nu,\hat{\Omega},t)$, then Eq. 1.22 can be rewritten as:

$$\begin{aligned}\frac{1}{c}\frac{\partial}{\partial t}I + \hat{\Omega}\cdot\nabla I + \sigma_a I = S\left(1+\frac{c^2}{2h\nu^3}I\right)\\ + \int_0^\infty\int_{4\pi}\sigma_s(\nu'\to\nu,\hat{\Omega}'\to\hat{\Omega})I(\nu',\Omega')\left(1+\frac{c^2}{2h\nu^3}I(\nu,\Omega)\right)d\hat{\Omega}'d\nu'\\ - \int_0^\infty\int_{4\pi}\sigma_s(\nu\to\nu',\hat{\Omega}\to\hat{\Omega}')I(\nu,\Omega)\left(1+\frac{c^2}{2h\nu'^3}I(\nu',\Omega')\right)d\hat{\Omega}'d\nu',\end{aligned} \tag{1.23}$$

where the total opacity, χ, has been split into the frequency-dependent scattering and frequency integrated absorption terms to account for the new dependence on ν' of the scattering out of ν. Eq. 1.23 is the most general form of the equation for radiative transfer attainable without invoking any assumptions about either the radiation field or the conditions of the plasma.

If the plasma is assumed to be at local thermodynamic equilibrium (LTE), and there is no nuclear or fluorescence decay radiation, then the source term depends only on the conditions of the plasma. In this case, the source term is defined by Kirchoff's law as:

$$S(\overrightarrow{r},\nu,\hat{\Omega},t) = \sigma_a^1(\overrightarrow{r},\nu,t)B_\nu(\overrightarrow{r},\nu,t), \tag{1.24}$$

where B_ν is the Planckian frequency distribution function given by:

$$B_\nu(\overrightarrow{r},\nu,t) = \frac{2h\nu^3}{c^2}\frac{1}{e^{h\nu/kT}-1}, \tag{1.25}$$

and σ_a^1 is a scaled photo-absorption cross-section given by, $\sigma_a^1 = \sigma_a(1-e^{-h\nu/kT})$. Inserting Eq. 1.24 into Eq. 1.23 and collecting terms that depend on σ_a^1 yields:

$$\begin{aligned}\frac{1}{c}\frac{\partial}{\partial t}I + \hat{\Omega}\cdot\nabla I &= \sigma_a^1(B_\nu - I) \\ &+ \int_0^\infty \int_{4\pi} \sigma_s(\nu' \to \nu, \hat{\Omega}' \to \hat{\Omega}) I(\nu', \Omega') \left(1 + \frac{c^2}{2h\nu^3} I(\nu, \Omega)\right) d\hat{\Omega}' d\nu' \\ &- \int_0^\infty \int_{4\pi} \sigma_s(\nu \to \nu', \hat{\Omega} \to \hat{\Omega}') I(\nu, \Omega) \left(1 + \frac{c^2}{2h\nu'^3} I(\nu', \Omega')\right) d\hat{\Omega}' d\nu'.\end{aligned} \tag{1.26}$$

This partial integro-differential equation is still quite non-linear, but can be solved by many of the standard transport approximations found in the literature. Of the deterministic methods, the ones that have received the most widespread use in high-energy density plasma computations are; P_n methods, flux-limited diffusion, discrete ordinates (S_n), and variable Eddington transport.

1.4.1 The P_n equations and flux-limited diffusion

Dividing Eq. 1.26 into an infinite set of partial differential equations parameterized by the variable $\hat{\Omega}$ can eliminate the dependence on the angle. The most general way to derive these equations is to expand the intensity, I, and the scattering cross-section, σ_s, into a set of orthogonal basis functions in the variable $\hat{\Omega}$. More specifically restricting the derivation to the case of a one-dimensional slab, the Legendre polynomials are a convenient set of functions to use as the basis set. In 1-D, the azimuthal integral can be carried out directly such that $d\hat{\Omega} = 2\pi \sin\theta d\theta = -2\pi\mu d\mu$, for $\mu \equiv \cos\theta$. Then, the photon intensity and scattering cross-section can be written as:

$$I(x, \nu, \mu, t) = \sum_{l=0}^{\infty} \frac{2l+1}{4\pi} I_l(x, \nu, t) P_l(\mu) \tag{1.27}$$

$$\sigma_s(x, \nu' \to \nu, \mu, t) = \sum_{l=0}^{\infty} \frac{2l+1}{4\pi} \sigma_{sl}(x, \nu' \to \nu, t) P_l(\mu) P_l(\mu'), \tag{1.28}$$

where $P_l(\mu)$ are the set of Legendre polynomials, and the angularly independent coefficients are given by:

$$I_l(x,\nu,t) = 2\pi \int_{-1}^{1} I(x,\nu,\mu,t) P_l(\mu) d\mu \tag{1.29}$$

$$\sigma_{sl}(x,\nu' \rightarrow \nu, t) = 2\pi \int_{-1}^{1} \sigma_s(x,\nu' \rightarrow \nu, \mu' \rightarrow \mu, t) P_l(\mu') P_l(\mu) d\mu, \tag{1.30}$$

Under this expansion, the index l in Eq. 1.27-1.30 then refers to the angular symmetry of each component of the radiation field. For example; I_0 and σ_{s0} represent the isotropic components of the photon field and scattering cross-section; I_1 and σ_{s1} represent the linearly anisotropic components; I_2 and σ_{s2} represent the quadratically anisotropic components; and so on. Substituting Eq. 1.27 and 1.28 into Eq. 1.26 and rearranging terms gives:

$$\begin{aligned}
&\frac{1}{c}\frac{\partial}{\partial t}\sum_{l=0}^{\infty}(2l+1)I_l P_l(\mu) + \mu\nabla\sum_{l=0}^{\infty}(2l+1)I_l P_l(\mu) = \sigma_a^1\left[4\pi B_\nu - \sum_{l=0}^{\infty}(2l+1)I_l P_l(\mu)\right] \\
&+ \int_0^\infty \left[\sum_{l=0}^{\infty}(2l+1)\sigma_{s,l}(\nu' \rightarrow \nu) P_l(\mu) 2\pi \int_{-1}^{1} I(\nu',\mu') P_l(\mu') d\mu' \left(1 + \frac{c^2}{2h\nu^3} I(\nu,\mu)\right)\right] d\nu' \\
&- \int_0^\infty \left[\sum_{l=0}^{\infty}(2l+1)\sigma_{s,l}(\nu \rightarrow \nu') P_l(\mu) I(\nu,\mu) \left(2\pi \int_{-1}^{1} P_l(\mu') d\mu' \right.\right. \\
&\qquad \left.\left. + \frac{c^2}{2h\nu'^3} 2\pi \int_{-1}^{1} I(\nu',\mu') P_l(\mu') d\mu'\right)\right] d\nu',
\end{aligned} \tag{1.31}$$

where the intensity terms under the frequency integrals have not yet been expanded for clarity. Because the Legendre polynomials are an orthogonal set of functions, then the integration of this equation over μ can be easily accomplished by first multiplying Eq. 1.31 by $P_n(\mu)(2n+1)/2$. Doing this and expanding the remaining terms in I gives:

$$
\begin{aligned}
&\left(\frac{2n+1}{2}\right)\left[\frac{1}{c}\frac{\partial}{\partial t}\sum_{l=0}^{\infty}(2l+1)I_lP_l(\mu)P_n(\mu)+\mu\nabla\sum_{l=0}^{\infty}(2l+1)I_lP_l(\mu)P_n(\mu)\right]\\
&=\left(\frac{2n+1}{2}\right)\left[\sigma_a^1\left(4\pi B_\nu P_n(\mu)-\sum_{l=0}^{\infty}(2l+1)I_lP_l(\mu)P_n(\mu)\right)\right.\\
&+\int_0^\infty\left[\sum_{l=0}^{\infty}(2l+1)\sigma_{s,l}(\nu'\rightarrow\nu)P_l(\mu)P_n(\mu)I_l(\nu')\right]d\nu'\\
&-\int_0^\infty\left[\sum_{l=0}^{\infty}\sum_{l'=0}^{\infty}(2l+1)(2l'+1)\sigma_{sl}(\nu\rightarrow\nu')\left(\int_{-1}^{1}P_l(\mu')d\mu'\right)I_{l'}(\nu)P_{l'}P_l(\mu)P_n(\mu)\right]d\nu'\\
&+\int_0^\infty\left[\frac{c^2}{8\pi h\nu^3}\sum_{l=0}^{\infty}\sum_{l'=0}^{\infty}(2l+1)(2l'+1)\sigma_{sl}(\nu'\rightarrow\nu))I_l(\nu')I_{l'}(\nu)P_{l'}P_l(\mu)P_n(\mu)\right]d\nu'\\
&-\left.\int_0^\infty\left[\frac{c^2}{8\pi h\nu'^3}\sum_{l=0}^{\infty}\sum_{l'=0}^{\infty}(2l+1)(2l'+1)\sigma_{sl}(\nu\rightarrow\nu'))I_l(\nu)I_{l'}(\nu')P_{l'}P_l(\mu)P_n(\mu)\right]d\nu'\right].
\end{aligned}
\tag{1.32}
$$

Finally, integrating over μ in the interval $[-1,1]$ provides the general form of the time-dependent P_n equations including stimulated emission and scattering processes in the form:

$$
\begin{aligned}
&(2n+1)\frac{1}{c}\frac{\partial}{\partial t}I_n+\nabla\Big[nI_{n-1}+(n+1)I_{n+1}\Big]=(2n+1)\sigma_a^1\left[2\pi B_\nu\int_{-1}^{1}P_n(\mu)d\mu-I_n\right]\\
&+(2n+1)\int_0^\infty\sigma_{sn}(\nu'\rightarrow\nu)I_n(\nu')d\nu'\\
&-\int_0^\infty\left[\frac{1}{8\pi}\sum_{l=0}^{\infty}\sum_{l'=0}^{\infty}\sigma_{sl}(\nu\rightarrow\nu'))I_{l'}(\nu)\left(2\pi\int_{-1}^{1}P_l(\mu')d\mu'\right)A_{nll'}\right]d\nu'\\
&+\int_0^\infty\frac{c^2}{16\pi h}\sum_{l=0}^{\infty}\sum_{l'=0}^{\infty}\left[\frac{1}{\nu^3}\sigma_{sl}(\nu'\rightarrow\nu))I_l(\nu')I_{l'}(\nu)-\frac{1}{\nu'^3}\sigma_{sl}(\nu\rightarrow\nu'))I_l(\nu)I_{l'}(\nu')\right]A_{nll'}d\nu'
\end{aligned}
\tag{1.33}
$$

where the coefficient $A_{nll'}$ is determined from Legendre orthogonality relations as:

$$
A_{nll'}\equiv(2n+1)(2l+1)(2l'+1)\int_{-1}^{1}P_{l'}(\mu)P_l(\mu)P_n(\mu)d\mu=\begin{bmatrix}2\delta_{l',l}\\ 6(l+1)\delta_{l',l+1}+6l\delta_{l',l-1}\\ \cdots\end{bmatrix}
\tag{1.34}
$$

These equations represent an infinite set of coupled partial differential equations and are exactly equivalent to Eq. 1.26 in 1-D.

Since it is obviously not reasonable to include the entire set of equations in the actual calculation of the photon intensity, Eq. 1.33 is truncated by an assumption on the directional dependence of the photon field. For example, the simplest subset of these equations typically considered in radiation transport computations are the P_1 equations. In this case, the P_n equations are 'closed' by assuming that $I_n = \sigma_{sn} = 0$ for $n \geq 2$. This is equivalent to assuming that the photon intensity and scattering cross-section have only isotropic and linearly anisotropic components. Assuming this closure and solving for the terms in $A_{nll'}$ gives the time-dependent P_1 equations including stimulated emission and scattering as:

$n = 0$:

$$\begin{aligned}\frac{1}{c}\frac{\partial}{\partial t}I_0 + \nabla I_1 = \sigma_a^1\Big[4\pi B_\nu - I_0\Big] + \int_0^\infty \sigma_{s0}(\nu' \to \nu)I_0(\nu')d\nu' - I_0\int_0^\infty \sigma_{s0}(\nu \to \nu')d\nu' \\ + \frac{c^2}{8\pi h}I_0\int_0^\infty \left[\frac{1}{\nu^3}\sigma_{s0}(\nu' \to \nu) - \frac{1}{\nu'^3}\sigma_{s0}(\nu \to \nu')\right]I_0(\nu')d\nu' \\ + \frac{c^2}{8\pi h}I_1\int_0^\infty \left[\frac{1}{\nu^3}\sigma_{s1}(\nu' \to \nu) - \frac{1}{\nu'^3}\sigma_{s1}(\nu \to \nu')\right]I_1(\nu')d\nu',\end{aligned} \tag{1.35}$$

$n = 1$:

$$\begin{aligned}\frac{1}{c}\frac{\partial}{\partial t}I_1 + \frac{1}{3}\nabla I_0 = -\sigma_a^1 I_1 + \int_0^\infty \sigma_{s1}(\nu' \to \nu)I_1(\nu')d\nu' - I_1\int_0^\infty \sigma_{s0}(\nu \to \nu')d\nu' \\ + \frac{3c^2}{8\pi h}I_0\int_0^\infty \left[\frac{1}{\nu^3}\sigma_{s1}(\nu' \to \nu) - \frac{1}{\nu'^3}\sigma_{s0}(\nu \to \nu')\right]I_1(\nu')d\nu' \\ + \frac{3c^2}{8\pi h}I_1\int_0^\infty \left[\frac{1}{\nu^3}\sigma_{s0}(\nu' \to \nu) - \frac{1}{\nu'^3}\sigma_{s1}(\nu \to \nu')\right]I_0(\nu')d\nu',\end{aligned} \tag{1.36}$$

This closed set of equations is then completely independent of the variable μ, and can be numerically solved in a computer program of the radiation transport. However, the solution to the P_1 equations is only good for radiation fields that have a very weak directional dependence. In a few dedicated radiation transport codes, the P_n equations are considered up to $n = 14$ [55] in order to include the effects of highly non-linear scattering cross-sections and the associated asymmetries of the propagating photon field.

As is evident by Eq. 1.35 and Eq. 1.36, even the simplest form of the time-dependent

P_n equations are rather complex and can be computationally expensive. This is a problem in coupled radiation-hydrodynamics calculations where the frequency dependence is often divided into ≥ 100 frequency groups. Thus, the P_1 equations are often further simplified by taking the diffusion approximation. In this approximation, it is assumed that the linear anisotropy of the intensity field has a much lower total intensity than the isotropic component ($|I_1| << I_0$). Furthermore, if it is assumed that the linear anisotropy is steady state, and that there are approximately no frequency changes during collisions (i.e. $\sigma_{sl} \approx \sigma_{sl}(\nu' \rightarrow \nu)\delta(\nu' - \nu)$), then Eq. 1.36 can be rewritten as:

$$I_1 = -\frac{1}{\sigma_{tr}} \nabla I_0, \tag{1.37}$$

where the radiative transfer cross-section has been defined as:

$$\sigma_{tr} = \sigma_a^1 + \int_0^\infty \sigma_{s0}(\nu \rightarrow \nu')d\nu' + \sigma_{s1} = \sigma_a^1 + \sigma_s + \sigma_{s1}. \tag{1.38}$$

Inserting Eq. 1.37 into Eq. 1.35, and neglecting terms proportional to $|I_1|^2$ then yields the diffusion equation including stimulated emission and scattering:

$$\begin{aligned} \frac{1}{c}\frac{\partial}{\partial t} I_0 - \nabla \cdot \frac{1}{3\sigma_{tr}} \nabla I_0 = \sigma_a^1 \Big[4\pi B_\nu - I_0 \Big] - \sigma_{s0} I_0 + \int_0^\infty \sigma_{s0}(\nu' \rightarrow \nu) I_0(\nu') d\nu' \\ + \frac{c^2}{8\pi h} I_0 \int_0^\infty \left[\frac{1}{\nu^3} \sigma_{s0}(\nu' \rightarrow \nu) - \frac{1}{\nu'^3} \sigma_{s0}(\nu \rightarrow \nu') \right] I_0(\nu') d\nu'. \end{aligned} \tag{1.39}$$

If it is again assumed that no energy change occurs in scattering, then the stimulated scattering terms identically cancel, and Eq. 1.39 can be approximated as:

$$\frac{\partial I_0}{\partial t} = \nabla \cdot cD \nabla I_0 + c\sigma_a^1 \Big[4\pi B_\nu - I_0 \Big], \tag{1.40}$$

where D is the diffusion coefficient defined as $D \equiv [3\sigma_{tr}]^{-1}$. This is the textbook form of the time-dependent diffusion equation, and is one of the options for the radiation transport algorithm in the BUCKY radiation-hydrodynamics code referenced throughout this thesis (see §4.2).

—

There are a number of issues associated with the implementation of Eq. 1.40. As was stated during the derivation, the diffusion approximation assumes that the radiation intensity is nearly isotropic everywhere in the medium. Thus, there must be a similar amount of radiation flowing in each direction for the diffusion equation to provide an accurate solution of the radiative transfer. If the opacity of the medium is very low, or if there are steep gradients in the intensity field, then the main component of the radiation field is no longer isotropic and the diffusion approximation breaks down. The extreme case occurs when the radiation is free-streaming. In this case $\sigma_{tr} \approx 0$, and Eq. 1.40 becomes:

$$\frac{\partial I_0}{\partial t} \text{“}\infty\text{”} \nabla I_0, \tag{1.41}$$

implying that the radiation propagation speed goes to infinity. To correct this unphysical result, a flux-limiter is applied to the diffusion coefficient that prevents the propagation from occurring faster than the speed of light [56, 57]. One very common limiter used in radiation transport is the ‘SUM’-limiter, which has the form:

$$D = \frac{1}{3\sigma_{tr} + \frac{1}{I_0}|\nabla I_0|}. \tag{1.42}$$

Inserting this into Eq. 1.40 and taking the limit as σ_{tr} goes to 0, then the intensity gradient becomes the dominant term in the denominator and the diffusion equation becomes:

$$\frac{\partial I_0}{\partial t} = c\nabla I_0, \tag{1.43}$$

which is the proper classical result in the free-streaming limit.

The problem with flux-limited diffusion is that, although it provides a good approximation to the transport equation in the optically thick and optically thin limits, the solution is ad-hoc in between. That is, the only restriction placed on the flux-limiter is

that it must converge to the proper form in the two extreme limits. Clearly, there are a number of different choices that one can make for the form of the flux-limiter to satisfy these requirements.

A few additional examples of commonly used flux-limiters are the 'MAX'-limiter:

$$D = \frac{1}{\max\left(3\sigma_{tr}, \frac{1}{I_0}|\nabla I_0|\right)}, \tag{1.44}$$

the Larsen-limiter:

$$D = \frac{1}{\left[\left(3\sigma_{tr}\right)^n + \left(\frac{1}{I_0}|\nabla I_0|\right)^n\right]^{1/n}}, \tag{1.45}$$

(for n a dimensionless parameter), and the simplified Levermore-Pomraning-limiter [58]:

$$D = \frac{1}{\sigma_{tr} R}\left[\coth R - \frac{1}{R}\right], \qquad \text{for} \qquad R \equiv \frac{|\nabla I_0|}{\sigma_{tr} I_0}. \tag{1.46}$$

Each of these converges to the same limits as the SUM-limiter, but have very different profiles in between. However, the SUM- and MAX-limiters represent the lower and upper bound of the total radiation flow attainable by most implementations of flux-limited diffusion. To illustrate this, Figure 1.17 shows the single group flux-limiter, $\tilde{D} = 3\sigma_{tr}D$, versus the scaled radiation energy gradient (R in Eq. 1.46) for the SUM-, MAX-, Larsen-, and Levermore-Pomraning-limiters. As required, each scaled diffusion coefficient approaches 1 as R goes to 0, and approaches 0 as R goes to infinity. However, at values of R between 1 and 10, the diffusion coefficient is quite a bit different across the different limiters. In this region, the sum limiter is by far the most restrictive (with the lowest diffusion coefficient) while the max limiter is the least restrictive (with the highest diffusion coefficient). Therefore, if the characteristics of the radiation field have an R value between about 1 and 10, then the radiation is neither free-streaming nor diffusing, and flux-limited diffusion theory is suspect.

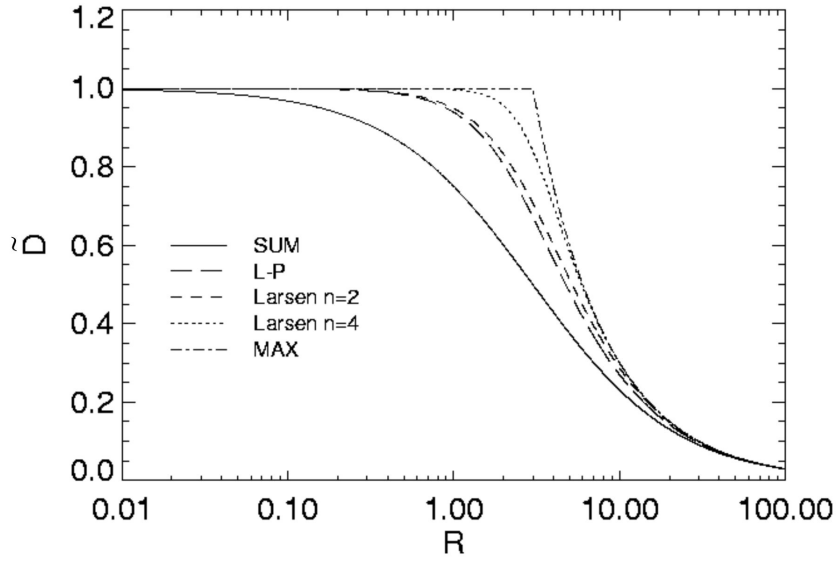

Figure 1.17: Flux-limiter factors, $\tilde{D} = 3\sigma_{tr}D$, versus the scaled radiation gradient, R, for some common flux-limiters.

1.4.2 Discrete ordinates and the method of short-characteristics

As was shown in §1.4.1 the flux-limited diffusion approximation breaks down in the region where the scaled energy gradient, R, is between about 1 and 10. If the characteristics of the radiation field and the medium are in this regime for a significant period of time, then a non-diffusive solution may be required in order to properly predict the radiative transfer rates. One alternative approach to solving the transport equation, which avoids an assumption on the angular distribution of the intensity field, is the method of discrete ordinates.

Rather than expanding the transport equation into an infinite set of equations that are independent of the variable $\hat{\Omega}$, the angular integral in Eq. 1.26 can be solved by a numerical approximation. Expanding the scattering cross-section into Legendre polyno-

	i	w_i	μ_i
$N = 2$	1	0.5000000000	0.2113248654
	2	0.5000000000	0.7886751346
$N = 5$	1	0.1184634425	0.0469100770
	2	0.2393143352	0.2307653449
	3	0.2844444444	0.5000000000
	4	0.2393143352	0.7692346551
	5	0.1184634425	0.9530899230

Table 1.1: Integration angle cosines and weights for discrete-ordinates and multi-angle short-characteristics.

mials as in Eq. 1.28, the 1-D planar transport equation can be written as:

$$\begin{aligned}\frac{1}{c}\frac{\partial}{\partial t}I + \mu\nabla I = \sigma_a^1\left[2\pi B_\nu - I\right] \\ + \frac{1}{2}\int_0^\infty \left(1 + \frac{c^2}{2h\nu^3}I(\nu)\right)\sum_{l=0}^{\infty}(2l+1)\sigma_{sl}(\nu' \to \nu)P_l(\mu)\left[\int_{-1}^{1}P_l(\mu')I(\nu',\mu')d\mu'\right]d\nu' \\ - \frac{1}{2}\int_0^\infty I(\nu)\sum_{l=0}^{\infty}(2l+1)\sigma_{sl}(\nu \to \nu')P_l(\mu)\left[\int_{-1}^{1}P_l(\mu')\left(1 + \frac{c^2}{2h\nu'^3}I(\nu',\mu')\right)d\mu'\right]d\nu',\end{aligned} \tag{1.47}$$

where the dependence on x, ν, and t has been implicitly assumed for brevity. Now, the angular integrals can be approximated by numerical quadrature using the generic formula:

$$\int_{-1}^{1} f(\mu)d\mu \approx \sum_{i=0}^{N} w_i f(\mu_i) \tag{1.48}$$

for w_i the integration weights at each quadrature node, μ_i, as given in Table 1.1. Applying this to Eq. 1.47 then yields the 1-D time-dependent discrete ordinates equation including stimulated emission and scattering:

$$\frac{1}{c}\frac{\partial}{\partial t}I(\mu_i) + \mu_i \nabla I(\mu_i) = \sigma_a^1 \left[2\pi B_\nu - I(\mu_i)\right] \tag{1.49}$$
$$+ \frac{1}{2}\int_0^\infty \left(1 + \frac{c^2}{2h\nu^3} I(\nu, \mu_i)\right) \sum_{l=0}^{L}\sum_{j=0}^{N} (2l+1)\sigma_{sl}(\nu' \to \nu) P_l(\mu_j) w_j P_l(\mu_j) I(\nu', \mu_j) d\nu'$$
$$- \frac{1}{2}\int_0^\infty I(\nu, \mu_i) \sum_{l=0}^{L}\sum_{j=0}^{N} (2l+1)\sigma_{sl}(\nu \to \nu') P_l(\mu_j) w_j P_l(\mu_j) \left(1 + \frac{c^2}{2h\nu'^3} I(\nu', \mu_j)\right) d\nu',$$

where the expansion in σ_{sl} has been cut-off after L terms, and the index $i = 0, 1, \ldots, N$ corresponds to the N different angles in the quadrature set. This equation is non-linear, and must be solved by assuming an initial form of I for the right hand side, and iterating until the solution converges. Because the quadrature sets are symmetric about $\mu = 0$, Eq. 1.49 corresponds to $N/2$ equations which propagate the radiation in the forward direction, and $N/2$ equations which propagate the radiation in the backward direction. The total radiation intensity is then found by integrating over all angles such that:

$$I_0(x, \nu, t) = \sum_{i=0}^{N} w_i I(x, \nu, \mu_i, t). \tag{1.50}$$

The quadratic dependence on I in Eq. 1.49 due to the stimulated emission and scattering terms can complicate the numerical convergence of the iterative solutions. If it is assumed that the contribution to the specific intensity from induced scattering is small, then the time-dependent discrete ordinates equation can be written as:

$$\frac{1}{c}\frac{\partial}{\partial t}I(\mu_i) + \mu_i \nabla I(\mu_i) + \chi_i I(\mu_i) = q_i, \tag{1.51}$$

$$\text{for} \qquad \chi_i = \frac{1}{2}\int_0^\infty I(\nu,\mu_i)\sum_{l=0}^{L}\sum_{j=0}^{N}(2l+1)\sigma_{sl}(\nu\rightarrow\nu')P_l(\mu_j)w_j P_l(\mu_j)d\nu' + \sigma_a^1$$

$$\text{and} \qquad q_i = \frac{1}{2}\int_0^\infty \sum_{l=0}^{L}\sum_{j=0}^{N}(2l+1)\sigma_{sl}(\nu'\rightarrow\nu)P_l(\mu_j)w_j P_l(\mu_j)I(\nu',\mu_j)d\nu' + 2\pi\sigma_a^1 B_\nu.$$

This is the form most commonly utilized in 1-D radiation transport codes. In contrast to the diffusion equation, discrete ordinates does not require a flux-limiter. This can be easily verified by taking the limit as all interaction cross-sections go to zero (free-streaming) in Eq. 1.51. In this case, the equation becomes $\frac{\partial}{\partial t}I_i = -c\mu_i\nabla I_i$ and the radiation simply propagates unattenuated throughout the medium. Thus, Eq. 1.51 is generally applicable for diffusive conditions, free-streaming conditions, and everywhere in-between.

—

The discrete ordinates equation can be discretized on a spatial mesh and solved iteratively by standard finite difference methods, or it can be recast into an optical depth grid and solved along characteristic rays by the multi-angle method of short-characteristics [60, 61].

If it is assumed that the radiation field is steady state over a particular time-step, and that scattering is not an important contribution to the transport dynamics, then Eq. 1.51 can be simplified to:

$$\mu_i\frac{\partial I(x,\nu,\mu_i,t)}{\partial x} = \sigma_a^1(x,\nu,t)\left[2\pi B_\nu(x,\nu,t) - I(x,\mu_i,\nu,t)\right]. \tag{1.52}$$

Defining the monochromatic optical depth, τ, as:

$$\partial\tau = \sigma_a^1\partial x, \tag{1.53}$$

then Eq. 1.52 can be transformed to optical depth space as:

$$\mu_i \frac{\partial I_i}{\partial \tau} = \left[2\pi B_\nu - I_i\right]. \tag{1.54}$$

Or, multiplying through by $\mu_i^{-1} e^{\frac{\tau}{\mu_i}}$ gives:

$$\frac{\partial}{\partial \tau}\left(I_i e^{\frac{\tau}{\mu_i}}\right) = \frac{2\pi}{\mu_i} B_\nu e^{\frac{\tau}{\mu_i}}. \tag{1.55}$$

Separating this equation into outward ($0 < \mu \leq 1$) and inward ($-1 \leq \mu < 0$) going rays, and integrating along characteristics (paths along each μ_i) from some nearby point in the slab (denoted by τ_{k-1} and τ_{k+1}) gives:

$$0 < \mu \leq 1: \qquad \int_{I_i^+(\tau_{k-1})e^{\frac{\tau_{k-1}}{\mu_i}}}^{I_i^+(\tau_k)e^{\frac{\tau_k}{\mu}}} d\left(I' e^{\frac{\tau'}{\mu}}\right) = \frac{2\pi}{\mu_i} \int_{\tau_{k-1}}^{\tau_k} B_\nu e^{\frac{\tau'}{\mu_i}} d\tau' \tag{1.56}$$

$$-1 \leq \mu < 0: \qquad \int_{I_i^-(\tau_{k+1})e^{\frac{\tau_{k+1}}{\mu_i}}}^{I_i^-(\tau_k)e^{\frac{\tau_k}{\mu_i}}} d\left(I' e^{\frac{\tau'}{\mu}}\right) = \frac{2\pi}{\mu_i} \int_{\tau_{k+1}}^{\tau_k} B_\nu e^{\frac{\tau'}{\mu_i}} d\tau'. \tag{1.57}$$

Finally, carrying out the integrals gives the analytic equations of multi-angle short-characteristics at the point τ_k:

$$I_i^+(\tau_k) = I_i^+(\tau_{k-1}) e^{-\Delta\tau_{i,k-1}} + 2\pi \int_0^{\Delta\tau_{i,k-1}} B_\nu e^{-\Delta\tau'} d\Delta\tau' \tag{1.58}$$

$$I_i^-(\tau_k) = I_i^-(\tau_{k+1}) e^{-\Delta\tau_{i,k}} + 2\pi \int_0^{\Delta\tau_{i,k}} B_\nu e^{-\Delta\tau'} d\Delta\tau', \tag{1.59}$$

where the optical depth interval, $\Delta\tau$, has been defined as:

$$\Delta\tau_{i,k} = \frac{(\tau_{k+1} - \tau_k)}{|\mu_i|}. \tag{1.60}$$

Eq. 1.58 and 1.59 can then be solved by sweeping forward and backward through the slab. The only difficulty lies in solving for the source integrals. Typically, it is sufficient to consider the source term to have only a linear or quadratic dependence on $\tau(x)$. In either case, the solution can be written as a three coefficient evaluation:

$$\int^{\pm} B_\nu e^{-\Delta\tau'} d\Delta\tau' = \alpha_k^{\pm} B_\nu(\tau_{k-1}) + \beta_k^{\pm} B_\nu(\tau_k) + \gamma_k^{\pm} B_\nu(\tau_{k+1}), \tag{1.61}$$

	Linear Interpolation	**Quadratic Interpolation**
α_k^+	$e_{0,k} - \frac{e_{1,k}}{\Delta\tau_{k-1}}$	$e_{0,k} + \frac{e_{2,k}-(\Delta\tau_k+2\Delta\tau_{k-1})e_{1,k}}{\Delta\tau_{k-1}(\Delta\tau_k+\Delta\tau_{k-1})}$
β_k^+	$\frac{e_{1,k}}{\Delta\tau_{k-1}}$	$\frac{(\Delta\tau_k+\Delta\tau_{k-1})e_{1,k}-e_{2,k}}{\Delta\tau_{k-1}\Delta\tau_k}$
γ_k^+	0	$\frac{e_{2,k}-\Delta\tau_{k-1}e_{1,k}}{\Delta\tau_k(\Delta\tau_k+\Delta\tau_{k-1})}$
α_k^-	0	$\frac{e_{2,k+1}-\Delta\tau_k e_{1,k+1}}{\Delta\tau_{k-1}(\Delta\tau_k+\Delta\tau_{k-1})}$
β_k^-	$\frac{e_{1,k+1}}{\Delta\tau_k}$	$\frac{(\Delta\tau_k+\Delta\tau_{k-1})e_{1,k+1}-e_{2,k+1}}{\Delta\tau_{k-1}\Delta\tau_k}$
γ_k^-	$e_{0,k+1} - \frac{e_{1,k+1}}{\Delta\tau_k}$	$e_{0,k+1} + \frac{e_{2,k+1}-(\Delta\tau_{k-1}+2\Delta\tau_k)e_{1,k+1}}{\Delta\tau_k(\Delta\tau_k+\Delta\tau_{k-1})}$

Table 1.2: Coefficients for solving the source integrals for linear or quadratic interpolation of B_ν in the multi-angle short-characteristics equations.

where the angular subscript, i, has been suppressed for clarity. Table 1.2 lists the values of these coefficients for both linear and quadratic interpolations of B_ν, where the exponential functions, $e_{(0,1,2),k}$ are given by:

$$e_{0,k} = 1 - e^{-\Delta\tau_{k-1}}$$

$$e_{1,k} = \Delta\tau_{k-1} - e_{0,k}$$

$$e_{2,k} = (\Delta\tau_{k-1})^2 - 2e_{1,k}.$$

Once I^+ and I^- have been determined at every point, τ_k, then the first moment of the specific intensity (the scalar flux) can be computed as:

$$I_0(\tau_k, \nu, t) = \sum_{i=1}^{N} w_i \left[I_i^+(\tau_k, \nu, t) + I_i^-(\tau_k, \nu, t) \right]. \tag{1.62}$$

It should be noted that, unlike the implementation of the diffusion equation, the method of short-characteristics described here is only applicable in planar geometry, and is only derived for time-independent radiation transport. This places serious restrictions on the usefulness of short-characteristics for many problems, and thought should always be given to its applicability before using it to model the radiation transport.

1.4.3 Other forms of approximate transport

There are many other approximate radiation transport techniques that have been developed for a range of different applications. However, only a few of these have been widely accepted as a significant benefit over those methods already discussed. Two notable examples of those that have been widely utilized in neutral particle transport are the variable Eddington method and time-independent integral transport.

In the derivation of the P_1 equations in §1.4.1, it was assumed that the quadratically anisotropic specific intensity was negligible ($I_2 \approx 0$). If instead it is assumed that $I_2 = fI_0$, for f the variable Eddington factor given by:

$$f \equiv \frac{\int_{-1}^{1} \mu'^2 I(\mu') d\mu'}{\int_{-1}^{1} I(\mu') d\mu'}, \tag{1.63}$$

then the Variable Eddington Factor (VEF) equations can be written as:

$$\text{n=0:} \qquad \frac{1}{c}\frac{\partial}{\partial t} I_0 + \nabla I_1 = \sigma_a^1 \left[4\pi B_\nu - I_0\right] - \sigma_s I_0 + \int_0^\infty \sigma_{s0}(\nu' \to \nu) I_0(\nu') d\nu', \tag{1.64}$$

$$\text{n=1:} \qquad \frac{1}{c}\frac{\partial}{\partial t} I_1 + \nabla (f I_0) = -\sigma_{tr} I_1, \tag{1.65}$$

where it is assumed that the stimulated scattering terms can be neglected. The Eddington factor must then be calculated to fit the problem of interest. For example, if $f = 1/3$, then the VEF equations are equivalent to the P_1 equations and can be reduced identically to the time-dependent diffusion equation. Since the diffusion equation is a very good approximation in optically thick media at thermal equilibrium, then $f = 1/3$ will force the VEF equations to produce the proper radiative transfer rates in the limit of diffusion.

The real advantage of the VEF method over the P_1 equations occurs when the radiation is nearly free-streaming. That is, in the optically thin limit, the P_1 equations can be shown to propagate radiation at a speed of $c/\sqrt{3}$. However, if the variable Eddington factor is chosen to be $f = 1$, then the VEF equations avoid this unphysical result by

propagating the radiation at a speed of c. Thus, as indicated by Eq. 1.63, the Eddington factor should be a function of the anisotropy of the specific intensity in the medium. The difficulty is in choosing the proper form of f such that the VEF equations will predict the correct transfer rates for all radiation fields. The issue becomes somewhat like that of the flux-limiter. Namely, the VEF equations can predict the proper radiative transfer rates at the limits of diffusion and free-streaming, but unless the Eddington factor is calculated from a transport calculation of the full specific intensity, I, then the VEF solutions can be unreliable in-between.

A final class of important deterministic radiation transport approximations is the integral transport method. This method has a significant advantage over those already discussed in that it does not, in principle, require making any a-priori assumptions about the distribution of the radiation field. Integral transport works by integrating the transport equation over angle and thereby solving directly for the scalar flux (which has been referred to here as I_0). It does, however, require making an assumption on the directionality of the scattering terms. In addition, little work if any has been conducted on determining the integration kernels required for a closed solution when including stimulated emission and/or scattering terms. Regardless, because the transport solution depends on both the dimensions and opacity of the plasma, the integration kernel must be re-evaluated for every frequency at every time-step. This is typically not practical for multi-group radiation-hydrodynamics calculations. For these reasons, integral transport has only been utilized in applications of neutron transport (with a few rare exceptions [62]) where scattering is assumed to be nearly isotropic [50].

Chapter 2

Literature Search

2.1 Computational Studies on the Radiation Transport Equation

As was discussed in §1.4, there are a number of different approximations to the transport equation. Each of these are valid under a particular range of conditions, and care must be taken to verify that these conditions are met in order to properly compute the radiative transfer rates. Because of this, there have been a number of studies conducted on the differing solutions that can arise by applying different transport methods to the same, sometimes even simplistic problem.

One such study was published recently by G.L. Olson et al. [57] on the subject of diffusion, P1, and variable Eddington transport. They first considered the simple case of a non-equilibrium radiative transfer problem consisting of an initially cold, homogeneous, infinite, and purely absorbing medium with constant opacity. Defining the material heat

capacity as a function of the plasma temperature in the form:

$$c_v = 4aT^3 \tag{2.1}$$

for a the radiation constant ($a \equiv 4\sigma_{SB}/c$), then the material energy balance equation can be written as:

$$\frac{1}{c}\frac{\partial T^4}{\partial t} = \sigma_a^1 \left(\frac{a}{C} I_0 - T^4\right). \tag{2.2}$$

Choosing $\sigma_a^1 = 1$ and inserting this result into the transport equation, then the first two of the mono-energetic P_n equations (i.e. the zeroth- and first-angular moments) can be written as:

$$\frac{\partial \hat{I}_0}{\partial \tau} + \frac{\partial \hat{I}_1}{\partial x} = \theta - \hat{I}_0 + \hat{S}, \tag{2.3}$$

$$\frac{\partial \hat{I}_1}{\partial \tau} + \frac{1}{3}\frac{\partial \hat{I}_0}{\partial x} + \frac{2}{3}\frac{\partial \hat{I}_2}{\partial x} = -\hat{I}_1, \tag{2.4}$$

where τ is the unit-less time variable, $\tau \equiv \sigma_a^1 ct = ct$, and the scaled transport variables are defined as:

$$\hat{I}_0 \equiv \frac{I_0}{caT_H^4} = \left(\frac{T_r}{T_H}\right)^4, \quad \hat{I}_1 \equiv \frac{I_1}{caT_H^4}, \quad \hat{I}_2 \equiv \frac{I_2}{caT_H^4}, \quad \theta \equiv \left(\frac{T}{T_H}\right), \quad \hat{S} \equiv \frac{S}{aT_H^4},$$

for T_H the hohlraum reference temperature. Finally, assuming that the internal radiation source is turned on at $\tau = 0$ with a magnitude of:

$$\hat{S} = \begin{cases} 1, & |x| \leq \frac{1}{2}, ct \leq 10 \\ 0, & \text{elsewhere} \end{cases}, \tag{2.5}$$

and setting an initial scaled temperature value of $\theta(x, 0) = 10^{-10}$, then Olson et al. were able to calculate an analytic solution to the transport equations in Eq. 2.3 and 2.4.

Figure 2.1(a) shows a comparison between the analytic calculation, and those solutions obtained by non-flux-limited diffusion, the P_1 equations, and the VEF method. In

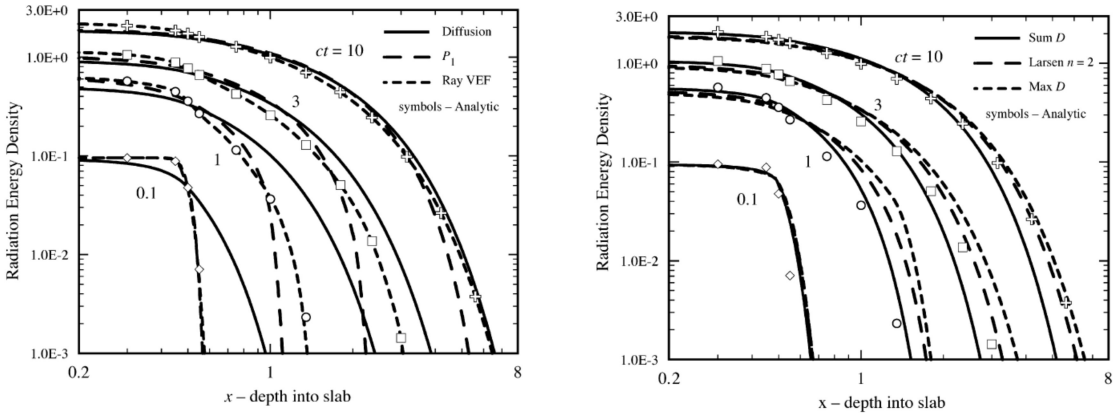

(a) **(b)**

Figure 2.1: An analytic benchmark solution to the coupled radiation transport and material energy equations compared to **(a)** diffusion, P_1, VEF, and **(b)** flux-limited diffusion for the SUM-, MAX-, and Larsen(n=2)-limiter [57].

this case, the variable Eddington factors were chosen by an independent discrete ordinates solution to the transport equation. Note from Figure 2.1(a) that, with the proper functional form of f, the VEF equations, and therefore the discrete ordinates solution, give a very accurate result at all times. On the other hand, non-limited diffusion propagates the radiation too quickly, especially at early times. This rapid transport occurs because the scaled energy gradient, R, defined in Eq. 1.46 becomes large near a boundary layer. As was shown in §1.4.1, in the limit as R goes to infinity, the diffusion approximation breaks down and predicts rapid, unphysical transport speeds. In the opposite sense, the P_1 equations propagate the radiation too slowly at later times, but give a good approximation at early times near the source boundary layer. The late time lag occurs because of the limiting propagation speed of $c/\sqrt{3}$ in the P_1 equations, which was discussed in §1.4.3.

Figure 2.1(b) shows the comparison between the analytical calculation and flux-limited diffusion solutions using the SUM-limiter given by Eq. 1.42; the MAX-limiter

given by Eq. 1.44; and the Larsen-limiter given by Eq. 1.45. All three flux-limiters give accurate results at early times near the boundary layer where the scaled energy gradient is large. This is expected since each limiter has the same form in the limiting case as R goes to infinity. Later in time, the SUM-limiter begins to lag behind the analytic solution as the radiation propagates through a region of intermediate R where the SUM-limiter is the most restrictive. In the opposite sense, the MAX-limiter propagates radiation out ahead of the analytic solution at all times, but gives a fairly good approximation by the time $\tau = 10$. This is fairly deep into the material where R is on the order of 1, and the MAX-limiter gives the equivalent solution as the non-limited diffusion approximation. The Larsen-limiter gives solutions that are similar to the MAX-limiter with a slightly better approximation to the analytic solution at each time. No matter which form of the flux limiter is applied, it is clear from Figure 2.1(a) that flux-limited diffusion is a significant improvement over non-limited diffusion.

—

The previous test problem is useful because it can be solved analytically, and therefore gives a direct benchmark by which to compare the various approximate transport methods. However, assuming a constant, temperature-independent opacity is not physical. To account for this, Olson et al. [57] proposed a related problem where the opacity is assumed to vary as the cube of the temperature in the form $\sigma_a^1 = \sigma_{a,0}^1 \hat{T}^{-3} = \sigma_{a,0}^1 \theta^{-3/4}$, for $\hat{T} = T/T_H$. Then, using the same form of the heat capacity as defined above, and setting $\sigma_{a,0}^1 = 1$, then Eq. 2.3 and 2.4 must be rewritten as:

$$\frac{\partial \hat{I}_0}{\partial \tau} + \frac{\partial \hat{I}_1}{\partial x} = \theta^{-3/4}(\theta - \hat{I}_0), \tag{2.6}$$

$$\frac{\partial \hat{I}_1}{\partial \tau} + \frac{1}{3}\frac{\partial \hat{I}_0}{\partial x} + \frac{2}{3}\frac{\partial \hat{I}_2}{\partial x} = -\theta^{-3/4}\hat{I}_1, \tag{2.7}$$

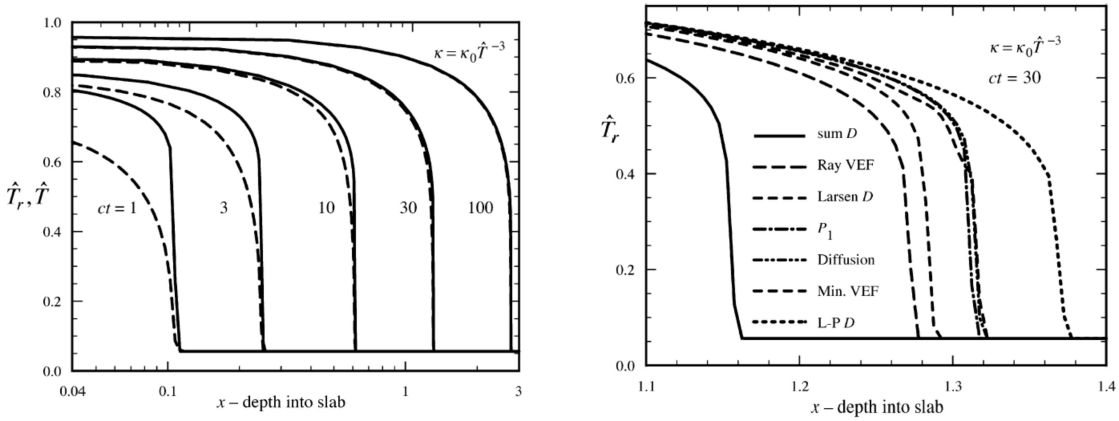

(a) **(b)**

Figure 2.2: (a) Normalized radiation (solid) and plasma (dashed) temperatures for the temperature-dependent opacity problem as calculated by the P_5 equations, **(b)** and the radiation temperatures for a few other transport approximations at $\tau = 30$ [57].

where it has been assumed that all internal source functions are negligible. These equations are non-linear and have no direct analytic solution. To develop a time-dependent approximation to this problem, Olson et al. applied a Marshak boundary condition at $\tau = x = 0$, and solved the radiation transport equation by the P_5 approximation. The results of this calculation for both the scaled radiation and material temperatures are shown in Figure 2.2(a). The radiation wave front stays sharp over the entire calculation due to the strong dependence of the opacity on the material temperature. This is in stark contrast to the solution shown in Figure 2.1(a), where the wave front rapidly spreads after a time of $\tau = 0.1$. The solution shown in Figure 2.2(a) is much more physical, and corresponds to what is often observed in high-energy density laboratory plasmas. This radiation temperature history was assumed to be a very good approximation in the absence of a direct analytic calculation, and is therefore taken as the 'benchmark' solution to Eq. 2.6 and 2.7.

A comparison between the benchmark solution in Figure 2.2(a), and the solution

calculated by a number of different transport approximations is shown in Figure 2.2(b) at a time of $\tau = 30$ (note the expanded spatial scale). The variable Eddington factors were again calculated by a discrete ordinates method, and give a VEF solution that falls directly along the P_5 benchmark solution (which is not shown for clarity). Non-limited diffusion, max-limited diffusion, and the P1 equations all provide approximately the same solution, which propagates the radiation front ahead of the benchmark solution by $\approx 4\%$ in x. Again, these methods allow too much radiation to flow in the region where $1 \leq R \leq 10$, and thus over-predict the radiative transfer rates. On the other hand, sum-limited diffusion is too restrictive, and propagates the radiation front behind the benchmark solution by $\approx 10\%$ in x. Larsen-limited diffusion with $n = 2$ gives the best diffusive approximation to the benchmark solution, and only propagates the radiation ahead by $\approx 1\%$. However, Olson et al. point out that this does not imply the Larsen limiter will always give the best approximation. Like all of the limiters discussed in this document, the Larsen limiter has no transport knowledge between the limits of diffusion and free-streaming, and therefore may not provide the best approximation in any other particular problem.

It is also noted that, although the material is optically thick ahead of the wave front, and that the front is far from the material boundary, there are still distinct differences between the diffusion approximation and a more detailed radiation transport calculation. This is because the sharp edge of the radiation wave front acts as an internal boundary where the radiation flow has a very strong directionality and therefore violates the primary requirement of diffusion. Thus, in the case of a strong radiation wave propagating through a plasma, simply being optically thick is not sufficient to assure the validity of the diffusion limit. When any one of the flux-limited diffusion approximations predicts a solution that is drastically different from any of the other flux-limiters, then a more de-

tailed transport calculation may predict a very different solution than any of the diffusion approximations [57].

—

There are many more publications in the literature about the differences between the various approximations to the transport equation than can be listed here [63–65]. The point is that, in the absence of an exact solution, an approximation must be made that necessarily limits the range of conditions over which that solution is applicable. Thus, when employing any approximate method to solve for the radiation flow in a particular problem, thought must be given as to where and when the approximations may break down.

2.2 Radiative Transfer Experiments in Low-Density Foams

Studies on the propagation of radiation in low-density ($< 50 mg/cc$) foams at high energy-density have only appeared in the open literature since about 1990. The majority of this work has been in the characterization of mid- to high-Z foams for laser beam smoothing studies in direct-drive ICF. It was discovered that, encasing an ICF capsule in a foam layer with a density approximately equivalent to the electron critical density, then the direct laser energy is deposited over a larger volume within the capsule ablator [22,66,67]. This can smooth out the 'speckling' of the laser beam spots and thereby reduce the Rayleigh-Taylor instability growth that has historically limited the direct-drive approach to ICF. Thus, there are many studies available in the literature that focus on the interaction of high-intensity laser radiation with low-density foams [68–70]. However, the laser energy

is of significantly longer wavelength, and correspondingly shorter mean free paths, than the x-ray radiation that exists inside a z-pinch driven dynamic hohlraum.

Of the experiments that have been conducted under high-temperature thermal radiation fields, the most recent is that of C.A. Back et al. [71, 72] on the measurement of supersonic heat waves through mid- to high-Z foams on the OMEGA laser. In these experiments, Back et al. irradiated $40 - 50mg/cc$ SiO_2 and Ta_2O_5 foams with a high-temperature thermal radiation pulse over a fairly short time duration. The foam samples were placed at one end of a gold 'halfraum' (one laser entrance hole), which was $1.2mm$ long with a $1.6mm$ diameter. Two $\approx 1ns$ square laser pulses produced a radiation temperature at the sample location that peaked at $\approx 190eV$, and lasted for a duration of $\approx 4ns$ (at a temperature above $100eV$). With this drive history, the radiation burn-through times (the time that it takes for the radiation to penetrate the back surface of the foam) were measured using a streaked x-ray spectrometer for foam samples up to $1mm$ thick.

The measured burn-through times are compared to analytic 1-D calculations as a function of total foam thickness for both Ta_2O_5 and SiO_2 foam experiments in Figure 2.3(a). The 1-D calculations of the SiO_2 burn-through times are conducted with the diffusion approximation for times greater than $1.1ns$, and a near-streaming calculation for earlier times. In contrast, the calculations of the Ta_2O_5 burn-through times are conducted with the diffusion approximation throughout since the total optical depth of the Ta_2O_5 is greater than 1 for all sample sizes (due to the high-Z of Ta). In every case, the calculations actually predict faster burn-through times than were measured in the experiments. The authors attributed this to an uncertainty in the late-time radiation pulse, pointing out that the 1-D calculations assume a constant $185eV - 190eV$ radiation temperature boundary condition. To address this, integrated 2-D calculations of the hohlraum tem-

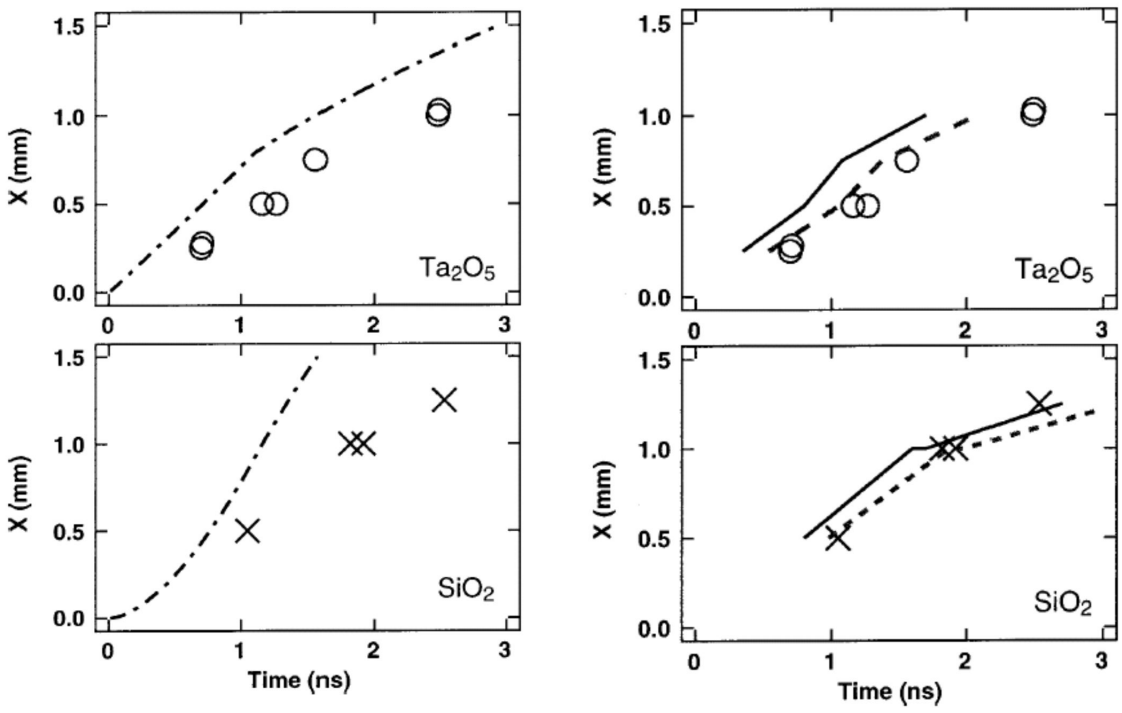

Figure 2.3: Radiation burn-through data for Ta_2O_5 and SiO_2 foams in comparison to **(a)** 1-D analytical models, and **(b)** 2-D integrated rad-hydro computations [71].

perature history and the sample radiation-hydrodynamics processes were conducted for each foam sample, and are compared to the experimental data in Figure 2.3(b). The solid curves are generated using the calculated radiation drive history, while the dashed curves are generated by correcting the calculated drive to better match the experimentally measured drive temperatures. The latter shows fairly good agreement, indicating that the applied radiation transport technique may provide an adequate solution of the radiation propagation speed. However, it is not known which radiation transport technique, or which flux-limiter (if any) was utilized in these simulations.

Some other work by T. Afshar-rad et al. [73] measured the propagation of radiation waves in low-density foams irradiated by a $1ns$ wide, $138 \pm 12eV$ blackbody produced

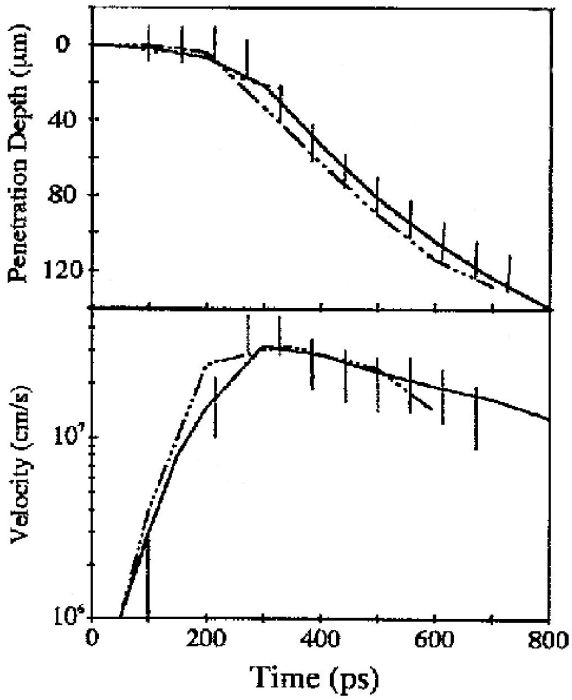

Figure 2.4: Position and velocity of the ionization wave front in a $50mg/cc$ triacrylate ($C_{15}H_20_6$) foam chemically doped with a chlorine monomer ($C_9H_3O_2Cl_{l5}$) under irradiation by a $\approx 140eV$ blackbody radiation drive [73].

by the VULCAN laser system at Rutherford Appleton Laboratory. These foams were $\approx$ $50mg/cc$ triacrylate ($C_{15}H_20_6$) chemically doped with a chlorine monomer ($C_9H_3O_2Cl_{l5}$) in samples about $200\mu m$ thick. Afshar-rad et al. measured the transmission of a $175eV$ backlighter through the width of the foam (perpendicular to the direction of the bulk radiation propagation) and thereby measured the propagation history of the radiation front over the entire foam sample. A comparison between the experimental data and both 1- and 2-D calculations are shown in Figure 2.4. The 2-D calculations were conducted using an implicit Monte Carlo radiation transport technique, but it is unknown which technique was used in the 1-D calculations. The ionization front is assumed to occur where the foam becomes 50% transparent to the backlighter radiation, at a calculated

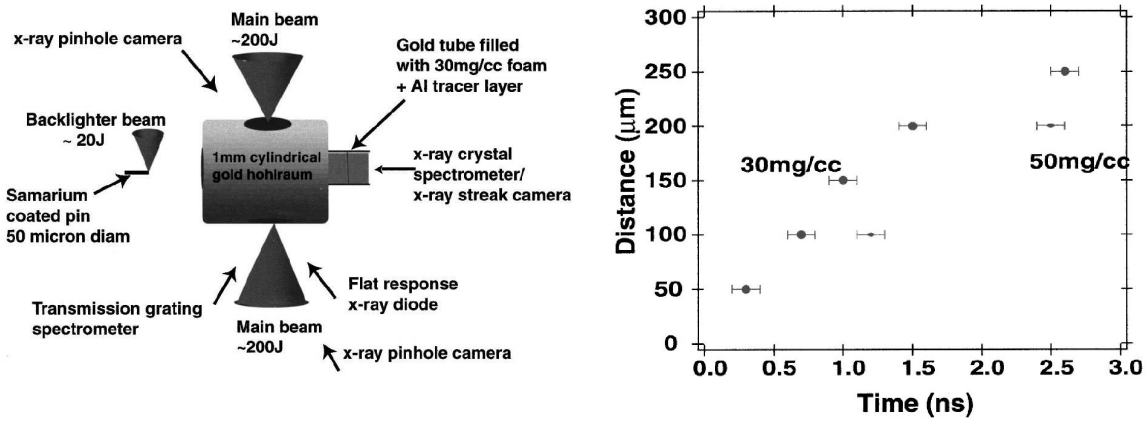

(a) (b)

Figure 2.5: **(a)** Experiment configuration for measuring the radiation propagation speed in CH foams on the TRIDENT laser. **(b)** Ionization front positions in $30 - 50mg/cc$ CH foam as measured by the ionization of an aluminum tracer layer [74].

foam temperature of $80eV$. With these assumptions, the propagation velocity of the ionization front was found to agree quite well with both the 1- and 2-D calculations. Again, for these optically thick mid-Z foams, the radiation propagation speed appears to be well modeled.

A study that is very relevant to this thesis was conducted recently by D. Hoarty et al. [74] on CH foam targets at the TRIDENT laser facility. In these experiments, they confined $30mg/cc, 300 - 500\mu m$ thick CH foams to a gold cylinder (to prevent rarefaction) on the end of a $1mm$ diameter gold hohlraum in a configuration shown in Figure 2.5(a). The primary diagnostic of the aluminum ionization history was a x-ray crystal spectrometer coupled to a x-ray streak camera system. By placing the aluminum tracer layer at different depths in the foam, Hoarty et al. were able to infer the velocity of the ionization front as it propagated through the foam under a measured drive temperature of $\approx 105eV$. The experimental data of the front position versus time are shown for both $30mg/cc$ and $50mg/cc$ CH foams in Figure 2.5(b). The first

three data points in the $30mg/cc$ foam indicate an initial front propagation speed of $\approx 14cm/\mu s$, while extrapolation of the data for the $50mg/cc$ foam indicates a front propagation speed of $\approx 8cm/\mu s$. However, the authors do not report any attempts to model the measured propagation. These TRIDENT experiments are an example of the kind which can be conducted on the Z machine at Sandia for foams that are of interest to z-pinch applications. Comparing similar data to detailed radiation-hydrodynamics models may provide more insight into the validity of various transport schemes and opacity models in low-density CH_2 foam.

There are only a few other radiation wave, shock propagation, or opacity studies in low-density foams irradiated by a high-temperature thermal radiation field to be found in the literature [75–79]. The most relevant of these was conducted by J.J. MacFarlane et al. [80] on the Z machine at Sandia. This experiment attempted to measure the length of time over which the central CH_2 foam in the dynamic hohlraum configuration was transparent enough to transmit radiation from an Au half-disk located at one end of the foam. Framing camera images were taken over 8 successive times just before the peak of the implosion. At about $6ns$ before peak implosion, the framing camera shows that the albedo emission of the Au half-disk is visible through the $1cm$ length of the foam. Atomic ionization models indicate that this corresponds to an electron temperature of $30 - 40eV$. However, 2-D simulations of this z-pinch configuration indicate that the electron temperature is less than this implying that the foam should be optically thick to the Au re-emission. Either the simulations do not properly calculate the incident radiation flux from the z-pinch plasma, or they under-predict the time it takes for the radiation to heat the CH_2 foam. This serves as one example of the importance in directly investigating the radiation propagation speed in CH_2 foam, and the need to understand which calculational methods are required to model the transfer process.

Chapter 3

Experiment Design

3.1 Motivation

In order to properly model the conditions of the radiation field in any plasma, a number of factors must be considered. First, a decision needs to be made about how to treat the spectral components of the problem. Typically this means choosing between either a Gray (single-group) model, or a more detailed multi-group calculation. Second, because the radiation transport depends heavily on the opacity of the material, a decision needs to be made about how to calculate the temperature and density dependent opacities. Because speed of calculation is often a primary concern, one can chose between doing a simple in-line calculation of the bulk atomic absorption (and scattering), or construct tables of opacities using a much more detailed atomic model relying on a-priori assumptions of the radiation field. Third, because no two radiation transport approximations are alike in either accuracy or speed, a decision needs to be made about how to model the radiation transport. The calculation can either be conducted using a very simple approximation that is rather fast but possibly not very accurate, or it can be conducted using a scheme

that more suitably represents true transport but at the cost of valuable computation time. Each of these factors can have a significant impact on the accuracy of the calculation, and each needs to be addressed in detail before one can truly have confidence in the computational model.

Many radiation-hydrodynamics codes that are utilized to model z-pinch processes rely on Gray (single group) diffusion as a means of simulating the radiation transport without requiring the complication and increased computation time of a multi-group solution. Because these codes utilize the Rosseland mean opacities, the radiation transport routines are best suited to simulate the transport of a blackbody radiation profile in a plasma at local thermodynamic equilibrium (LTE). This is an appropriate approximation for the case of an optically thick plasma within a thermal radiation field, and thus provides an acceptable solution for many applications in high-temperature, high-density physics. However, if any of the aforementioned conditions are violated, Gray diffusion may not correctly predict the solution in many types of materials. This is particularly true for a low-Z, low density CH_2 foam where the mean free paths can be longer than a millimeter.

Figure 3.1(a) shows the radiation profiles in a $5mg/cc\, CH_2$ plasma as calculated by the BUCKY 1-D radiation-hydrodynamics code (see §4.2) for both Gray and multi-group flux-limited diffusion. These profiles are plotted at times of 4, 7, and $10ns$ for the radiation drive shown in Figure 3.1(b). In the multi-group calculation, it is assumed that the radiation has a planckian distribution at the radiation temperature of the drive flux, and the multi-group opacities are taken from DTA calculations using EOSOPA (see §4.3) for 100 log spaced energy groups between 0.1 and $10^5 eV$. As can be seen in Figure 3.1(a), the calculation using Gray diffusion shows much steeper gradients in the radiation intensity, and severely under-predicts the depth of penetration into the plasma.

To further demonstrate this characteristic, Figure 3.2 shows the BUCKY modeled

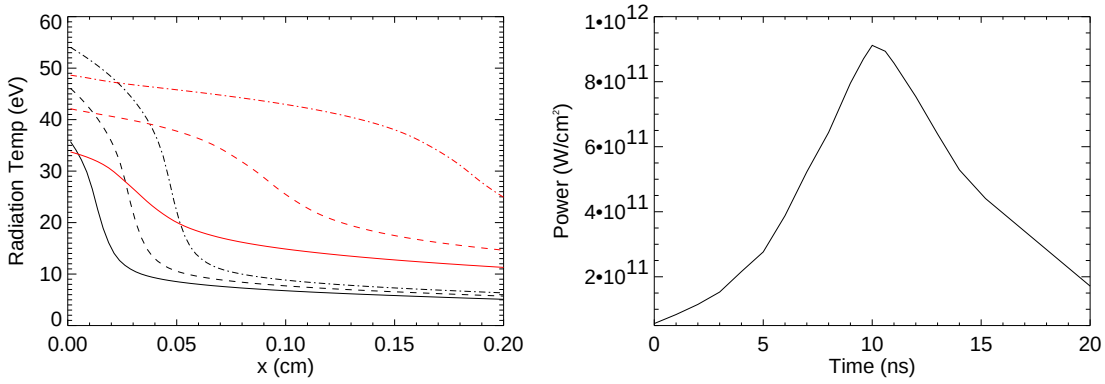

(a) **(b)**

Figure 3.1: **(a)** Flux-equivalent radiation temperature profiles in $5mg/cc\ CH_2$ foam calculated by Gray (black) and 100 group flux-limited diffusion (red) at times of $4ns$ (solid), $7ns$ (dashed), and $10ns$ (dot-dashed) for the blackbody drive history shown in **(b)**.

radiation spectrum and the EOSOPA modeled DTA multi-group Rosseland mean opacity at a depth of $1.0mm$ in the $5mg/cc\ CH_2$ at $7ns$ into the simulation. At this point, the temperature of the plasma is a relatively cool $5.4eV$, and the carbon K-shell is well populated. This results in a very strong influence of the K-edge ($1s^2 2s^n 2p^m \rightarrow 1s^1 2s^n 2p^m + e^-$) on the radiation transport. As seen in the figure, there is a window in the opacity just below an energy of $315eV$ which passes the radiation in a fairly narrow spectral band. The resulting radiation spectrum contains a total flux of $4.3 * 10^{10} W/cm^2$, $> 90\%$ of which is contained in photons with energies in the range $140eV \leq h\nu \leq 315eV$. Blackbody radiation spectra with a color-temperature between $26eV$ and $140eV$ have $> 20\%$ of the total flux in this energy range, which can thereby create a non-equilibrium between the plasma and the radiation field. Correctly modeling the radiation flux in this situation requires a multi-group radiation transport solution. If the temperature of the CH_2 plasma becomes high enough to ionize the outer electrons in the carbon, then free-free interactions help the plasma relax to a state of equilibrium where Gray diffusion

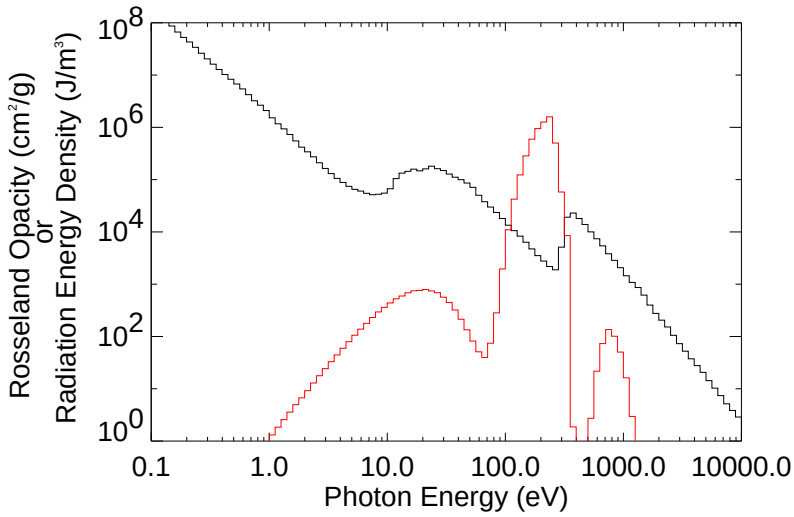

Figure 3.2: 100 group Rosseland opacity (black) and radiation energy density (red) at a depth of $1mm$ and a time of $7ns$ for the BUCKY simulation in Figure 3.1.

may again be an adequate approximation.

To make matters worse, if the spectrum deviates from a blackbody, then the location of the carbon K-edge with respect to even modest temperature blackbody curves requires a very detailed treatment of the incident radiation spectra. To illustrate this, Figure 3.3(a) shows the BUCKY modeled radiation profiles in the same $5mg/cc$ CH_2 plasma assuming that the incident flux shown in Figure 3.1(b) has a planckian distribution dictated by either the radiation temperature of the incident flux, or a color-temperature that is two times higher. The incident spectral histories assumed for each of these calculations are shown in Figure 3.3(b). The BUCKY models again use multi-group flux-limited diffusion assuming 100 log spaced energy groups between 0.1 and 10^5eV. Figure 3.3(a) demonstrates how the change in incident spectra leads to a very different radiation profile near the peak of the radiation drive. Because the Planckian distribution of the higher color-temperatures has a much greater fraction of the total energy above the carbon K-edge, the calculated penetration is lower (even though the average photon energy is

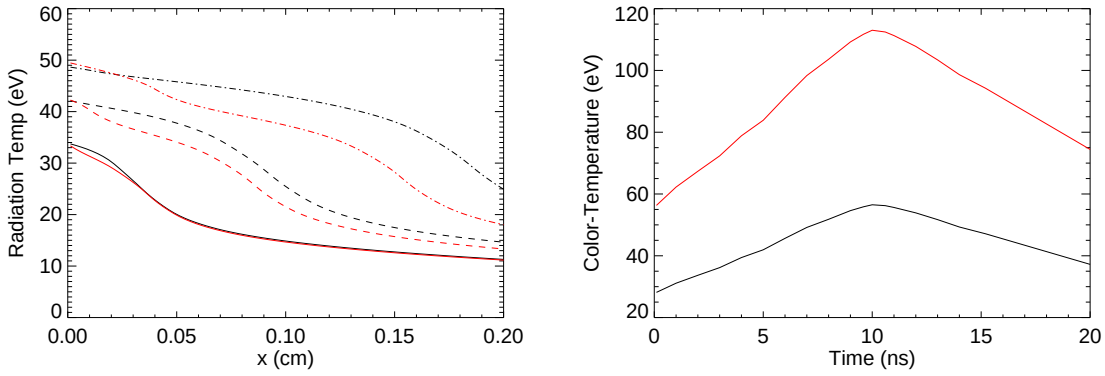

(a) **(b)**

Figure 3.3: **(a)** Flux-equivalent radiation temperature profiles in $5mg/cc\ CH_2$ foam calculated using 100 group flux-limited diffusion at times of $4ns$ (solid), $7ns$ (dashed), and $10ns$ (dot-dashed)for the lower (black) and higher (red) color-temperature profiles shown in **(b)** and the drive flux profile shown in Figure 3.1(b).

much higher). Clearly, properly modeling the incident spectra is paramount in properly modeling the radiative transfer.

Because of the importance of the carbon K-edge, modeling the details of the penetration deep into the CH_2 plasma also requires a good treatment of the shape of that edge. That is, what is often referred to as the K-edge consists of many transitions between and out of excited states in addition to the dominant bound-free transition from the ground state. To illustrate, Figure 3.4(a) shows the BUCKY calculated flux-equivalent radiation temperatures in the CH_2 foam using EOSOPA calculated DTA opacities that either do or do not include the effect of transitions between inner excited states. The calculations are relatively similar. The case which does not include the effect of the inner excited states predicts flux-equivalent radiation temperatures that are approximately 10% higher ($\approx 50\%$ in flux) at $x = 0.2cm$.

Figure 3.4(b) shows the 500 group Rosseland averaged DTA opacities of CH_2 at $T_e = 6.95eV$ and $n_i = 6.95 \times 10^{20} cm^{-3}$ as calculated by EOSOPA both including the

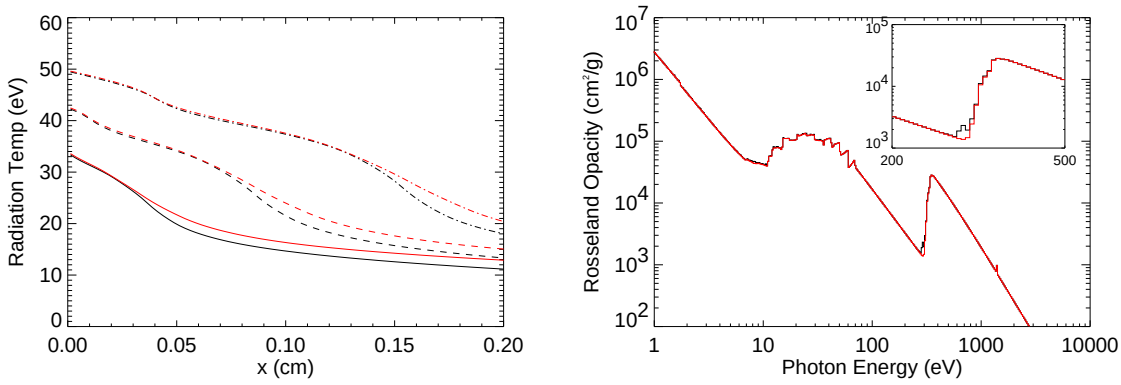

(a) **(b)**

Figure 3.4: **(a)** Flux-equivalent radiation temperature profiles in $5mg/cc\ CH_2$ foam calculated using 100 group flux-limited diffusion at times of $4ns$ (solid), $7ns$ (dashed), and $10ns$ (dot-dashed)for EOSOPA modeled CH_2 opacities that either do (black) or do not (red) include the effect of transitions between inner excited energy levels. **(b)** Comparison between the EOSOPA modeled Rosseland opacities including (black) or not including (red) the effect of transitions between inner excited energy levels.

transitions between excited states, and that calculated for just the photo-ionization. The opacities are almost equivalent with the exception of the few energy bins that lie just below the K-edge (at $\approx 300eV$). The inset in Figure 3.4(b) shows an expanded view of this region, which reveals about a factor of two difference in the opacity within this very limited range. This is not a very large deviation from the total opacity, but in the context of the radiation spectrum shown in Figure 3.2, and as demonstrated from Figure 3.4(a), it can have a $\approx 50\%$ effect on the penetrating flux.

The case shown in Figure 3.4(a) is actually a best-case scenario in the differences between calculated opacities. That is, one would not expect that transitions between excited states play much of a role in the transport of radiation at these densities. Where significant differences can arise between different opacity codes is in the calculation of the excited state populations, or even the splitting between energy levels. These can have

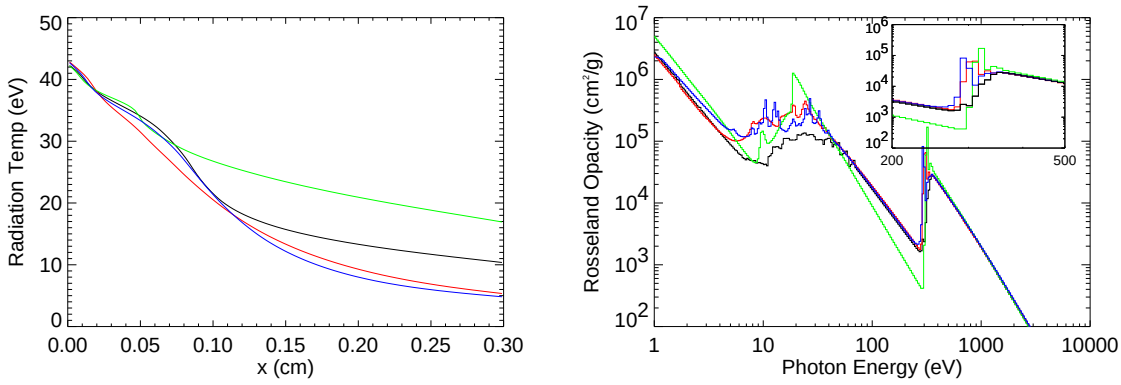

(a) **(b)**

Figure 3.5: **(a)** Flux-equivalent radiation temperature profiles in $5mg/cc\ CH_2$ foam calculated using 100 group flux-limited diffusion at a time of $7ns$ for CH_2 opacities that are modeled by EOSOPA using a DTA (black) or UTA (red) model, XSN (green), and TOPS (blue). **(b)** Opacity in CH_2 for $T_e = 6.95eV$ and $n_i = 6.95 * 10^{20}$ as calculated by EOSOPA DTA (black) and UTA (red), as well as that calculated by XSN (green), and TOPS (blue).

a significant effect on the rates and energies of the bound-free transitions that make up the bulk of the opacity.

As an example, Figure 3.5(a) shows the influence that different opacity models have on the calculation of the radiation distribution at $7ns$ in a $5mg/cc\ CH_2$ plasma driven by the incident flux history in Figure 3.1(b) with the higher color-temperature history in Figure 3.3(b). The calculations are done using opacity tables generated by 4 different opacity models: EOSOPA DTA, EOSOPA UTA, XSN, and LEDCOP (mixed using TOPS). Each of the calculations here are done for the default values of the many adjustable parameters in each code assuming a condition of LTE. EOSOPA uses either a DTA or UTA model; XSN uses an average-atom model; and LEDCOP uses a DTA model similar to that in EOSOPA. As evidenced by the figure, the 4 different opacity tables lead to 4 different solutions of the radiation distribution.

Figure 3.5(b) shows the 500 group Rosseland opacities in $5mg/cc\ CH_2$ as calculated by these 4 different opacity codes for a temperature of $6.95eV$ and a density of $6.95 \times 10^{20} cm^{-3}$. While the overall structure of the opacities are similar, there are remarkable differences in the positions, amplitudes, and shape of the carbon K- and L-shell edges. These are the areas where the details of the excited-state energy level positions and populations are important, and each model has a different method of solving for these values. It is generally accepted that a DTA model is the most comprehensive, and typically most accurate, of the atomic models tested here. However, DTA calculations are far more complex, and are only applicable in atoms where there are few enough electrons that the combinations of wave-functions can be practically calculated. Thus, DTA models are typically only applied for atomic numbers less than 37. Above this, a UTA model is commonly considered an acceptable method of calculation. The XSN average-atom calculations use the least amount of detail (and have the most number of "knobs"), but are very quick and can be run in-line with the radiation-hydrodynamics model.

The effect of the differences in the opacity tables on a calculation of the radiation transport will of course depend on the incident spectra. If that spectra is fairly hot ($> 140eV$), then it probably does not have much of an impact on the penetration. If however, this spectra has a color-temperature between ≈ 20 and $140eV$, then the effect can be on the order of that shown in Figure 3.5(a). If this level of detail in the radiation transport is important, then the model that is used to calculate the opacities must be an important consideration.

One final consideration in the modeling of the radiation field is in the method that should be used to solve the radiation transport equation. As discussed in §1.4, there are a number of different approximations that can be used, each of which having a different

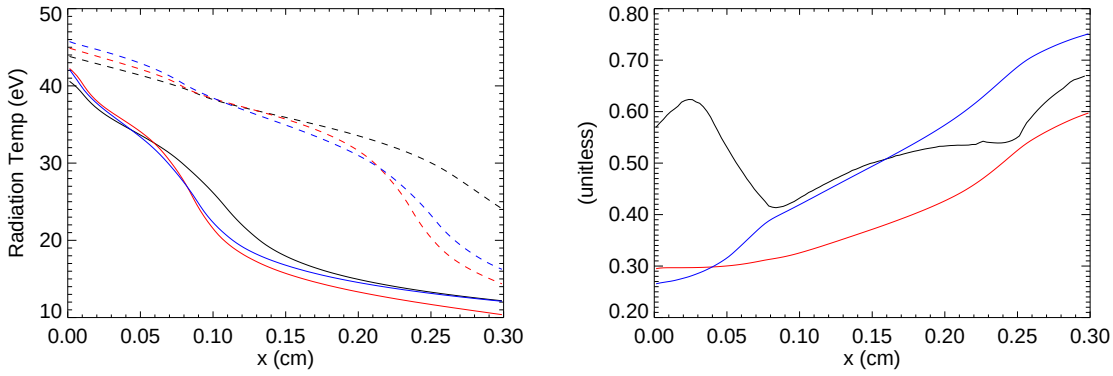

(a) **(b)**

Figure 3.6: **(a)** Flux-equivalent radiation temperature profiles in $5mg/cc\ CH_2$ foam calculated using 100 group diffusion (black), flux-limited diffusion (red), and short-characteristics (blue) at times of $7ns$ (solid) and $14ns$ (dashed). **(b)** Spectrally averaged flux-limiter $< 3\sigma_R D >$ (black), Eddington factor $< f >$ (red), and flux-factor η (blue) at $14ns$.

level of accuracy for a particular problem. As noted in §4.2, BUCKY can be used with either diffusion (flux-limited or not), or multi-angle short-characteristics. In Appendix B, it has been shown that each can be applicable for a different set of problems, but that short-characteristics very closely approximates true transport in cases where the radiation field is time-independent. However, if the radiation field is dynamically changing on a sufficiently short time scale, flux-limited diffusion will provide a much more accurate result.

Figure 3.6(a) shows the radiation profiles at 7 and $14ns$ in $5mg/cc\ CH_2$ as calculated by BUCKY for diffusion, flux-limited diffusion (SUM-limiter), and short-characteristics. Again, the calculation was conducted using 100 log spaced energy groups between 0.1 and $10^5 eV$ for the radiation drive shown in Figure 3.1(b) assuming the high color-temperature history shown in Figure 3.3(b)[a]. At a time of $7ns$ into the simulation, all three approx-

[a]The high color-temperature drive is used here because it more closely resembles the spectra that is calculated for the experiments discussed in Chapter 6.

imations predict similar radiation profiles. The flux-limited solution closely follows the short-characteristics result for $0 < x < 0.1cm$ while the diffusion solution follows the short-characteristics result for $0.2 < x < 0.3cm$. In contrast, the three solutions are rather different at $14ns$. At this time, the diffusion approximation predicts much higher radiation fluences near the back of the sample than the short-characteristics result, but the flux-limited solution agrees with short-characteristics to within 15% throughout the sample.

To better visualize the effect of the flux-limiter on the diffusion solution, Figure 3.6(b) shows the spectrally averaged flux-limiter, $< 3\sigma_R D >$, given by the equation:

$$\langle 3\sigma_R D \rangle = \frac{\int_0^\infty \frac{3\sigma_R(x,\nu)E(x,\nu)}{3\sigma_R(x,\nu)+E(x,\nu)^{-1}\left|\frac{\partial E}{\partial x}\right|}d\nu}{\int_0^\infty E(x,\nu)d\nu}, \tag{3.1}$$

at a time of $14ns$ for the conditions modeled by short-characteristics (as an example). According to Figure 1.17, the closer this value is to 1, the more diffusive the transport calculation is. However, in many cases the flux-limiter is simply an *ad-hoc* extrapolation between the diffusive and free-streaming limits, and in all cases the strength of the flux-limiter depends only on the gradient in the radiation field. To truly diagnose the isotropy of the radiation flow, and thus make a determination of the applicability of the diffusion approximation, requires a calculation of the (angularly dependent) specific intensity.

To illustrate, Figure 3.6(b) also shows the spectrally averaged Eddington factor, $< f >$, and flux factor, $< \eta >$, given by:

$$< f > = \frac{\int_0^\infty E(x,\nu)\frac{\int_{-1}^1 \mu^2 I(x,\mu,\nu)d\mu}{\int_{-1}^1 I(x,\mu,\nu)d\mu}d\nu}{\int_0^\infty E(x,\nu)d\nu} \tag{3.2}$$

$$< \eta > = \frac{\int_0^\infty E(x,\nu)\frac{\left|\int_{-1}^1 \mu I(x,\mu,\nu)d\mu\right|}{\int_{-1}^1 I(x,\mu,\nu)d\mu}d\nu}{\int_0^\infty E(x,\nu)d\nu}, \tag{3.3}$$

as calculated by short-characteristics at a time of $14ns$. When the radiation field is

highly isotropic, $< f > \approx 1/3$ and $< \eta > \approx 0$. When the radiation field is anisotropic (i.e. streaming), $< f > \approx < \eta > \approx 1$. The figure illustrates that, the radiation field is fairly isotropic and diffusive near the front of the CH_2 plasma, and approaches a free-streaming limit near the back. This is what one might expect, but is in stark contrast to what is indicated by the plot of the flux-limiter. The flux-limiter appears to be the strongest (has the lowest value) at $x \approx 0.08$, and then it steadily becomes more diffusive as x increases. Based off this comparison, it is rather remarkable that flux-limited diffusion can predict a reasonable solution at all. Looking carefully at the details, it was determined that the flux-limiter is the strongest where the gradient in the radiation intensity is at its peak. This is precisely where the streaming term in the transport equation is the most important, and where it is therefore most important to limit the diffusion coefficient. Thus, the fact that the general trend in the flux-limiter is incorrect has little effect on the accuracy of the solution as long as the diffusion coefficient is properly limited at the position of the wave-front. Of course, there is no guarantee that the flux-limiter will accurately limit the diffusion coefficient, even where it is most important.

As a check on the validity of the time-independence assumption in the short- characteristics solution, the simulations in Figure 3.6(a) were also conducted for time-independent flux-limited diffusion. After the first $\approx 100ps$, the result was virtually identical to the time-dependent case suggesting that the dE/dt term in the transport equation is of small consequence for the time-scales of interest in this problem. This would indicate that short-characteristics should be applicable, and in lieu of the discussion in Appendix B, should also be the most accurate. However, Figure 3.6(a) indicates that flux-limited diffusion is not a bad approximation, and can predict the results of the short-characteristics solution to within $< 20\%$ (in temperature).

—

All of the studies discussed above are based on simplifications of reality, but serve as an example of the effect that any one of these considerations can have on the accuracy of a calculation. One approximation they all share, however, is in the uniformity of the CH_2 medium. That is, all the calculations discussed in this thesis (and utilized throughout the community) assume that the CH_2 foam can be accurately modeled as a uniformly distributed high-density gas. At room temperature, that is a bad assumption. Figure 3.7 shows an SEM image of a $10mg/cc\ CH$ foam manufactured at Sandia National Laboratories' Target Fabrication lab [81]. This foam is very similar to the $5mg/cc\ CH_2$ foams studied in this thesis, and has numerous 'cells' with diameters ranging from $5 - 20\mu m$. Clearly, this foam does not have a uniform density. However, as the foam vaporizes, the differential pressure between the walls of the cells and the void in-between will cause the gaseous CH_2 to fill the gaps. After a sufficient time, the material will reach a pressure equilibrium and be well approximated by a uniform gas.

The open question is whether or not this happens on a time scale sufficient for the uniform gas approximation to hold in the experiments of interest for this thesis. If not, it is unclear what effect the non-homogeneous structure of the foam medium may have on the radiative transfer. However, if the observables in the experiment are well chosen, and can be well modeled under these assumptions, then it will at least show that the inhomogeneity of the CH_2 foam is not an important consideration in modeling the transport.

In the end, each approximation discussed in this section must be understood in the context of the others for a calculation of the radiative transfer to be a true representation of reality. Due to the high number of permutations in these approximations, there may not be a unique combination of them that provides a good solution. In addition, some may prove to not have an effect that can be resolved in a reasonable experiment.

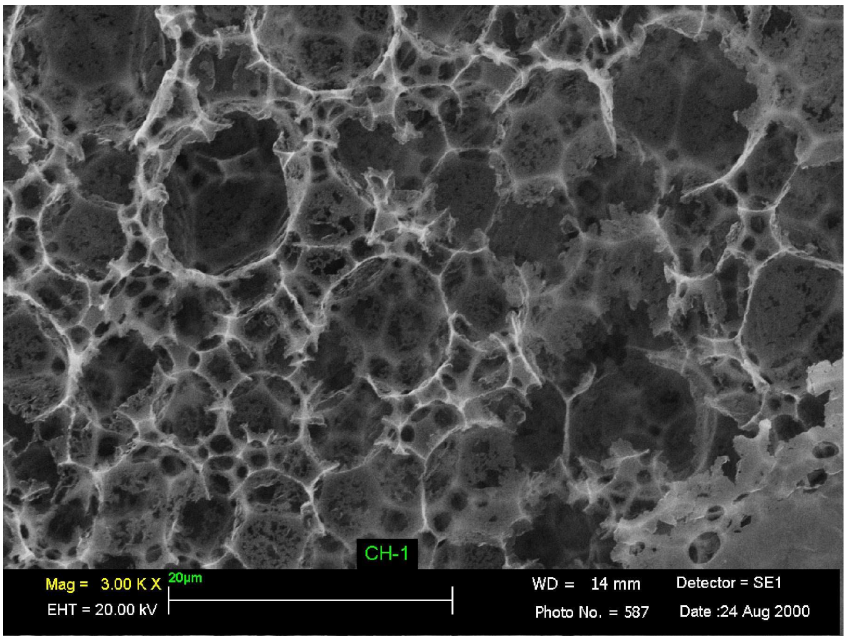

Figure 3.7: SEM image of the microscopic structure in a $10mg/cc\ CH$ foam. The cells in this image have diameters ranging from $5 - 20\mu m$ [81].

The important thing is to identify which approximations provide an adequate solution of the radiative transfer so that one can have confidence in the calculated distribution of radiation throughout a CH_2 foam. This is best tested through a series of experiments, with well chosen observables, that rely sensitively on any one (or all) of these approximations.

3.2 Experimental Method

The ideal way to investigate the radiative transfer in a material is to expose it to a radiation source and measure how long it takes the different frequencies to transit the sample. The complication is in reaching conditions in the foam that are relevant to the issues posed in §3.1, verifying those conditions, and then measuring the radiation transport. At the energy-densities of interest, the CH_2 foam is hydrodynamically active,

creating a complex environment where the radiative processes feed the hydrodynamics and visa versa. Therefore, isolating individual phenomena is typically not practical, and measurements of the radiative transfer must be understood in the context of all the physical processes occurring in the plasma over the course of the experiment. In this situation, one relies heavily on the calculations to model the dynamic conditions in the sample, and then make inferences on the radiation transport from the calculational result. Since the calculations are what we are trying to verify, we need to identify observables in the experiment that constrain the calculations in as many ways as possible. Preferably, these observables are sensitive to the time it takes different frequencies of radiation to transit the sample, so that the constraints on the calculations are directly relevant to the radiation transport.

The approach taken in this thesis is to constrain the radiation-hydrodynamics calculations by measuring the temperature and density conditions in tracer layers buried at known locations in the $5mg/cc\ CH_2$ foam. One method for diagnosing these conditions is to measure the absorption spectrum of radiation passing through the embedded tracer layers. This is a well established method for measuring the properties of radiatively heated materials [82–85]. Because different charge-states of an atom absorb different x-ray wavelengths, spectrally resolving the radiation passing through the tracer provides a telltale signature of the relative ionization states that existed at the time the spectrum was observed. The absorption spectrum can then be related to the possible temperatures and densities in the plasma by detailed calculations of the atomic energy levels and transition probabilities in combination with the local collisional and radiative ionization rates.

To illustrate, Figure 3.8(a) shows the calculated transmission spectra for an aluminum plasma at a range of temperatures and densities assuming a spectral resolu-

tion of $E/\Delta E \approx 1000$. Each of the features in the spectra correspond to a set of K-α transitions in aluminum atoms at different charge-states. For example, the feature at the longest wavelength corresponds to K-α transitions in fluorine-like aluminum ($1s^{(2)}2s^{(2)}2p^5 + \gamma \rightarrow 1s^{(1)}2s^{(2)}2p^{(6)}$), and the feature at the shortest wavelength corresponds to K-α transitions in helium-like aluminum ($1s^{(2)} + \gamma \rightarrow 1s^{(1)}2p^{(1)}$). The relative depths of these absorption features are proportional to the percent of each ionization state that exists in the hot plasma.

To better relate the plasma conditions to the charge state, Figure 3.8(b) shows the relative ionization states as a function of density at each of the temperatures shown in Figure 3.8(a). As evidenced by the figure, the average ionization state of the atoms increases (moves toward a higher positive charge) with increasing temperature, and decreases with increasing density. Given this information, it is clear that a K-α absorption spectrum can dictate the relative ionization states in the plasma, which in turn can be related to the possible combinations of temperature and density at the time the spectrum was observed.

For the experiments described in this thesis, the tracer layers are composed of very thin ($1000 - 3000$Å) foils of aluminum or magnesium-fluoride that are buried in the $5mg/cc\ CH_2$ foam. These low-Z materials are used because the atomic physics of each is well-understood, and the relative ionization states and associated energy level populations can be calculated in detail. In addition, the opacity structure of these materials is ideal for coupling to the radiation that is passing through the foam. Figure 3.9 shows EOSOPA calculated 500 group Planck averaged opacities for CH_2 ($T_e = 50eV$, $\rho = 5mg/cc$), Al ($T_e = 35eV$, $\rho = 10mg/cc$), and MgF_2 ($T_e = 35eV$, $\rho = 10mg/cc$). As discussed in §3.1, the K-shell edge of carbon dictates the penetrating spectrum at the temperatures and densities that are expected in these experiments. In this situation, the majority of the

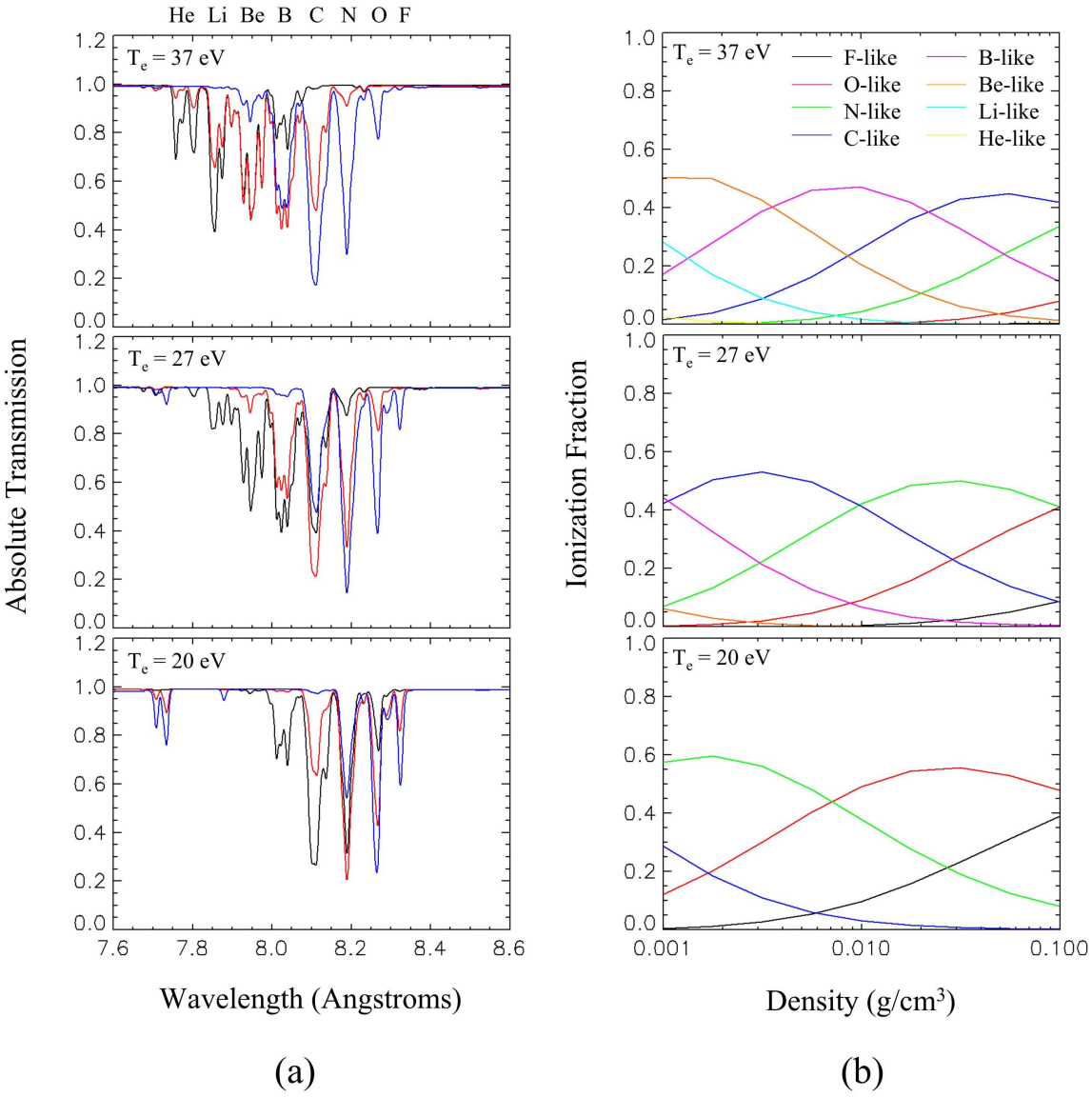

Figure 3.8: **(a)** EOSOPA calculated Al absorption spectra at densities of $0.001 g/cc$ (black), $0.01 g/cc$ (red) and $0.1 g/cc$(blue). **(b)** Al ionization fractions as a function of density for the temperatures shown in (a).

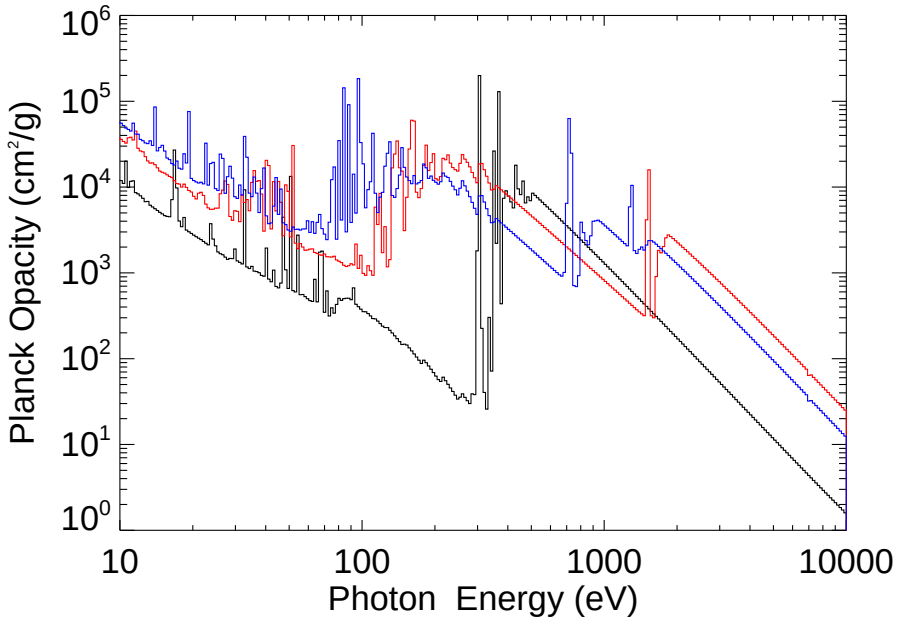

Figure 3.9: EOSOPA calculated group opacities for $5mg/cc\ CH_2$ at $T_e = 50eV$ (black), $27mg/cc\ Al$ at $T_e = 35eV$ (red), and $30mg/cc\ MgF_2$ at $T_e = 35eV$ (blue).

radiation that passes through the foam is in the frequency range just below the K-edge at $\approx 300eV$. Both Al and Mg have an L-shell edge that lies directly in the path of this penetrating radiation, so that the bound-free heating is sensitive to the radiation transport through the foam. This opacity structure should make these materials a good diagnostic for constraining the radiation-hydrodynamics models.

Therefore, the basic experimental method in this thesis is to use the z-pinch radiation source at Sandia National Laboratory's Z facility (as described in §1.3.2) to heat the foam, and then spectrally resolve the high-energy z-pinch radiation that passes through the sample as a measure of the relative ionization states that existed in the tracers. It is then up to a radiation-hydrodynamics code to reproduce the density and temperature conditions in the plasma in order to demonstrate an understanding of the integrated physics (including the radiative transfer) occurring throughout the experiment.

3.3 Experiment Geometry

There are a number of complications involved in designing experiments on the Z machine. The limited number of shots available for dedicated experiments means that careful planning and detailed modeling must be conducted in order to get the most out of any single shot. This 'dedicated' shot mode is expensive and requires front-line programmatic priority to attain shot time. The other approach to conducting experiments on the Z machine is that of a 'ride-along' experiment. In this configuration, the experimental package is placed external to the z-pinch hardware around the perimeter of the primary hohlraum (see §1.3). Radiation emitted from the pinch can escape through one of the 9 or 18 radiation exit holes (REH) and then be used to drive a sample placed outside the REH along the primary diagnostic line-of-sight (LOS). As long as the experimenter is flexible about the z-pinch load which drives the sample, this approach has the advantage of not requiring dedicated shot time and can be done at lower cost and higher frequency.

Figure 3.10 shows both a schematic of this ride-along experimental set-up and a picture of such an experiment on Z. There are up to 7 diagnostics that monitor the z-pinch performance, and up to 2 spectrometers on each sample that measure the observable of interest. The 7 z-pinch diagnostics [86–89] are a filtered x-ray diode array (XRD), filtered photo-conducting diamond array (PCD), bolometer, time-integrated crystal spectrometer (TIXTL), PIN-diode based transmission grating spectrometer (TGS), framing x-ray pinhole camera (FPC), and the Energy-Space-Time (EST) 1-D streaked imager. The XRD and bolometer are used in conjunction to measure the z-pinch power as a function of time; the PCD, TIXTL, and grating spectrometer are used to measure the z-pinch spectrum; and the EST and pinhole camera monitor the z-pinch radius at early and late times respectively. The spectrometers that measure the observables in each sam-

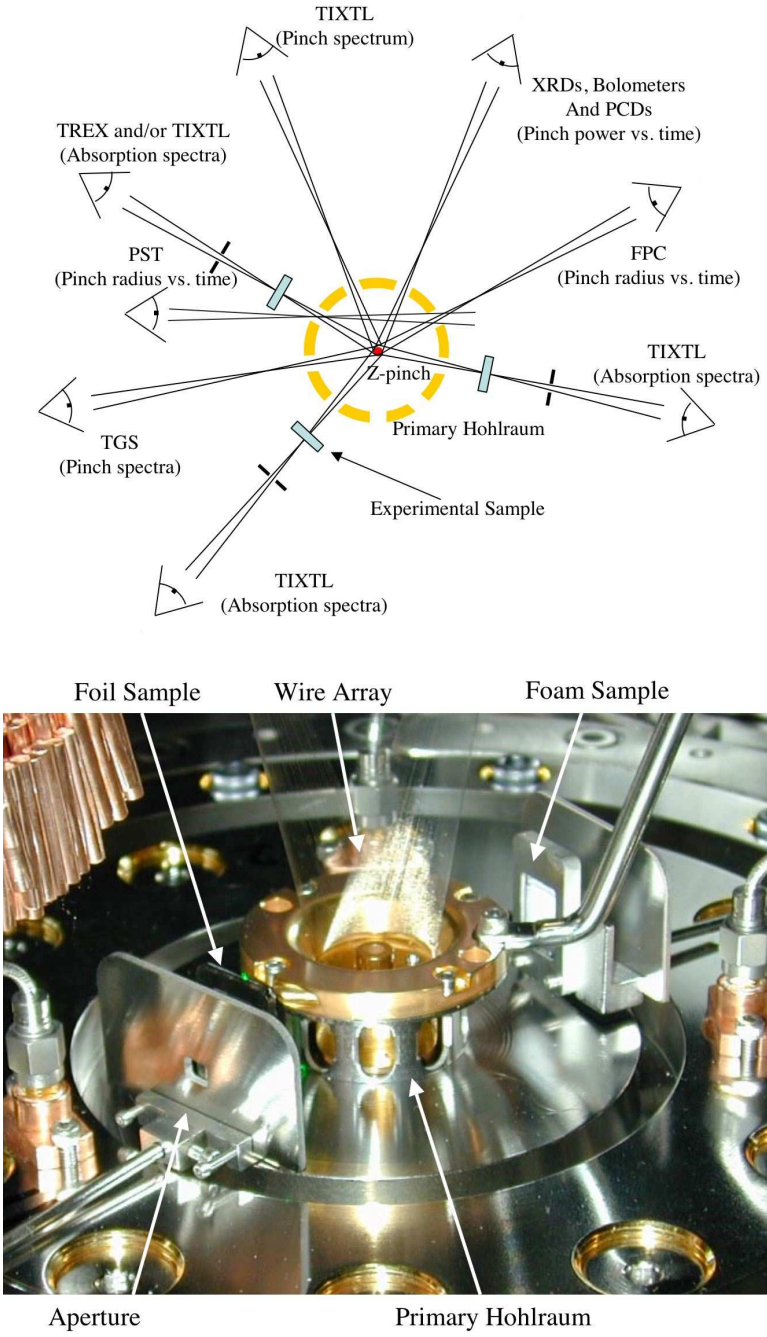

Figure 3.10: Top-view schematic and photograph of the fielding geometry for 'ride-along' experiments on Sandia National Laboratory's Z machine.

ple are either a time- and space-resolved elliptical crystal spectrometer (TREX), or a time-integrated, space-resolved convex crystal spectrometer (TIXTL) (see Appendix A). When all fielded on a single shot, these diagnostics provide a comprehensive measurement of the z-pinch dynamics, and the details of the observable to be measured in the sample.

This experiment configuration has a number of advantages over similar experiments at other high-energy-density facilities (such as laser driven hohlraums). Because there are typically ≥ 9 radiation exit holes in the z-pinch primary, a number of samples can be tested on a single shot. In addition, the rather large size of the z-pinch diode allows for the use of cm-scale samples, or even multiple samples on a single REH. This large scale size allows for samples to be apertured far from the edges such that the hydrodynamics can be well-modeled in 1-D. Finally, the z-pinch radiation spectra has a wide distribution of photon energies which can both heat and backlight a sample placed outside the REH.

3.3.1 The Z-pinch Backlighter

Figure 3.11 shows the measured z-pinch spectrum at peak power from an experiment on Z [90]. This spectrum consists of a thermal component ($T_r \approx 160eV$), along with a high-energy non-thermal 'tail' that contains $\approx 10\%$ of the radiated power in the energy range $1keV < h\nu < 6keV$. The portion of the spectrum with an energy $< 1keV$ can be thought of as the 'heater', while the portion $> 1keV$ acts as a backlighter. Figure 3.12(a) shows a time-integrated spectrum of a tungsten z-pinch on Z in the spectral range $4\text{Å} \leq \lambda \leq 14\text{Å}$. There are a number of features in this spectrum that are of particular interest. To help identify a few of these, a $160eV$ blackbody spectrum (scaled by $5 \times 10^{-11} cm^2 s$) and an example cross-section of a tungsten plasma are also shown in the figure. The cross-section curve was calculated using a relativistic UTA model for a tungsten plasma at LTE with various temperature and density gradients. These cross-sections are shown because they

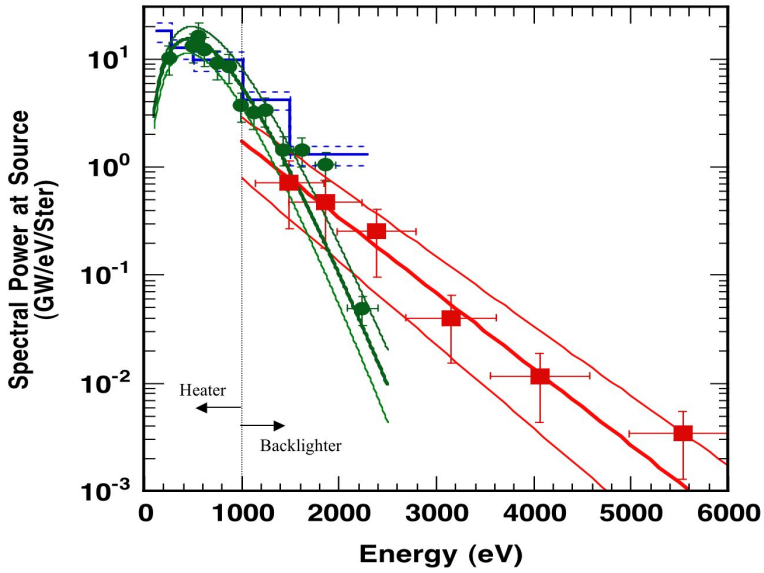

Figure 3.11: Example spectrum recorded at peak power on Z. The data was taken by the XRDs (blue lines), TGS (green symbols), and PCDs (red lines). The 'heater', below $\approx 1000eV$, is best fit by a blackbody spectrum at $162 \pm 7eV$ (green lines), while the backlighter is best fit by an exponential curve of the form $(8.7 \pm 4.1) \exp[-E/(619 \pm 55)]$ (red lines) [90].

can be related to the emission intensity of a bound-bound transition. As labeled on the figure, the obvious emission features are attributed to 4 M-shell unresolved transition arrays (UTAs). The position and relative strengths of these features are very sensitive to temperature and density. As an example of this sensitivity, Figure 3.12(b) shows line-outs of a few different axial locations in a time-integrated, space-resolved spectrum taken on Z. Note that there are significant differences in the relative amplitudes and spectral positions of the bound-bound emission features, but the shape of the 'continuum' above ≈ 7.5Å is fairly consistent. The differences in the tungsten M-shell features are believed to be due to hot spots distributed along the length of the z-pinch.

To further investigate issues associated with the consistency of the backlighter spectrum, Figure 3.13(a) and (b) show time-integrated spectra of a tungsten z-pinch taken

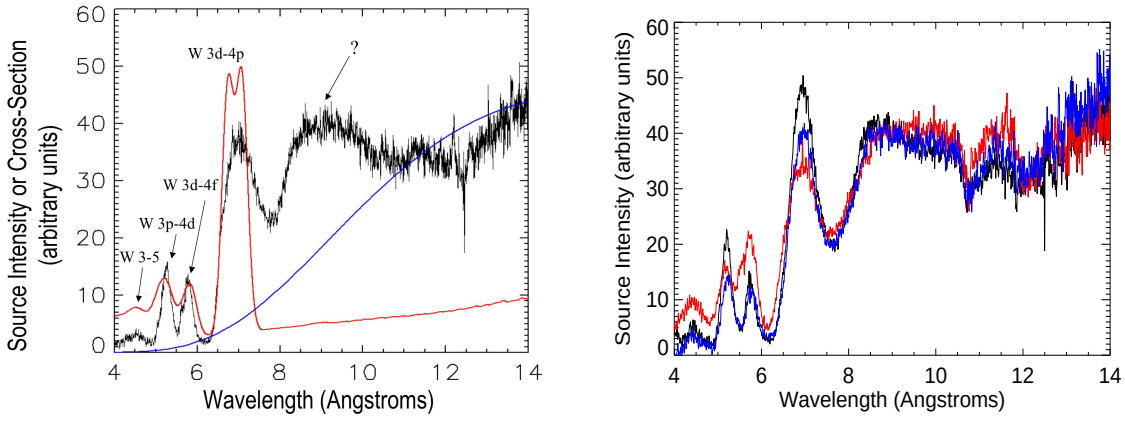

(a) **(b)**

Figure 3.12: **(a)** Time integrated tungsten z-pinch spectrum (black), JATBASE calculated UTA total cross-section for a tungsten plasma with temperature and density gradients (red), and a planckian spectrum at a radiation temperature of $160eV$. **(b)** Time-integrated spectrum recorded on Z for 3 different axial positions along a tungsten z-pinch.

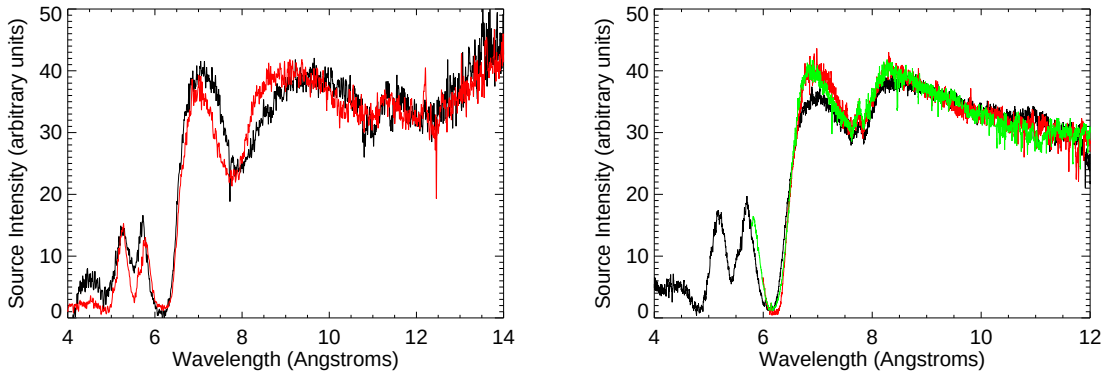

(a) **(b)**

Figure 3.13: **(a)** Time-integrated spectra of tungsten z-pinches from 2 different shots on Z. **(b)** Time-integrated spectra of a tungsten z-pinch as seen through 3 different lines-of-sight on Z.

from multiple shots and multiple lines-of-sight on Z[b]. The shape of the continuum is quite consistent even between shots, but there are noticeable differences in the primary tungsten UTA features. These dynamics make the shape and position of the tungsten bound-bound emission features difficult to predict, but provide some level of confidence in the consistency of the continuum.

It is therefore not recommended that the tungsten z-pinch backlighter be used in the range < 7.5Å unless the backlighter structure can be reasonably determined directly from the spectrum of interest. When this is not the case, the most smooth part of the backlighter is typically in the range $8.5\text{Å} < \lambda < 10.5\text{Å}$, which makes it ideal for the measurement of K-α absorption in Mg ($9.169\text{Å} \leq \lambda \leq 9.887\text{Å}$). The spectral range from $7.5 - 8.5$Å is in the region where the backlighter intensity transitions from the continuum to the bound-bound emission. The source of the large dip in the intensity through this region is not understood, but is somewhat consistent between lines of sight, along the length of the z-pinch, and on a shot-to-shot basis. Thus, if one is interested in a spectrum of the Al K-α complex ($7.757\text{Å} \leq \lambda \leq 8.338\text{Å}$), it is important to make sure that the continuum is either measured, or can be well-fit.

[b]Each spectrum was recorded on a z-pinch with the dynamic hohlraum geometry as discussed in §1.3.2.

Chapter 4

Experiment Modeling

As shown in Chapter 2 and discussed in the considerations for the experiment design in Chapter 3, understanding the data from integrated experiments at high energy density requires detailed computer modeling of nearly every physical process. In many cases, these models must include calculations of the time-, frequency-, and spatial-dependence of the radiation source (i.e. the driver); a calculation of the radiation propagation and associated hydrodynamic response in the experimental sample; and a post-processing calculation of the rad-hydro data to simulate the observable in the experimental data. In the most extreme cases, these calculations must be combined into one integrated simulation (on a very sophisticated multi-dimensional computer code) in order to account for important details of the dynamic conditions in the experiment. In many other instances, one can utilize a combination of simulations, each specialized to calculate a particular aspect of the experiment, and piece together a synthetic data set to be compared to the experimental results. This is the approach taken in this thesis.

A flow-diagram of the calculational method used to model a ride-along experiment on Z is shown in Figure 4.1. There are three primary steps: First, the data on the

z-pinch performance is incorporated in a 3-D view-factor simulation to determine the time-dependent radiation spectra on the experimental sample. This calculation must represent the experimental geometry, which usually includes the z-pinch, primary hohlraum, upper anode, and the experimental sample. In this model, the albedos of each surface are determined by 1-D rad-hydro simulations of the plasma re-emission driven by the view-factor modeled incident drive spectra. Since the albedo calculation depends on the assumed albedo in the view-factor simulation, this process is iterated until the resulting power at the surface of the sample converges at every time-step. Second, the view-factor modeled drive spectra at the sample surface are input into a 1-D rad-hydro simulation of the sample dynamics. This simulation provides the time-dependent temperature and density conditions inside the tracer layer buried in the experimental sample, and can be calculated for any choice of radiation transport, material opacity, and equation-of-state.

Once the conditions in the sample have been computed, the accuracy of the calculations can be evaluated in two different ways. One method is to compute the absorption spectra directly from the calculated tracer conditions. In these calculations, the time-dependent temperature and density conditions from the rad-hydro model are input into a detailed configuration analysis (DCA) calculation of the atomic ionization and energy level distributions in the tracer layer. Folding in the spectral resolution of the diagnostic with the DCA modeled frequency-dependent opacities provides simulated absorption spectra that can be compared directly to the experimental data. The other method for evaluating the accuracy of the rad-hydro models comes from a statistical comparison between experimental and calculated absorption spectra. In this method, the χ^2 goodness-of-fit is computed between the experimental data and DCA point calculations of the absorption spectra over a range of temperatures and densities. This analysis provides a statistical range of tracer conditions that most accurately describe the measured

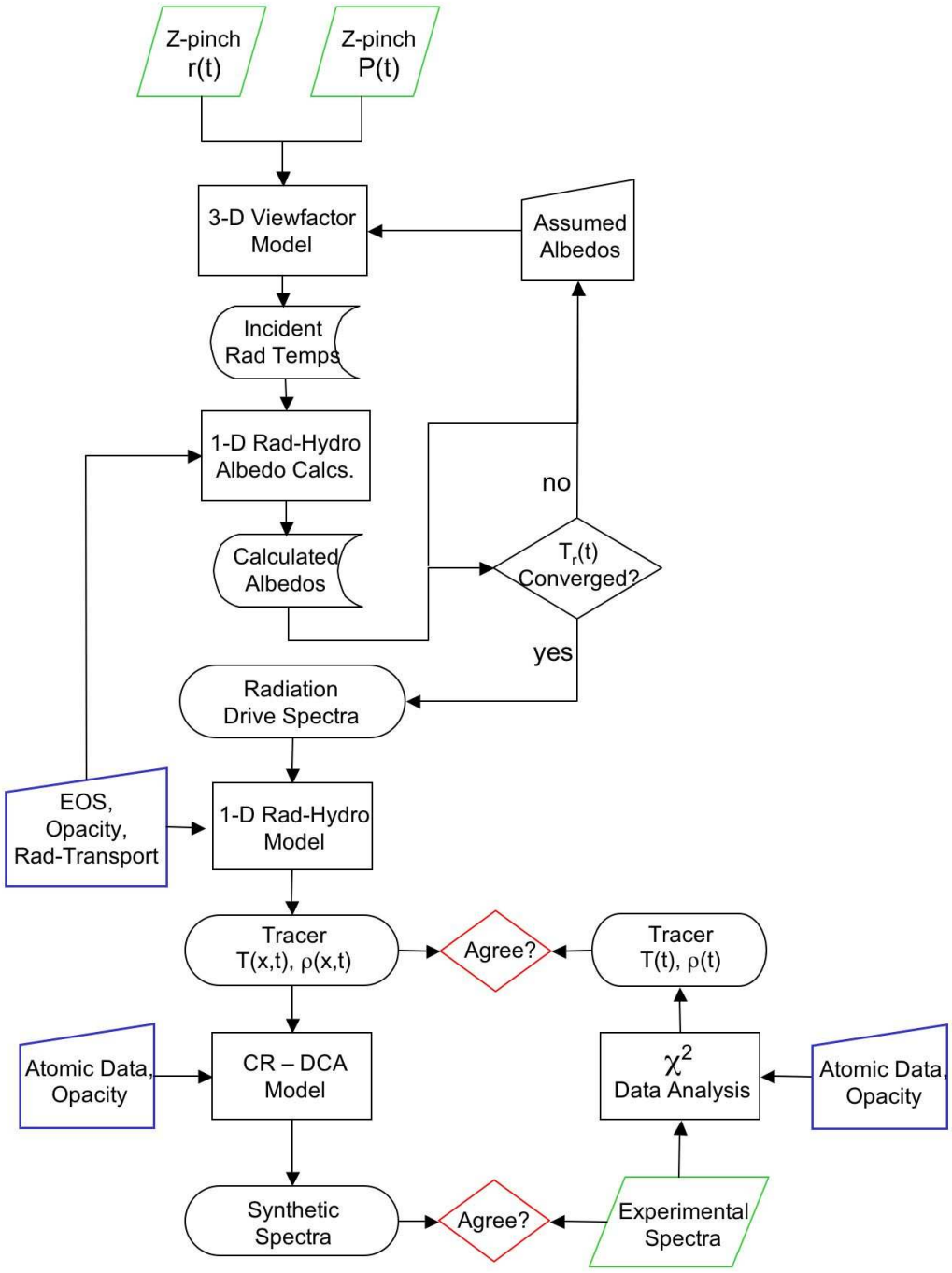

Figure 4.1: Flow-diagram of the computational method used to analyze ride-along experiments in this thesis.

spectra, which can then be compared to the calculated tracer conditions in an accurate, consistent, and unbiased way.

The computer codes that are utilized to conduct the simulations in this thesis are: VISRAD [92], a 3-D view-factor code for calculating the spatial and spectral dependence of a radiation source in complex geometry; BUCKY [11], a 1-D radiation hydrodynamics code; EOSOPA [91] and PROPACEOS [93], two codes for computing the opacities of high-temperature plasmas with detailed atomic models; SPECT3D [94], a code for computing the detailed spectral properties of multi-dimensional plasmas; and SPECTROFIT, a new code developed to conduct automated chi-squared analysis between experimental and calculated spectra. These codes, and the sensitivity of the calculated solutions on their various options and input parameters, will be discussed in detail in §4.1 - §4.5.

4.1 VISRAD

One of the primary difficulties in simulating the radiation-hydrodynamics processes of a complex experiment is in determining the boundary condition on the sample surface. In any kind of experiment that drives a sample by indirect radiation, it is important to know the distribution of radiation sources that fall within that sample's field-of-view. This is particularly true if there is not a well-defined localized source. In fast z-pinches, this complication is associated with the albedo re-emission of the high-Z power flow surfaces that are in close proximity to the intense z-pinch. Clearly, if these surfaces fall within the field-of-view of the sample, then the radiation spectra that drives the sample will contain contributions from multiple sources (with multiple temperatures). It is therefore necessary to calculate the space- and time-dependent spectra of the radiation that drives the sample, with careful consideration of the contributions from every hot surface. This

can be done with a 3-D view factor calculation such as that in VISRAD [92], a 3-D view factor code developed at Prism Computational Sciences.

VISRAD conducts a power balance by solving the radiosity equation:

$$B_i - \alpha_i \sum_j \Gamma_{ji} B_j = E_i, \tag{4.1}$$

where B_i is the flux emitted by surface i, α_i is the albedo of surface i, Γ_{ji} is the fraction of energy leaving surface j that reaches i, and E_i is the power emitted from i due to external sources. The user builds a 3-D grid of surface elements composed of planes, cylinders, and spheres, and assigns an albedo and source power to every element. VISRAD then solves Eq. 4.1 at every element, i, for the incident radiation that arrives from every other element, j. The geometric attenuation and additional considerations for the field-of-view (whether or not an obstruction exists in the straight-line path between j and i) is incorporated in the coefficient Γ_{ji}. Finally, assuming that each surface element emits its radiation intensity, B_i, in a black body distribution, then the VISRAD calculations will combine the individual spectrum from each element i to determine the total spectrum incident on any surface in the grid. Therefore, if the time- and space-dependent power sources are known (the z-pinch radius and power), and the albedos of the surface elements have been previously calculated, then a separate view factor calculation can be conducted at every time in the simulation to obtain a time-dependent radiation spectrum at any surface element in the grid. These data can then be input as a time- and frequency-dependent radiation boundary condition in a radiation-hydrodynamics calculation of the sample response for the purpose of designing future experiments, or comparing a calculational model to existing experimental data.

—

In applying any computational method to model an experimental result, it is important to

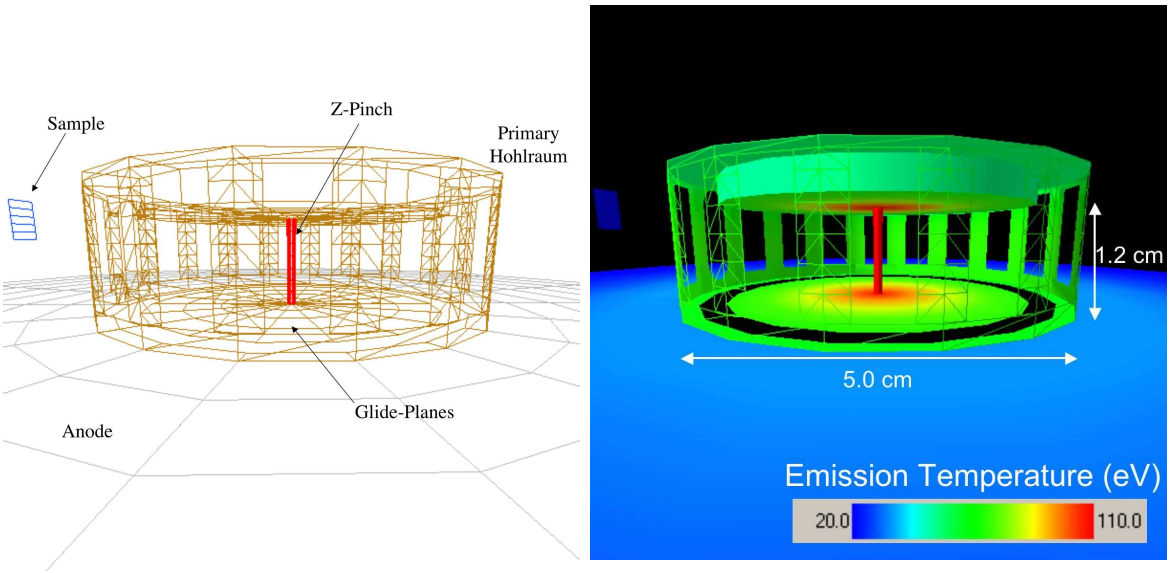

(a) **(b)**

Figure 4.2: **(a)** Example 3-D VISRAD grid for modeling a ride-along experiment at Sandia's Z facility. **(b)** VISRAD modeled emission temperatures for a z-pinch temperature of $T_r = 216eV$.

study the sensitivity of the model on those parameters that are either unknown or contain significant uncertainties. In §3.1, the radiation transport model of the experiments in this thesis was shown to be sensitive to the radiation drive spectra. As explained above, the approach taken in this thesis is to model these drive spectra in VISRAD for the experiment geometry described in §3.3. Figure 4.2(a) shows an example 3-D grid used in VISRAD to model a standard ride-along experiment on Z. As seen in the figure, the sample's field-of-view includes a portion of both the z-pinch and the diode hardware. Each of these surfaces is given a characteristic power source and/or albedo, so that the sample is exposed to radiation from multiple sources that emit over a range of temperatures. In this situation, the degree of uncertainty in the radiation drive spectra depends on the degree of uncertainty in the power sources and albedos. As described in §3.3, the time-dependent z-pinch power is measured on Z by the XRDs and bolometers (20% uncertainty), and the

z-pinch radii are measured by a combination of pinhole and streak cameras ($10 - 20\%$ uncertainty). However, the albedos of each surface are calculated based on the incident radiation spectra and therefore contain an unknown level of uncertainty.

To investigate the effects that each of these uncertainties has on the sample drive, a sensitivity study was conducted where the drive spectra was calculated in VISRAD as a function of the variation in each individual parameter. Figure 4.2(b) shows the calculated emission temperatures of the surfaces in the example VISRAD grid in Figure 4.2(a). In this calculation, the sample is placed at a radial distance of $4.3cm$ from the z axis and centered at a height of $1.219cm$ above the anode surface. The z-pinch is $1.2cm$ tall with a radius of $0.06cm$, and is radiating at a power of $101TW$ ($T_r \approx 216eV$). The primary hohlraum wall is at a radius of $2.5cm$ and is given an albedo of 0.694. The z-pinch glide-planes (inside top and bottom of the hohlraum) are given an albedo of 0.724, and the outer anode (surface outside the hohlraum) is given an albedo of 0.449. Figure 4.3 shows the total spectrum incident on the sample surface for this calculation, and the contribution to that spectrum from the major surfaces in the grid. The average energy of the total spectrum is $666eV$ compared to the average energy of the z-pinch, which is $828eV$, and the average energy of the flux-equivalent $52eV$ blackbody, which is $199eV$. Also shown in Figure 4.3 is a pie chart of the percent contribution of each surface to the total flux on the sample. As one might expect, the pinch makes up the dominant fraction of the drive spectrum, but a considerable 30% comes from the other surfaces.

To illustrate the effect that the uncertainties in each of these contributions has on the drive spectrum, Figure 4.4 shows the results of a sensitivity study where the z-pinch power, z-pinch radius, and the albedo of each surface is independently varied by $\pm 20\%$. Figure 4.4(a) shows the percent variation in the total drive flux, and Figure 4.4(b) shows the percent variation in the average energy of the drive spectrum. It is clear from both

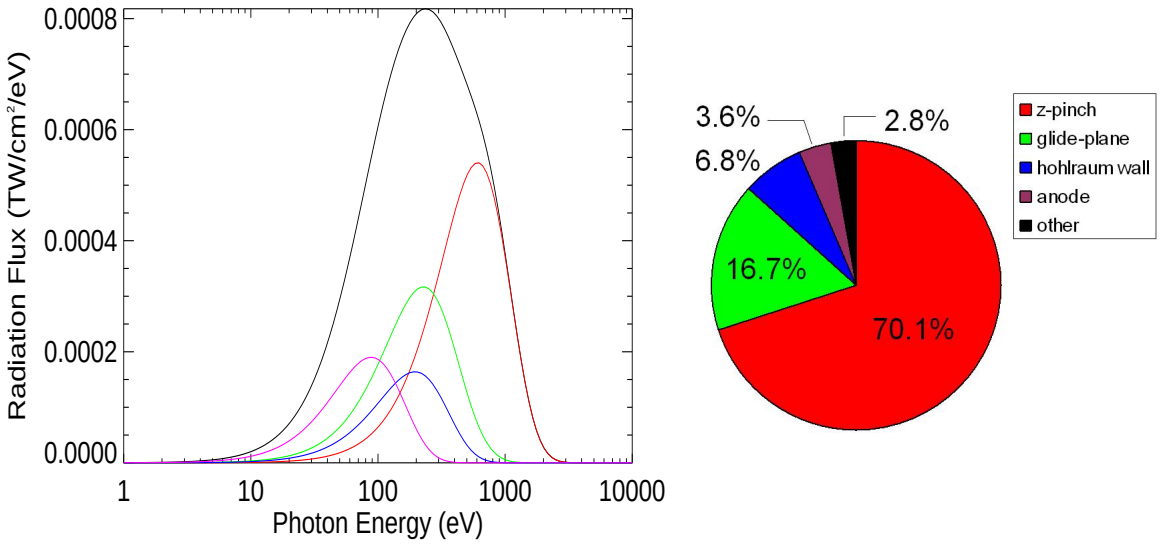

Figure 4.3: Total incident radiation spectrum (black) on the surface of the experimental sample. This spectrum is a convolution of spectra from the z-pinch (red), lower glide plane (green), hohlraum wall (blue), and outer anode (purple). The pie chart shows the fraction of the total spectrum from each surface in the VISRAD calculation.

figures that the uncertainty of the z-pinch power is the dominant source of uncertainty in the drive spectrum. There is a nearly one-to-one relationship in the uncertainty of the drive flux to the uncertainty in the z-pinch power, but the maximum change in the average spectral energy is only $\approx 5\%$ (which is not that surprising since $T_r \sim I_0^{1/4}$).

The exact fractions of the total drive spectrum from each surface, and the exact sensitivity of that spectrum on variations in the parameters of these surfaces is different at each time-step and for different diode geometries. However, calculations suggest that the final results are similar to that in the example described above. Thus, the most important component in the view-factor calculation is the time-dependent radiation power of the z-pinch, which makes it the most important parameter to directly measure on every experiment with the highest possible degree of accuracy.

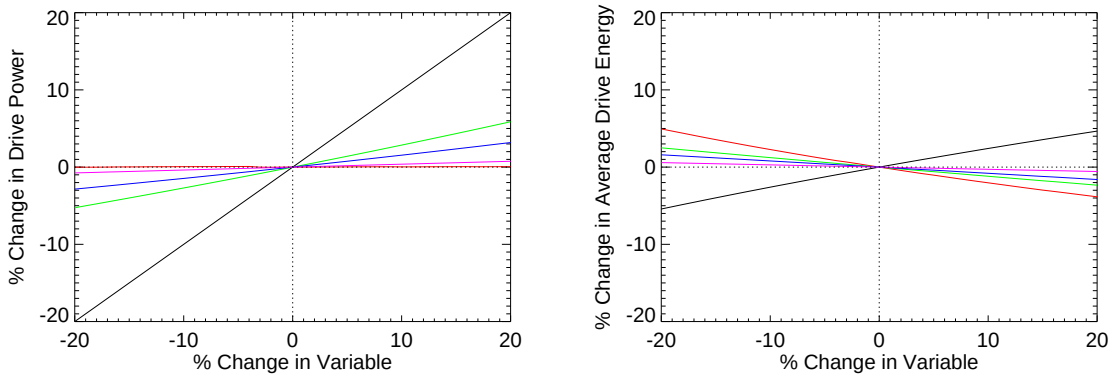

(a) **(b)**

Figure 4.4: Percent variation in the **(a)** drive flux and **(b)** average spectral energy versus the percent variation in the z-pinch power (black), z-pinch radius (red), glide-plane albedo (green), hohlraum wall albedo (blue), and anode albedo (purple).

4.2 BUCKY

As discussed in §1.2, the radiation power-density required for ICF is very high. This high radiation flux rapidly heats the sample material causing hydrodynamic motion that changes the sample conditions and effects the radiative transfer. Thus, simulating the sample response at high radiation powers requires integrated calculations of the radiation-hydrodynamics processes within the experimental sample. These types of calculations can be conducted with BUCKY, a 1-D radiation-hydrodynamics code developed at the University of Wisconsin Fusion Technology Institute [11].

BUCKY essentially solves 4 + n coupled partial differential equations in Lagrangian coordinates (for n the number of frequency groups in the multi-group radiation transport calculation). These are:

- Mass Conservation:

$$\frac{\partial V}{\partial t} = \frac{\partial}{\partial m}\left(r^{\delta-1}u\right), \tag{4.2}$$

where V is the specific volume ($1/\rho$), u is the fluid velocity, r is the position of the Lagrangian fluid particle, m is the Lagrangian mass, and δ is a coefficient which depends on the coordinate system (= 1 for planer, 2 for cylindrical, and 3 for spherical coordinates).

- Momentum Conservation:

$$\frac{\partial u}{\partial t} = -r^{\delta-1}\frac{\partial}{\partial m}(P_e + P_i + P_r + q) + \dot{u}_{TN}, \tag{4.3}$$

where P_e, P_i, and P_r are the electron, ion, and radiation pressures, q is the Von Neumann artificial viscosity (to prevent discontinuities across shock fronts), and $\dot{u}_{TN}$ is the change in velocity due to the slowing of non-thermal particles (typically fusion reaction products).

- Energy Conservation:

$$c_{v_e}\frac{\partial T_e}{\partial t} = \frac{\partial}{\partial m}\left(r^{\delta-1}\kappa_e\frac{\partial T_e}{\partial r}\right) - \omega_c(T_e - T_i) - \left[\frac{\partial \epsilon_e}{\partial V} + P_e\right]\frac{\partial V}{\partial t} - A + J + S_e \tag{4.4}$$

$$c_{v_i}\frac{\partial T_i}{\partial t} = \frac{\partial}{\partial m}\left(r^{\delta-1}\kappa_i\frac{\partial T_i}{\partial r}\right) - \omega_c(T_e - T_i) - \left[\frac{\partial \epsilon_i}{\partial V} + P_i\right]\frac{\partial V}{\partial t} - q\frac{\partial V}{\partial t} + S_i, \tag{4.5}$$

where T is the temperature, c_v is the specific heat capacity, κ is the conductivity, ω_c is the electron-ion collision rate, ϵ is the specific energy, A is the radiative heating, J is the radiative cooling, S is the contribution from external sources, and the subscripts e and i refer to electrons and ions respectively.

- Radiation Transport: Multi-group radiation transport is computed using a choice of flux-limited diffusion or multi-angle short characteristics (see Appendix B).

As indicated by the energy conservation equations, BUCKY can calculate the transfer of energy in a plasma where electrons and ions are not in thermal equilibrium. In this mode, ions and electrons are assumed to have Maxwellian distributions characterized by their individual temperatures, and thermal conduction is controlled using the Spitzer conductivity of each species (flux-limited for electrons) coupled by a thermal relaxation term. The electron and ion pressure terms in the energy and momentum conservation equations are determined from tabulated equation of state data typically taken from the Sesame equation of state tables. The radiative heating, radiative cooling, and the radiation pressure terms are calculated from the radiation energy density which is computed by one of the radiation transport equations. These rates, and the radiation transport model, utilize Rosseland and Planck averaged multi-group opacities that are typically generated by the EOSOPA or PROPACEOS codes. Finally, energy deposition from external sources is calculated for a user-supplied time history of ion beam (or target debris) energy, laser beam energy, x-ray energy, and/or neutron and charged particle energy from thermonuclear reactions.

One of the primary features of BUCKY, which sets it apart from many other radiation-hydrodynamics codes, is the ability to simulate the thermonuclear burn in a hot, dense plasma. The fusion burn equations calculate the reaction rates for DT, DD, and D^3He fusion reactions and deposit the fusion energy through a radial escape probability model (for neutrons) or a time-, energy-, and species-dependent stopping power model (for ions). An example of the integrated fusion burn calculation for a BUCKY modeled ICF capsule is shown in §1.2. Thus, BUCKY can be used to not only design experiments on present day laboratory-scale plasmas (as is done in this thesis), but also to design baseline ignition and reactor scale ICF targets.

4.2.1 Radiation Transport Issues in BUCKY

As inferred from the discussion above, there are number of different physical models available in BUCKY, each of which has adjustable parameters or utilizes information drawn from a variety of different data tables. This mostly includes models used for the equation-of-state, opacity, and radiation transport. The effect of multiple variations in the latter two were discussed in detail in describing the motive for this thesis in §3.1, and it will be shown in Chapter 6 that the various equation-of-state models have very little effect on the calculated results. However, before drawing any conclusions on the differences in the calculations associated with different physical models, it is important to verify that those models are properly implemented.

In the process of analyzing the experiments described in Chapter 6, it was discovered that, in every case, flux-limited diffusion in BUCKY was predicting radiative transfer speeds that were slower than indicated by the data. As an example of this, Figure 4.5(a) shows measurements of the temperature in tracers at two separate locations in a $5mg/cc\ CH_2$ foam, and that calculated by flux-limited diffusion using the SUM limiter in BUCKY. This difference was first attributed to inadequacies in the approximations of the diffusion equation, and the ad-hoc nature of the flux-limiter. However, further investigation into the BUCKY calculations suggested that there were instead some inadequacies in the implementation of the boundary conditions and flux-limiters.

To illustrate how this understanding came about, Figure 4.5(b)-(d) show comparisons between BUCKY diffusion calculations and some analytic solutions derived by Su and Olson (see §B.5). Figure 4.5(b) is a comparison of diffusion (no flux-limiter) to the Marshak wave problem for a semi-infinite slab [98] at 3 different times. At each time, the BUCKY solution predicts a slower radiation flow in comparison to the analytic solutions.

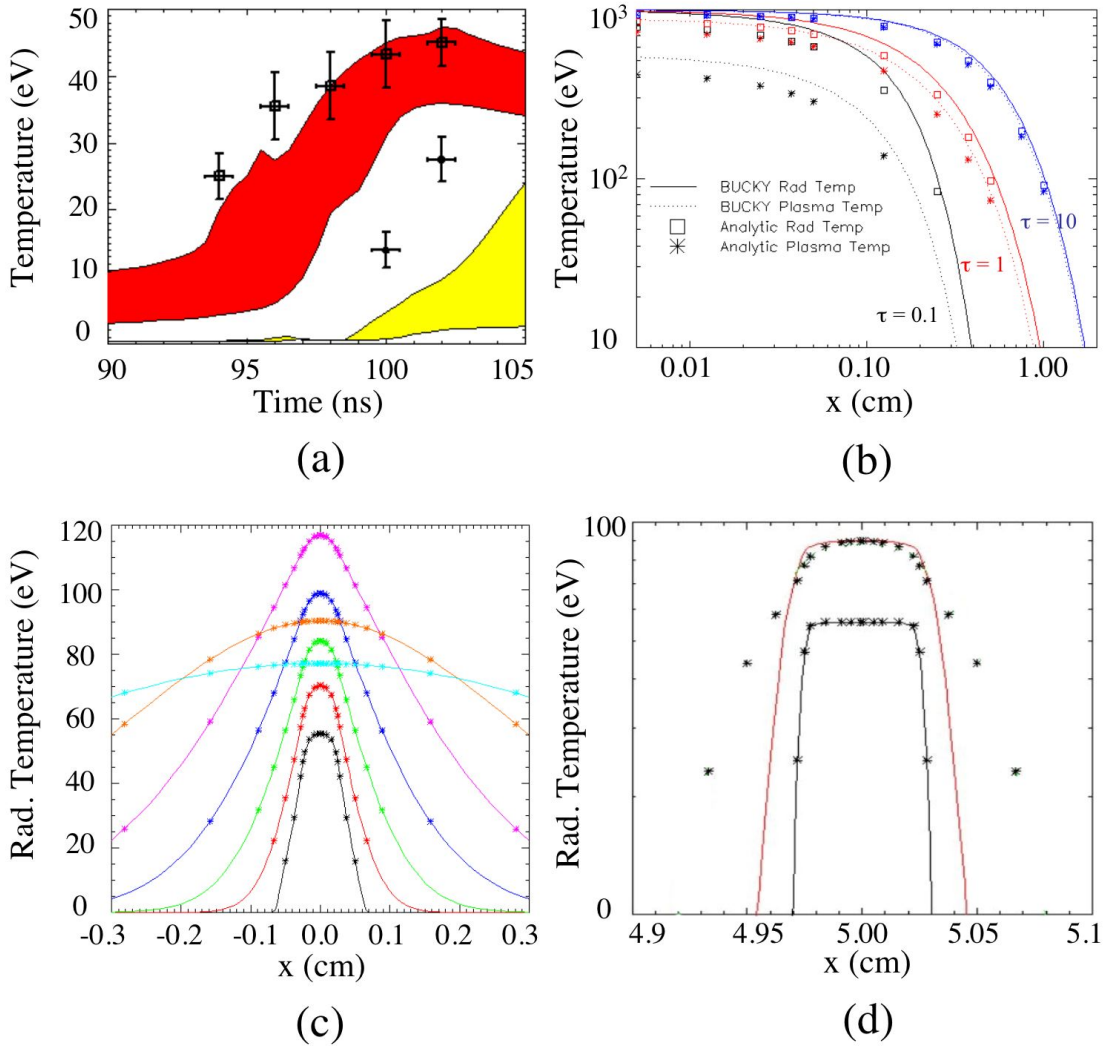

Figure 4.5: Comparison between BUCKY calculations using the original implementation of flux-limited diffusion and; (a) experimental electron temperatures, (b) the analytic Marshak wave solution, (c) the diffusion solution to the Su and Olson finite source problem, (d) the transport solution to the finite source problem. All analytic or experimental data points are plotted as symbols.

Figure 4.5(c) is a comparison of diffusion to the problem of a time-dependent finite source in an infinite slab [99]. In this case, the BUCKY solutions accurately reproduce those for analytic diffusion. The only functional difference between these two calculations is the existence of the boundary in the Marshak wave problem. This suggested an inadequacy in the implementation of the diffusion boundary conditions. In addition, Figure 4.5(d) shows a comparison between flux-limited diffusion in BUCKY (SUM limiter) and an analytic solution to true transport for the problem of a time-dependent finite source in an infinite slab. In this case, the BUCKY flux-limited solution does not approximate the transport solution very well, even though the diffusion solutions were quite similar. This suggested that either flux-limited diffusion is not a good approximation under the conditions in this problem, or there were inadequacies in the implementation of the flux-limiter in BUCKY.

Appendix B describes a complete verification suite that was designed to test each component of both the flux-limited diffusion and short-characteristics finite difference equations as implemented in BUCKY. Through these tests, the diffusion equations in BUCKY were re-implemented with a more careful treatment of the boundary conditions, and a consistent implementation of the flux-limiter. Figure 4.6(a)-(d) show the same comparisons as in Figure 4.5(a)-(d), only with the new implementation of flux-limited diffusion. As evidenced in Figure 4.6(c), the new flux-limited diffusion solutions still reproduce the Su and Olson result in an infinite medium, but Figure 4.6(b) shows that it now also closely follows the solutions to the Marshak wave problem. In addition, Figure 4.6(d) illustrates the better comparison between the Su and Olson transport solution in an infinite medium, and that calculated by the new implementation of flux-limited diffusion in BUCKY (SUM limiter). Finally, Figure 4.6(a) shows how the combination of these improvements leads to a much better agreement between the flux-limited diffusion

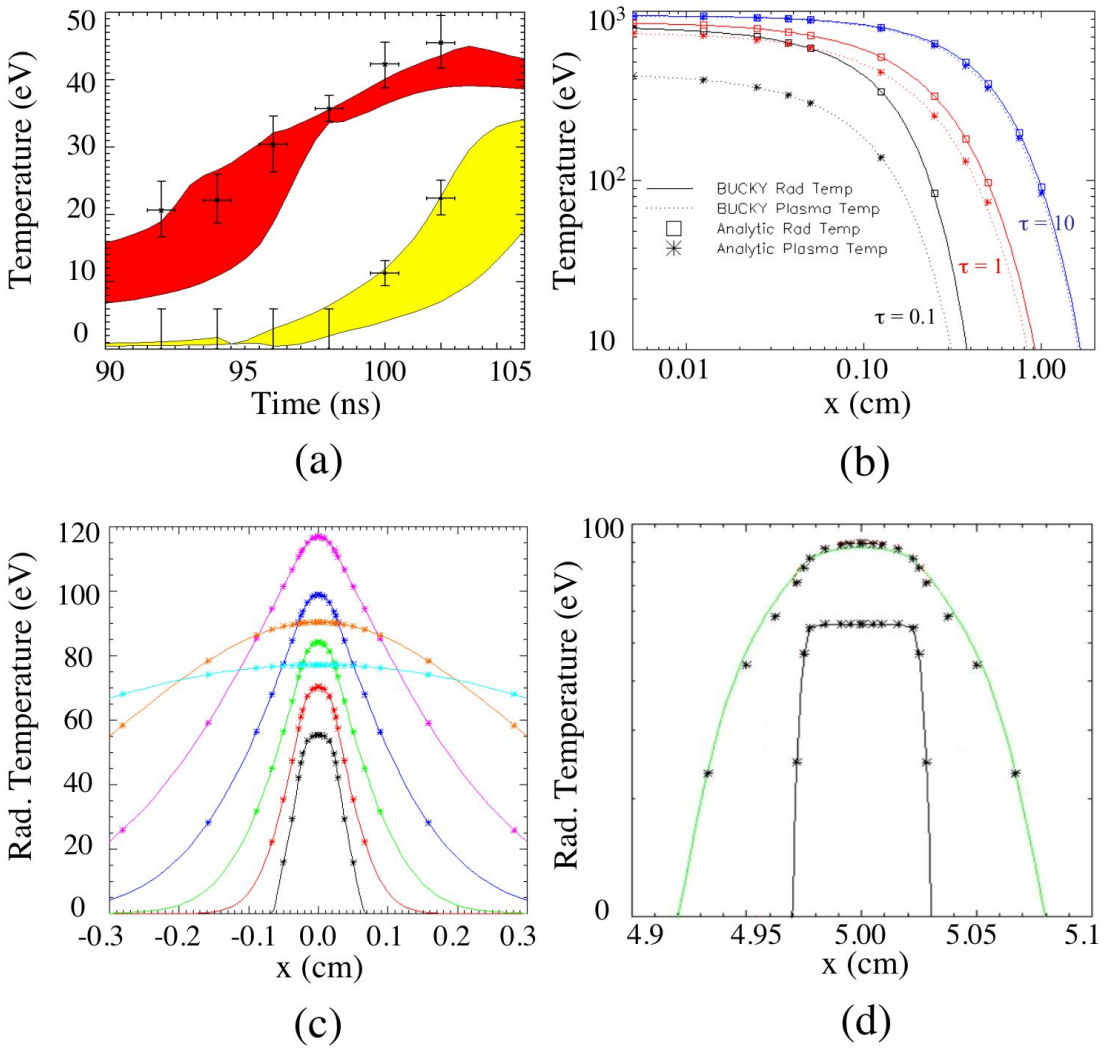

Figure 4.6: Comparison between BUCKY calculations using the new implementation of flux-limited diffusion and; (a) experimental electron temperatures, (b) the analytic Marshak wave solution, (c) the diffusion solution to the Su and Olson finite source problem, (d) the transport solution to the finite source problem. All analytic or experimental data points are plotted as symbols. In contrast to Figure 4.5(a)-(d), these figures show the increased accuracy with the new implementation of flux-limited diffusion.

solution in the rad-hydro simulation of the CH_2 foam experiment than that shown in Figure 4.5(a).

As described in detail in Appendix B, the new implementation of flux-limited diffusion and short-characteristics in BUCKY were determined to be accurate, and therefore provide a high level of confidence in the radiation transport portion of the BUCKY simulations.

4.3 EOSOPA and PROPACEOS

When the details of the radiation transport are important, the radiation-hydrodynamics models must include high-quality multi-group plasma opacity data across the entire range of temperature and density conditions in the simulation. Depending on the conditions of the plasma, as well as the atomic number of the elements or mixtures being simulated, there are a number of different methods that can be applied to calculate the atomic cross-section data and charge state population distributions that ultimately determine the plasma opacities. For the simulations described in this thesis, these opacities are calculated with either EOSOPA [91][a], a code developed at the University of Wisconsin Fusion Technology Institute, or PROPACEOS [93], a code developed at Prism Computational Sciences. These codes determine, among other things, the opacity of a given element or mixture based on the charge-state populations of the ions in the plasma. That is, each solves the self-similar rate equation for the change in charge-state population densities due to collisional and photo-absorption/emission processes of the form:

$$\frac{\partial \overrightarrow{f}(n,t)}{\partial T} = \overleftrightarrow{A}\,\overrightarrow{f}(n,t), \tag{4.6}$$

[a] Because multiple versions of EOSOPA exist in the community, it is noted that the version discussed in this thesis is that which is contained in JATBASE [100], a PC application which wraps together EOSOPA, UTAOPA, and RSSUTA.

where $\overrightarrow{f}(n,t)$ is the array of fractional charge-state populations (the population vector) as a function of density and temperature, and $\overleftrightarrow{A}$ is the rate matrix as determined by the particular plasma model applied.

The terms in Eq. 4.6 depend on the state of the plasma, the energy distribution of the photon field in the plasma, and the atomic cross-sections as a function of photon energy. The state of the plasma is divided into three regimes within EOSOPA and PROPACEOS. For dense plasmas, where the electrons and ions have equivalent energy distributions, the plasma is considered to be in local thermodynamic equilibrium (LTE), and the charge-state populations, N_z, are given by the familiar Saha equation:

$$\frac{N_{z+1}}{N_z} = 2\left(\frac{2\pi m_e kT}{h^2}\right)^{3/2} N_e^{-1} \frac{\sum_m g_m^{(z+1)} \exp\frac{-\epsilon_m-\epsilon_0}{kT}}{\sum_{m'} g_{m'}^{(z+1)} \exp\frac{-\epsilon_{m'}-\epsilon_0}{kT}} e^{-\Phi_z/kT}, \tag{4.7}$$

where ϵ_m and g_m are the energy and gaunt factor of level m, and Φ_z is the ionization potential of charge state z. For very low density and optically thin plasmas, the plasma is assumed to be in coronal equilibrium (CE) where the rate of ionization, $I_{z,z+1}$, is approximately equal to the rate of recombination, $R_{z+1,z}$. In particular, the dominant processes are assumed to be electron impact ionization and radiative recombination such that, in CE, the charge-state populations are calculated by equating these two rates as a function of density and temperature in the plasma in the form:

$$\frac{N_{z+1}}{N_z} = \frac{I_{z,z+1}(T_e,n_e)}{R_{z+1,z}(T_e,n_e)}. \tag{4.8}$$

At intermediate densities and optical depths, EOSOPA and PROPACEOS assume a collisional radiative equilibrium (CRE) where the photon field is assumed to be approximately black-body, the free electrons are assumed to have a Maxwellian distribution, and the coupled system is assumed to be in a steady state. In this case, the charge-state populations are determined by equating the sum over the various atomic ionization/excitation rate coefficients to their corresponding inverse processes (i.e. recombination).

Once the charge-state populations (N_z) are known at each density and temperature, then the total opacities are calculated from a weighted combination of the atomic cross-sections for the various energy bins in the multi-group frequency structure. In this way, not only are EOSOPA and PROPACEOS data dependent on the particular plasma model applied in the calculation, but also on the atomic physics model applied to generate the atomic cross-sections. These cross-sections are determined by ATBASE [95], a code also developed at the University of Wisconsin Fusion Technology Institute.

ATBASE solves the different energy levels available to a given atom by determining the eigenfunctions and eigenvalues of the Schrödinger equation through either the Hartree-Fock approximation, or the local potential approximation of the electron wave functions. In the latter, ATBASE contains four possible functional forms for the local potential; the Hartree (H) potential, the Hartree-Slater (HS) potential, the Hartree-Fock-Slater (HFS) potential, and the Hartree-Plus-Statistical-Exchange (HX) potential. Once the possible energy levels have been determined, the set of possible atomic transitions and their associated oscillator strengths can be determined by either detailed term accounting (DTA) or the unresolved transition array (UTA) method. Thus, there is great flexibility in the methods by which to calculate the various atomic cross-sections. One notable limitation in the current version of ATBASE is the inability to compute the collisional and recombination rate coefficients under the UTA method. This limits the UTA method to only the LTE approximation. Since this limitation does not exist under the DTA method, the opacities calculated for non-LTE plasmas are done using detailed term accounting.

To this point, EOSOPA and PROPACEOS have been described as containing the same physics, and the primary equations in each code are essentially the same. There are, however, a few important differences. First, the occupational probabilities in EOSOPA

are calculated at LTE using the Boltzmann statistical partition function over all plasma conditions. This can cause inaccuracies in the number of free electrons at low temperatures and high densities (near cold solid conditions), which in turn can lead to inaccuracies in the free-free opacities at low photon energies. In PROPACEOS, this has been 'fixed' by assuming the Hummer-Mihalas partition function [97], which contains some corrections for long-range bonding forces that effectively reduce the number of free electrons. Second, EOSOPA assumes a fit to the Hartree-Fock calculations around bound-free edges in the opacity, which occasionally do not accurately reproduce the calculations. To avoid this, PROPACEOS utilizes tabulated data points of the Hartree-Fock calculations that are produced by ATBASE at photon energies within a factor of 100 times the threshold energy. Third, EOSOPA uses a semi-empirical procedure to calculate the stark broadening of bound-bound transitions, while PROPACEOS uses a fit to quantum mechanical calculations of the broadening for individual configurations.

In all, these differences are rather minor, but can have a noticeable effect on the calculated opacity. As an example, Figure 4.7(a) shows EOSOPA and PROPACEOS calculated 500 group Planck opacities of an aluminum plasma at $1.0g/cc$ and $1.0eV$. The K-edge ($\approx 1500eV$) and L-edge opacities ($\approx 300eV$) have very similar shapes, but differ by a factor of ≈ 10 in amplitude. Additionally, the entire shape of the opacities at energies $< 50eV$ are noticeably different. However, this calculation is in the region where all the differences listed above are most pronounced. Figure 4.7(b) shows EOSOPA and PROPACEOS calculated Planck opacities of an aluminum plasma at $0.01g/cc$ and $50eV$. In this case, the calculations are almost identical.

In the end, EOSOPA and PROPACEOS generate: the mean charge-state of the plasma, $\overline{z}$; the Rosseland mean group opacity, σ_R; the Planck mean emission group opacity, $\sigma_{p,e}$; and the Plank mean absorption group opacity, $\sigma_{p,a}$. These data are then read

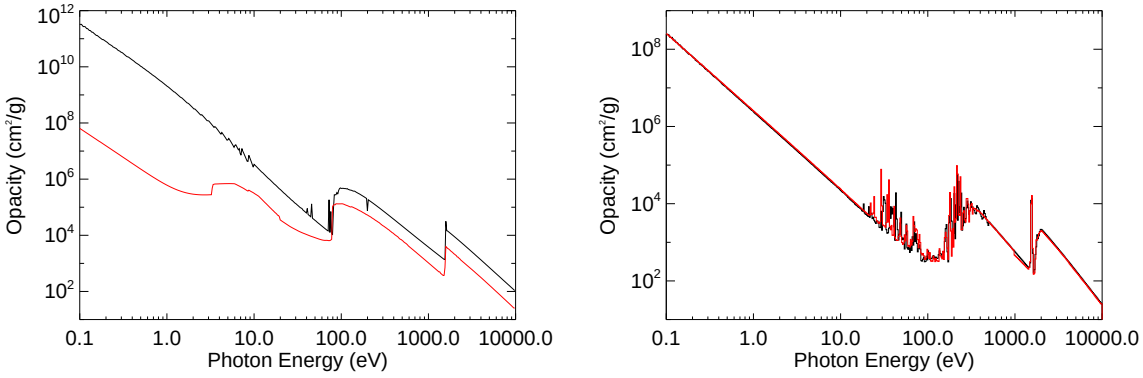

(a) (b)

Figure 4.7: Planck absorption opacities in aluminum as calculated by EOSOPA (black) and PROPACEOS (red) for (a) 1.0 eV and 1.0 g/cc (b) 50 eV and 0.01 g/cc.

into the BUCKY radiation-hydrodynamics code (see §4.2) and the SPECT3D collisional-radiative post-processing code (see §4.4) as part of the equations for computing the radiative transfer rates.

4.4 SPECT3D

Once a complete radiation-hydrodynamics calculation of a particular experiment has been conducted, it is necessary to post-process the computational data for comparison to the information provided by the experimental diagnostics. If the primary diagnostic on the experiment is a spectrometer, then the temperature and density data from the computation must be converted into emission or absorption spectra at the diagnostic location. One computer code that can be applied to calculate this detailed spectra is SPECT3D [94], a system of codes developed by Prism Computational Sciences to simulate the spectral and radiative properties of multi-dimensional plasmas.

There are essentially two different components to a SPECT3D calculation. The first is

a definition of the atomic model, which is compiled from data generated by the ATBASE atomic data code (see §4.3). Contained in the ATBASE data files are the collisional and radiative cross section data for the large number of energy levels needed to compute the level populations and the associated detailed emission or absorption spectra. The user can individually specify which atomic energy levels are considered in the model so as to minimize the computation time while maintaining the spectral details of interest. The second component in a SPECT3D calculation is the actual computation of the absorption or emission spectra along the line-of-sight of the diagnostic. There are a few different opacity models that can be used for this calculation. These are; (1) a multi-group table look-up, (2) a local thermodynamic equilibrium (LTE) approximation, and (3) a collisional-radiative (C-R) approximation including either no photo-processes, photo-excitation with a local escape probability model, or photo-excitation and photo-ionization calculated from non-local radiation.

Once these specifications have been defined, SPECT3D conducts a detailed configuration analysis (DCA) of the sample plasma to determine the populations of the various ionization-states and energy levels. This is then used to calculate the absorption of the backlighter radiation in combination with the total radiation emission from the hot plasma to produce a detailed spectrum emerging from the sample. In this way, SPECT3D provides a means for post-processing BUCKY rad-hydro data that can be directly compared to experimentally observed spectra.

—

As described above, there are various approximations available in SPECT3D for modeling the detailed radiation-transport and ionization balance in the calculation of the simulated absorption spectra. It is therefore necessary to determine which is most suited to model the conditions in the tracer layers described in Chapter 3. To help investi-

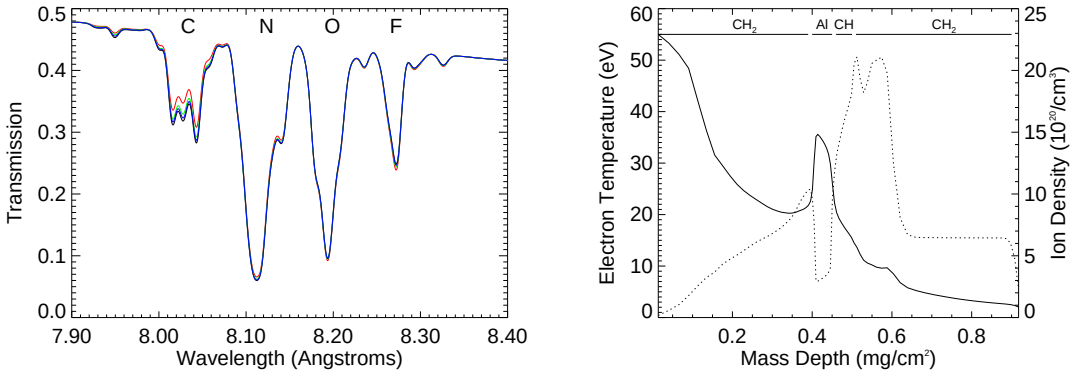

(a) **(b)**

Figure 4.8: (a) SPECT3D calculated absorption spectrum for DCA populations calculated assuming; LTE (black), C-R assuming only collisional processes (red), C-R assuming a local blackbody radiation spectrum with a radiation escape probability model and no photo-ionization (green), and C-R assuming non-local radiation transported from everywhere in the sample and the backlighter (blue). **(b)** Electron temperature (solid) and ion density (dotted) profiles used for the calculations in (a). The sample consists of a 1500Å layer of aluminum on a 5000Å CH substrate tamped on either side by $0.85mm$ of $5mg/cc\ CH_2$ foam.

gate this, Figure 4.8(a) shows SPECT3D calculated absorption spectra in aluminum for 4 different combinations of approximations. These approximations are; LTE, C-R assuming only collisional processes, C-R assuming a local blackbody radiation spectrum with a radiation escape probability model and no photo-ionization, and C-R assuming non-local radiation transported from everywhere in the sample and the backlighter. The electron temperature and ion density profiles that were used for the calculations are shown in Figure 4.8(b)[b]. This sample consists of a $0.15\mu m$ aluminum tracer backed by a $0.5\mu m\ CH$ layer that is tamped on either side by $0.83mm$ of $5mg/cc\ CH_2$ foam. As seen in Figure 4.8(a), all approximations predict very similar absorption spectra. The largest deviation from the average case is in the C-R modeled spectrum assuming only

[b]The sample conditions in Figure 4.8(b) are typical of the conditions that may exist in a foam sample as described in Chapter 6

collisional processes. In this case, the calculation predicts the lowest average charge state, which shows up as a decrease in the absorption of the carbon-like K-α feature. This is not entirely surprising since this particular model does not include the effects of photo-ionization, which would tend to increase the average ionization state. The most complete model is the C-R calculation including photo-excitation and photo-ionization from non-local radiation. The average ionization state and resulting absorption spectrum from this calculation are very similar to the simple case assuming LTE. The largest difference between these two models is in the amount of time it takes the computer to do the calculation. The LTE case takes a few minutes, the C-R case with non-local radiation takes a few hours.

It is therefore concluded that, for sample conditions similar to that in Figure 4.8(b), an LTE approximation is adequate and by far the most efficient.

4.5 SPECTROFIT

Without regard to any of the simulations discussed in §4.1-§4.4, once an experimental spectrum has been corrected for the film and spectrometer response (see Appendix A), it can be directly compared to atomic/plasma calculations of the spectral features. As discussed in §3.2, the charge-state distribution in a plasma is a function of both the temperature and density. Once an experimental spectrum has been properly processed, it is a diagnostic of the possible temperature and density combinations that existed in the plasma at the time the spectrum was observed.

SPECTROFIT is a code that was developed to directly compare experimental absorption spectra to atomic/plasma calculations. In order to provide a quantitative analysis, the code calculates chi-squared values of the goodness-of-fit over a range of temperatures

and densities. This calculation can then be processed to provide the best-fit and $+1\sigma$ contours across the chi-squared topography in order to identify the most likely combinations of temperature and density in the plasma.

In SPECTROFIT, the model spectra are taken from tables of detailed frequency dependent opacities, σ_ν, that are calculated by EOSOPA or SPECT3D. These opacities are given in units of cm^2/g, so that the absolute transmission, T'_a, is calculated as:

$$T'_a(\nu) = e^{-\sigma_\nu A}, \tag{4.9}$$

where A is the areal density of the plasma (in g/cm^2). This must then be convoluted with the spectral resolution, $\Delta\nu$, of the experimental data by the relation:

$$T_a(\nu) = \mathcal{F}^{-1}\big\{\mathcal{F}\{T'_a(\nu)\} \times \mathcal{F}\{G(\nu)\}\big\}, \tag{4.10}$$

where $\mathcal{F}$ denotes the Fourier transform, and $G(\nu)$ is the Gaussian distribution function given by:

$$G(\nu) = \exp[-4\ln(2)(\nu/\Delta\nu)^2]. \tag{4.11}$$

Thus, to do a chi-squared comparison between the data and the calculations, the user must specify the areal density of the experimental plasma as well as the resolution of the spectrometer.

Before one can make this comparison, the experimental and model spectra must each be put on a common axis. As discussed in Appendix A, once the data has been corrected for the film and spectrometer response, the spectral amplitudes are given in $J/sr/A$. This is not very useful for comparing to the models because the plasma opacity calculations typically have no knowledge of the backlighter source intensity. If the backlighter spectrum is measured on the experiment, then the experimental data can be divided by the backlighter continuum to give an absolute transmission spectrum. This is the ideal

form of the data for a quantitative analysis since the absolute transmission can be readily determined from the calculated opacities. Unfortunately, experimentally obtaining both backlighter and absorption spectra is not always feasible. In these cases, both the data and the calculations need to be converted to *relative* transmission spectra. This conversion is accomplished by removing the absorption features from the spectrum, filtering the 'continuum', and dividing the spectrum by the result. However, obtaining the calculated relative transmission spectra over a range of temperatures and densities can be rather tricky. Since the charge-states change with the temperature and density, the location of the absorption features also change. Therefore, a different continuum must be defined for every combination of temperature and density. It is not practical for the user to do this by hand across the entire range of the calculation. To account for this, the user must specify wavelength ranges over which the chi-squared comparison will be done. At each temperature and density in the SPECTROFIT grid, these ranges are removed from the calculated spectrum, and the result is divided into the original spectrum assuming a linear interpolation between points. This is equivalent to dividing by a continuum that is linear across the features of interest, which is a good assumption for many calculated K-α spectra.

Once the data and calculation are on the same axis, SPECTROFIT calculates the reduced chi-squared of the fit for a selected range of temperature and density by the equation:

$$\chi^2 = \frac{s^2}{< \sigma_\nu^2 >}, \tag{4.12}$$

where the average standard deviation is given by,

$$< \sigma_\nu^2 >= \left[\frac{1}{N} \sum_{i=0}^{N} \frac{1}{\sigma_{\nu,i}^2} \right]^{-1}, \tag{4.13}$$

and the variance is given by:

$$s^2 = \frac{1}{N-2} \sum_{i=1}^{N} \left[\frac{<\sigma_\nu^2>}{\sigma_{\nu,i}^2} \right] \left[T_a(\nu_i) - T_e(\nu_i) \right]^2 , \tag{4.14}$$

where T_a and T_e are the calculated and experimental spectra, and the sums are taken over the N points of interest in the spectra. The standard deviation of the data, σ_i, must be specified by the user for each point in the experimental spectrum. In this way, the data can be assumed to follow the statistics that is most appropriate for the spectrum of interest (whether that be a Poisson distribution or some other measured statistical deviation).

Once χ^2 has been calculated at each assumed temperature and density, the results can be displayed as a 3-D surface plot or a 2-D contour plot in increments of $+1\sigma$ over the minimum χ^2. As an example, Figure 4.9(a) shows a simulated absolute transmission spectrum constructed by adding random Poisson noise to the EOSOPA calculated transmission of a $50eV$ aluminum plasma at an ion density of $6.77 \times 10^{20} cm^{-3}$. Using SPECTROFIT, this spectrum was compared to EOSOPA calculated spectra over a range of 60 different temperatures from $20 - 80eV$ and 30 densities from $6.7 \times 10^{18} - 6.7 \times 10^{22} cm^{-3}$. Figure 4.9(b) shows the 3-D surface plot of the SPECTROFIT calculated χ^2 versus the 1800 combinations of temperatures and densities in the grid. The minimum value of χ^2 in this grid is 1.0017 at a temperature of $50eV$ and an ion density of $6.77 \times 10^{20} cm^{-3}$. This is precisely the value that was used to construct the simulated data, and a χ^2 value of ≈ 1 signifies that the fit is exactly within the uncertainty in the data. However, as is usually the case with K-α distributions, there are a number of temperature and density combinations that give a χ^2 value that is very close to the minimum. To illustrate, Figure 4.10 shows a contour plot in temperature-density phase space, where each contour represents an increase of 1 over the minimum χ^2. Even in this idealized example, where

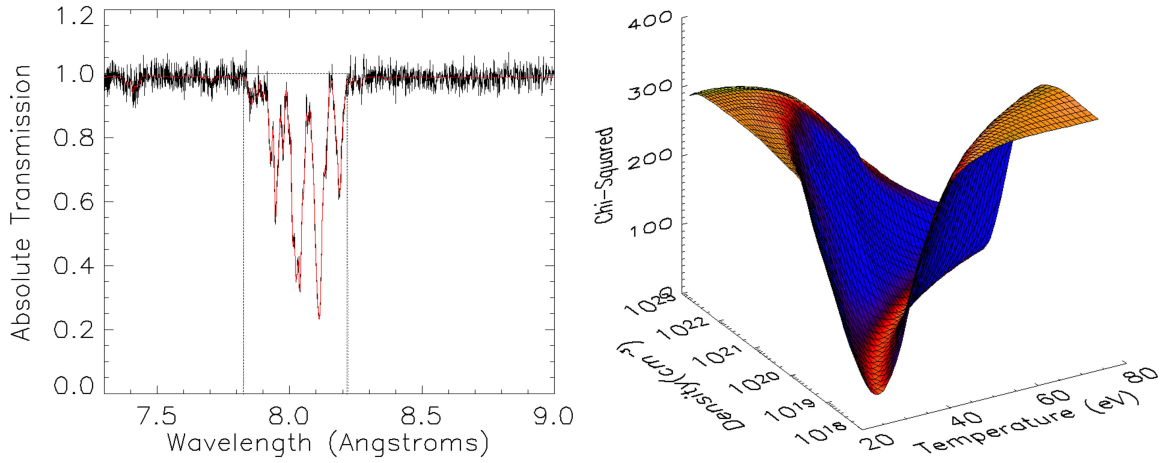

(a) (b)

Figure 4.9: **(a)** Spectrum calculated by EOSOPA for an Al plasma at $T_e = 50eV$ and $n_i = 6.77 \times 10^{20} cm^{-3}$ both with random Poisson noise (black) and without (red). The weights in the SPECTROFIT calculation were across the K-α complex only (dotted). **(b)** χ^2 surface plot of the SPECTROFIT calculation. The minimum value is 1.0017 at $T_e = 50eV$ and $n_i = 6.77 \times 10^{20} cm^{-3}$.

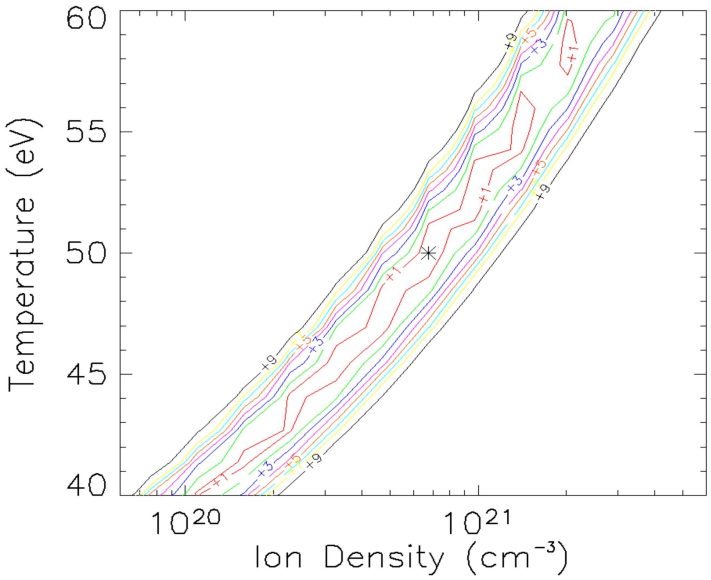

Figure 4.10: Contour plot of the SPECTROFIT calculation in Figure 4.9. Each contour represents an increment of 1σ over the minimum χ^2 (represented by the symbol).

the data spectrum is taken directly from one of the points in the calculation, there is a wide range of densities and temperatures that are within 1σ of the minimum χ^2. For this reason, attempts are often made to place limits on the density of the plasma so that the temperature can be more precisely determined. If the range of possible densities in the experimental plasma are known, then a graph like this can be used to determine the possible range of temperatures.

In the less ideal case of an experimental spectrum that contains a gradient in the temperature and/or density, the error-bars from the chi-squared fitting results can be much larger. Figure 4.11(a) shows an aluminum K-α absorption spectrum taken on Sandia's Z machine, and Figure 4.11(b) shows the surface plot from a SPECTROFIT calculation on this data. In this case, there is believed to be a $\approx 5eV$ gradient in the electron temperature and a $\approx 3 \times 10^{20} cm^{-3}$ gradient in the ion density. Figure 4.12 shows 2-D contours from the surface plot shown in Figure 4.11(b). The minimum χ^2 for the fitting calculation was 1.78 at a temperature of $64.4eV$ and an ion density of $4.17 \times 10^{21} cm^{-3}$. However, the contour plot shows that each density in the grid has a corresponding temperature that is within 1σ of the best fit. It is then necessary to specify a range of densities in order to identify the corresponding range of temperatures that are most likely to reproduce the experimental spectrum. As an example, radiation-hydrodynamics simulations predict that the ion density of the aluminum plasma in Figure 4.11(a) is from $7 - 10 \times 10^{19} cm^{-3}$ around the time that the data was taken. According to the SPECTROFIT calculation represented by Figure 4.12, that corresponds to an electron temperature of $38.4 \pm 2.7eV$. The rad-hydro simulation suggests that the electron temperature is between 34 and $39eV$. This is in good agreement with the SPECTROFIT results and is therefore in good agreement with the experimental data. In this way, experimental data can be easily compared to rad-hydro calculations in an unbiased and quantitative way.

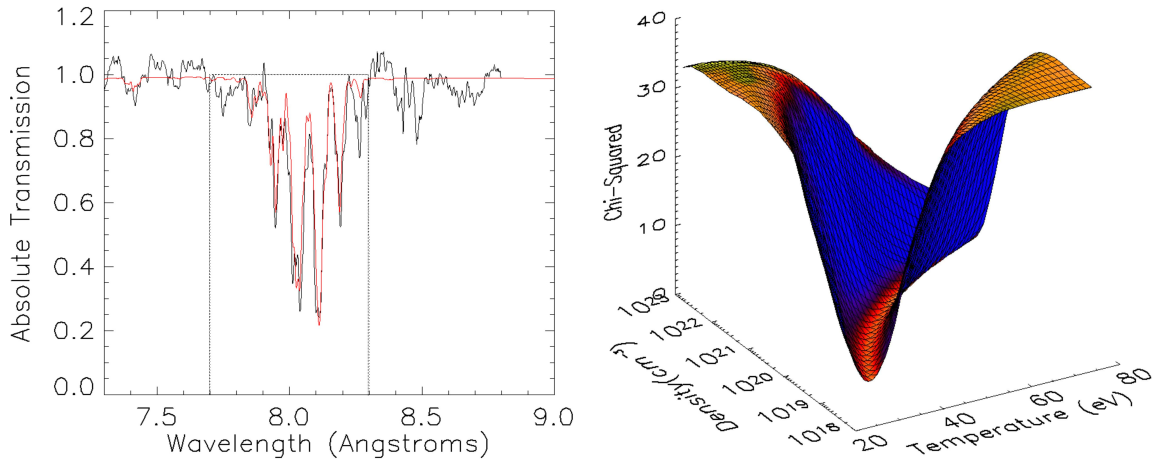

(a) (b)

Figure 4.11: (a) Aluminum K-α spectrum from an experiment on Sandia's Z machine (black), and that calculated by EOSOPA for an Al plasma at $T_e = 64.4eV$ and $n_i = 4.17 \times 10^{21} cm^{-3}$ (red). The weights in the SPECTROFIT calculation were across the K-α complex only (dotted). (b) χ^2 surface plot of the SPECTROFIT calculation. The minimum value is 1.78 at $T_e = 64.4eV$ and $n_i = 4.17 \times 10^{21} cm^{-3}$.

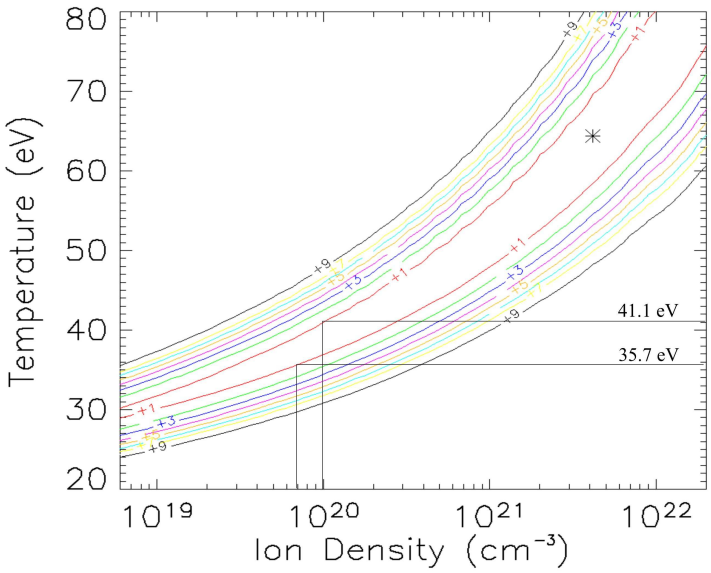

Figure 4.12: Contour plot of the SPECTROFIT calculation for the spectrum in Figure 4.11. Each contour represents an increment of 1σ over the minimum χ^2 (represented by the symbol).

Chapter 5

Thin Foil Experiments - Verification of the Experimental and Computational Methods

To recap the discussions of the last two chapters, the proposed experimental method is to use radiation from the z-pinch on Sandia's Z facility to drive and backlight a foam sample, which contains thin tracer layer(s) of Al and/or MgF_2. The conditions in the tracers are measured by the distribution of ionization states as evidenced by the tracers' absorption spectra. The computational method is then to model both the z-pinch radiation that drives the sample and the integrated radiation-hydrodynamics of the sample response. The calculated conditions in the tracer layers are then compared to those derived from the experimental data. Once the models can provide good agreement to the constraints in the experiment, then the details of the radiative transfer process are derived from the calculations.

These proposed methods are somewhat complex, and rely on multiple computations to interpret the experimental data and draw conclusions about the radiative transfer. It is therefore necessary to verify both the experimental approach and the computational methods. The objective of this chapter is to describe the data and analysis from ex-

periments on the Z facility intended to demonstrate an understanding of the heating and atomic absorption features of both mixed and separated Al and MgF_2 plasmas. As discussed in §3.2, these are the candidate materials to act as tracer diagnostics in the radiative transfer experiments that are the central focus of this thesis. It is therefore necessary to validate the calculations of the temperature and density distributions in these materials in order to gain confidence in the analysis procedures.

Section 5.1 describes two experiments that were fielded at the Z facility to measure the K-α absorption spectra from radiatively heated Al and Mg; one where the Al and MgF_2 were mixed by multi-layer deposition, and one where the Al was deposited in front of the MgF_2 along one line-of-sight, and the MgF_2 in front of the Al along a separate line-of-sight. Section 5.2 presents the data from these two experiments, along with a chi-squared comparison between the data and calculations of the K-α absorption over a range of temperatures and densities. Section 5.3 describes the computational modeling of the experiments including the calculation of the radiation drive spectra, the radiation-hydrodynamics modeling of the sample response, and the DCA spectral post-processing of the rad-hydro calculations. Finally, §5.4 summarizes the important conclusions from these experiments, and discusses the impact they may have on the radiative transfer experiments in CH_2 foam.

5.1 Experiment Configuration

Figure 5.1 shows top- and side-view schematics of the ride-along geometry on the Z facility as configured for these experiments. The primary geometric parameters of interest are defined in this figure as the pinch height, h_p, the initial pinch radius, r_p, the primary hohlraum radius, r_c, the width of the LOS holes, w_s, the distance from the pinch axis

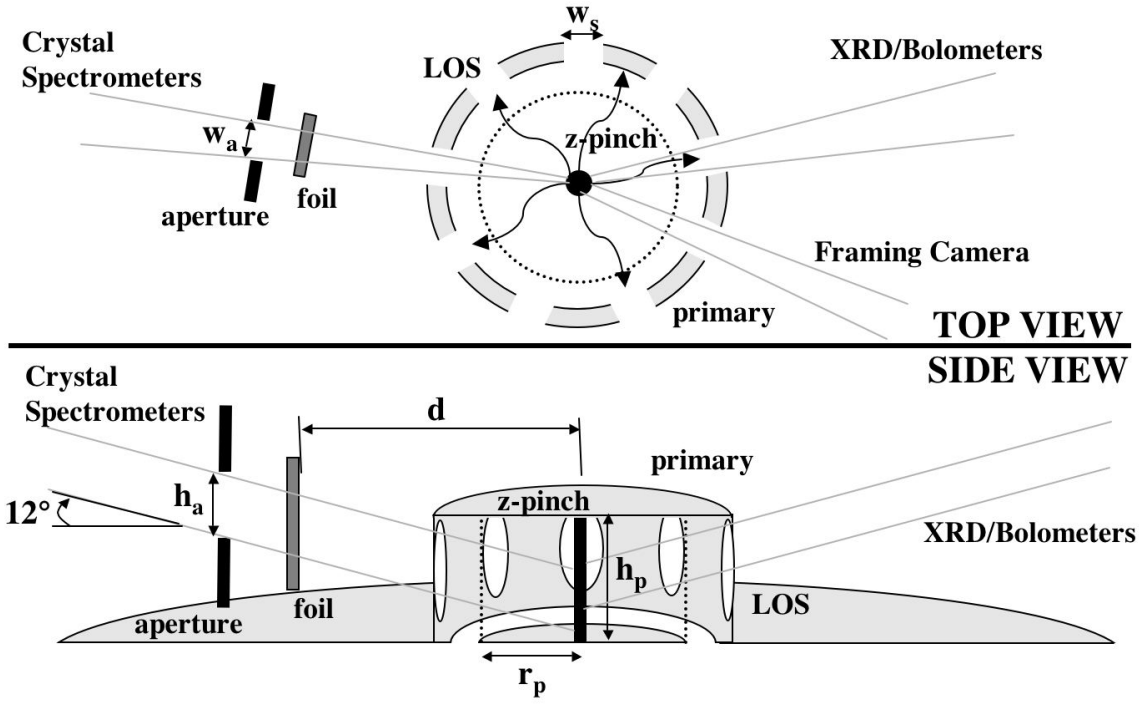

Figure 5.1: Schematic diagram of the sample placement and diagnostic LOS for the ride-along experiment geometry.

to the experimental sample, d, the aperture width, w_a, and the aperture height, h_a. Table 5.1 lists these quantities and the parameters of the z-pinch wire arrays as fielded on Z shots z597 and z1031.

Figure 5.2 shows schematic drawings of the samples fielded on these shots. The experimental sample on z597 consisted of 7 alternating layers of 200Å thick Al or MgF_2, creating a 2800Å thick $Al + MgF_2$ foil tamped on either side by $1.2\mu m$ of CH. On shot z1031, two different samples were fielded simultaneously on two separate LOS. One sample, placed along a line-of-sight designated as LOS 13/14, consisted of a 1500Å thick layer of Al on the pinch facing side of a 1000Å layer of MgF_2 and tamped on either side

Shot #	$r_p\,(mm)$	$h_p\,(mm)$	**Wire #**	**Wire Diam.**	$w_s\,(mm)$	$d\,(mm)$	$w_a\,(mm)$	$h_a\,(mm)$
z597	10	10	300	$11.4\mu m$	5.6	39.6	8.26	2.49
z1031	20 outer 10 inner	12	240 outer 120 inner	$7.8\mu m$	4.8	43.3	4	6

Table 5.1: Geometric parameters and z-pinch configurations for the experiments on shots z597 and z1031. z597 was a single array tungsten z-pinch with no central target, and z1031 was a nested array tungsten z-pinch with a $3mm$ radius, $14mg/cc\ CH_2$ axial foam target.

by $1.0\mu m$ of CH. The other sample, on LOS 21/22, contained a 3100Å layer of MgF_2 on the pinch facing side of a 1500Å layer of Al, and also tamped on either side by $1.0\mu m$ of CH.

As indicated in Figure 5.1, absorption spectra from these samples were measured along each sample's LOS by a time-integrated convex crystal spectrometer (TIXTL). The spectrometers were fielded with a source-to-crystal distance of $455cm$, and a crystal-to-film distance of $7.1cm$. Each contained a potassium acid phlalate (KAP) crystal with a $2d$ spacing of 26.62Å that was positioned to view a spectral range of $\approx 5 - 11$Å in first order. These crystals were bent to a $101.6mm$ radius, which provided a spectral resolution of $\lambda/\Delta\lambda \approx 750$. To both protect the crystals and eliminate the softer components of the x-ray spectrum, the TIXTLs were filtered between the source and crystal by $38.1\mu m$ of Be on z597 and $8.5\mu m$ of Be on z1031. On shot z597, time-resolved absorption spectra were also measured using a 6-strip micro-channel plate (MCP) assembled at the detection plane of a convex crystal spectrometer with a $101.6mm$ radius KAP crystal. This spectrometer had a source-to-crystal distance of $640cm$, and a crystal-to-detector distance of $14.1cm$.

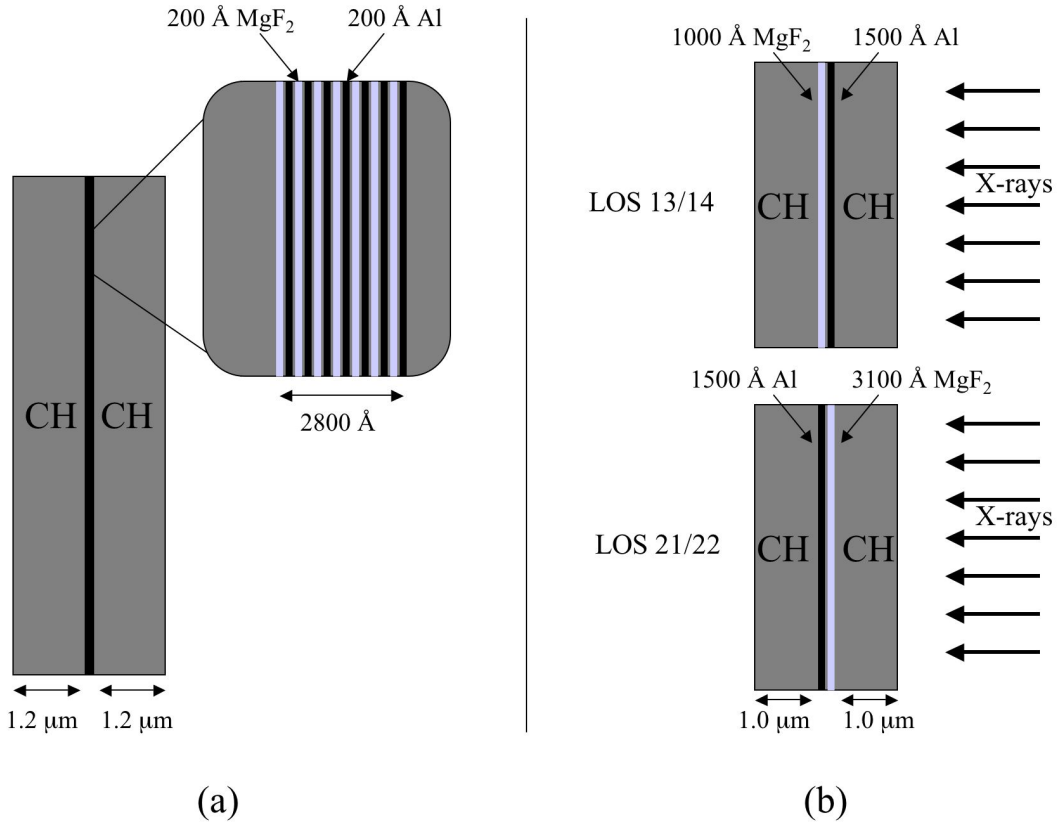

Figure 5.2: Schematic drawings of the samples used on shots **(a)** z597 and **(b)** z1031.

It was filtered between the source and crystal by $8.5\mu m$ of Be, and between the crystal and MCP by $12.7\mu m$ of Be. The $40mm$ long MCP striplines provided a spectral range of $\approx 7.0 - 10.2$Å in first order, and were pulsed in an open circuit configuration by a $2.1ns$ FWHM signal peaked at $-294V$ (over a $-100V$ DC bias), for a gain FWHM of $\approx 1.0ns$.

The z-pinch performance on these shots was measured by a suite of diagnostics looking through LOS other than those used by the experimental samples. The primary z-pinch diagnostic that was utilized for these experiments was an array of filtered x-ray diodes (XRDs), which provided the pinch power history when normalized by a bolometer viewing from the same angle on the same line-of-sight.

5.2 Experimental Data

Figure 5.3 shows the time-dependent z-pinch powers, temperatures, and radii from shots z597 and z1031 on the Z facility. The time-axis in this figure, and throughout the remainder of this chapter, has been shifted so that the peak of the x-ray emission power occurs at $100ns$. The powers are determined from kimfol filtered XRD measurements that have been normalized by bolometer data [86, 87, 101]. According to this data, z597 produced $1140 \pm 230kJ$ in a $6.6ns$ FWHM pulse peaked at $124 \pm 25TW$, and z1031 produced $870 \pm 170kJ$ in a $3.7ns$ FWHM pulse peaked at $110 \pm 22TW$.

The z-pinch radii are determined from models of the implosion trajectory at times $< 93ns$, and from experimental data on similar load geometries at time $\geq 93ns$[a]. The temperatures for both shots are then calculated from the pinch power and radius time histories by assuming that the z-pinch is a uniform cylindrical surface emitter. This method has been compared to transmission grating measurements of the z-pinch emission spectra on other experiments, and was found to be in good agreement [90].

It is important to note that, around the time of peak z-pinch emission, calculations suggest that the conditions in the experimental sample are relatively insensitive to the absolute intensity and spectrum of the radiation drive at times $< 70ns$. Thus, it is not necessary to have a very accurate knowledge of the z-pinch radius and emission power during the foot-pulse. In addition, the view-factor sensitivity study discussed in §4.1

[a]Data on multiple Z experiments suggests that the implosion trajectory depends on the initial geometry of the z-pinch [102]. For example, $2cm$ radius z-pinches follow a trajectory that is well modeled by a 0-D model of the circuit inductance. Thus, the z-pinch trajectory on shot z1031 is taken from a 0-D calculation using Screamer [103] for times $< 93ns$. On the other hand, $1cm$ radius z-pinches have a trajectory that supports a 2-D plasma pre-fill model that is significantly delayed with respect to the 0-D calculations [104]. Thus, for times $< 93ns$, the z-pinch trajectory on shot z597 is taken from a 2-D pre-fill model that has been tuned to agree with the self-emission data of the z-pinch run-in [104]. At times $\geq 93ns$, the z-pinch radii on z597 are taken from analysis of the z-pinch thermal spectra on shots with a similar geometry, and on z1031 are taken from pinhole camera measurements published by Sanford et. al. [105].

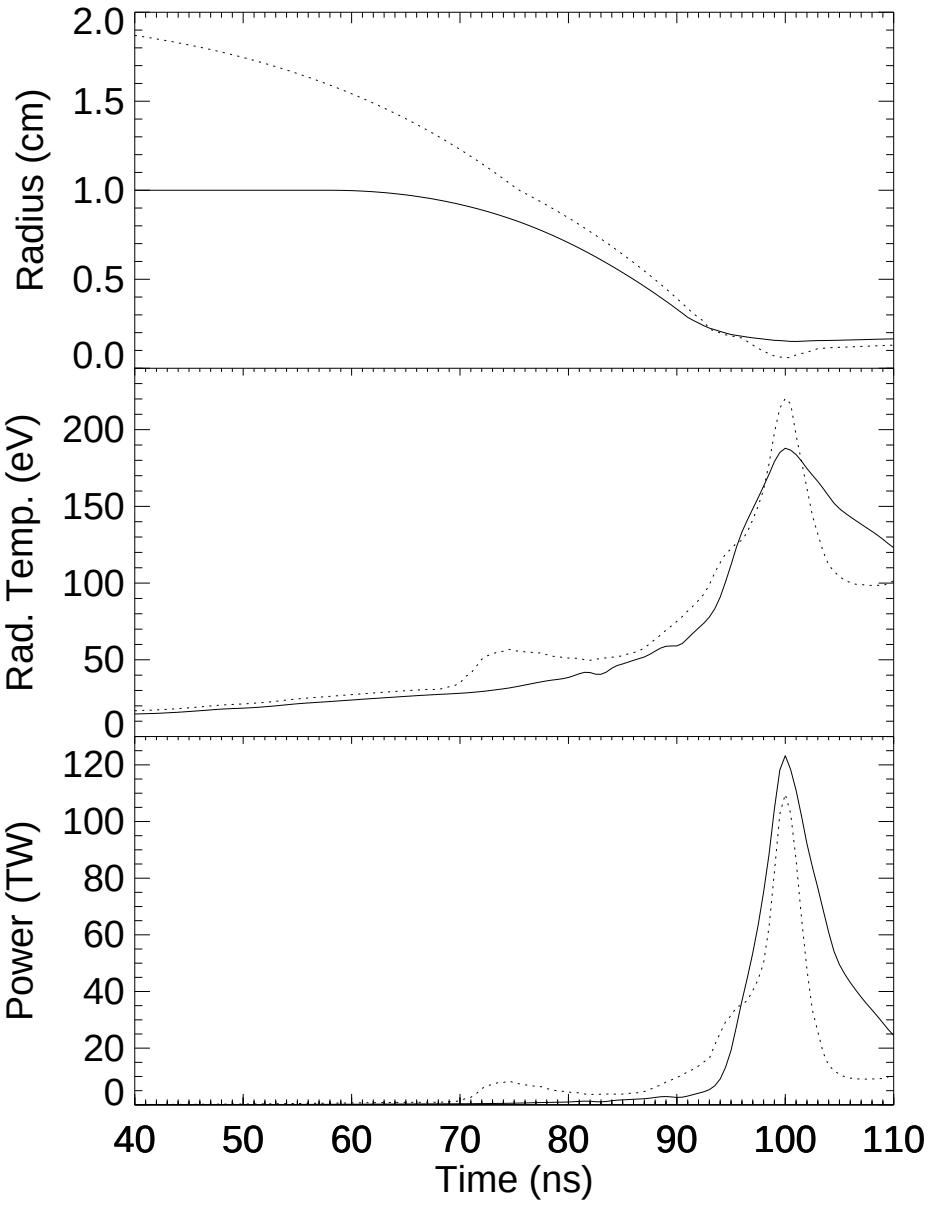

Figure 5.3: Z-pinch power, temperature, and radius profiles for shot z597 (solid) and z1031 (dotted) on Z. The power is measured by a kimfol filtered XRD normalized to bolometer measurements of the total radiated energy. The radii are taken from calculations at times $< 93ns$, and from self-emission data on similar shots for times $\geq 93ns$. The temperature is calculated from the power and radius profiles assuming the z-pinch is a uniform cylindrical surface emitter.

revealed that the amplitude and spectra of the radiation drive at the sample surface are only weakly sensitive to the absolute z-pinch emission spectrum. For these reasons, the greatest emphasis has been put on understanding the z-pinch emission power on the specific shots of interest, while assuming a radius history that is more generic to the general class of z-pinch in each experiment. This procedure simplifies the data analysis required to calculate the radiation drive on the sample surface, and reduces the number of diagnostics that must be fielded in the primary experiment.

Figure 5.4(a) and (b) show the raw film data and associated spectral lineouts as recorded by the time-integrated convex crystal spectrometers on shots z597 and z1031. The lineouts have been processed by the EXRAY code (see Appendix A) to determine the wavelength scale, and to apply the appropriate corrections for the film response, filter transmission, crystal reflectivity (using the MDP reflectivity model), and the crystal geometry. In addition, the x-ray background has been subtracted from the data, where the background was determined by processing an unilluminated strip of the film in the same manner as the data.

Likewise, Figure 5.5(a) and (b) show the raw film data and associated spectral lineouts from the time-resolved convex crystal spectrometer on shot z597. Again, the lineouts have been corrected by the EXRAY code, including a correction for the efficiency of the gold MCP. This data is shown for the 4 frames that had a reasonable signal level, which span times from $97.6 \pm 0.5ns$ to $103.6 \pm 0.5ns$ in $2ns$ intervals on the time-base of Figure 5.3.

As discussed in §4.5, the absorption spectra shown in Figures 5.4 and 5.5 can be used to derive the possible combinations of temperature and density in the foils through an automated χ^2 comparison to calculated spectra. However, because the calculations have no knowledge of the backlighter structure, the data in the figures must be converted to either a relative or absolute transmission spectra. The latter requires a direct measure of

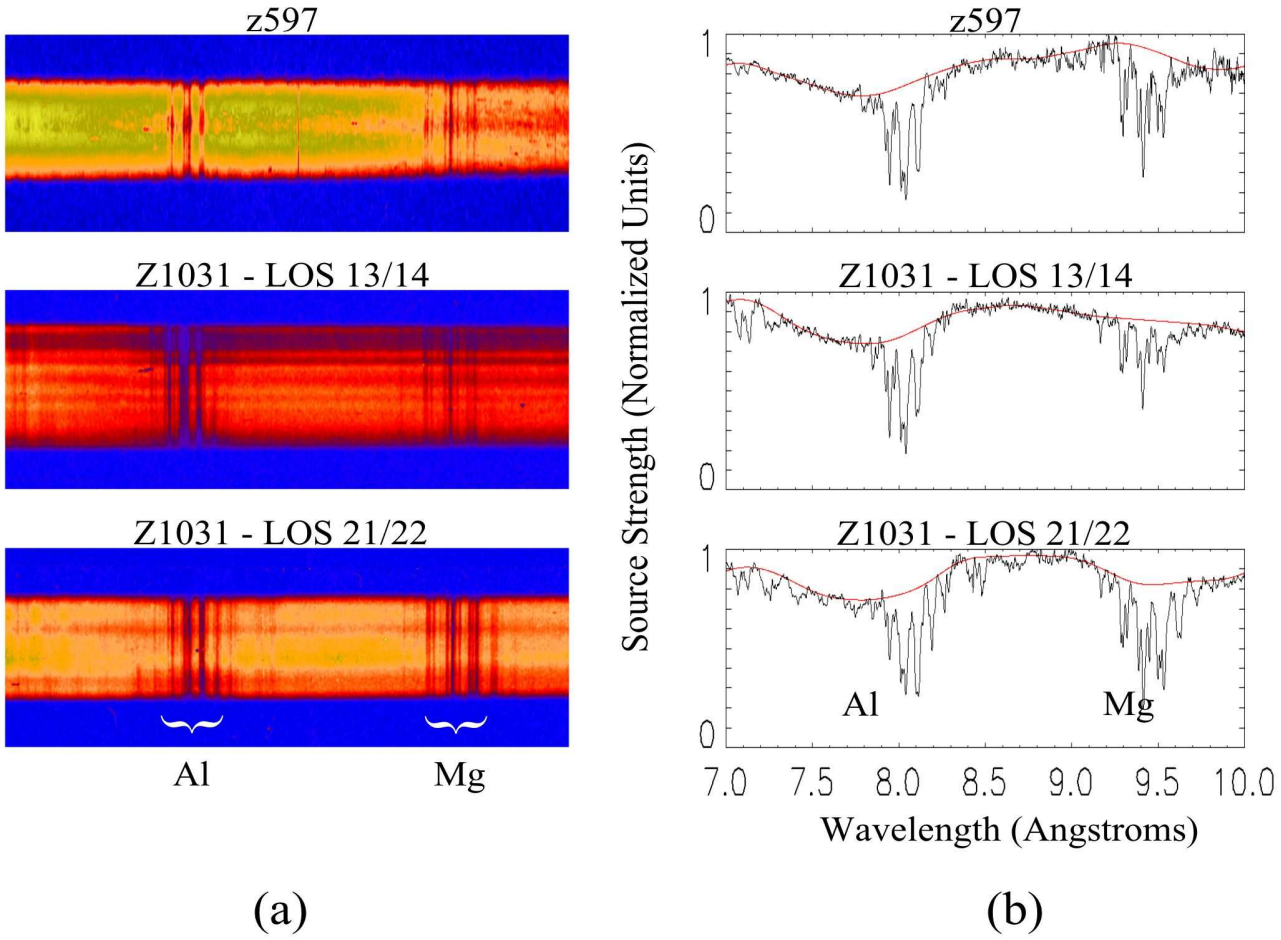

Figure 5.4: **(a)** Raw film data and **(b)** normalized spectral lineouts from the TIXTLs on shots z597 and z1031. The lineouts have been processed for the film response, filter transmission, crystal reflectivity, and the crystal geometry.

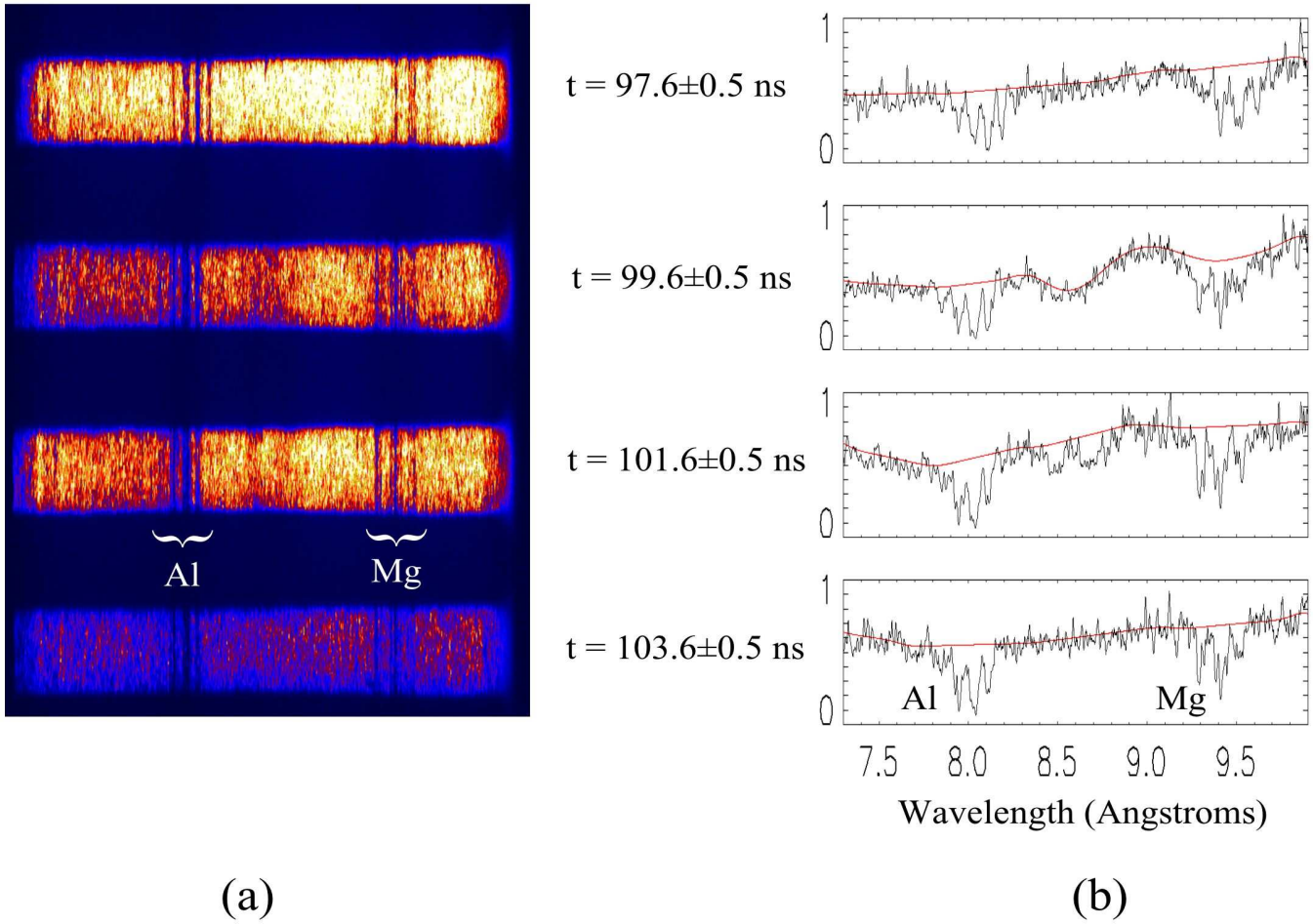

Figure 5.5: **(a)** Raw film data and **(b)** normalized spectral lineouts from the time-resolved spectrometer on shot z597. The lineouts are shown in normalized units, and have been processed for the film response, filter transmission, crystal reflectivity, and the crystal geometry.

the backlighter spectra, which was not possible on these experiments. Thus, the spectra in the figures must be converted to a relative transmission by the division of an assumed continuum. For these spectra, that continuum was determined by removing the absorption features, and filtering the remaining signal by a 0.5Å boxcar filter. The resulting continuum is overlaid on the data in Figures 5.4 and 5.5. The relative transmission is then calculated by dividing the measured signal by this continuum, and is shown for both the time-integrated and time-resolved data in Figure 5.6 and 5.7 respectively. This is considered an acceptable procedure since the important information about the sample conditions is contained in the relative intensities of the absorption features, which are relatively unchanged by the division of the continuum.

The possible combinations of temperature and density in the plasmas can then be determined by the SPECTROFIT code for each of the measured transmission spectra. Using this code, the weighted χ^2 between the unsmoothed transmission data and SPECT3D calculations was computed for 1800 combinations of temperature and density over the ranges $20 \leq T_e \leq 80eV$ and $1 \times 10^{19} \leq n_i \leq 1 \times 10^{23} cm^{-3}$. The statistical deviations in the intensity of each point in the data was determined from independent calibration experiments described in Appendix C. Each comparison was restricted to the spectral range of the K-α features, where the absolute depths of the measured absorption were allowed to uniformly vary by $\pm 10\%$[b]. The resulting χ^2 contour plots for the time-integrated spectra are shown in Figure 5.8 for shot z597, and Figures 5.9 and 5.10 for LOS 13/14 and 21/22 on shot z1031. Each contour in these plots corresponds to an increase of 1 over the minimum χ^2. This implies that there is a $\approx 68.3\%$ probability that the plasmas that produced each spectra have a temperature and density that is

[b]This is done to optimize the χ^2 at each temperature and density point, in an effort to account for possible systematic errors induced in the data from the background subtraction (due to a lack of knowledge about the energy of the background x-rays).

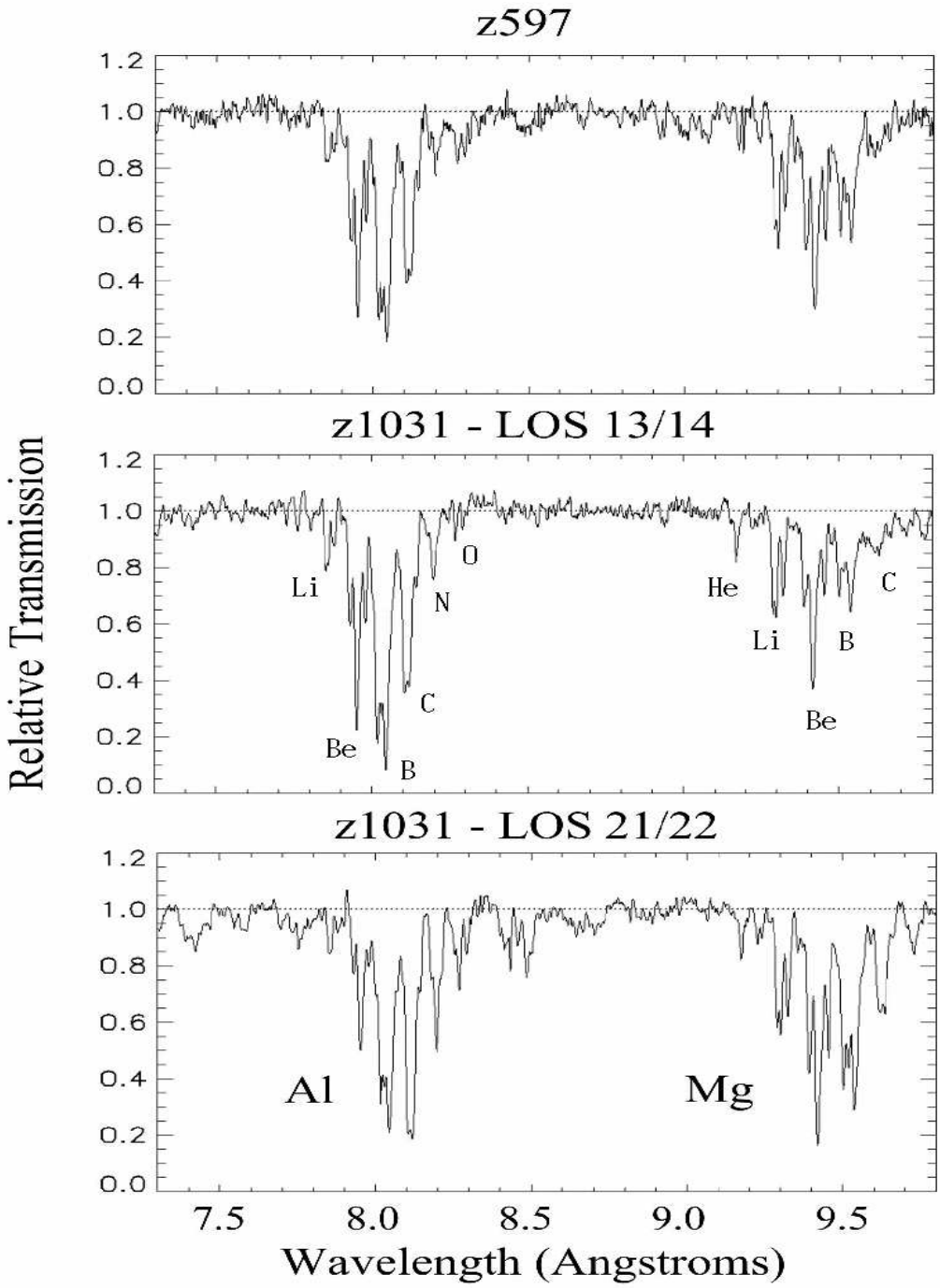

Figure 5.6: Relative transmission spectra from the time-integrated convex crystal spectrometers on shots z597 and z1031.

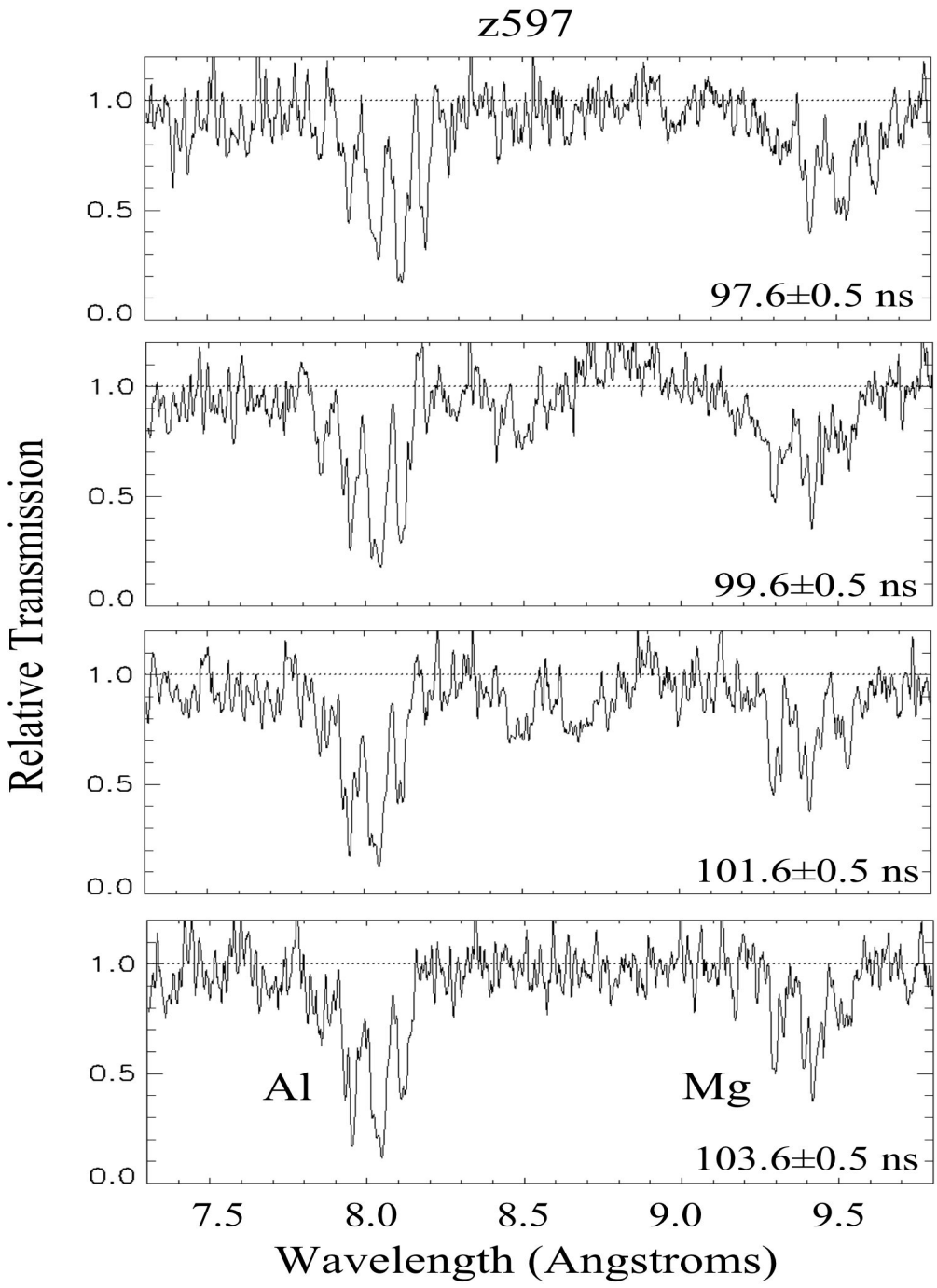

Figure 5.7: Relative transmission spectra from the time-resolved convex crystal spectrometer on shot z597.

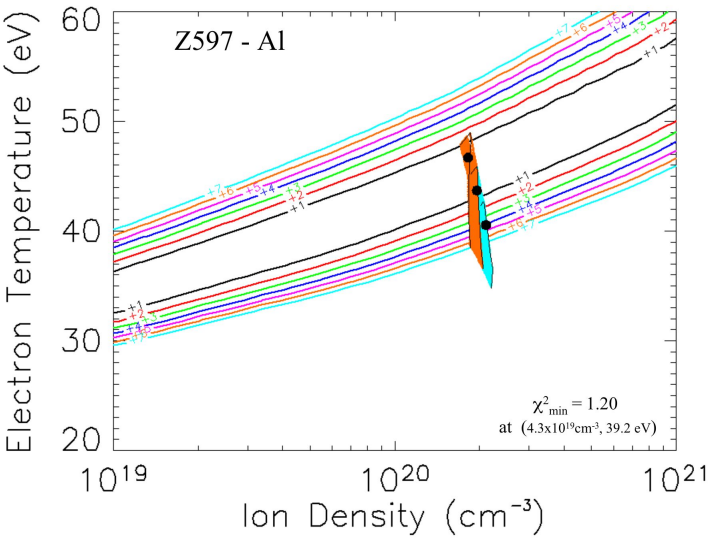

(a)

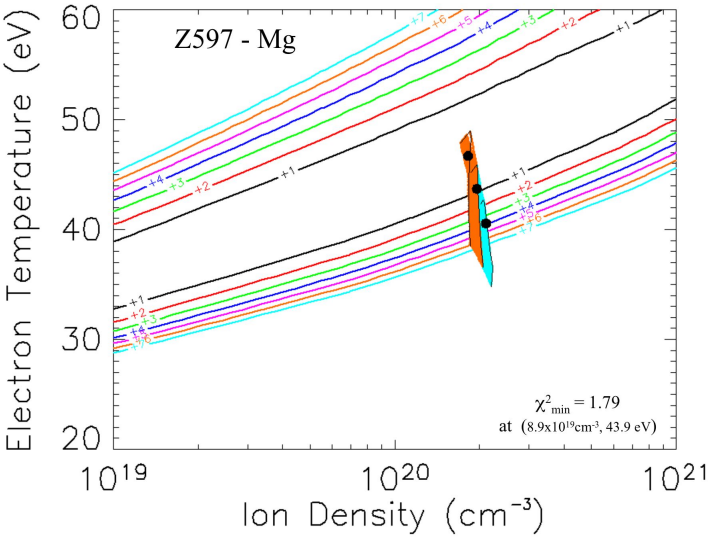

(b)

Figure 5.8: Contour plots from the SPECTROFIT χ^2 comparisons between the data and calculations of the K-α absorption features in **(a)** aluminum and **(b)** magnesium on shot z597. Each contour represents an increment of 1 over the minimum χ^2 in the calculations. The shaded regions correspond to plasma conditions from BUCKY rad-hydro calculations assuming z-pinch emission powers of $80-100\%$ (blue) and $100-120\%$ (orange) of the measured value.

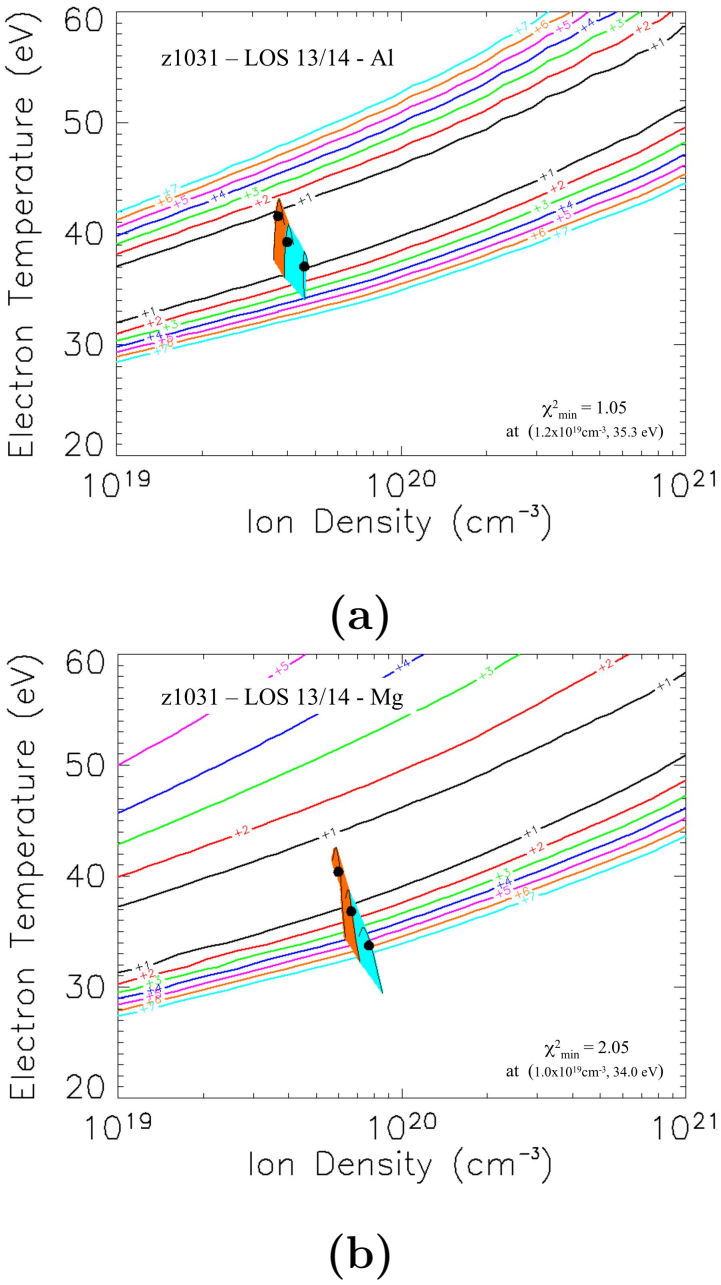

Figure 5.9: Contour plots from the SPECTROFIT χ^2 comparisons between the data and calculations of the K-α absorption features in **(a)** aluminum and **(b)** magnesium from LOS 13/14 on shot z1031. Each contour represents an increment of 1 over the minimum χ^2 in the calculations. The shaded regions correspond to plasma conditions from BUCKY rad-hydro calculations assuming z-pinch emission powers of $80 - 100\%$ (blue) and $100 - 120\%$ (orange) of the measured value.

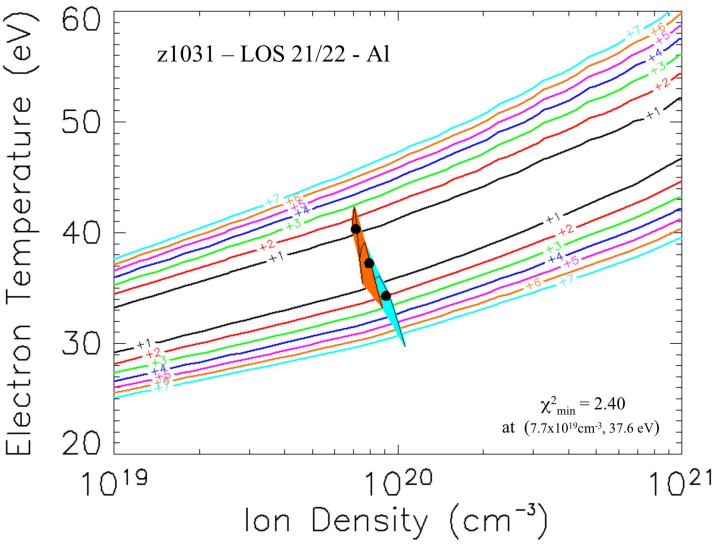

(a)

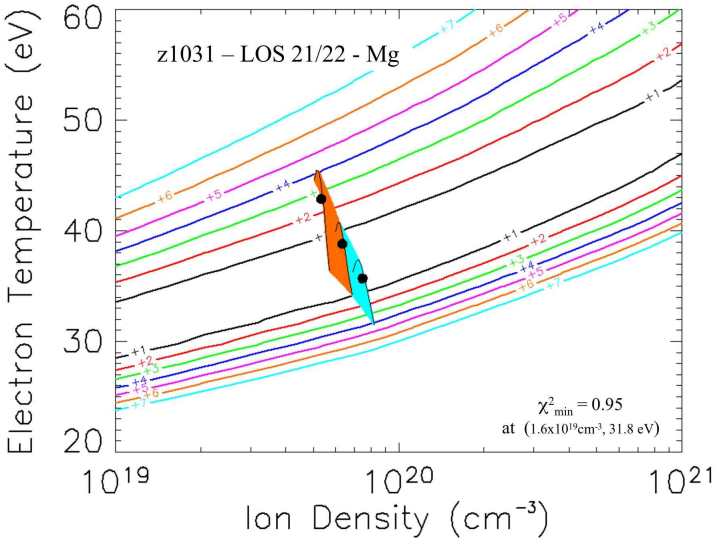

(b)

Figure 5.10: Contour plots from the SPECTROFIT χ^2 comparisons between the data and calculations of the K-α absorption features in **(a)** aluminum and **(b)** magnesium from LOS 21/22 on shot z1031. Each contour represents an increment of 1 over the minimum χ^2 in the calculations. The shaded regions correspond to plasma conditions from BUCKY rad-hydro calculations assuming z-pinch emission powers of $80 - 100\%$ (blue) and $100 - 120\%$ (orange) of the measured value.

within the $+1\sigma$ contour. To illustrate the quality of fit between the data and calculation, Figure 5.11 overlays the aluminum data from z597 with the calculated spectra at an ion density of $1 \times 10^{20} cm^{-3}$ and the temperatures corresponding to confidence levels of $+0\sigma$, $+1\sigma$, and $+2\sigma$. It is visually clear from this figure that the spectrum calculated at the minimum χ^2 is a much better match to the data than that at each of the other confidence levels. This is as it should be for a reasonable χ^2 analysis, and provides a visual check on the calculations.

The contour plots in Figure 5.8-5.10 contain a great deal of important information, but are difficult to compare to each other. To help visualize the comparison of the conditions in the various tracer materials, Figure 5.12(a) and (b) overlay only the $+1\sigma$ contours from shot z597 and z1031 respectively. The fit in Figure 5.12(a) was from the absorption spectra in the sample that contained a mixed foil of Al and MgF_2. As seen in the figure, the possible combinations of temperature and density derived from the Al and Mg absorption features are approximately equivalent[c]. This is what one would expect from a mixed foil whose constituents are in thermodynamic equilibrium (ie. they should be at the same temperature and density).

In contrast, Figure 5.12(b) shows the comparison in the Al and MgF_2 foils on z1031 where they were positioned in sequence along the direction of the heating radiation. From a cartoon picture of this experiment, one might expect that the material which is first in the sequence would be hotter (and probably less dense) then the one behind it. However, in looking at the figure, it is evident that the possible range of material conditions is equivalent for both the Al and MgF_2 in each sample. This does not necessarily mean that each material is at the same temperature. They may (and probably do) have different

[c]The larger error bars on the fit to the Mg data is a reflection of the larger statistical fluctuations in the film response at the intensity level of the Mg K-α wavelengths.

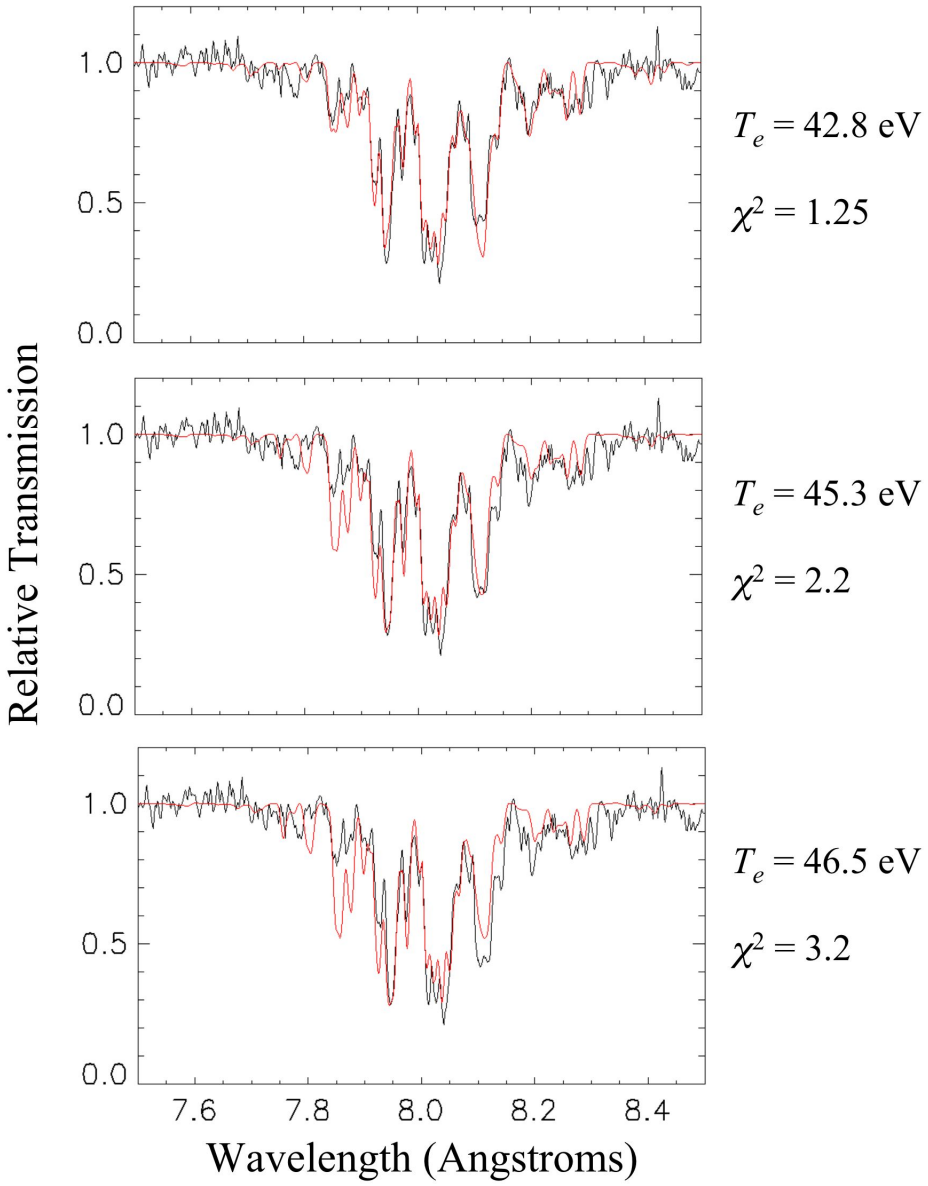

Figure 5.11: Comparison between the time-integrated aluminum K-α absorption spectrum taken on shot z597 and three calculated spectra in the SPECTROFIT χ^2 computation. Each calculated spectra is from an Al/MgF_2 plasma at an ion density of $10^{20} cm^{-3}$.

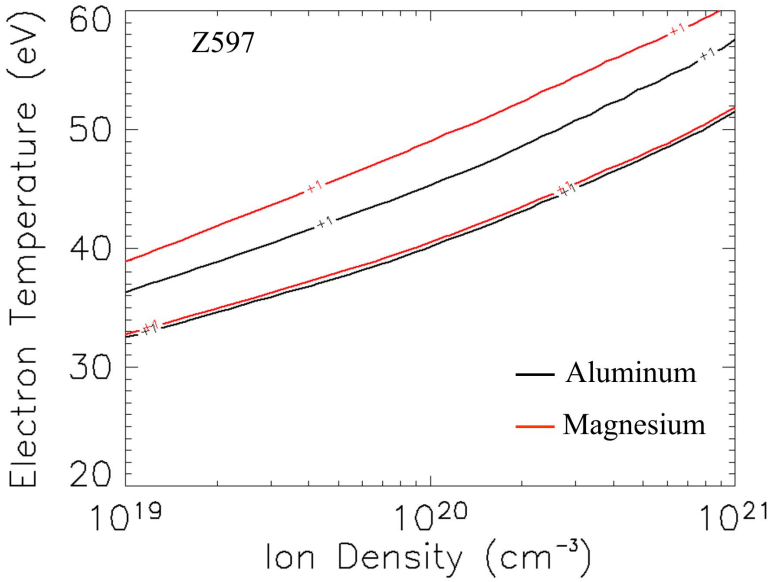

(a)

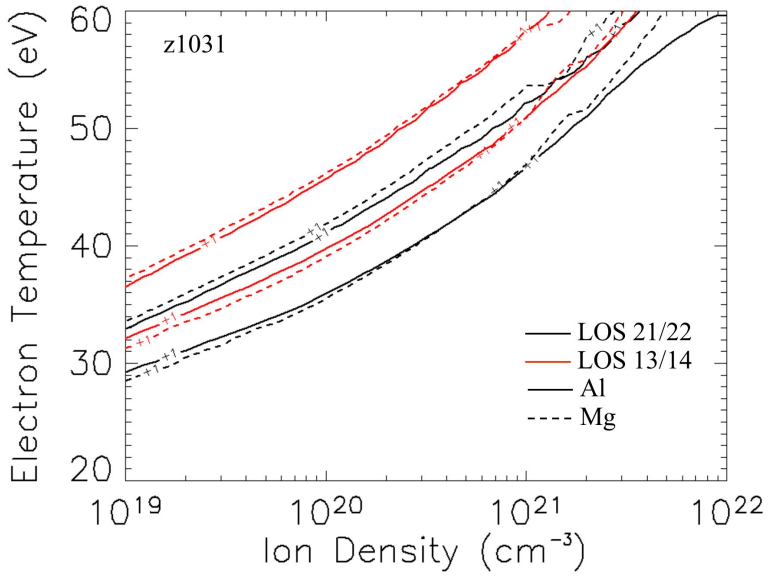

(b)

Figure 5.12: $+1\sigma$ contours from the SPECTROFIT χ^2 comparisons between the data and calculations of the K-α absorption features from shots **(a)** z597 **(b)** z1031.

densities. However, it implies that, if the material that is second in the sequence has a lower temperature, then it must also have a lower density. This is somewhat surprising, and is a good example of an experimental result that puts a tight constraint on the computational models.

One other piece of information that can be drawn from the statistical fits in Figure 5.12(b) is the relative temperature at the foil location along each line-of-sight. It is clear from the figure that the range of most probable conditions in the foils on LOS 13/14 is either $\approx 10\%$ hotter, or $\approx 300\%$ less dense. Since each foil was tamped by the same amount of CH, and each was placed at the same distance from the z-pinch, it is possible that the radiation power escaping from the z-pinch was different along each LOS. However, there is a small overlap in the 1σ contours that makes it difficult to say with a statistical certainty that this is indeed the case. Regardless, a calculation of the foil response on each LOS can be used to identify what power variation may produce such a difference in the plasma conditions. This will be addressed in §5.3.

In addition to the time-integrated data, The $+1\sigma$ contours for each spectrum in the time-resolved data on z597 are shown in Figure 5.13. These fits show that the plasma heats up and/or expands up to $t = 100ns$, and then either cools and expands or remains fairly stagnant at times later than that. Again, this information is drawn straight from the experimental data, and should place a significant constraint on the models.

As a point of special importance, the data that has been heretofore referred to as time-integrated is really a measure of the plasma conditions around the time of the peak x-ray emission. To illustrate, Figure 5.14 shows the normalized signals from an XRD that is filtered by $10.0\mu m$ of Be and $0.8\mu m$ of vanadium. The combination of the XRD sensitivity and the filter transmission fraction makes this signal a diagnostic of the z-pinch emission over the range $2.5\text{Å} < \lambda < 12.4\text{Å}$. Thus, it is effectively a measure of

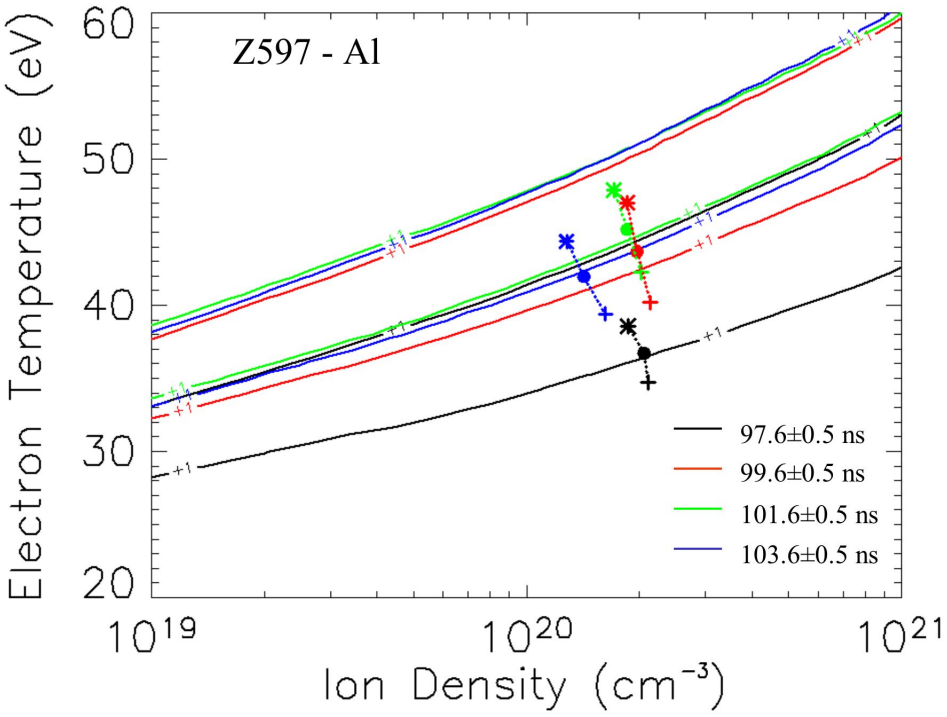

Figure 5.13: $+1\sigma$ contours from the SPECTROFIT χ^2 comparisons between the time-resolved data and calculations of the K-α absorption features on shot z597. The symbols correspond to mass-averaged plasma conditions from BUCKY rad-hydro calculations assuming z-pinch emission powers of 80% (cross), 100% (circle), and 120% (star) of the measured value.

the backlighter time history. This is an important point because it constrains the time-integrated data (and therefore the plasma conditions) to a certain window over the course of the z-pinch emission. Specifically, it implies that the time-integrated data can then be considered as the absorption spectra through the experimental samples corresponding to a time of $100.5 \pm 2.0ns$ on z597 and $100.5 \pm 1.4ns$ on z1031.

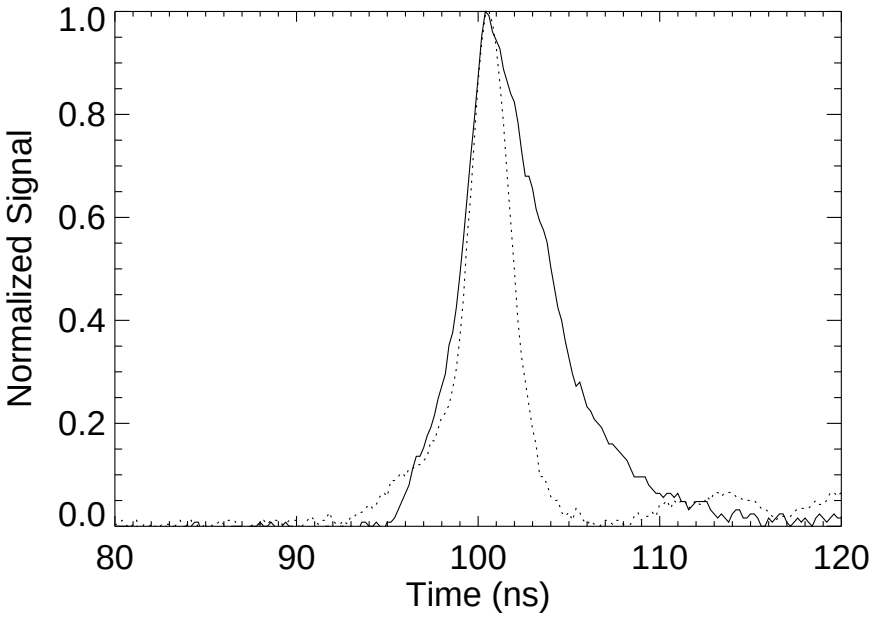

Figure 5.14: Normalized signals from an XRD filtered by $10\mu m$ of beryllium and $0.8\mu m$ of vanadium on shots z597 (solid) and z1031 (dotted). This signal provides a time-history for the backlighter pulse in the spectral range $2.5\text{Å} < \lambda < 12.4\text{Å}$.

5.3 Experiment Modeling

Shots z597 and z1031 had very different z-pinch geometries, and the samples had very different fields-of-view. Thus, determining the radiation drive on the surface of each sample required that each experiment be modeled with a separate view-factor calculation. An example of the VISRAD view-factor grid for each experiment geometry is shown in Figure 5.15. In these models, the z-pinch radius and power histories from Figure 5.3 were input as the power source, and an albedo was prescribed for each surface element. VISRAD was then used to calculate the time-dependent incident radiation spectrum at each surface, which were input into BUCKY 1-D rad-hydro calculations of the surface albedo. For this work, these albedos were calculated for three primary objects; the outer

anode, z-pinch glideplanes, and the primary hohlraum (as labeled in Figure 5.15). Each was calculated for a spectral drive history averaged over a few surface elements in the object, and the resulting albedo was input back into the view-factor model for every surface element in the object. As discussed in Chapter 4, this model was iterated until the radiation power on the surface of the experimental sample changed by less than 1% between 2 subsequent iterations at every time-step in the calculation. This took 5 iterations for both experiment geometries, and the resulting albedos of the 3 primary objects are shown in Figure 5.16.

The resulting radiation power on the surface of each sample as calculated by their respective VISRAD view-factor model is shown in Figure 5.17(a). Each drive history in this figure was calculated for the nominal (measured) z-pinch power, and reaches peak radiation powers of $1.15 TW/cm^2$ and $0.76 TW/cm^2$ on shots z597 and z1031 respectively. The calculated radiation spectra on the surface of each sample at the time of peak z-pinch power ($100 ns$) is shown in Figure 5.17(b). The peak energy of these spectra is $410 eV$ for shot z597 and $235 eV$ for shot z1031. The lower peak energy of the drive from shot z1031 is a reflection of both the lower z-pinch power, and the greater amount of gold hardware in the sample's field-of-view. At the peak of the radiation drive, the z-pinch emission was calculated to contribute 76% of the drive flux on shot z597, and 70% on shot z1031.

The drive histories from Figure 5.17(a) were applied as a time- and frequency-dependent radiation boundary condition in radiation-hydrodynamics calculations of the sample response. These simulations were done with the BUCKY 1-D lagrangian rad-hydro code using multi-angle short-characteristics radiation transport for 100 log-spaced photon energy groups from $0.1 - 10^4 eV$. The opacities of each material were calculated from PROPACEOS tables that contained 39 temperature points from $0.1 - 100 eV$, and 41 log-spaced density points from $10^{19} - 10^{23} cm^{-3}$. The equation-of-state for the CH and

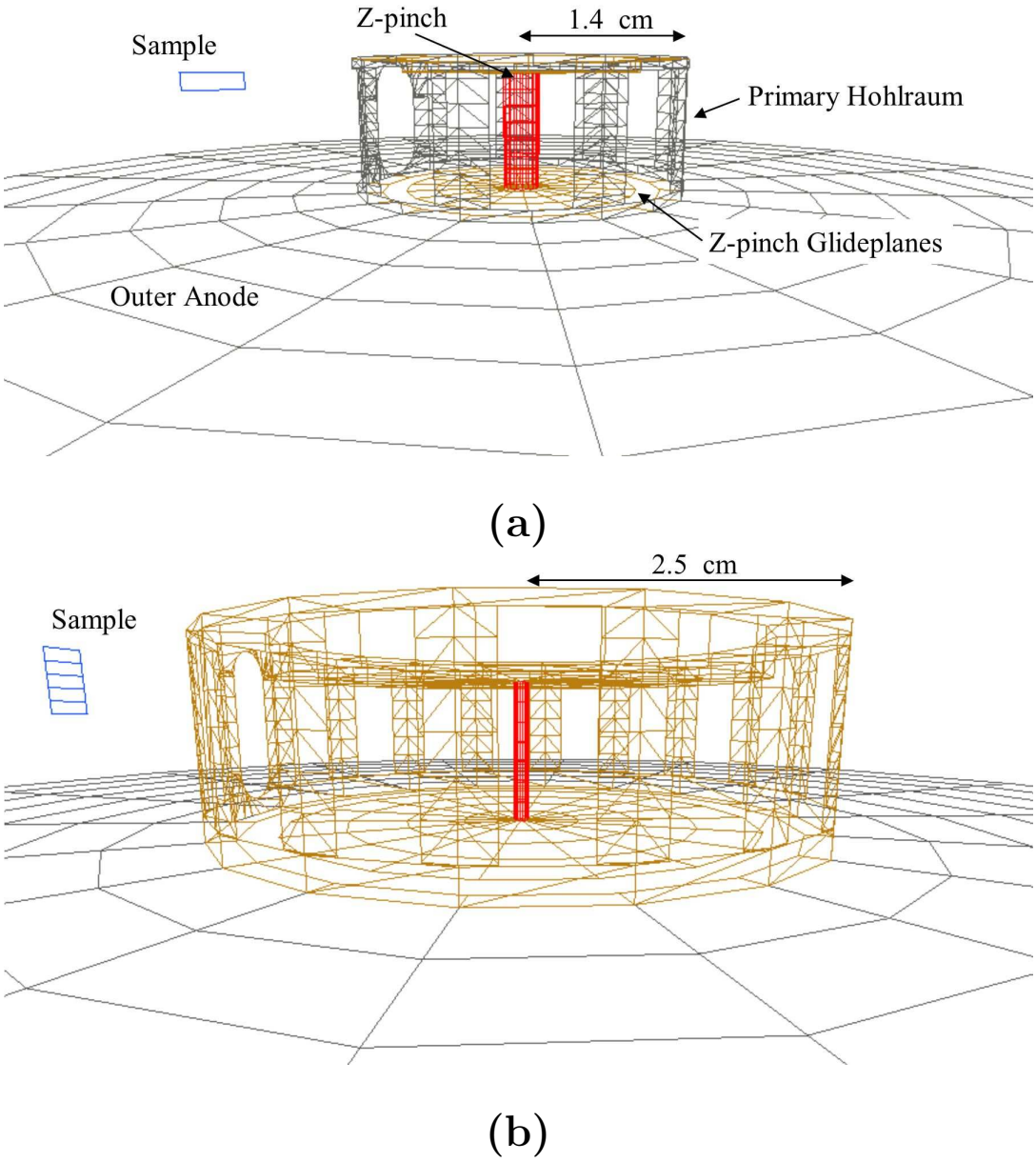

Figure 5.15: View factor grids for shots **(a)** z597 and **(b)** z1031 at peak z-pinch power. Each grid is shown from the same viewing distance revealing the much different geometries in the two experiments.

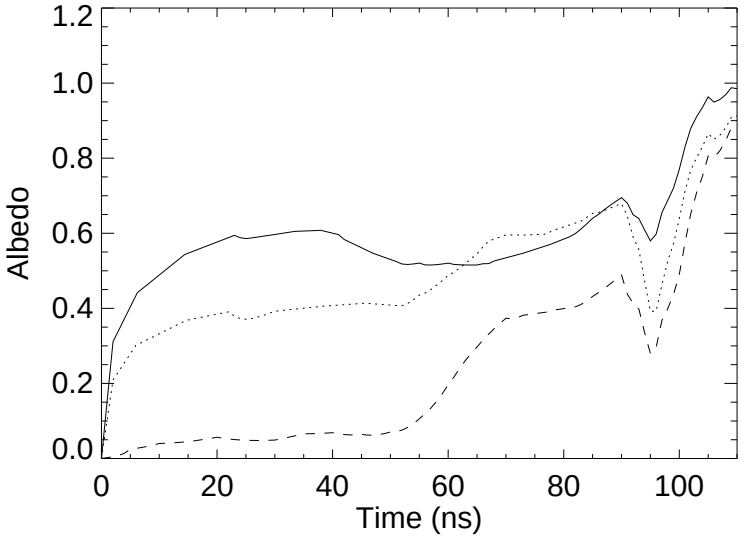

(a)

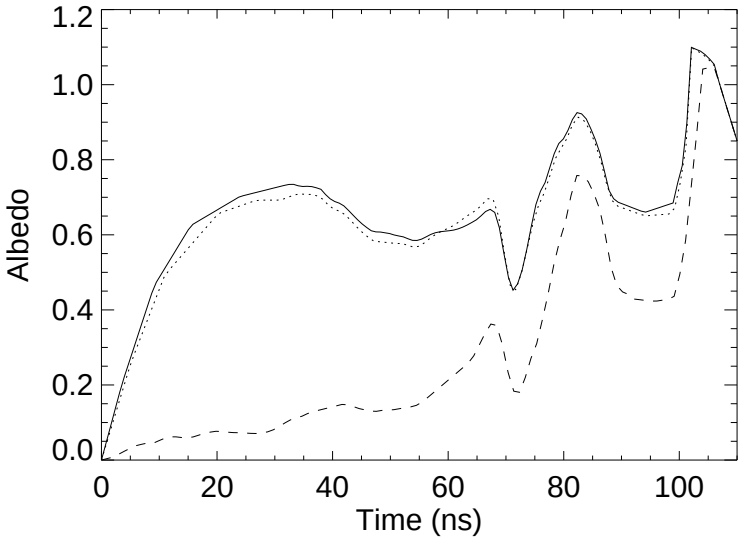

(b)

Figure 5.16: BUCKY calculated albedo histories used for the final view factor calculations of shots **(a)** z597 and **(b)** z1031. The albedos are shown for the pinch glideplanes (solid), the primary hohlraum (dotted), and the outer anode (dashed).

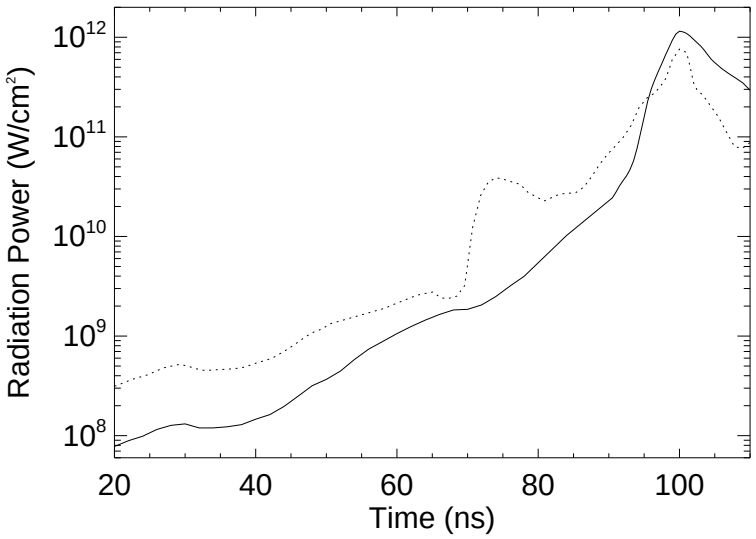

(a)

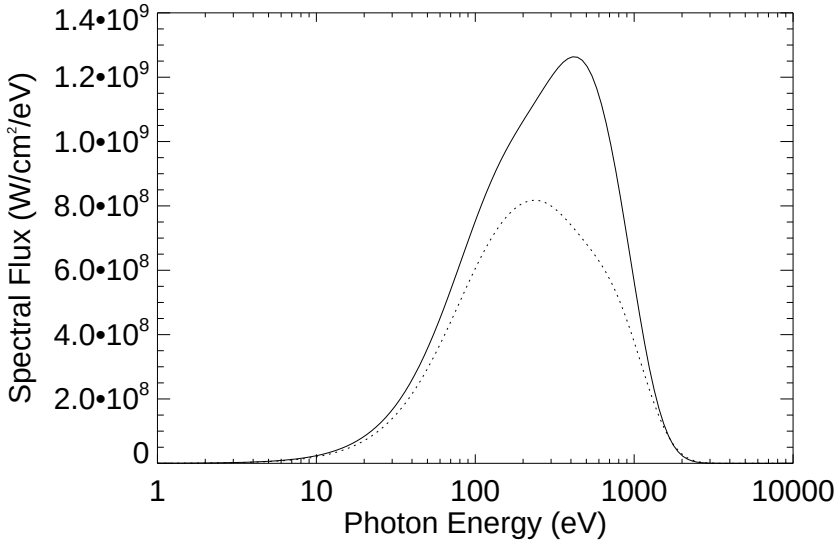

(b)

Figure 5.17: VISRAD modeled **(a)** radiation drive powers and **(b)** peak drive spectrum (at $t = 100ns$) for shots z597(solid) and z1031(dotted).

Al materials were taken from the SESAME EOS tables, and those for the MgF_2 and $Al/MgF2$ materials were taken from QEOS calculations [106]. The rad-hydro models were begun at $t = 0ns$, and ended at a time of $110ns$ using a quiet-start vaporization model set at a temperature of $0.4eV$. These calculations (including the view-factor simulations) were then repeated for each sample assuming the z-pinch power was 20% lower and then 20% higher than the measured value. This was done to account for the uncertainty in the z-pinch power measurements, which were shown in §4.1 to be the dominant uncertainty in the calculated radiation drive.

The mass-averaged temperature-density phase space of the calculated conditions in the Al and MgF_2 foils are shown on the χ^2 contour plots in Figures 5.8-5.10 over the times corresponding to the width of the backlighter time-history ($100.5 \pm 2.0ns$ on shot z597, and $100.5 \pm 1.5ns$ on shot z1031). These calculations are shown as a blue shaded region corresponding to the calculated conditions assuming the pinch power ranged from $80 - 100\%$ of the nominal value, and as an orange shaded region for the calculated conditions assuming the power ranged from $100 - 120\%$ of the nominal value. The lines in each shaded region correspond to the calculated mass-averaged conditions in the Al and/or MgF_2 over the backlighter time (time follows along each line). The calculations are shown in this way because it provides a quick visual way to compare to the data. If the calculated conditions are going to be a good approximation to those observed in the experiment, then part of the shaded region must fall within the $+1\sigma$ contours. This can be further constrained by calculating the time-averaged conditions in the foils weighted by the backlighter pulse histories shown in Figure 5.14. These points are over-plotted on each contour plot as a large dot corresponding to assumed pinch powers of; 80%, 100%, and 120% of the nominal value. Since the data recorded on the time-integrated spectrometers are truly a measure of the mass- and time-averaged conditions in the foils,

then these points are the best diagnostic of the comparison between the data and the rad-hydro models.

5.3.1 Calculations In Mixed Al and MgF_2

First consider the calculations of shot z597 (with the mixed layers of Al and MgF_2). It is clear from Figure 5.8 that the calculated temperature and density of the Al/MgF_2 layer is well within the $+1\sigma$ contours for pinch powers that range anywhere from $100-120\%$ of the nominal value. However, there is a great deal of the calculated phase-space at these powers which lies outside the most probable values. This does not necessarily signify a disagreement between the data and calculations. Remember that the backlighter time-history was sharply peaked at a time of $100.5ns$, and the data is a measure of the time-averaged foil conditions.

This can be further investigated by a comparison to the time-resolved data on this shot. The calculated conditions over each of the time-frames in the time-resolved data are overlaid on the $+1\sigma$ contour plots in Figure 5.13. The calculated points are mass- and time-averaged (weighted by the backlighter and micro-channel-plate pulse histories) over each time-frame, and are shown for pinch powers of; 80%, 100%, and 120% of the nominal value. As seen in the figure, the calculated values again compare well to the data for pinch powers that range anywhere from $100-120\%$ of the nominal value.

All these comparisons provide confidence that the view-factor calculations and rad-hydro models together predict temperature and density conditions in the sample that are consistent with the measured values. With these constraints in place, the models can be used to investigate the dynamics happening in the sample. Figure 5.18(a)-(d) show some details of the conditions calculated by the rad-hydro model assuming a pinch power that is 10% higher than the measured values at all times. Figure 5.18(a) shows the time

history of the average temperature and density in the Al/MgF_2 layer (the electron and ion temperatures are in very close equilibrium). The temperature peaks at about $47eV$ at a time of $101ns$, while the density decreases to a value of about $1.7 \times 10^{20} cm^{-3}$ and remains approximately constant over times of $97ns \leq t \leq 103ns$.

Figure 5.18(b) (c), and (d) show the temperature, density, and pressure profiles in the sample at times of $97.6ns$, $99.6ns$, $101.6ns$, and $103.6ns$ (corresponding to the frames in the time-resolved data). At each time, the calculations predict an $\approx 5eV$ gradient in the temperature of the Al/MgF_2, and almost no gradient in the density. One point of interest in these calculations is the noticeable jump in the conditions at the interface of the CH tamper and the Al/MgF_2. That is, the Al/MgF_2 is hotter than the surrounding CH at times $< 99ns$, and cooler at later times. This is strong evidence that the frequency-dependent radiative heating and cooling dominate the sample dynamics.

To illustrate the important effects of the driving radiation spectra, Figure 5.19(a) and (b) show the drive spectrum and some sample opacities at times of $85ns$ and $100ns$ respectively. The opacities are shown for three representative positions in the sample; the front of the CH tamper, the back of the CH tamper (just in front of the Al/MgF_2), and the front of the Al/MgF_2. Due to the distribution of the drive spectra, the CH is heated through different mechanisms at different times. Early in time ($t < 92ns$), the CH is heated primarily through free-free absorption and carbon L-shell photo-ionization. At photon energies of $100 - 300eV$, this is a relatively inefficient means of absorption and much of the CH remains relatively cold over the foot-pulse of the radiation drive. Later in time ($t > 92ns$), the average energy of the drive spectrum increases to the point that the CH is heated primarily through photo-ionization out of the carbon K-shell ($h\nu \approx 350eV$). At all times, the Al/MgF_2 portion of the sample is heated out of the combined F, Mg, and Al L-shells ($h\nu \approx 100 - 200eV$).

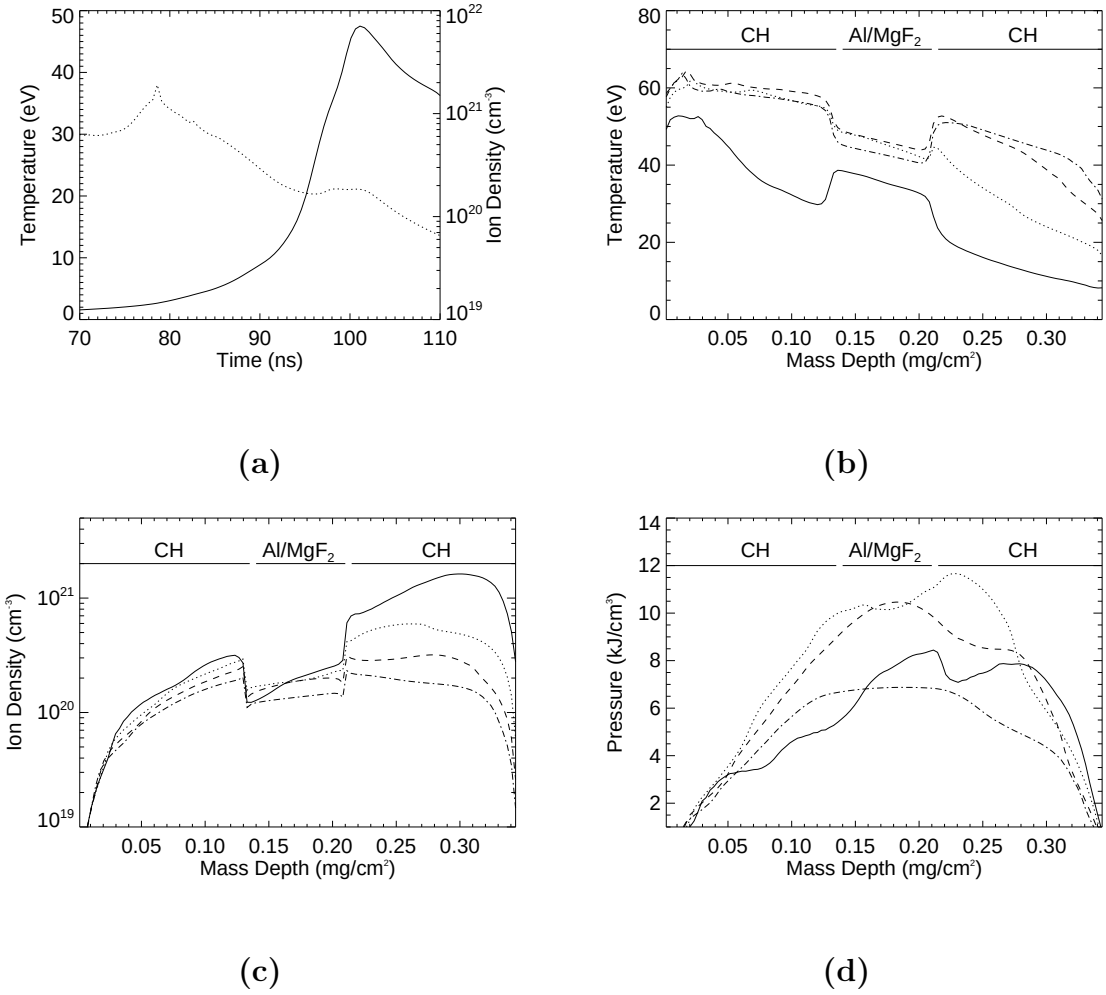

Figure 5.18: (a) Mass averaged temperature (solid) and density (dotted) conditions in the Al/MgF_2 foil on shot z597 as calculated by BUCKY. **(b)** Temperature, **(c)** density, and **(d)** pressure profiles in the experimental sample as calculated by BUCKY for times of 97.6ns (solid), 99.6ns (dotted), 101.6ns (dashed), and 103.6ns (dot-dashed). The driving radiation is incident from the left.

The discontinuities in the temperature and density profiles of the sample can be explained by the opacities. At early times, the driving radiation at energies just below the C K-shell pass through the tamper (largely unattenuated) and are readily absorbed in the Al/MgF_2. This creates a situation where there is a large gradient in the tamper, and the Al/MgF_2 is heated to temperatures above the surrounding CH. As an example,

the spectrum in Figure 5.19 (a) is shown to have a peak intensity at a photon energy of $126eV$, which lies below the C K-shell and above the F L-shell. However, as the carbon is ionized, the heating radiation at the C K-shell energies penetrates deeper into the tamper, and the temperature gradient decreases. At late times, the drive spectra are peaked around $400eV$, which couples better to the CH tamper than during the foot pulse. The CH is more efficiently heated and a lower fraction of the total drive spectra reaches the Al/MgF_2. At the same time, the high opacity of the Al/MgF_2 at photon energies around $150eV$ makes it a more efficient radiator at the blackbody temperature of the plasma ($\approx 45eV$), which causes it to more quickly cool. This all creates a situation where the tamper eventually reaches a higher peak temperature than the Al/MgF_2, and results in a thermal distribution like that shown in Figure 5.18(b). The density of the sample then adjusts to maintain a smooth pressure profile with no discontinuities (except at positions of a shock front as seen at the back of the Al/MgF_2 at $97.6ns$).

As a final check on the comparison between the calculated and measured conditions in the Al/MgF_2 sample, Figures 5.20 and 5.21 show the time-integrated and time-resolved absorption spectra on shot z597 overlaid by the spectra calculated from the radiation-hydrodynamics model. The calculations are done with the SPECT3D spectral post-processing code using a detailed configuration analysis (DCA) of the Al/MgF_2 at the temperatures and densities dictated by the rad-hydro calculation. Each spectrum is calculated under an assumption of LTE, and is averaged over the times corresponding to the data as weighted by the time-dependent intensity of the backlighter. As seen in the figures, the comparison between the measured and calculated spectra is quite good. The χ^2 between the calculated and measured time-integrated spectra across the combination of the Al and Mg absorption features was calculated to be 2.16. This is within 1σ of the minimum χ^2 found in the SPECTROFIT analysis of each K-α complex. The χ^2

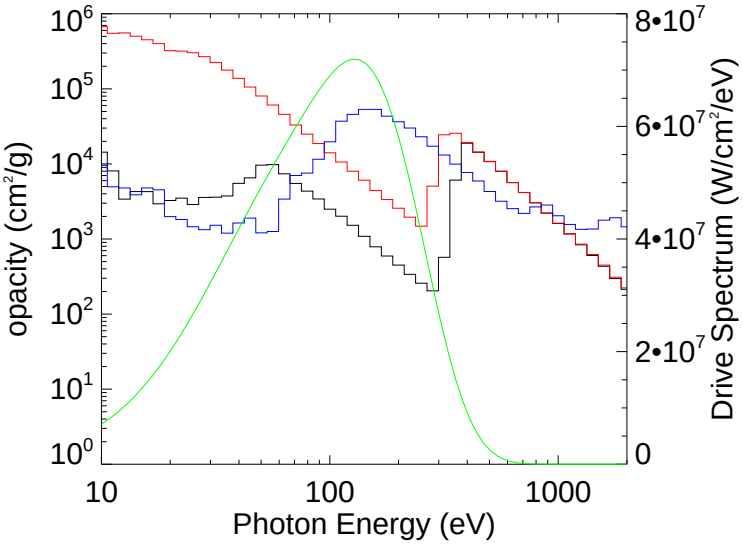

(a)

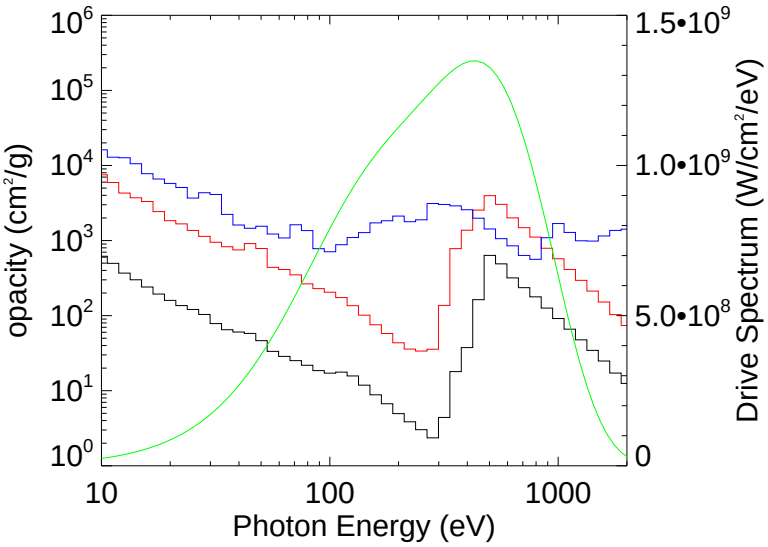

(b)

Figure 5.19: 100 group opacities at the front of the CH tamper (black), the back of the CH tamper (just in front of the Al/MgF_2) (red), and the front of the Al/MgF_2 (blue) at times of **(a)** $85ns$ and **(b)** $100ns$ in a BUCKY simulation of shot z597. Also shown is the VISRAD modeled drive-spectrum on the front of the sample at each time (green).

between the measured and calculated time-resolved spectra were also determined to be within 1σ of the minimum found in the SPECTROFIT analysis. Qualitatively, the largest deviations between these spectra are in the absorption features at either end of each K-α series as seen in the time-integrated data (in which the data is of higher quality). The calculated absorption of the Al Li- and N-like features are slightly deeper than those in the data. The same is true for the calculated Mg He- and C-like features. This may indicate a slightly larger gradient in the calculated conditions than existed in the experiment. However, the χ^2 between these spectra is within the statistical uncertainties determined from the SPECTROFIT calculation, and therefore considered to be in good agreement.

5.3.2 Calculations In Separated Al and MgF_2

The calculated dynamics that occur in the separated Al and MgF_2 layers on shot z1031 are very similar to those discussed above for the mixed foil from shot z597. As seen in the contour plots of Figure 5.9 and 5.10, the calculated phase-space of the samples on both lines-of-sight contain regions that are within 1σ of the experimental data. By inspection of these plots, it appears that the calculations would compare best to the data (fall the closest to the mid-way point between the 1σ contours) by assuming a pinch power that is $\approx 10\%$ higher than the measured value on LOS 13/14 and $\approx 10\%$ lower on LOS 21/22. The differing conditions between these foils was first noted in the overlay of the $+1\sigma$ contours from each LOS in Figure 5.12(b). According to these calculations, that difference could correspond to an azimuthal z-pinch power variation of $\approx 20\%$.

In addition to the difference in the average conditions along each LOS, it is rather interesting to note from Figure 5.12(b) that there are no statistically significant differences in the $T-\rho$ phase-space of the Al and MgF_2 foils from either LOS. It is possible that the

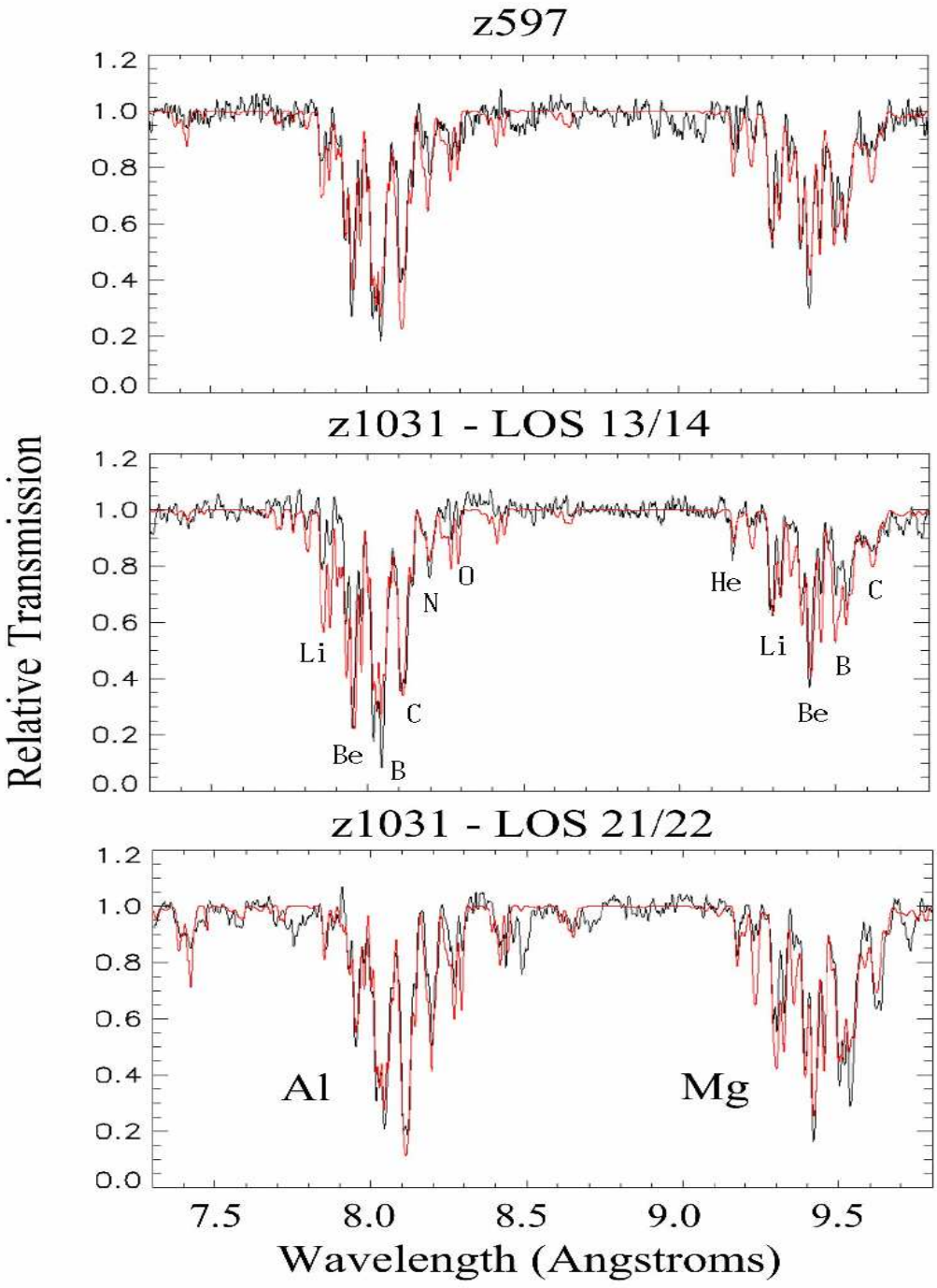

Figure 5.20: Comparison between the SPECT3D calculated relative transmission spectra (red) and the data from the time-integrated spectrometer data on shots z597 and z1031.

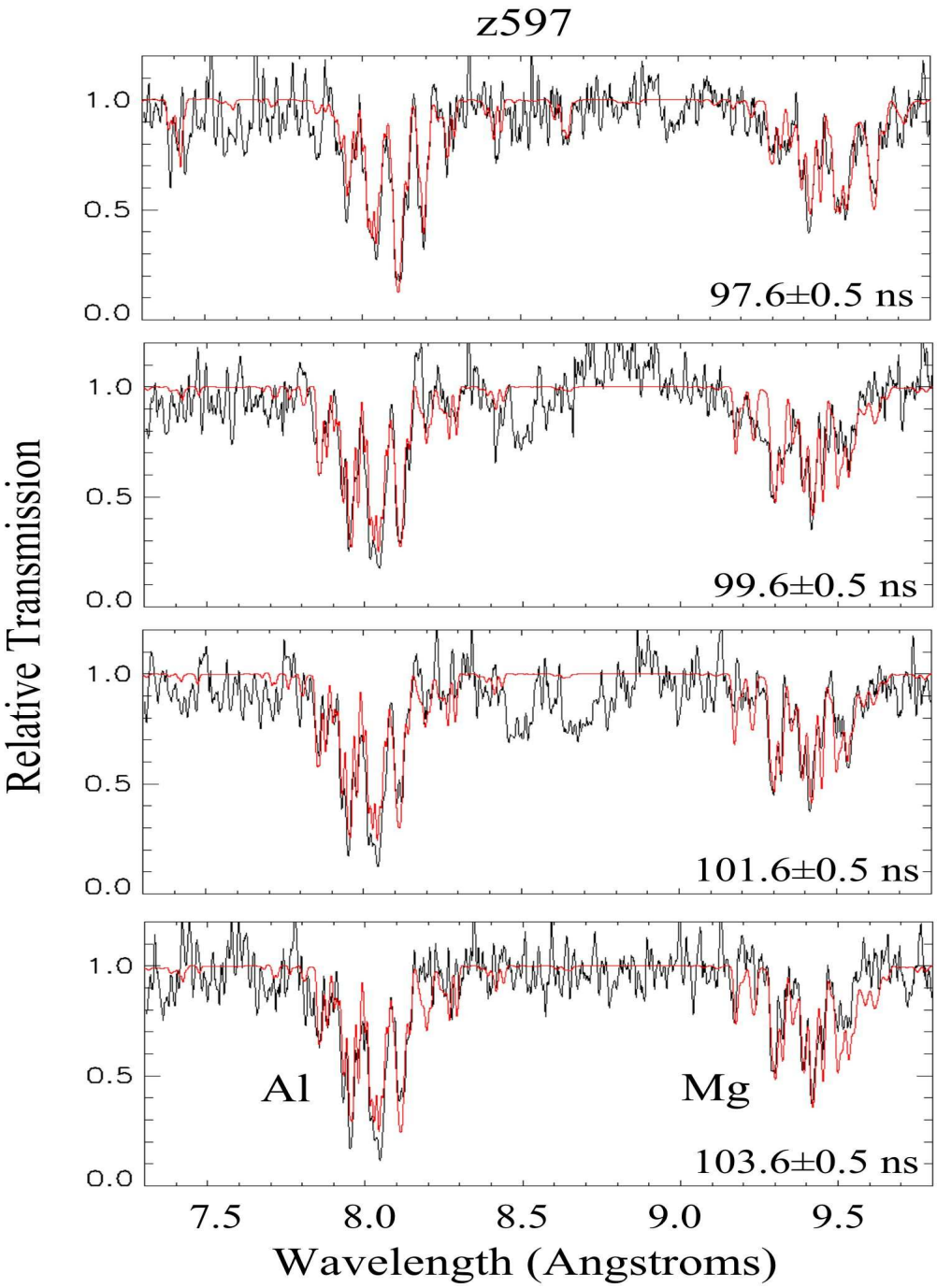

Figure 5.21: Comparison between the SPECT3D calculated relative transmission spectra (red) and the data from the time-resolved spectrometer data on shot z597.

temperature in the forward material is higher, but that implies that the density is also higher. Since the neighboring materials must maintain some sort of pressure balance, it is somewhat illogical that this could be the case ($P \propto T\rho$). The most likely situation is that the two materials have very similar temperatures (and densities), even though each may contain a gradients. This is more evidence that the frequency-dependent heating is the dominant factor in the sample dynamics.

Figure 5.22(a) and (b) show the temperature profiles in the samples on LOS 13/14 and LOS 21/22 for times of $99ns$, $100.6ns$, and $102ns$ (corresponding to the peak and half-max powers of the backlighter pulse). The calculations assume a pinch power that is 10% higher than the measured value on LOS 13/14 and 10% lower on LOS 21/22. As in the discussion from z597, there is a discontinuity in the temperature at the boundary of the foils and the CH tamper. However, there is also a discontinuity at the boundary between the Al and MgF_2. That is, the temperature at the front of the rear foil is higher than that at the back of the forward foil (irrespective of their orientation along the LOS). Even though the Al and MgF_2 each contain an $\approx 5eV$ gradient, their average temperatures differ by less than $2eV$ at almost every time.

To demonstrate the frequency-dependent heating that causes this effect, Figure 5.23(a) and (b) show the calculated net radiation heating as a function of photon energy at the time of peak drive power for the Al and MgF_2 foils on LOS13/14 and LOS 21/22 respectively. In both cases, the Al is primarily heated in the range $200eV < h\nu < 300eV$ corresponding to photo-ionization out of the L-shell. The MgF_2 is primarily heated in the range $900eV < h\nu < 1100eV$ corresponding to photo-ionization out of the F and Mg K-shells, and has some contribution to the heating around $200eV$ corresponding to absorption by the Mg L-shell.

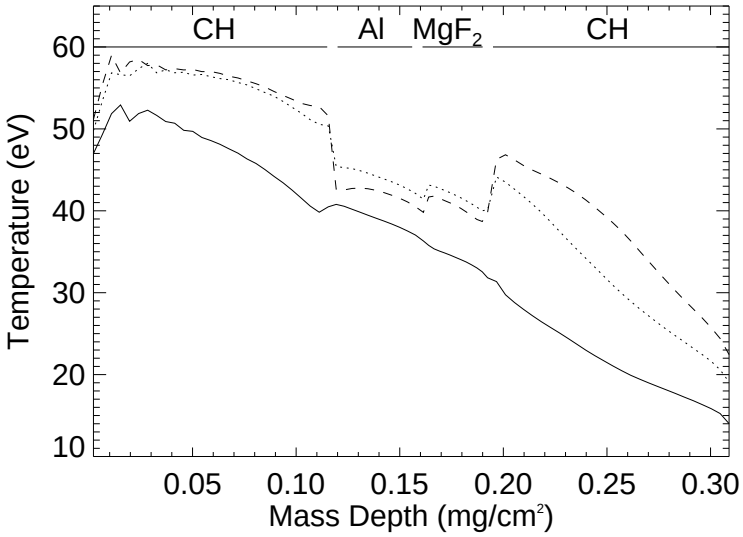

(a)

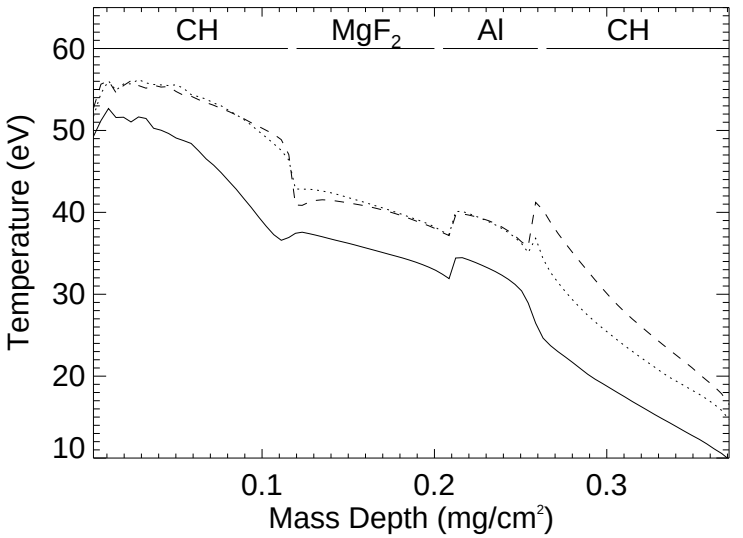

(b)

Figure 5.22: Temperature profiles in the experimental samples on **(a)** LOS 13/14 and **(b)** LOS 21/22 as calculated by BUCKY for times of $99ns$ (solid), $100.6ns$ (dotted), and $102ns$ (dashed).

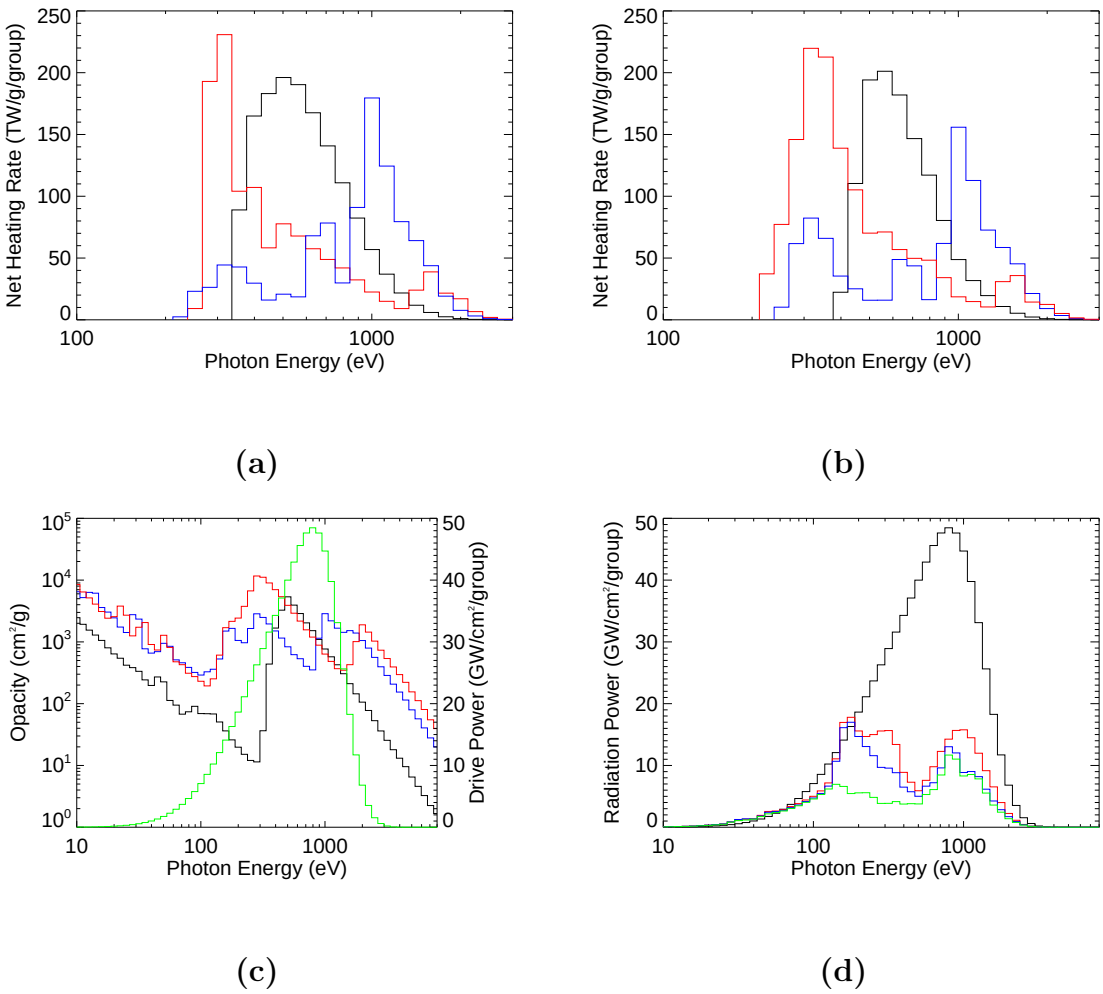

Figure 5.23: Calculated net radiation heating at $100ns$ in the CH (black), Al (red), and MgF_2 (blue) layers in the samples on **(a)** LOS 13/14 and **(b)** LOS 21/22. **(c)** Example opacities in the CH (black), Al (red), and MgF_2 (blue) layers within the sample on LOS 21/22. **(d)** Calculated radiation spectrum on LOS 21/22 at the front of the sample (black), the interface between the CH and MgF_2 (red), the interface between the MgF_2 and Al(blue), and the interface between the Al and the rear CH tamper (green).

To further demonstrate this characteristic, Figure 5.23(c) shows the drive spectrum and representative opacities in the CH, MgF_2, and Al at the time corresponding to the plots in (a) and (b). In addition, Figure 5.23(d) shows the radiation spectrum at the front of the sample, and at the interfaces between each layer in the sample on LOS21/22. The CH plasma absorbs the bulk of the radiation in the range $350eV < h\nu < 450eV$ (corresponding to the carbon K-shell). The MgF_2 primarily absorbs radiation in the ranges $200eV < h\nu < 350eV$ and $h\nu > 800eV$. The Al then absorbs most of the radiation left that is passed below $350eV$. Clearly, these dynamics can only be captured by a multi-group treatment of the radiation transport.

As a final check on the comparison between the calculated and measured conditions in the Al and MgF_2 foils, Figure 5.20(a) shows the time-integrated absorption spectra from each LOS on shot z1031 overlaid by the spectra calculated from the radiation-hydrodynamics model. The calculations are done with the SPECT3D spectral post-processing code using a detailed configuration analysis (DCA) of the Al or MgF_2 at the temperatures and densities dictated by the rad-hydro calculation. Each spectrum is calculated under an assumption of LTE, and is averaged over the time-dependent intensity of the backlighter. As seen in the figures, the comparison between the measured and calculated spectra is quite good. The χ^2 between the calculated and measured spectra over the combined Al and Mg features were computed to be 2.98 on LOS13/14, and 1.36 on LOS 21/22. Each of these is within 1σ of the largest minimum χ^2 found for each element in the SPECTROFIT calculations.

In addition to the χ^2 of the combined absorption features, the calculated and measured spectra were compared over the K-α complex of each element. These were also found to be within 1σ of the minimum SPECTROFIT value, with the exception of the Al complex in the sample on LOS13/14 (in which the Al was deposited in front of the MgF_2). In this

case, the χ^2 was determined to be 2.34, an increase of about 1.3 over the SPECTROFIT minimum. The primary culprit for this disagreement is the Li-like feature at $8.8 - 8.9$Å. The calculation severely over-predicts the depth of this feature, which indicates that the Al is over-ionized in the calculation (on average). Given that the N-like feature at the long wavelength end of the K-α complex is in good agreement, it can be deduced that the calculated ionization gradient in the Al layer is larger that that in the experiment. Since the ionization distribution is much more sensitive to temperature than density, this probably implies that the calculated peak temperatures in the Al sample are too high either in time or space (or both). The correct fix to this calculation should result in a lower average ionization state in the Al without significantly affecting either the Al B-like through C-like ionization fractions or the ionization distribution in the MgF_2. There are a large number of permutations on the drive spectra or opacities that could cause such a discrepancy. One explanation could be a spectrum at the front of the Al layer that has too many photons at $\approx 300eV$. A close look at the BUCKY calculations showed that the heating in the energy bin at $320eV$ is a factor of 2 larger at the front of the Al than the back, and contributes $\approx 10\%$ of the total heating at the front of that layer. Thus, the discrepancy between the data and calculations could be caused by a drive spectrum that is slightly too cold, a CH opacity that is slightly too low, or an Al opacity that is slightly too high at $h\nu \approx 320eV$. This is just speculation.

Given all the assumptions that go into simulating the experiments, the overall comparison is considered to be good, and the overlay of the $T - \rho$ phase space on the χ^2 contour plots if Figures 5.9 and 5.10 indicate that the average calculated conditions are within the uncertainties imposed by the spectral data and the measured z-pinch power.

5.4 Foil Experiment Summary

The understanding of the radiative heating and the associated K-α absorption features in thin foils of Al and MgF_2 on Sandia's Z facility have been demonstrated. Given that each experiment discussed in this chapter had very different z-pinch geometries and very different emission power histories, these results provide confidence in both the methods used to simulate the frequency-dependent driving radiation spectra, and in the physical models that are applied to simulate the radiation-hydrodynamics processes.

A similar set of experiments and the associated computational analysis was recently published by J.J. MacFarlane and J.E. Bailey et al. for Al foils directly attached to the primary hohlraum on Z [107]. Their experiments utilized z-pinches with much different power histories then those discussed in this chapter, and the samples had a much different total field-of-view. They concluded that "the evolution of the Al ionization distribution was successfully measured and modeled" in each experiment.

In the MacFarlane/Bailey experiments and in the ones presented in this chapter, the calculations that successfully reproduce the experimental data indicate that frequency-dependent radiative heating and cooling play the dominant role in determining the time-dependent temperature and density conditions in the foils. This is an important result because it places a restriction on the computational methods that must be used to model the dynamics in similar samples heated by z-pinch radiation. In addition, the role of the radiation field in determining the foil conditions supports the hypothesis made in §3.2 that the conditions of these materials can be used as a diagnostic of the magnitude and distribution of the radiation field at the location of the foils. With these conclusions, the experimental tools and computational methods are suitably well developed to investigate the radiative transfer in low density CH_2 foam.

Chapter 6

Foam Experiments on Z

The radiative transfer in $5mg/cc$ CH_2 foam was studied through three generations of experiments. These ranged from the simple case of a single tracer on a single line-of-sight to a much more complex experiment involving multiple tracers on multiple lines-of-sight. The design of these experiments was driven by the need to progressively tighten the constraints on the computational models, since these models are what eventually reveal the characteristics of the radiative transfer.

The discussion of the foam experiments is broken up into three sections, each describing the experimental geometry and acquired spectra, as well as the computational models that successfully reproduced the data. Section 6.1 discusses the first experiment, which measured the time-dependent heating of a single Al tracer buried in a single foam sample. Section 6.2 discusses the second experiment, which measured the time-dependent heating of Al and MgF_2 tracers placed at different depths. Section 6.3 discusses the last experiment, which measured the conditions in six MgF_2 tracers buried at four different depths within foam samples placed on three separate lines-of-sight. Finally, §6.4 summarizes these experiments, discusses the effects of different models on the calculated results,

Shot #	$r_p\,(mm)$	$h_p\,(mm)$	**Wire #**	**Wire Diam.**	$w_s\,(mm)$	$d\,(mm)$	$w_a\,(mm)$	$h_a\,(mm)$
z817	10	10	300	$11.34\mu m$	5.76	37.5	2.75	3.0

Table 6.1: Geometric parameters and z-pinch configurations for the foam transport experiment on shot z817. z817 was a single array tungsten z-pinch with no central target.

and puts the results in the perspective of the dynamic-hohlraum.

6.1 Time-Resolved Measurements of a Single Al Tracer

6.1.1 Experiment Configuration

The first experiment on the radiative transfer in CH_2 foam measured the time-dependent absorption spectra of a single Al tracer fielded in the ride-along geometry on shot z817. Table 6.1 lists the important parameters of the experiment configuration for the quantities as defined in Figure 5.1, and Figure 6.1 shows a schematic of the foam sample. The sample was composed of a $5mg/cc$ CH_2 foam that was $10mm$ wide, $13mm$ tall, and $2mm$ thick. The tracer layer was buried at a depth of $1mm$ (halfway into the foam), and was composed of a 1373Å thick Al layer on the pinch-facing side of a 5000Å thick CH substrate. The thicknesses of the tracer foil were verified by a profilometer, which was calibrated by a quartz gauge. A limiting aperture was placed between the spectrometer and the sample to provide a $2.75mm$ wide by $3.0mm$ tall field-of-view about the center of the foam. Figure 6.2 shows pictures of the pinch facing surface of the foam target, as well as a backlit picture revealing the macroscopic structure of the foam and the location of the apertured area with respect to the tracer foil. The depth of the tracer layer was

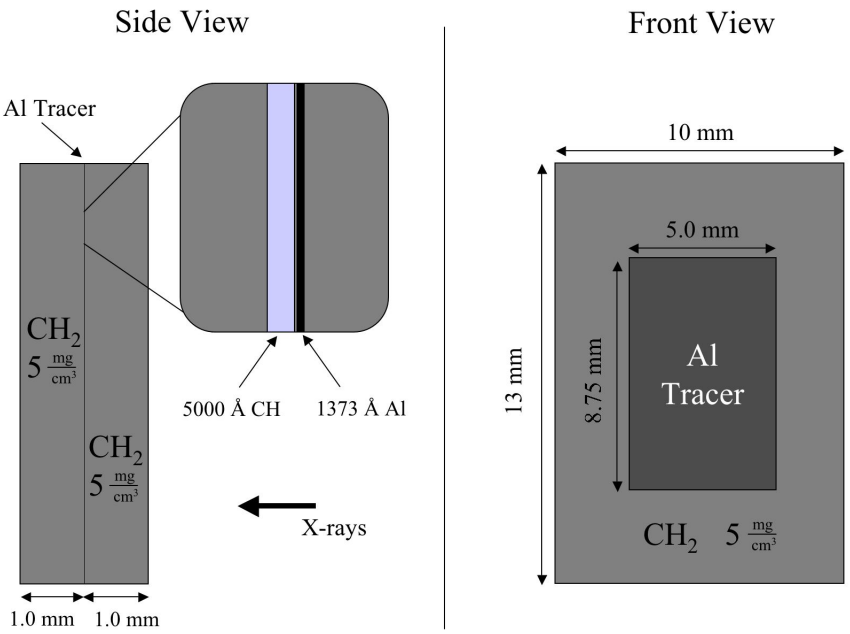

Figure 6.1: Schematic diagram of the foam sample geometry for the ride-along experiment on shot z817.

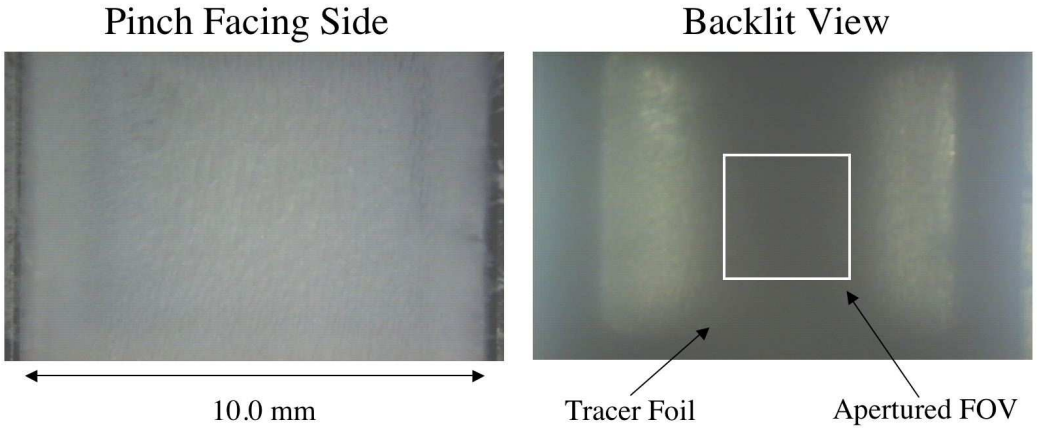

Figure 6.2: Photographs of the pinch facing surface of the foam on shot z817. The white box corresponds to the apertured field-of-view of the spectrometer.

controlled by a metal spacer that held the foil at $1.0 \pm 0.01mm$ from the front surface of the foam frame, which was then filled with the foam solution. After the foam gelled and before it completely solidified, a flat scalpel was used to shear off the excess foam material to provide a flat surface along the front edge.

Absorption spectra through the Al tracer layer were taken by a time-resolved elliptical crystal spectrometer (TREX). In this spectrometer, an ammonium dihydrogen phosphate (ADP) crystal with a $2d$ spacing of 10.64Å was bent to an elliptical curvature that had a $4059.6mm$ focal length and an eccentricity of $\epsilon = 0.9778$ (see Appendix A). A $3.0mm$ wide crossover slit was placed at the elliptical crossover focus, and a 6 strip gold MCP was assembled at a distance of $74mm$ from the crossover. The $40mm$ long MCP striplines provided a spectral range of $7.23\text{Å} \leq \lambda \leq 8.98\text{Å}$ in first order, and were pulsed in an open circuit configuration by a $2.1ns$ FWHM signal peaked at $-344V$ (over a $-300V$ DC bias), for a gain FWHM of $\approx 1.1ns$. The spectrometer was filtered between the source and the crystal by $1.5\mu m$ of mylar, and between the crystal and MCP by $8.5\mu m$ of Be. Defects in the crystal curvature limited the spectral resolution to $\lambda/\Delta\lambda \approx 600$.

The z-pinch performance on these shots was measured by a suite of diagnostics looking through LOS other than that used by the experimental sample. The primary z-pinch diagnostic that was utilized for these experiments was an array of filtered x-ray diodes (XRDs), which provided the pinch power history when normalized by a bolometer viewing from the same angle on the same line-of-sight.

6.1.2 Experimental Data

Figure 6.3 shows the time-dependent z-pinch power, temperature, and radius from shot z817 on the Z facility. The time-axis in this figure, and throughout the remainder of this section, has been shifted so that the peak of the x-ray emission power occurs at $100ns$.

The powers are determined from filtered XRD measurements that have been normalized by bolometer data. According to this data, z817 produced $1150 \pm 230kJ$ in a $11.8ns$ FWHM pulse peaked at $86 \pm 17TW$[a]. The z-pinch radii are determined from models of the implosion trajectory at times $< 93ns$, and from experimental data on similar load geometries at times $\geq 93ns$ [104] (see footnote (a) on pg. 117). The temperatures were then determined from the pinch power and radius time histories by assuming that the z-pinch is a uniform cylindrical surface emitter. The backlighter time-history in the x-ray range $2.5\text{Å} < \lambda < 12.4\text{Å}$ is also shown in the figure. To illustrate the relative timing, the peak of this curve has been normalized to the peak of the total x-ray power, and indicates a backlighter time history of $100\,^{+6.5}_{-2.3}\,ns$.

Figure 6.4(a) and (b) show the raw film data and associated spectral lineouts as recorded by the space-integrated time-resolved elliptical crystal spectrometer on shot z817. The data correspond to frames that span times from $93.3 \pm 0.55ns$ to $103.3 \pm 0.55ns$ in $2ns$ intervals on the time base in Figure 6.3. A step-wedge was used to convert the raw film data from film density units to exposure, where the step-wedge was exposed on TMAX P3200 film under the same green wavelength as the P43 phosphor used in the experiment. The lineouts have been processed by the EXRAY code (see Appendix A) to determine the wavelength scale, and to apply the appropriate corrections for the filter transmission and the crystal geometry. No reflectivity curves for ADP crystals exist in the literature, so the data has not been corrected for crystal reflectivity. However, since the analysis of this data only requires the relative transmission in the spectral range around the absorption features ($7.9\text{Å} \leq \lambda \leq 8.4\text{Å}$), then this correction should have

[a]For unknown reasons, the power pulse from this z-pinch was double-peaked and much more extended than others of a similar geometry. However, it produced a similar total x-ray yield. Since the ride-along experiment is simply an observer of the output radiation, the reasons behind the z-pinch emission history are not very important (as long as the emission is well measured).

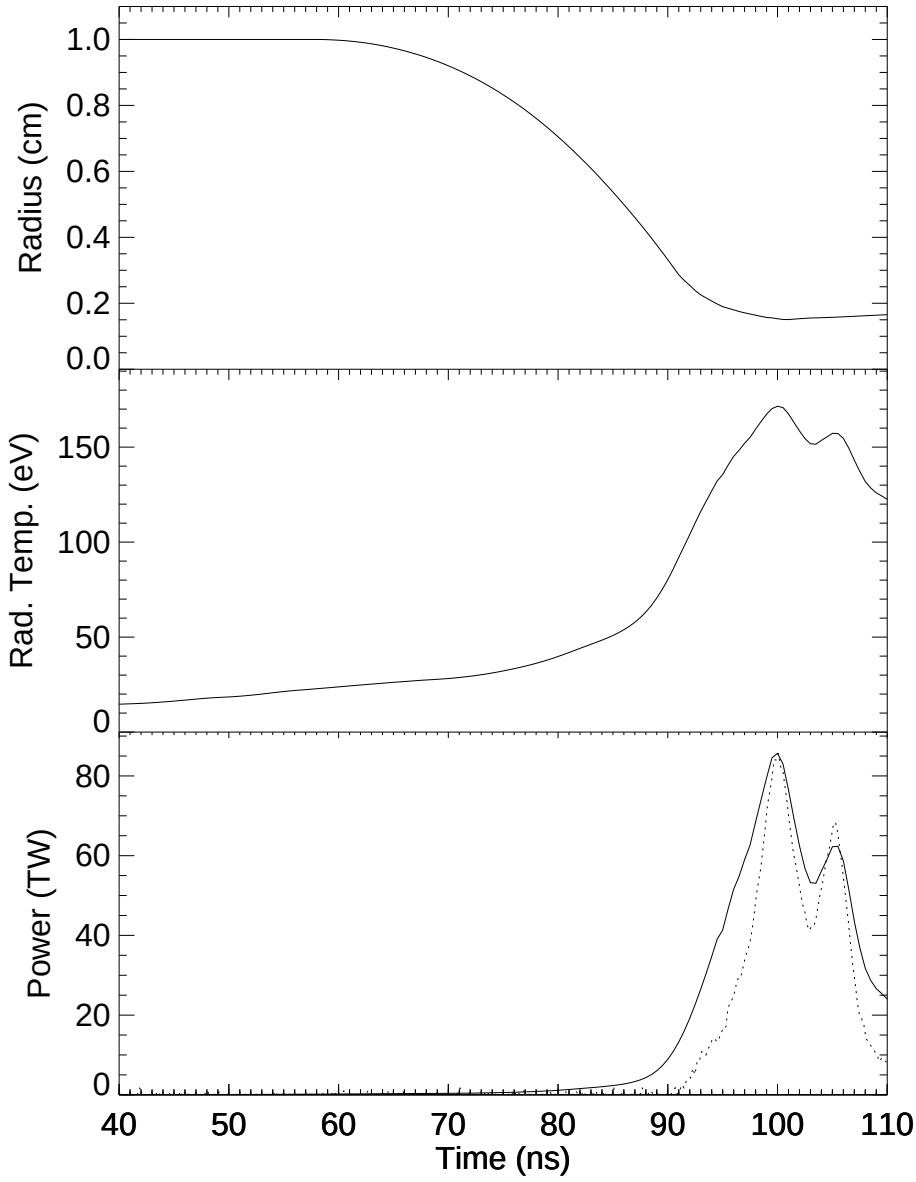

Figure 6.3: Z-pinch power, temperature, and radius profiles for shot z817 on Z. The power is measured by a kimfol filtered XRD normalized to bolometer measurements of the total radiated energy. The radii are taken from calculations at times $< 93ns$, and from self-emission data on similar shots for times $\geq 93ns$. The temperature is calculated from the power and radius profiles assuming the z-pinch is a uniform cylindrical surface emitter. Also shown in this figure is the time-history of the x-ray emission in the spectral range $2.5\text{Å} < \lambda < 12.4\text{Å}$ as normalized to the peak of the total z-pinch power (dotted).

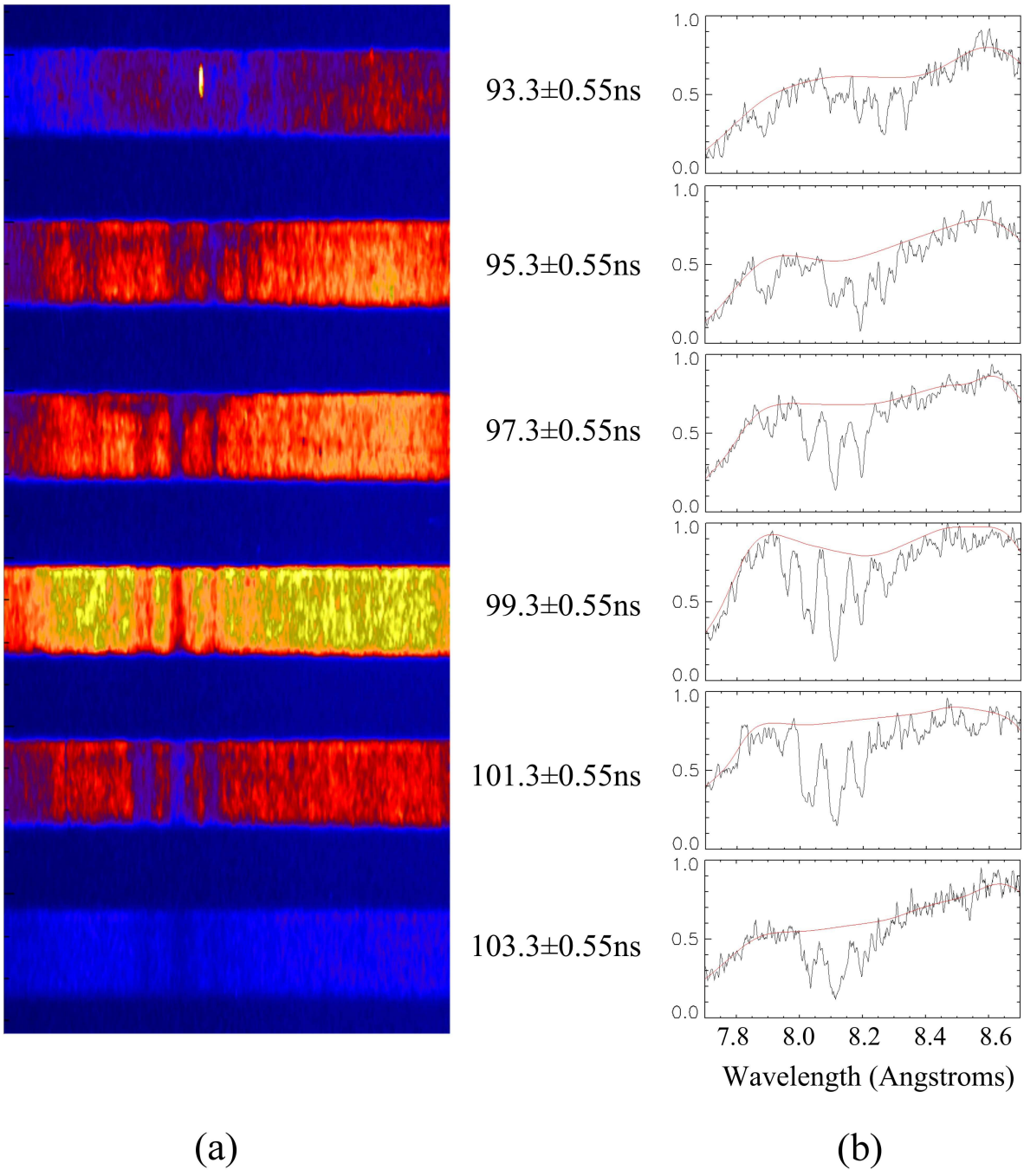

Figure 6.4: **(a)** Raw film data and **(b)** normalized spectral lineouts from the TREX on shot z817. The lineouts have been processed for the film response, filter transmission, and the crystal geometry.

little effect on the data analysis (ADP contains no materials that have an absorption edge in this spectral range).

In order to compare to the calculations of the K-α absorption spectra, the data must be converted to a relative transmission by the division of an assumed continuum. For these spectra, that continuum was determined by removing the absorption features, and filtering the remaining signal by a 0.3Å boxcar filter. The resulting continuum is overlaid on the data in Figure 6.4. The relative transmission was then calculated by dividing the measured signal by this continuum, and is shown for each of the time-frames in Figure 6.5. This is considered an acceptable procedure since the important information about the sample conditions is contained in the relative intensities of the absorption features, which are relatively unchanged by the division of the continuum.

Through a statistical comparison between calculated Al absorption spectra and the relative transmission spectra in Figure 6.5, the possible combinations of temperature and density in the plasma at times corresponding to each data frame can be determined by the SPECTROFIT code. Using this code, the weighted χ^2 between the unsmoothed transmission data and SPECT3D calculations was computed for 2627 combinations of temperature and density over the ranges $10eV \leq T_e \leq 80eV$ and $6 \times 10^{18} cm^{-3} \leq n_i \leq 6 \times 10^{23} cm^{-3}$. The statistical deviations in the intensity of each point in the data, σ_i, were determined by assuming Poisson statistics through the relation:

$$\sigma_i = \sigma_0 \sqrt{\frac{I_i}{I_0}}, \tag{6.1}$$

where I_0 and σ_0 are the average intensity and deviation in the range $8.6\text{Å} \leq \lambda \leq 8.8\text{Å}$ and I_i is the intensity at point i. The range used to calculate the average deviation was chosen because it contained no spectral features, and could be reasonably fit by a first-order polynomial. Each χ^2 comparison was then restricted to the spectral range of

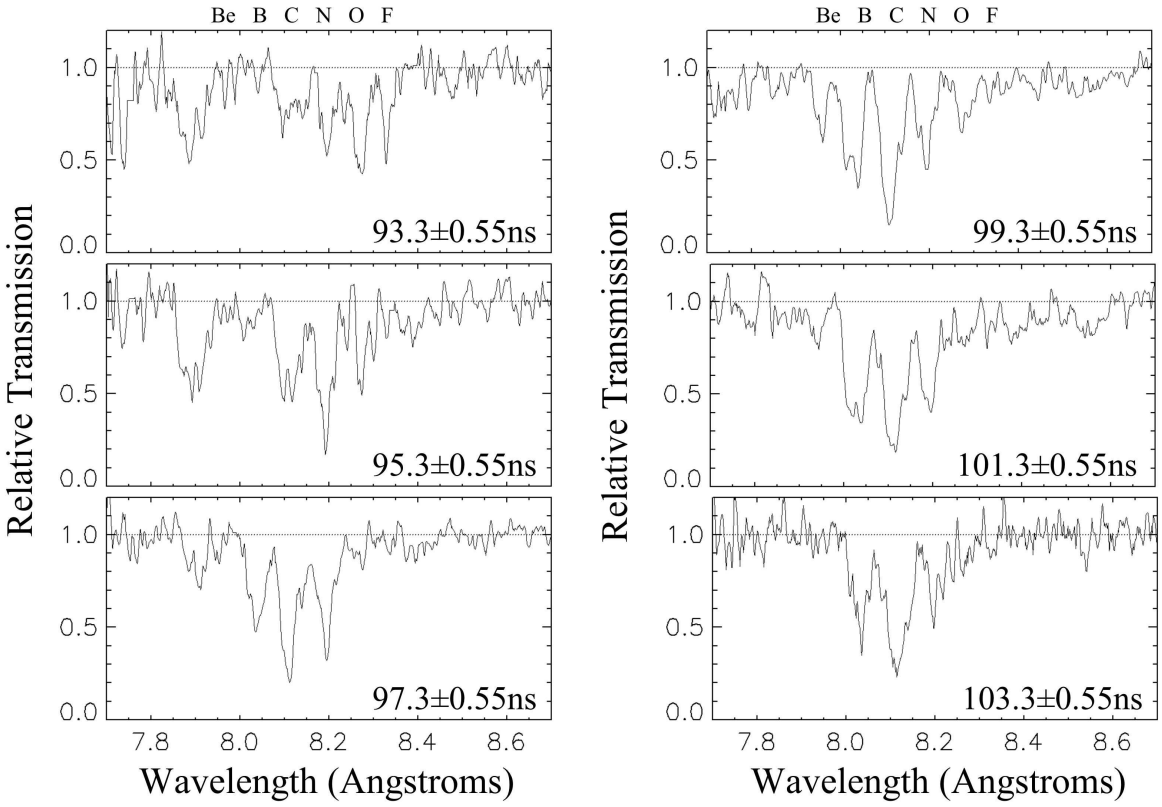

Figure 6.5: Relative transmission spectra of the *Al* K-α series from the time-resolved elliptical crystal spectrometer on shot z817.

the K-α features, where the absolute depths of the measured absorption were allowed to uniformly vary by $\pm 10\%$ (see footnote (b) on page 122). The resulting χ^2 contour plots for each time frame are shown in Figure 6.6(a)-(f).

As seen in the figures, the tracer temperature increases and/or the density decreases in the first two frames, and then the contours remain fairly constant throughout the remainder of the pulse. The χ^2 contours in the first frame, $t = 93.3 \pm 0.55ns$, are very wide due to the low signal level and correspondingly high statistical fluctuations. In contrast, the contours in the fifth frame, $t = 101.3 \pm 0.55ns$, are narrow due to the high signal level and correspondingly low statistical fluctuations.

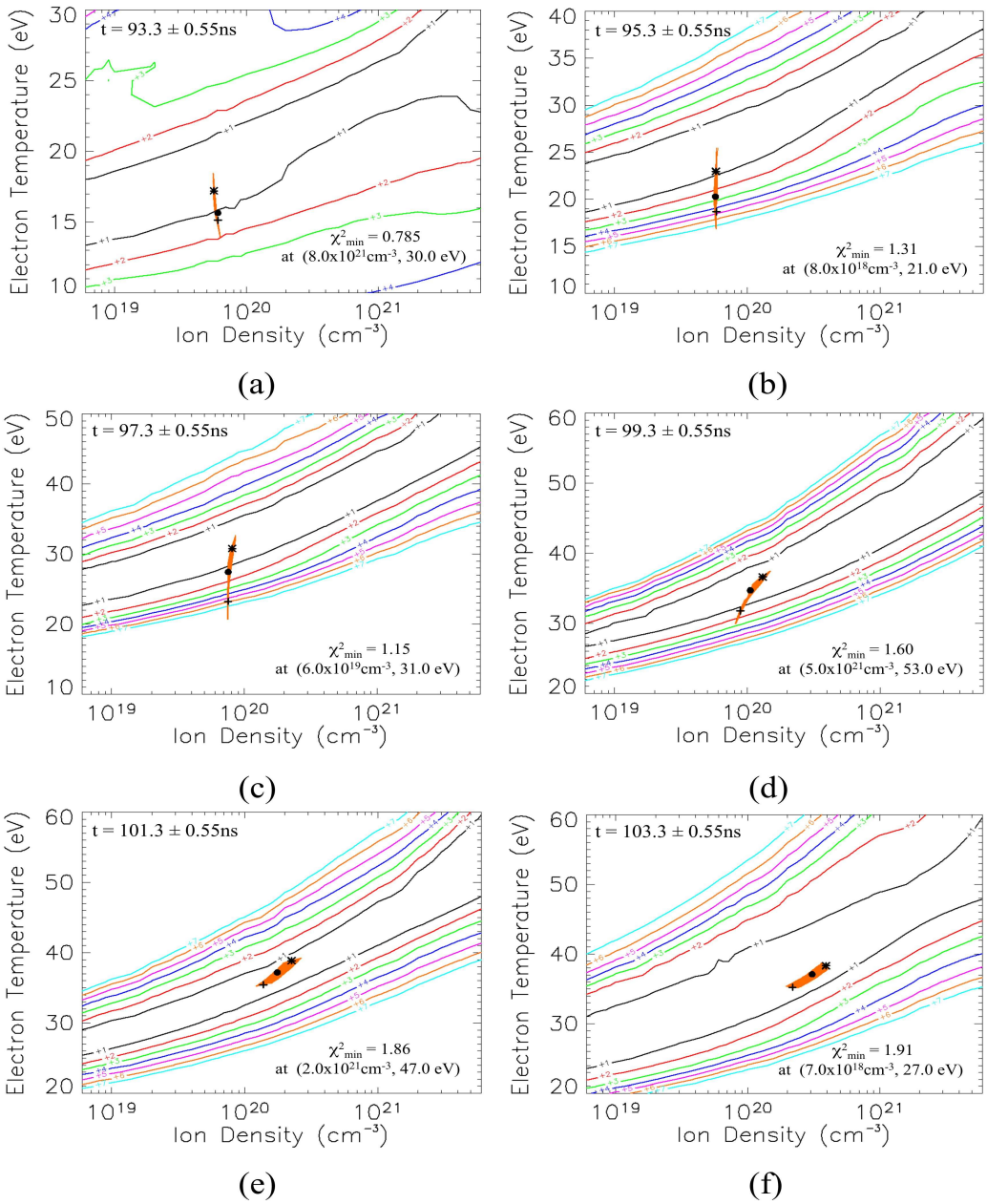

Figure 6.6: Contour plots from the SPECTROFIT χ^2 comparisons between the data from shot z817 and calculations of the *Al* K-α absorption features at times of **(a)** $93.3 \pm 0.55ns$, **(b)** $95.3 \pm 0.55ns$, **(c)** $97.3 \pm 0.55ns$, **(d)** $99.3 \pm 0.55ns$,**(e)** $101.3 \pm 0.55ns$, and **(f)** $103.3 \pm 0.55ns$. The symbols correspond to simulated mass- and time-averaged conditions in the tracer across each time frame assuming z-pinch emission powers of 80% (cross), 100% (dot), and 120% (star) of the measured value. The orange shaded regions correspond to the mass-averaged range of these simulations over each time-frame.

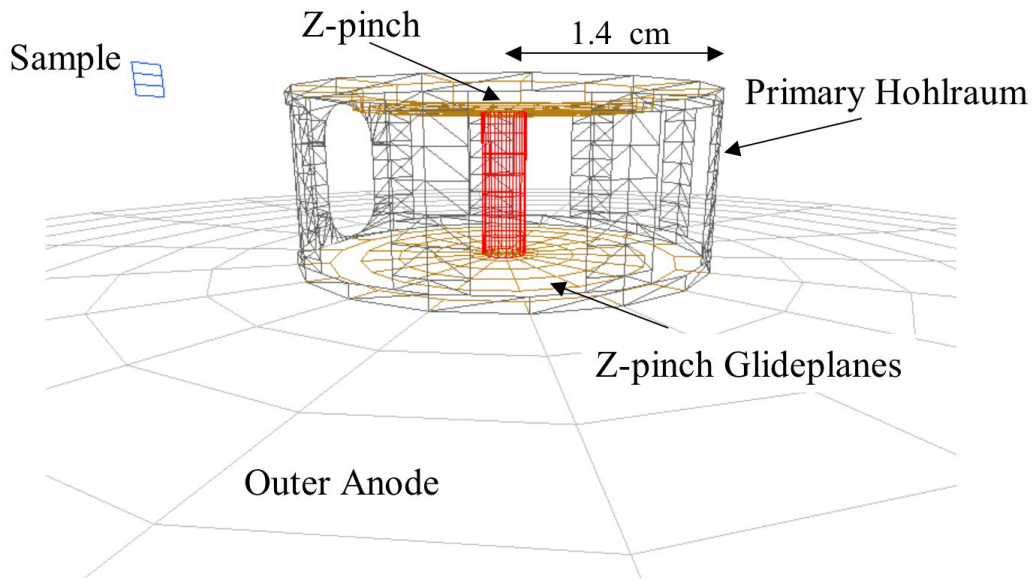

Figure 6.7: Calculational grid for the VISRAD view-factor model of shot z817 at the time of peak z-pinch power.

6.1.3 Experiment Modeling

The experiment described in §6.1.1-6.1.2 was modeled using the procedure described in Chapter 4. As described in that chapter, the first step in simulating the dynamics of the experiment requires a calculation of the time- and frequency-dependent radiation drive on the sample surface. These calculations were done using the VISRAD view-factor code. An example of the 3-D VISRAD grid for the geometry described in §6.1.1 is shown in Figure 6.7. In this model, the z-pinch radius and power histories from Figure 6.3 were input as the power source (shown in red on Figure 6.7), and an independent view-factor calculation was conducted for 37 time-steps over the range $0ns \leq t \leq 110ns$. It took 6 iterations on these view-factor calculations for the albedos to stabilize, and the resulting drive power on the sample to converge within 1% on 2 successive iterations (as described in §4.1).

The resulting albedos of the the outer anode, z-pinch glideplanes, and the primary

hohlraum (as labeled in Figure 6.7) are shown in Figure 6.8(a), and the final drive power on the sample surface is shown in Figure 6.8(b). This drive history was calculated for the nominal (measured) z-pinch power, and reaches a peak radiation power of $0.82TW$. At the time of peak z-pinch emission ($t = 100ns$), the driving radiation spectrum peaks at $290eV$, and has an average energy of $542eV$. At this time, the contributions to the drive flux from each of the major objects in the view-factor grid were calculated to be; 70% from the z-pinch, 13% from the bottom glide-plane, 9% from the outer anode, and 8% from the primary hohlraum wall.

The drive history from Figure 6.8(b) was applied as a time- and frequency-dependent radiation boundary condition in radiation-hydrodynamics calculations of the sample response. These simulations were done with the BUCKY 1-D Lagrangian rad-hydro code using multi-angle short-characteristics radiation transport for 500 log-spaced photon energy groups from $0.1 - 10^4eV$. The opacities of each material were calculated from PROPACEOS tables that contained 39 temperature points from $0.1 - 100eV$, and 41 log-spaced density points from $10^{19} - 10^{23}cm^{-3}$. The equation-of-state for each material was taken from the SESAME EOS tables. The rad-hydro models were begun at $t = 0ns$, and ended at a time of $110ns$ using a quiet-start vaporization model set at a temperature of $0.4eV$. These calculations (including the view-factor simulations) were then repeated for each sample assuming the z-pinch power was 20% lower and then 20% higher than the measured value. This was done to account for the uncertainty in the z-pinch power measurements, which were shown in §4.1 to be the dominant uncertainty in the calculated radiation drive.

The mass-averaged temperature-density phase space of the calculated conditions in the Al foil are shown on the χ^2 contour plots in Figures 6.6(a)-(f) over the times corresponding to each data frame. These calculations are shown as an orange shaded re-

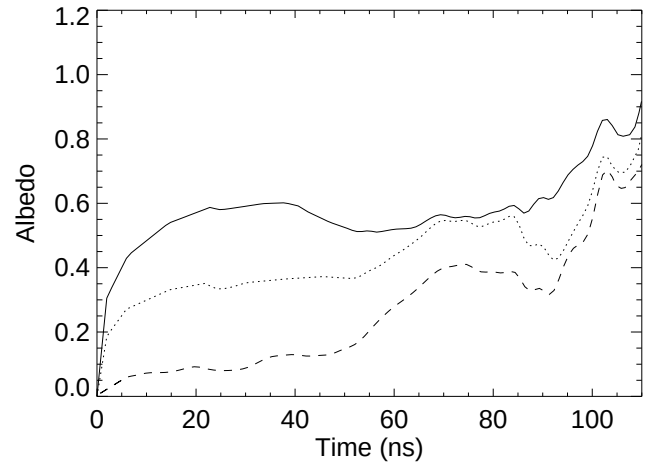

(a)

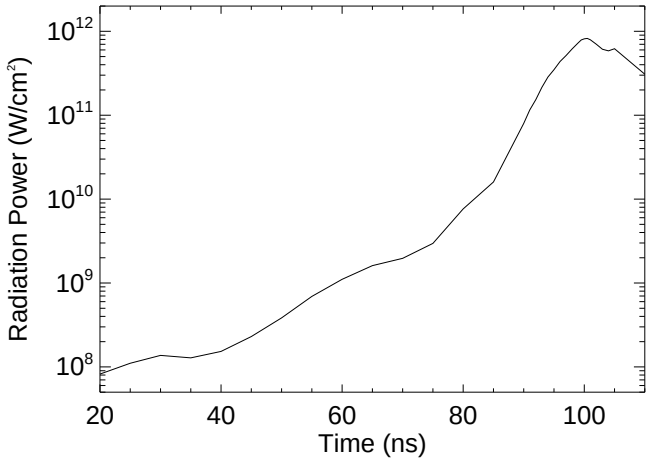

(b)

Figure 6.8: (a) BUCKY calculated albedo histories used for the final view factor calculations of shot z817. The albedos are shown for the pinch glideplanes (solid), the primary hohlraum (dotted), and the outer anode (dashed). **(b)** VISRAD modeled radiation power history on the surface of the foam sample on shot z817.

gion corresponding to the calculated conditions assuming the pinch power ranged from $80 - 120\%$ of the nominal value. The calculations are shown in this way because it provides a quick visual way to compare to the data. If the calculated conditions are going to be a good approximation to those observed in the experiment, then part of the shaded region must fall within the $+1\sigma$ contours. This can be further constrained by calculating the conditions in the foils averaged over the time in the data frame as weighted by the backlighter and micro-channel-plate pulse histories. These points are over-plotted on each contour plot as a symbol corresponding to assumed pinch powers of; 80%, 100%, and 120% of the nominal value. Since the data recorded on the spectrometers are truly a measure of the mass- and time-averaged conditions over each time-frame, then these points are the best diagnostic of the comparison between the data and the rad-hydro models.

The phase-space plots in Figures 6.6(a)-(f) reveal an interesting feature of the calculated dynamics. Early in time, $t < 99ns$, the conditions in the tracer as derived from the experimental data can only be fit by the calculations assuming a pinch power that is higher than the nominal value. In particular, the contours at $t = 95.3 \pm 0.55ns$ show that the data can only be fit within 1σ by assuming a pinch power that is higher by 20% (the full extent of the quoted error bar in the power measurement). At later times, however, the data can be fit within $+1\sigma$ by pinch powers anywhere within the uncertainties in the power measurement. This is true even for the $+1\sigma$ contour at $t = 101.3 \pm 0.55ns$, which is quite narrow. The reason for this difference in the graphical comparison between the measured and calculated plasma conditions is in the orientation of the calculated phase-space. In Figures 6.6(a)-(c) this phase-space is oriented almost directly along the temperature axis. Physically, this implies that the Al has expanded to some equilibrium with the surrounding plasma, and any additional radiation goes into heating the

Al without any rapid hydrodynamic motion. In Figures 6.6(d)-(f), the phase-space tilts to almost align with the $+1\sigma$ contour. The interesting thing about this tilting is that the calculated conditions under the higher power radiation drive are actually at a higher density. This implies the presence of an ablatively driven shock front. The higher the driving radiation power on the surface of the foam, the stronger the shock front is, and the quicker it reaches the position of the Al tracer.

Figure 6.9 shows the time history of the average temperature[b] and density in the Al layer as calculated by BUCKY assuming a pinch emission power that was 10% higher than the nominal value at all times. The figure indicates that the temperature slowly increases to about $15eV$ at $t \approx 94ns$, and then rapidly increases up to a peak of about $38eV$ at a time of $102.5ns$. Meanwhile, the density decreases to a minimum value of about $7 \times 10^{19} cm^{-3}$ at $t \approx 97ns$ and then the plasma re-compresses to a value of about $4 \times 10^{20} cm^{-3}$ at $t \approx 106ns$. This increase in density is due to the passage of the ablative shock front as discussed above. Note, however, that the slope of the compression is not very steep, indicating that the shock front is not very strong.

To further investigate the details of the calculated dynamics in the CH_2 foam, Figures 6.10(a) and (b) show the spatial profiles of the electron temperature and ion density in the sample at times of $93ns$, $95ns$, $97ns$, $99ns$, $101ns$, and $103ns$ (corresponding to the frames in the time-resolved data). Again, these calculations were done assuming a pinch emission power that was 10% higher than the nominal value at all times. Early in time, the calculations predict a large gradient in the temperature and density of the Al ($\approx 8eV$ and $\approx 6 \times 10^{19} cm^{-3}$). At later times the temperature gradients drop to $< 2eV$, and almost no gradient in the density. In addition, the ion density in the CH_2 shows the presence of multiple shocks; a weak ablatively driven shock coming from the left side of

[b]The electron and ion temperatures were calculated to be in close equilibrium.

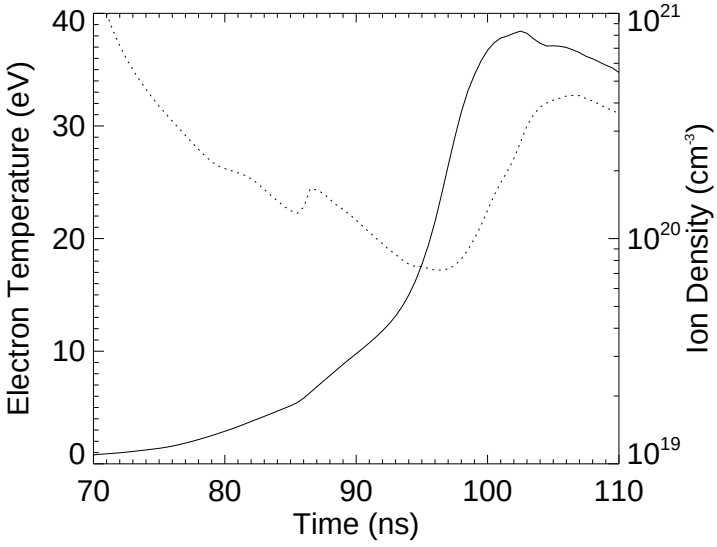

Figure 6.9: Mass averaged temperature (solid) and density (dotted) conditions in the *Al* tracer on shot z817 as calculated by BUCKY.

the figure, and two stronger shocks diverging from the *Al* tracer. The latter two are due to a compression of the CH_2 as the *Al* expands. As seen in the temperature profiles, the *Al* tracer is at a higher temperature than the surrounding foam for each of the time frames in the figure. As discussed in detail in Chapter 5, this is due to the frequency-dependent radiation heating of the *Al* layer. As this layer heats up, its internal pressure increases causing it to expand at a faster rate than the surrounding materials.

To better visualize these important hydrodynamics, Figure 6.11 shows the time-dependent mass contours calculated by BUCKY for the entire foam sample. As the *Al* is heated, it first expands into the lower density CH_2 foam in front of it before building enough pressure against the CH substrate to cause it to move. When the CH finally does release, it launches a shock into the rear portion of the foam sample, which quickly dissipates. Later in time, $t \approx 98ns$, the ablatively driven shock reaches the tracer layer, compresses it by about a factor of 5, and sweeps it toward the back of the sample.

These dynamics are rather complex, but the phase-space plots indicate that the resulting conditions in the Al tracer are in good agreement with the recorded data.

As alluded to above, all these dynamics are driven by the frequency-dependent heating of the CH_2 foam and the Al tracer. The dominant mechanism for radiation heating in the Al layer is photo-ionization out of the L-shell ($h\nu \approx 200 - 300eV$), which lies just below the carbon K-edge ($h\nu \approx 300 - 400eV$). To illustrate, Figure 6.12 shows the radiation spectrum at the boundary between the foam and the tracer overlaid with the opacities of the CH_2 and Al on either side of the boundary. These plots are shown for a simulation time of $98.0ns$. As seen in the figure, the radiation spectrum is sharply peaked in the range $220eV \leq h\nu \leq 300eV$. This is due to a filtering of the drive spectrum by the carbon K-shell. By the time the radiation field has penetrated the $0.5mg/cm^2$ thickness of the CH_2 foam, those frequencies that are easily absorbed by the carbon have already been filtered out, and the resulting spectrum propagates through the deeper portions of the foam without much interaction. However, this filtered spectrum is sharply peaked at the location of the Al L-shell, which has a high photo-ionization cross-section. This results in a situation where the Al has a much higher reaction rate with the radiation spectrum than the adjacent CH_2, and the tracer is therefore heated to a higher temperature than the surrounding foam.

As a final check on the comparison between the calculated Al conditions and those recorded in the experiment, Figure 6.13 shows the time-resolved absorption spectra on shot z817 overlaid by the spectra calculated from the radiation-hydrodynamics model assuming a 10% increase in the z-pinch emission powers over the nominal values. The calculations are done with the SPECT3D spectral post-processing code using a detailed configuration analysis (DCA) of the Al at the temperatures and densities dictated by the rad-hydro calculation. Each spectrum is calculated under an assumption of LTE, and is

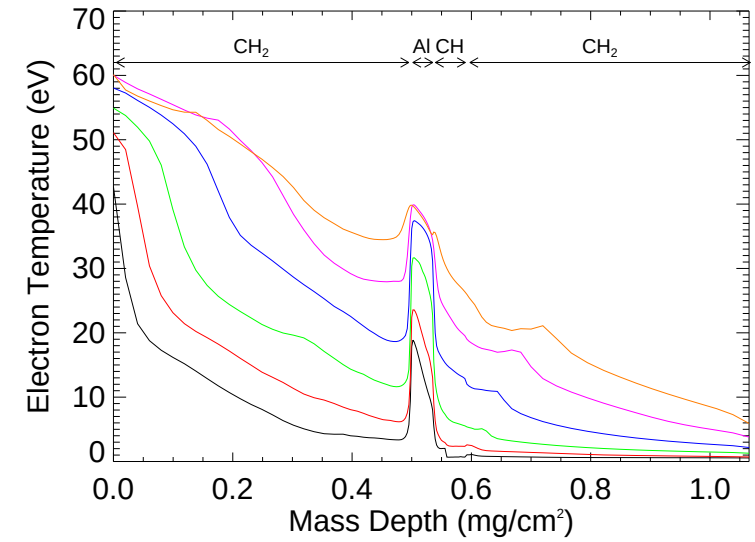

(a)

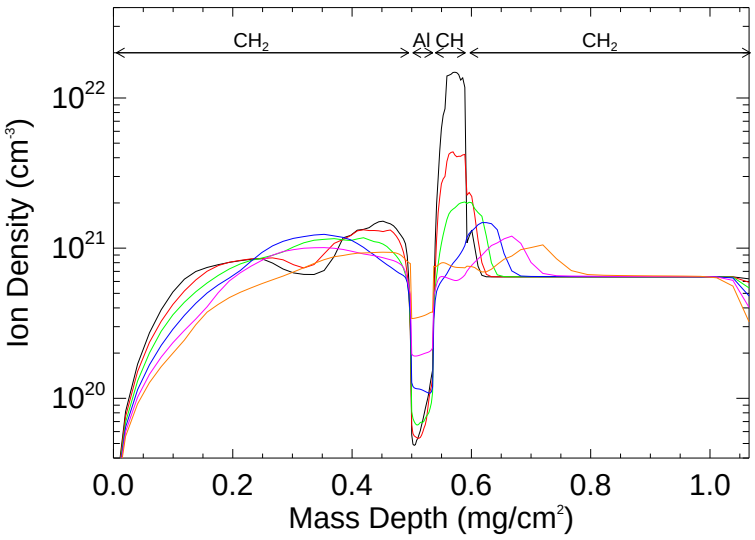

(b)

Figure 6.10: **(a)** Electron temperature and **(b)** ion density profiles in the experimental sample on shot z817 as calculated by BUCKY for times of 93ns (black), 95ns (red), 97ns (green), 99ns (blue), 101ns (purple), and 103ns (orange).

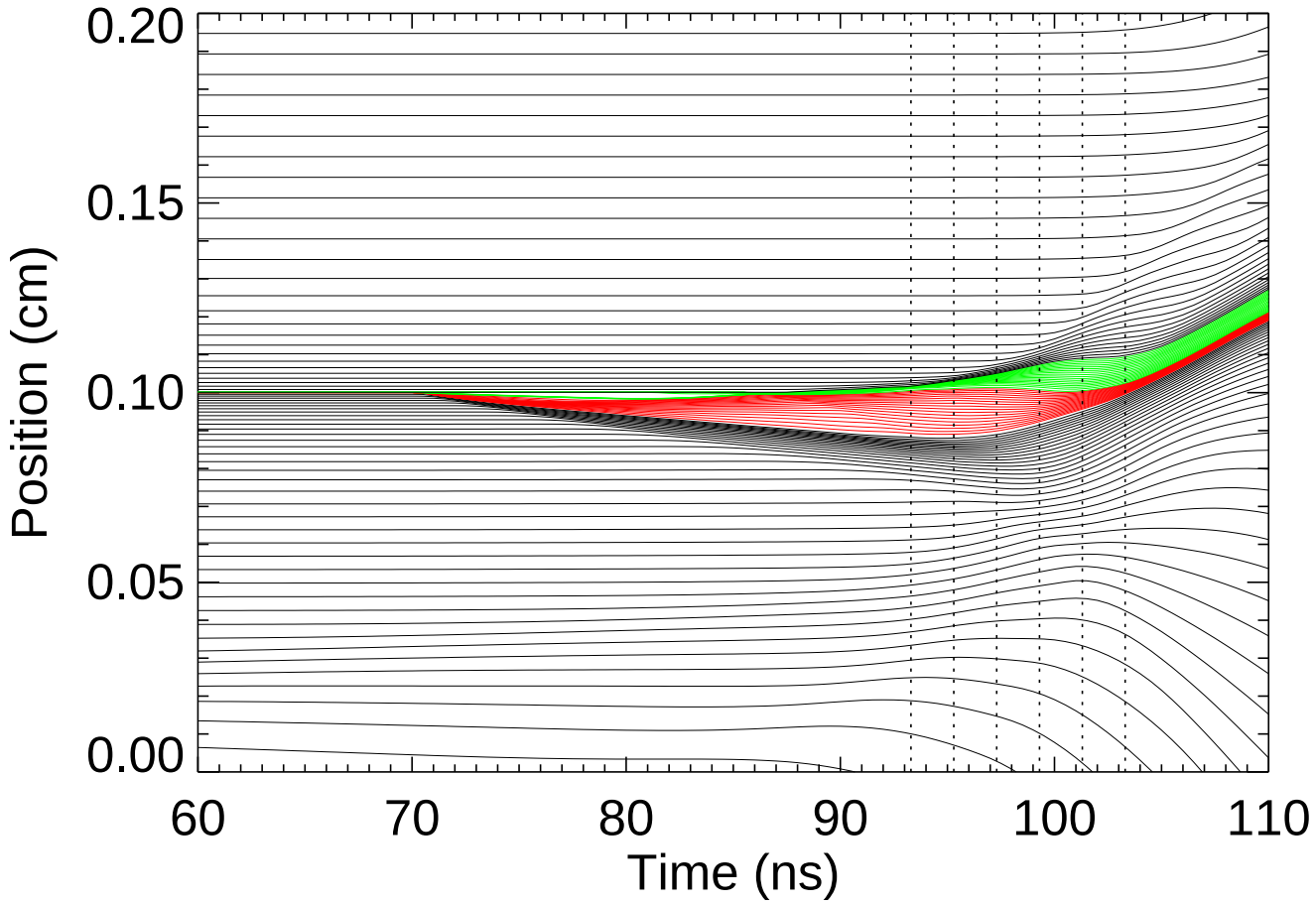

Figure 6.11: Mass contours (Lagrangian zone positions) for the CH_2 (black) foam, the Al tracer (red), and the CH substrate (green) as a function of time for a BUCKY calculation of the foam experiment on shot z817. The dotted lines correspond to the center of each frame in the time-resolved data.

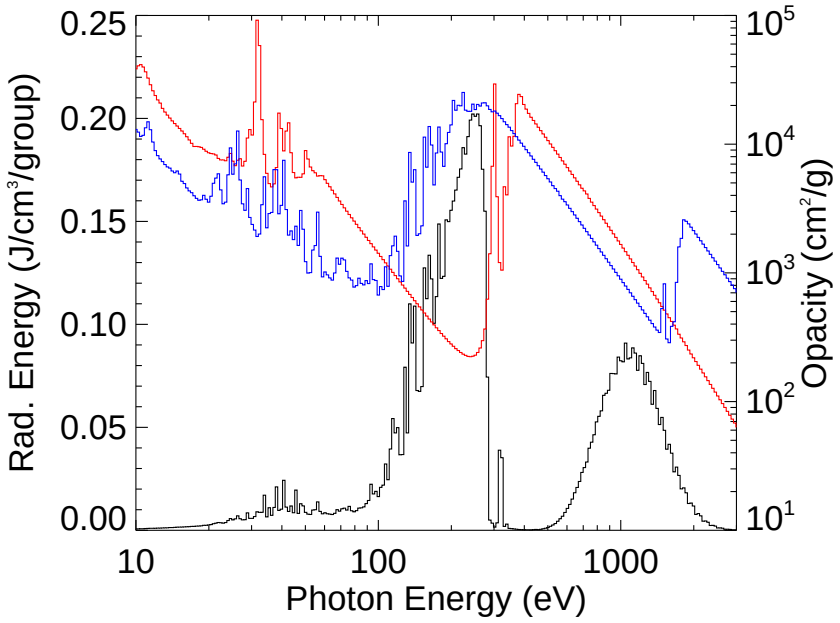

Figure 6.12: BUCKY calculated radiation spectrum (black) at the boundary between the CH_2 foam and Al tracer at a simulation time of $98.0ns$. Also shown are the multi-group opacities of the CH_2 (red) and Al (blue) on either side of the boundary.

averaged over the times corresponding to the data as weighted by the time-dependent intensity of the backlighter and the micro-channel-plate pulse history. As seen in the figures, the measured and calculated spectra are in fair agreement. Frames 3-6 are calculated to be within 1σ of the minimum χ^2 found in the SPECTROFIT analysis. Frames 1 and 2 were calculated to have a χ^2 of 2.04 and 2.57, where the minimum χ^2 in the SPECTROFIT analysis was found to be 0.79 and 1.31 respectively. That places the statistical fit of these two frames just outside the 1σ probability.

There are a few possible reasons for this minor discrepancy. First, the 1σ level only contains $\approx 68.3\%$ of the probability of a given measurement. Thus, there is a $\approx 31.7\%$ probability that the actual charge states in the plasma are indicative of a spectrum that is outside the 1σ level (but less than a 5% probability it is outside 2σ). Second, the first and

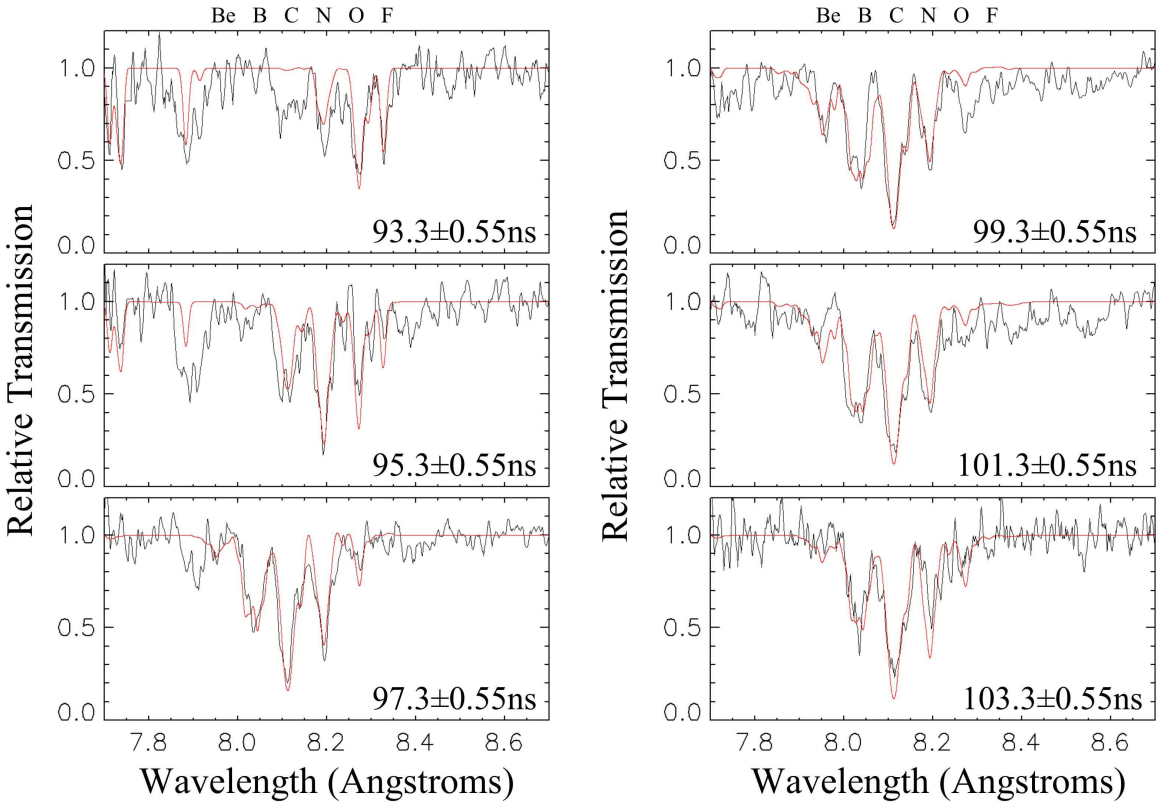

Figure 6.13: Comparison between the SPECT3D calculated relative transmission spectra (red) and the time-resolved data from shot z817.

second frames in the data show an unusually wide (and noisy) dip in the intensity around the C-like K-α feature. The origin of this 'defect' is not known, but it is responsible for putting the goodness-of-fit outside the 1σ level. Finally, it is possible that the assumed z-pinch power is too low early in time. This is the most difficult domain in which to unfold the true z-pinch power from the XRD data. The spectra from the z-pinch is much different $6ns$ before peak emission than it is at the peak, and the XRD unfolds rely on a normalization with integrated energy measurements recorded by a set of bolometers. Since the XRD filtering makes their response sensitive to the incident spectrum, and the normalizations are optimized for the response at peak z-pinch emission, it is very possible

that the relative difference between the early and late z-pinch powers are not precisely represented by the XRDs.

Regardless, given the uncertainties in the data and the calculations, the temperature-density phase-space plots overlaid on the χ^2 contours in Figure 6.6 demonstrate that the experimental data from shot z817 can be adequately reproduced by the computational methods and associated data tables as applied in this section.

6.2 Time-Resolved Measurements of Separated Al and MgF_2 Tracers

6.2.1 Experiment Configuration

The second experiment on the radiative transfer in CH_2 foam measured the time-dependent absorption spectra of both Al and MgF_2 tracers fielded in the ride-along geometry on shot z874. Table 6.2 lists the important parameters of the experiment configuration for the quantities as defined in Figure 5.1, and Figure 6.14 shows a schematic of the foam sample. The sample was composed of $5mg/cc\ CH_2$ foam that was $8.76mm$ wide, $8.76mm$ tall, and $1.676mm$ thick. An Al tracer layer was placed at a depth of $0.838mm$ (halfway into the foam), and a MgF_2 tracer layer was placed at a depth of $1.676mm$ (the back of the sample). The Al tracer was composed of a 1508Å layer of Al on a 4754Å CH substrate, and the MgF_2 tracer was composed of a 2932Å layer of MgF_2 on a 9700Å CH substrate. The thicknesses of the tracer foils were verified by a profilometer, which was calibrated by a quartz gauge. A limiting aperture was placed between the spectrometer and the sample to provide a $5.0mm$ wide by $4.0mm$ tall field-of-view about the center of the foam. The sample was constructed of two separate sections of CH_2 foam that

Shot #	$r_p\,(mm)$	$h_p\,(mm)$	**Wire #**	**Wire Diam.**	$w_s\,(mm)$	$d\,(mm)$	$w_a\,(mm)$	$h_a\,(mm)$
z874	10	10	90	$20.69\mu m$	5.6	32.0	5.0	4.0

Table 6.2: Geometric parameters and z-pinch configurations for the foam transport experiment on shot z874. z874 was a single array tungsten z-pinch with no central target.

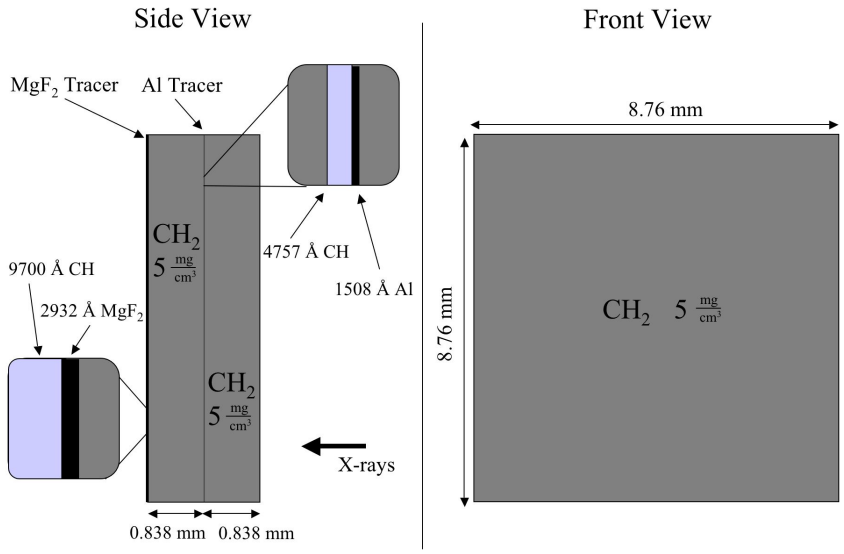

Figure 6.14: Schematic diagram of the foam sample geometry for the ride-along experiment on shot z874.

were cast into steel frames with a $0.838mm$ thickness. The tracer layers were attached to the back of each frame (with the metal foil facing inside), and the CH_2 foam was cast inside the frames. After the foam gelled and before it completely solidified, a flat scalpel was used to shear off the excess foam material to provide a flat surface along the front edges. After the foam was solidified, the frames were attached together to create the total $1.676mm$ thick sample with an Al tracer halfway in and a MgF_2 tracer at the back. Figure 6.15 shows pictures of the pinch-facing surface of each foam frame before they were assembled together.

Absorption spectra through the Al and MgF_2 tracer layers were taken by a time-

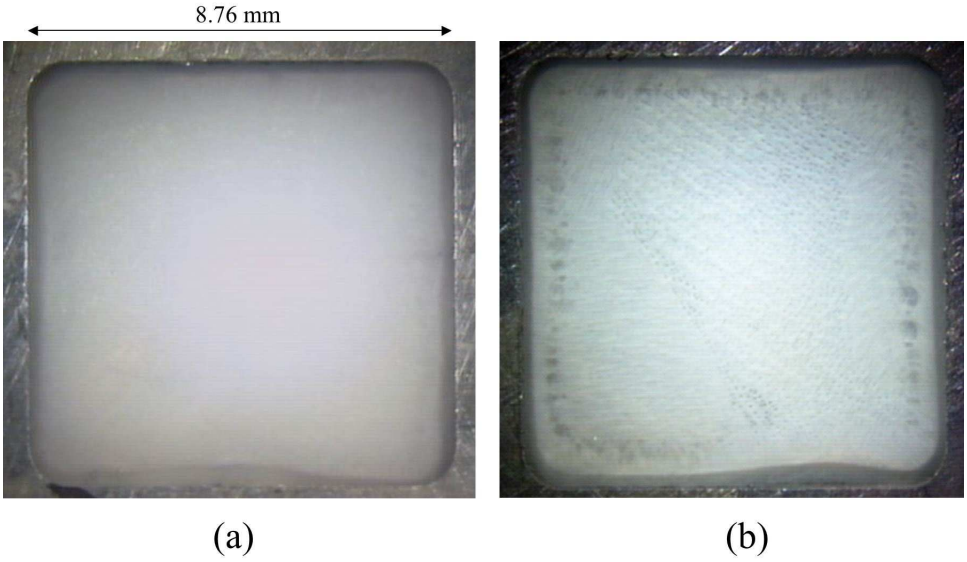

Figure 6.15: Photographs of the pinch facing surface of the **(a)** front and **(b)** back sections of the foam target on shot z874.

resolved elliptical crystal spectrometer (TREX). In this spectrometer, a Mica crystal with a $2d$ spacing of 19.84Å was bent to an elliptical curvature that had a $4100.0mm$ focal length and an eccentricity of $\epsilon = 0.9927$ (see Appendix A). A $3.0mm$ wide crossover slit was placed at the elliptical crossover focus, and a 6 strip gold MCP was assembled at a distance of $76.3mm$ from the crossover. The $40mm$ long MCP striplines provided a spectral range of 6.1Å $\leq \lambda \leq$ 10.0Å in first order, and were pulsed in an open circuit configuration by a $2.1ns$ FWHM signal peaked at $-325V$ (over a $-200V$ DC bias), for a gain FWHM of $\approx 1.1ns$. The spectrometer was filtered between the source and the crystal by $1.5\mu m$ of mylar, and between the crystal and MCP by $8.5\mu m$ of Be. Defects in the crystal curvature limited the spectral resolution to $\lambda/\Delta\lambda \approx 600$.

The z-pinch performance on these shots was measured by a suite of diagnostics looking through LOS other than that used by the experimental sample. The primary z-pinch diagnostic that was utilized for these experiments was an array of filtered x-ray diodes (XRDs), which provided the pinch power history when normalized by a bolometer viewing

from the same angle on the same line-of-sight.

6.2.2 Experimental Data

Figure 6.16 shows the time-dependent z-pinch power, temperature, and radius from shot z874 on the Z facility. The time-axis in this figure, and throughout the remainder of this section, has been shifted so that the peak of the x-ray emission power occurs at $100ns$. The powers are determined from kimfol filtered XRD measurements that have been normalized by bolometer data. According to this data, z874 produced $810 \pm 162kJ$ in a $8.7ns$ FWHM pulse peaked at $67 \pm 13TW$. The power pulse from this z-pinch is extended because of the low number of wires in the array, which is known to cause a wider and lower power x-ray output than an array with ≈ 300 wires. The z-pinch radii are determined from models of the implosion trajectory for low wire-number z-pinches at times $< 93ns$, and from experimental data on similar load geometries for times $\geq 93ns$. The temperatures were then determined from the pinch power and radius time histories by assuming that the z-pinch is a uniform cylindrical surface emitter. The backlighter time-history in the x-ray range $2.5\text{Å} < \lambda < 12.4\text{Å}$ is also shown in the figure. To illustrate the relative timing, the peak of this curve has been normalized to the peak of the total x-ray power, and indicates a backlighter time history of $100\,^{+3.0}_{-2.2}\,ns$.

Figure 6.17(a) and (b) show the raw film data and associated spectral lineouts as recorded by the space-integrated time-resolved elliptical crystal spectrometer on shot z817. The data correspond to frames that span times from $92.0 \pm 0.55ns$ to $102.0 \pm 0.55ns$ in $2ns$ intervals on the time base in Figure 6.3. A step-wedge was used to convert the raw film data from film density units to exposure, where the step-wedge was exposed on TMAX P3200 film under the same green wavelength as the P43 phosphor used in the experiment. The lineouts in the figure have been processed by the EXRAY code (see

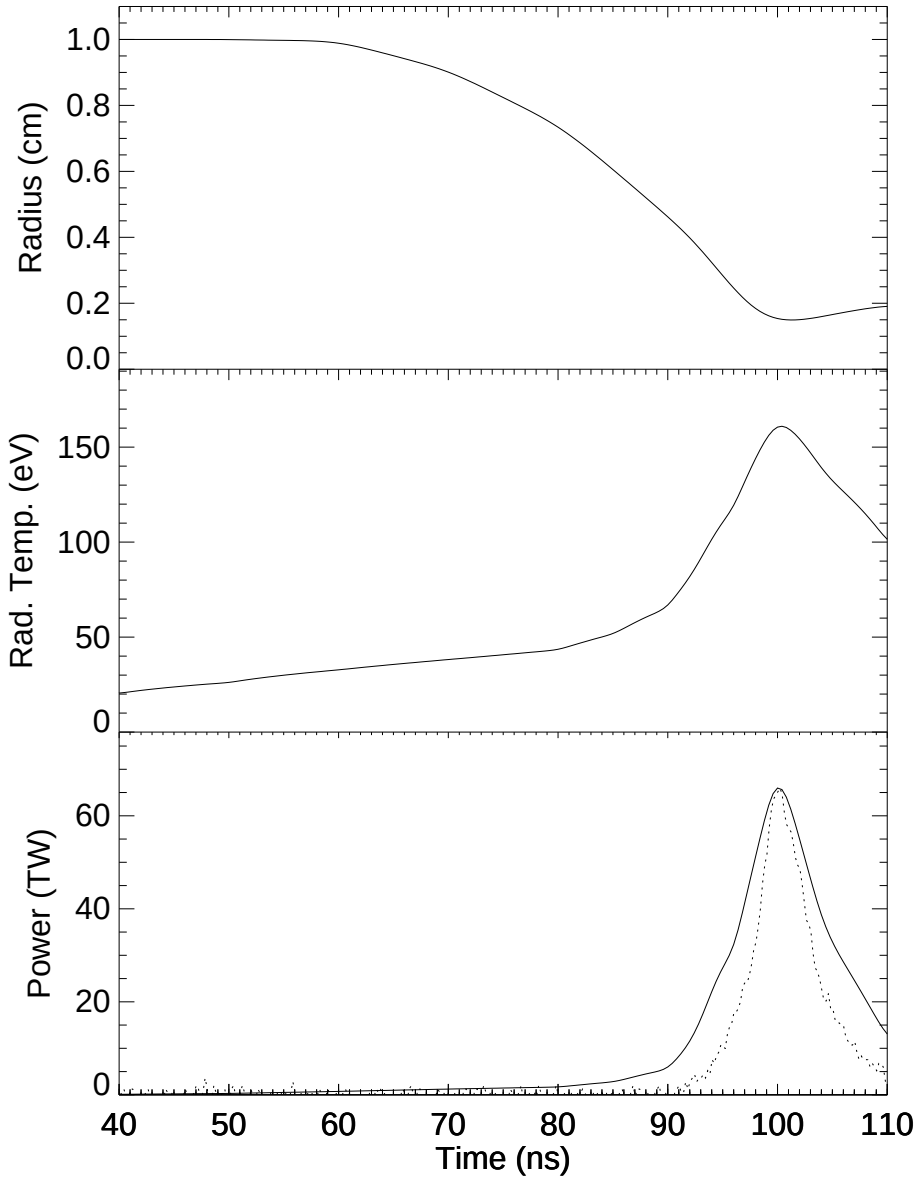

Figure 6.16: Z-pinch power, temperature, and radius profiles for shot z874 on Z. The power is measured by a kimfol filtered XRD normalized to bolometer measurements of the total radiated energy. The radii are taken from calculations at times $< 93ns$, and from self-emission on similar shots for times $\geq 93ns$. The temperature is calculated from the power and radius profiles assuming the z-pinch is a uniform cylindrical surface emitter. Also shown in this figure is the time-history of the x-ray emission in the spectral range $2.5\text{Å} < \lambda < 12.4\text{Å}$ as normalized to the peak of the total z-pinch power (dotted).

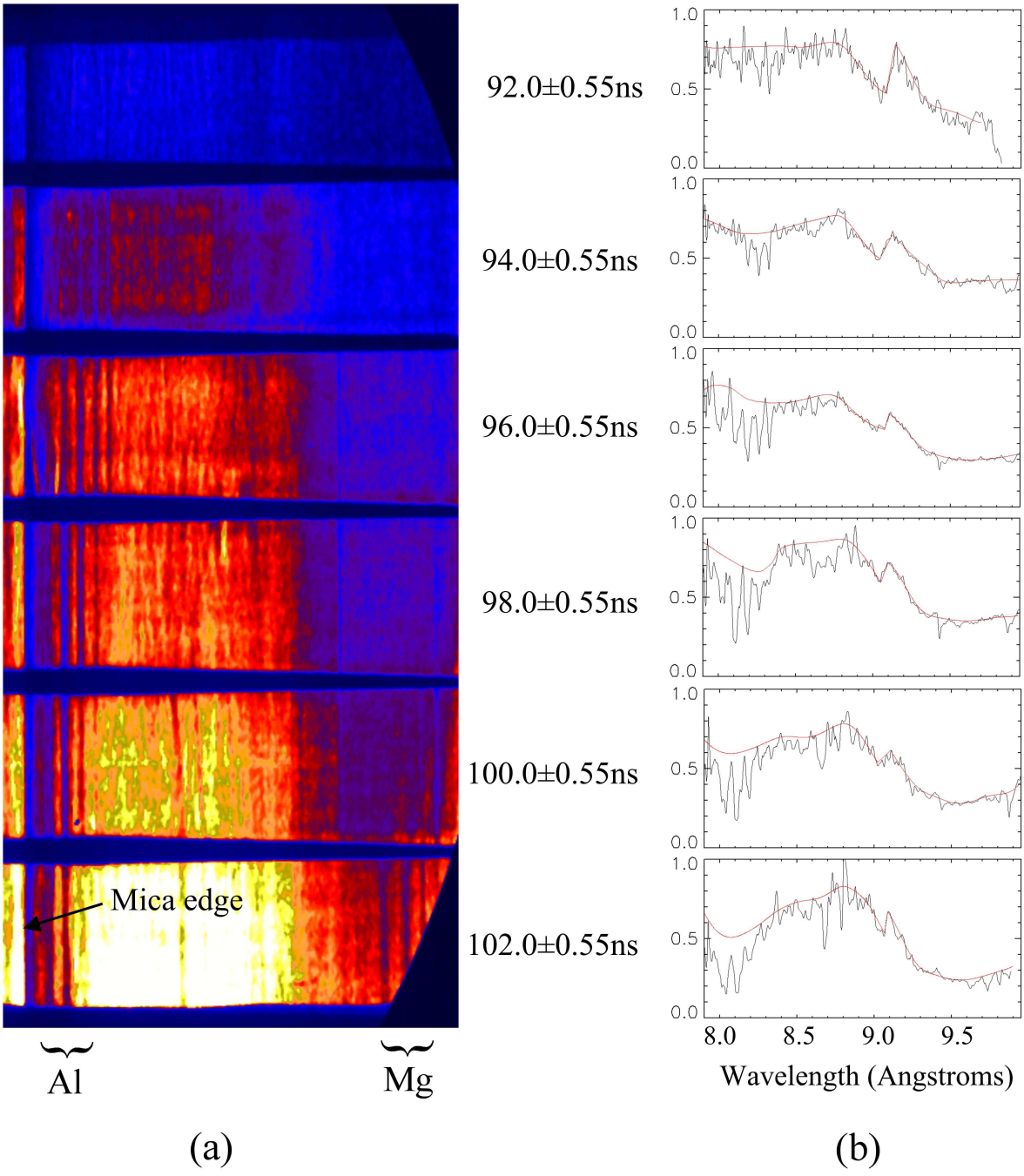

Figure 6.17: **(a)** Raw film data and **(b)** normalized spectral lineouts from the TREX on shot z874. The lineouts have been processed for the film response, filter transmission, crystal reflectivity, and the crystal geometry.

Appendix A) to determine the wavelength scale, and to apply the appropriate corrections for the filter transmission, crystal reflectivity, and the crystal geometry.

One area of complication experienced in the data reduction process was in applying the appropriate crystal reflectivity corrections. As seen in Figure 6.17(a), there is an absorption edge in the Mica crystal at $\lambda \approx 7.8$Å corresponding to the Al constituent in Mica ($\approx 14\%$ by number). This edge is not well defined by published models of the reflectivity [7], but occurs in a critical spectral location for understanding the Al absorption features. To account for this edge, a three curve fit was applied to the data continuum in frame 1 ($t = 92ns$) over the range $7.85\text{Å} \leq \lambda \leq 8.45\text{Å}$. This frame was used because the absorption features are the farthest away from the edge, and are relatively weak. The data (processed only by the filter and crystal geometry corrections) and resulting curve fit are shown in Figure 6.18. The fit was done by assuming a third order polynomial in the range $7.85\text{Å} \leq \lambda \leq 7.9\text{Å}$, a first order polynomial in the range $7.9\text{Å} \leq \lambda \leq 7.934\text{Å}$, and a third order polynomial in the range $7.964\text{Å} \leq \lambda \leq 8.45\text{Å}$. For each time frame, this fit was scaled by the average intensity of the data over the range of fit, and then divided into the data to remove the structure. The remainder of the data was then scaled by a constant to make a smooth transition at 7.85Å and 8.45Å.

In order to compare to the calculations of the K-α absorption spectra, the data must be converted to a relative transmission by the division of an assumed continuum. For these spectra, that continuum was determined by removing the absorption features, and filtering the remaining signal by a 0.3Å boxcar filter. The resulting continuum is overlayed on the data in Figure 6.17. The relative transmission was then calculated by dividing the measured signal by this continuum, and is shown for each of the time-frames in Figure 6.19. This is considered an acceptable procedure since the important information about the sample conditions is contained in the relative intensities of the absorption

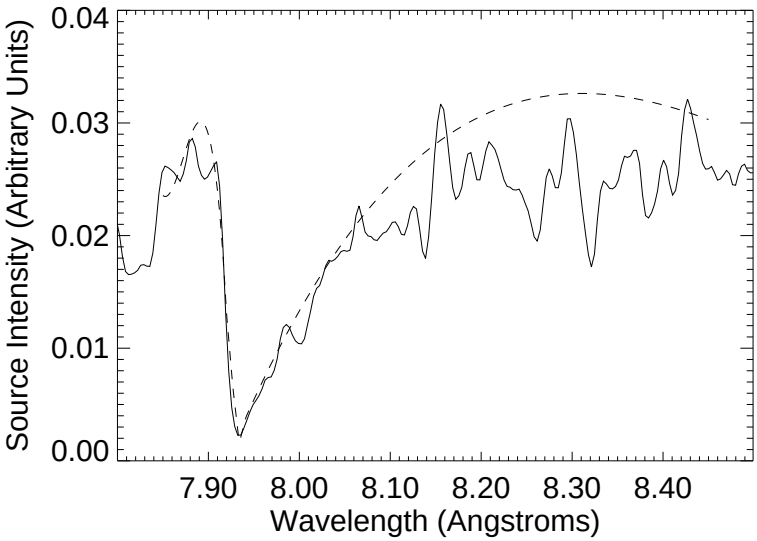

Figure 6.18: Data lineout from frame 1 in Figure 6.17(a) processed for filter transmission and crystal geometry (solid), and a 3 curve fit to the Al absorption edge in Mica (dashed).

features, which are relatively unchanged by the division of the continuum.

One interesting note regarding the continuum shown in Figure 6.17(b) is the emission/absorption feature at 9.0Å. This feature is at too short of a wavelength to be an absorption edge in Mg or F, and too long of a wavelength to be from Al. In addition, there are no known absorption edges in the Mica crystal at this wavelength. Thus, the origin of this spectral feature is unknown. The most likely origin is a macroscopic defect on the surface of the crystal, which limits the amount of radiation that hits the crystal in the range just under the 'edge'. Again, since the important information about the sample conditions is contained in the relative intensities of the absorption features that are far from the location of this feature, it should have little effect on the data analysis.

Through a statistical comparison between calculated Al and MgF_2 absorption spectra and the relative transmission spectra in Figure 6.19, the possible combinations of temperature and density in the plasma at times corresponding to each data frame and

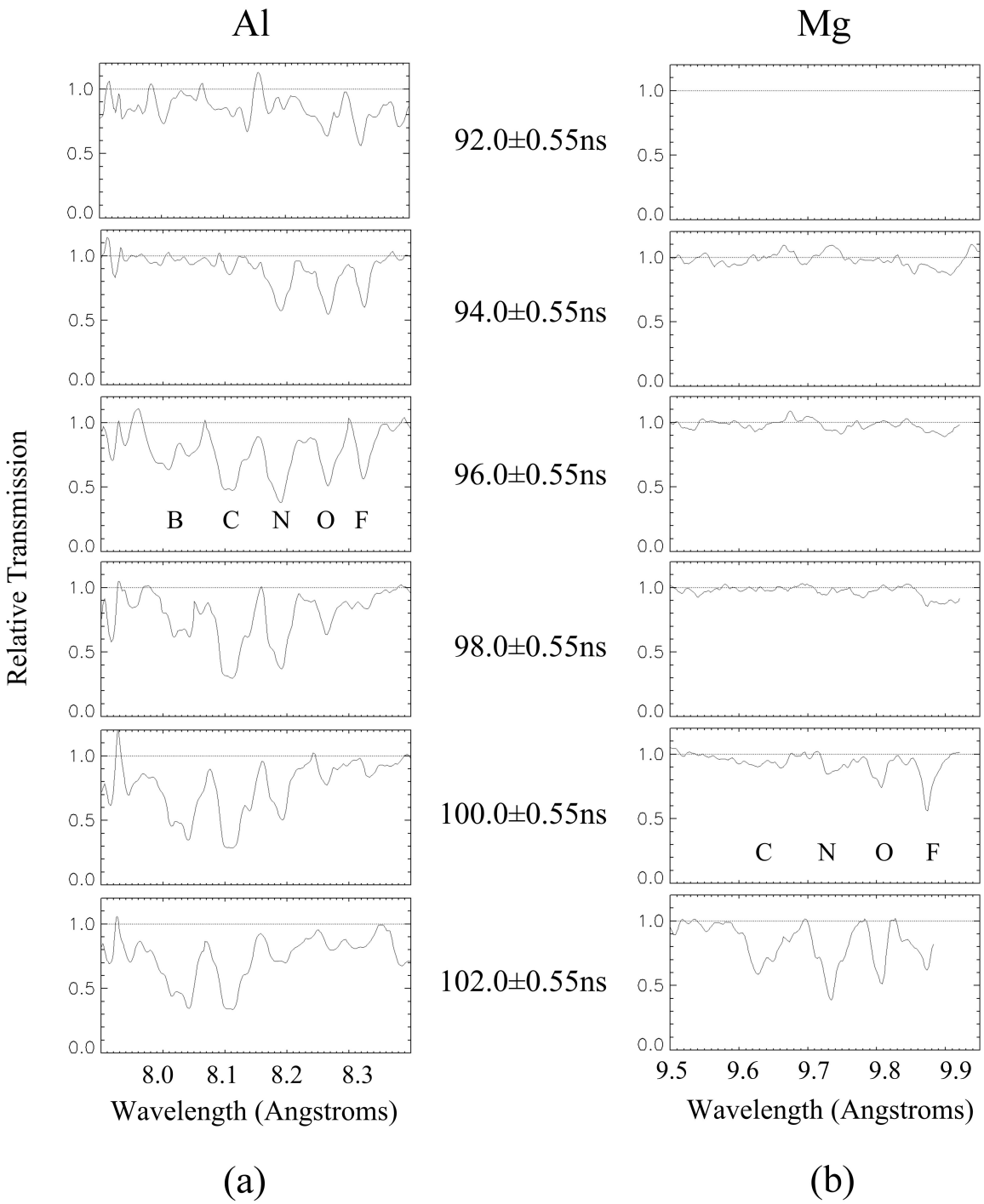

Figure 6.19: Relative transmission spectra of the **(a)** *Al* and **(b)** *Mg* K-α series from the time-resolved elliptical crystal spectrometer on shot z874.

each tracer layer can be determined by the SPECTROFIT code. Using this code, the weighted χ^2 between the unsmoothed transmission data and SPECT3D calculations was computed for 2627 combinations of temperature and density over the ranges $10eV \leq T_e \leq 80eV$ and $6 \times 10^{18} cm^{-3} \leq n_i \leq 6 \times 10^{23} cm^{-3}$ for the Al calculations, and 2220 combinations of temperature and density over the ranges $1eV \leq T_e \leq 60eV$ and $6 \times 10^{18} cm^{-3} \leq n_i \leq 6 \times 10^{23} cm^{-3}$ for the MgF_2 calculations. The statistical deviations in the intensity of each point in the data were determined by assuming Poisson statistics through the relation given in Eq. 6.1, where σ_0 was calculated over the range 9.1Å $\leq \lambda \leq$ 9.3Å. Each χ^2 comparison was then restricted to the spectral range of the Al or Mg K-α features, where the absolute depths of the measured absorption were allowed to uniformly vary by $\pm 10\%$ (see footnote (b) on page 122). The resulting χ^2 contour plots for each time frame are shown in Figure 6.20(a)-(f) for the Al spectra and Figure 6.21(a)-(f) for the Mg spectra.

As seen in Figure 6.20, the Al tracer temperature increases and/or the density decreases up to $t = 100ns$, and then the contours remain fairly constant. In contrast, Figure 6.21 shows that the MgF_2 tracer remains cold up to $t = 98ns$ and then increases in temperature and/or expands up through $t = 102ns$. For the Mg absorption data, the data in frame 1 ($t = 92 \pm 0.55ns$) was too weak and erratic for a meaningfull χ^2 calculation. The data in frames 2 and 3 could be fit to calculated Mg absorption features even though no K-α features are observable in the data (since the lack of absorption is also a usefull diagnostic[c]). The data in frame 4 showed a strange dip around the F-like Mg K-α line, which the χ^2 fitting took to fit better in the presence of the calculated F-like K-α line. SPECTROFIT therefore found a closed $+1\sigma$ contour around $T_e \approx 6 - 10eV$. This

[c]note that the minimum χ^2 for these comparisons is very close to 1, which provides confidence in the calculated standard deviations in the data.

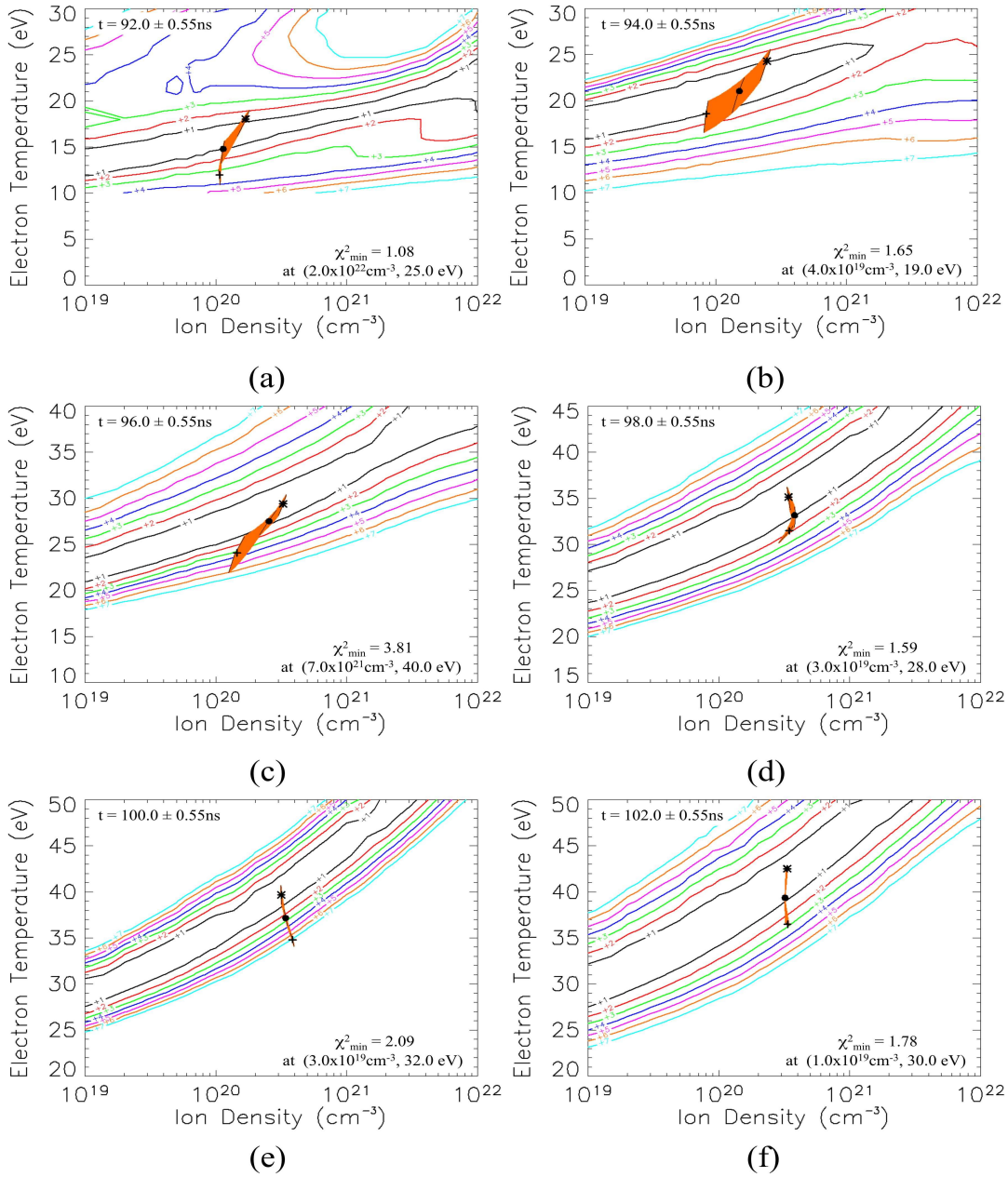

Figure 6.20: Contour plots from the SPECTROFIT χ^2 comparisons between the *Al* data from shot z874 and calculations of the *Al* K-α absorption features at times of **(a)** $92.0 \pm 0.55ns$, **(b)** $94.0 \pm 0.55ns$, **(c)** $96.0 \pm 0.55ns$, **(d)** $98.0 \pm 0.55ns$,**(e)** $100.0 \pm 0.55ns$, and **(f)** $102.0 \pm 0.55ns$. The symbols correspond to simulated mass- and time-averaged conditions in the tracer across each time frame assuming z-pinch emission powers of 80% (cross), 100% (dot), and 120% (star) of the measured value. The orange shaded regions correspond to the mass-averaged range of these simulations over each time-frame.

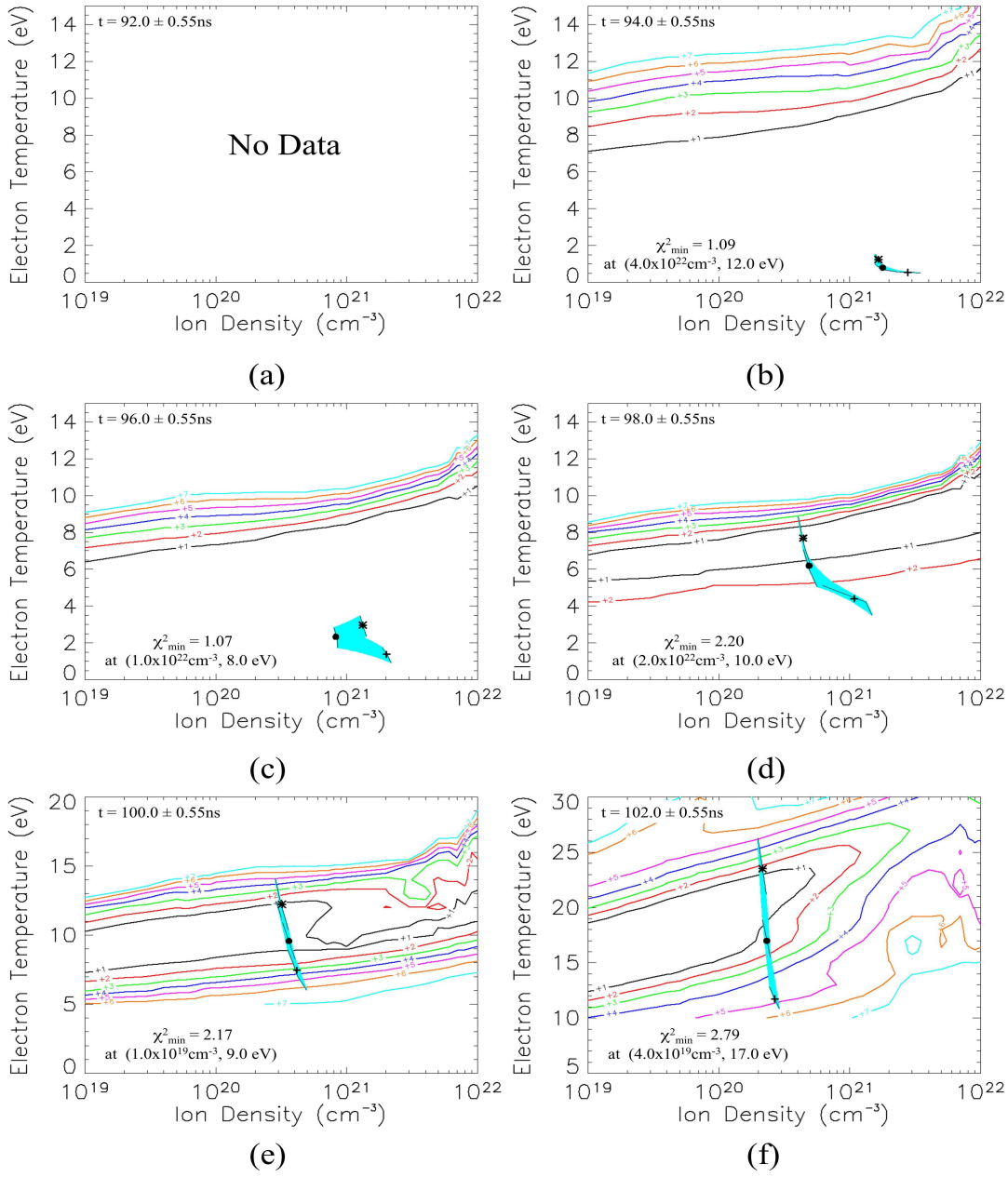

Figure 6.21: Contour plots from the SPECTROFIT χ^2 comparisons between the MgF_2 data from shot z874 and calculations of the Mg K-α absorption features in a MgF_2 plasma at times of **(a)** $92.0 \pm 0.55ns$, **(b)** $94.0 \pm 0.55ns$, **(c)** $96.0 \pm 0.55ns$, **(d)** $98.0 \pm 0.55ns$,**(e)** $100.0 \pm 0.55ns$, and **(f)** $102.0 \pm 0.55ns$. The symbols correspond to simulated mass- and time-averaged conditions in the tracer across each time frame assuming z-pinch emission powers of 80% (cross), 100% (dot), and 120% (star) of the measured value. The blue shaded regions correspond to the mass-averaged range of these simulations over each time-frame.

may simply be an artifact in the data, and should not be given a great deal of weight.

To better relate the Al conditions to those in the MgF_2, the $+1\sigma$ contour for each tracer are plotted together for each time frame in Figure 6.22(a)-(f). As one might expect, the MgF_2 tracer, which is $0.838mm$ deeper into the CH_2 foam, remains colder than the Al tracer at all times, and it takes longer to heat-up.

6.2.3 Experiment Modeling

The experiment described in §6.2.1-6.2.2 was modeled using the procedure described in Chapter 4. As described in that chapter, the first step in simulating the dynamics of the experiment requires a calculation of the time- and frequency-dependent radiation drive on the sample surface. These calculations were done using the VISRAD view-factor code. An example of the 3-D VISRAD grid for the geometry described in §6.2.1 is shown in Figure 6.23. In this model, the z-pinch radius and power histories from Figure 6.16 were input as the power source (shown in red on Figure 6.23), and an independent view-factor calculation was conducted for 31 time-steps over the range $0ns \leq t \leq 110ns$. It took 5 iterations on these view-factor calculations for the albedos to stabilize, and the resulting drive power on the sample to converge within 1% on 2 successive iterations (as described in §4.1).

The resulting albedos of the the outer anode, z-pinch glideplanes, and the primary hohlraum (as labeled in Figure 6.23) are shown in Figure 6.24(a), and the final drive power on the sample surface is shown in Figure 6.24(b). This drive history was calculated for the nominal (measured) z-pinch power, and reaches a peak radiation power of $0.97TW$. At the time of peak z-pinch emission ($t = 100ns$), the driving radiation spectrum peaks at $310eV$, and has an average energy of $537eV$. At this time, the contributions to the drive flux from each of the major objects in the view-factor grid were calculated to be;

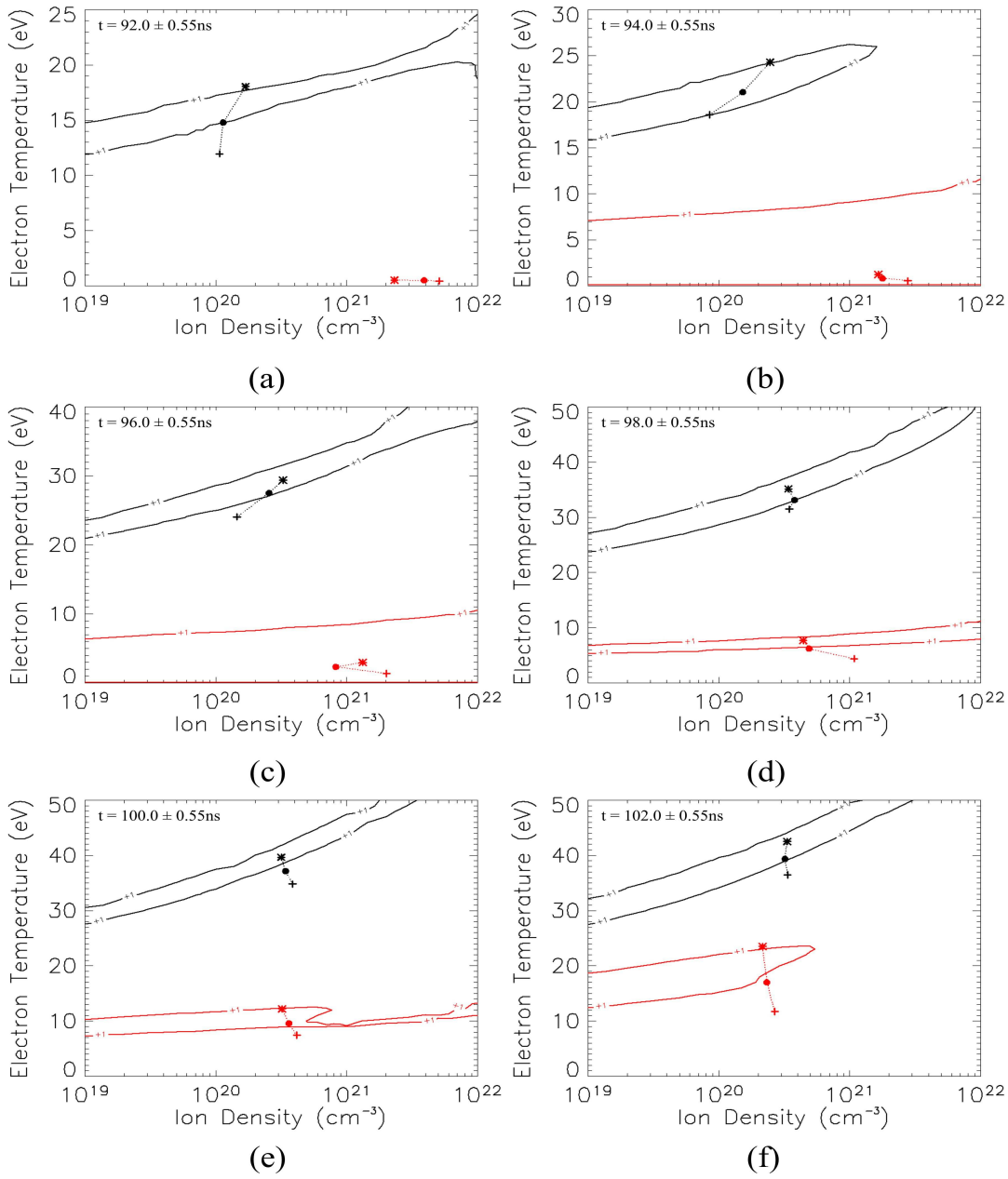

Figure 6.22: $+1\sigma$ contours from the SPECTROFIT χ^2 comparisons between the Al (black) and MgF_2 (red) data from shot z874 and calculations of the K-α absorption features at times of **(a)** $92.0 \pm 0.55ns$, **(b)** $94.0 \pm 0.55ns$, **(c)** $96.0 \pm 0.55ns$, **(d)** $98.0 \pm 0.55ns$,**(e)** $100.0 \pm 0.55ns$, and **(f)** $102.0 \pm 0.55ns$. The points correspond to mass- and time-averaged plasma conditions from BUCKY rad-hydro calculations assuming z-pinch emission powers of 80% (cross), 100% (dot), and 120% (star) of the measured value.

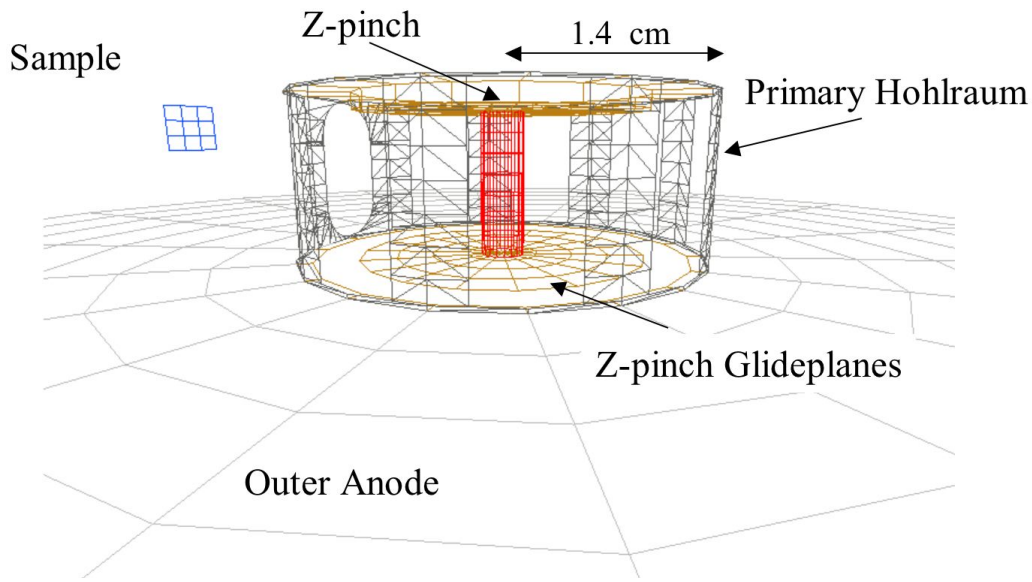

Figure 6.23: Calculational grid for the VISRAD view-factor model of shot z874 at the time of peak z-pinch power.

74% from the z-pinch, 12% from the bottom glide-plane, 8% from the outer anode, and 6% from the primary hohlraum wall.

The drive history from Figure 6.24(b) was applied as a time- and frequency-dependent radiation boundary condition in radiation-hydrodynamics calculations of the sample response. These simulations were done with the BUCKY 1-D Lagrangian rad-hydro code using multi-angle short-characteristics radiation transport for 500 log-spaced photon energy groups from $0.1 - 10^4 eV$. The opacities of each material were calculated from PROPACEOS tables that contained 39 temperature points from $0.1 - 100eV$, and 41 log-spaced density points from $10^{19} - 10^{23} cm^{-3}$. The equation-of-state for the CH_2, CH, and Al materials were taken from the SESAME EOS tables and those for the MgF_2 were taken from QEOS calculations. The rad-hydro models were begun at $t = 0ns$, and ended at a time of $110ns$ using a quiet-start vaporization model set at a temperature of $0.4eV$. These calculations (including the view-factor simulations) were then repeated for

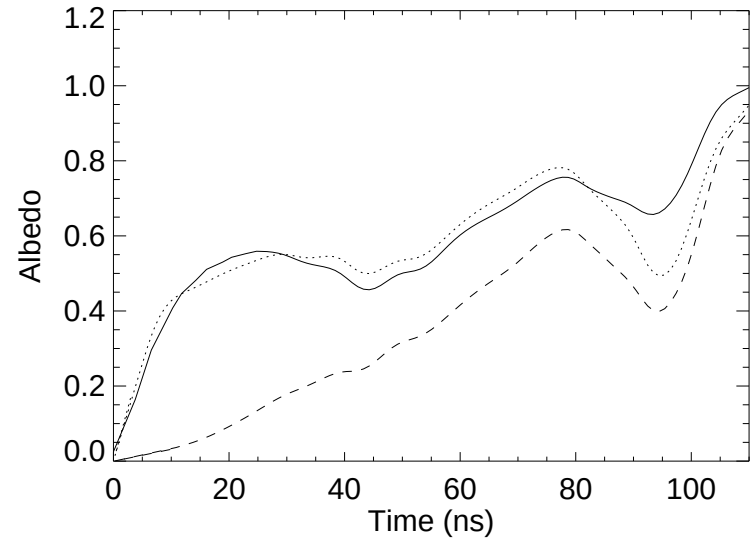

(a)

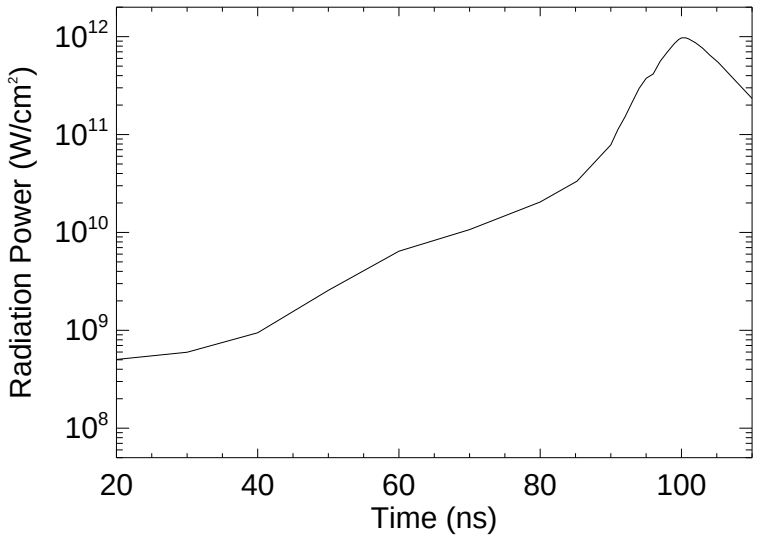

(b)

Figure 6.24: **(a)** BUCKY calculated albedo histories used for the final view factor calculations of shot z874. The albedos are shown for the pinch glideplanes (solid), the primary hohlraum (dotted), and the outer anode (dashed). **(b)** VISRAD modeled radiation power history on the surface of the foam sample on shot z874.

each sample assuming the z-pinch power was 20% lower and then 20% higher than the measured value. This was done to account for the uncertainty in the z-pinch power measurements, which were shown in §4.1 to be the dominant uncertainty in the calculated radiation drive.

The mass-averaged temperature-density phase space of the calculated conditions in the Al foil are shown on the χ^2 contour plots in Figures 6.20(a)-(f) over the times corresponding to each data frame. Likewise, The mass-averaged temperature-density phase space of the calculated conditions in the MgF_2 foil are shown on the χ^2 contour plots in Figures 6.21(a)-(f). These calculations are shown as a shaded region corresponding to the calculated conditions assuming the pinch power ranged from $80 - 120\%$ of the nominal value. The calculations are shown in this way because it provides a quick visual way to compare to the data. If the calculated conditions are going to be a good approximation to those observed in the experiment, then part of the shaded region must fall within the $+1\sigma$ contours. This can be further constrained by calculating the conditions in the foils averaged over the time in the data frame as weighted by the backlighter and micro-channel-plate pulse histories. These points are over-plotted on each contour plot and the $+1\sigma$ contour plots in Figures 6.22(a)-(f) as a symbol corresponding to assumed pinch powers of; 80%, 100%, and 120% of the nominal value. Since the data recorded on the spectrometers are truly a measure of the mass- and time-averaged conditions over each time-frame, then these points are the best diagnostic of the comparison between the data and the rad-hydro models.

The plots in Figures 6.22(a)-(f) represent a significant improvement in the experimental constraints over those from the experiment on shot z817. Namely, if the calculations are going to be a good representation of the experimental conditions, they must simultaneously reproduce the spectral features in two different tracers at two separate locations

within the experimental sample. In addition, there are six time-frames over the z-pinch pulse that this comparison can be made, five of which contain useful data in both the Al and MgF_2. As seen in Figure 6.22, the data from each of these time-frames and each of these tracers can be represented within 1σ by the rad-hydro calculations for z-pinch powers that range somewhere between $100 - 120\%$ of the nominal values.

With these constraints in place, the models can be used to investigate the dynamics happening in the sample. Figure 6.25 shows the time history of the average temperature[d] and density in the Al and MgF_2 layers as calculated by BUCKY assuming a pinch emission power that was 10% higher than the nominal value at all times. The figure indicates that the Al slowly heats to a temperature of about $12eV$ at $t \approx 90ns$, and then increases during the main drive pulse up to a peak of about $41eV$ at a time of $103ns$. The MgF_2 stays at a very low temperature ($< 3eV$) up to a time of $96ns$, and then increases to a peak of about $33eV$ at $t \approx 107ns$ with approximately the same slope as the heating in the Al layer. Meanwhile, the density in the Al decreases to a minimum value of about $1 \times 10^{20} cm^{-3}$ at $t \approx 85 - 90ns$ and then the plasma re-compresses to a value of about $4 \times 10^{20} cm^{-3}$ at $t \approx 98ns$. The density in the MgF_2 decreases to a minimum of about $2 \times 10^{20} cm^{-3}$, and then rapidly re-compresses to a peak density of about $4 \times 10^{20} cm^{-3}$ at $t \approx 109ns$. This re-compression of the two tracer layers is due to the passage of an ablative shock front as discussed in §6.1.3.

To further investigate the details of the calculated dynamics in the CH_2 foam and each of the tracers, Figures 6.26(a) and (b) show the spatial profiles of the electron temperature and ion density in the sample at times of $92ns$, $94ns$, $96ns$, $98ns$, $100ns$, and $102ns$ (corresponding to the frames in the time-resolved data). Again, these calculations were done assuming a pinch emission power that was 10% higher than the nominal value at all

[d]The electron and ion temperatures were calculated to be close equilibrium.

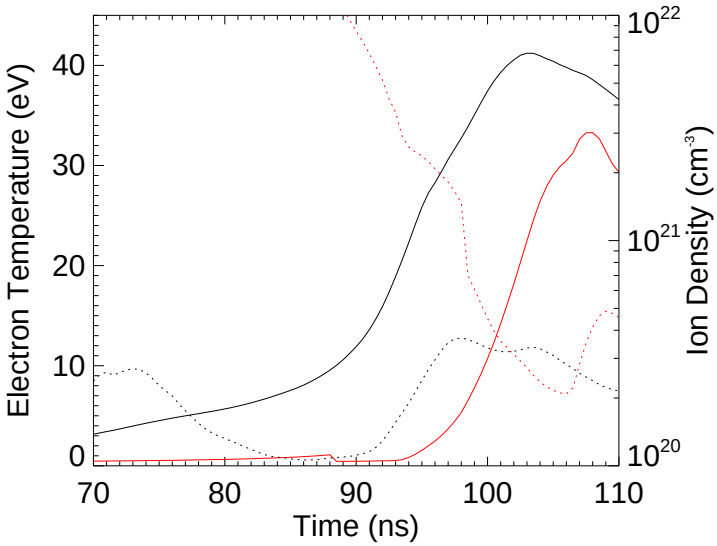

Figure 6.25: Mass averaged temperature (solid) and density (dotted) conditions in the Al (black) and MgF_2 (red) tracers on shot z874 as calculated by BUCKY.

times. The dynamics of the Al tracer are very similar to those discussed in §6.1.3. Early in time, the calculations predict a large gradient in the temperature and density of the Al ($\approx 8eV$ and $\approx 2 \times 10^{20} cm^{-3}$). At later times the temperature gradients drop to $< 2eV$, and almost no gradient in the density. As the tracer heats up above the temperature of the surrounding CH and CH_2, it launches a shock wave into each material, which propagate away from the Al.

The MgF_2 layer shows a much more complicated set of features. The temperature profile is fairly flat and cold early in time, and then heats up to an average temperature of about $20eV$ with a $\approx 10eV$ gradient at $t = 102ns$. The density of the MgF_2 shows a strong discontinuity early in time as the tracer tries to expand against the cold CH_2 foam in front of it and the CH substrate behind it. This expansion launches a shock wave in each material, which propagates away from the MgF_2 tracer. As in the case of the Al tracer both in this experiment and on shot z817, the MgF_2 heats to higher temperatures

than the CH_2 foam directly in front of it.

To better visualize the important hydrodynamics, Figure 6.27 shows the time-dependent mass contours calculated by BUCKY for the experiment on shot z874. The Al layer expands primarily into the lower density CH_2 foam in front of it, and is seen to have already started expanding by $t = 70ns$. This expansion launches a small shock into the CH_2 foam, and pushes the CH substrate toward the back of the sample. In contrast, the MgF_2 layer does not begin to move until about $88ns$, at which time it also expands primarily into the CH_2 foam in front of it. In doing so, however, the pressure in the colder CH_2 foam and CH substrate resist, which launches a shock in the MgF_2 layer (that was seen in the density discontinuity in Figure 6.26(b)). At a time of about $87ns$, the ablatively driven shock coming from the front surface of the sample reaches the Al tracer layer, compresses it by about a factor of 4, and sweeps it toward the back of the sample. This shock front then propagates deeper into the sample, and reaches the MgF_2 layer at a time of about $106ns$. The MgF_2 is compressed by about a factor of 2, and then is also swept toward the back.

Even though the dynamics of the CH_2 sample and the embedded tracers are rather complex, the phase-space plots in Figure 6.22 indicate that the resulting conditions calculated in the Al and MgF_2 tracers are in good agreement with the recorded data. As has been discussed and demonstrated throughout this thesis, these dynamics are influenced primarily by the driving radiation and the associated transfer of that radiation through the sample. To illustrate some details of the radiative transfer process, Figure 6.28(a)-(c) show calculations of the frequency dependent spectra, opacities, and net radiation heating at a few different places throughout the sample at the time of peak z-pinch power ($t = 100ns$). Figure 6.28(a) shows the radiation spectrum at the front boundary of the Al tracer, the back boundary of the Al tracer, and the front boundary of the MgF_2 tracer.

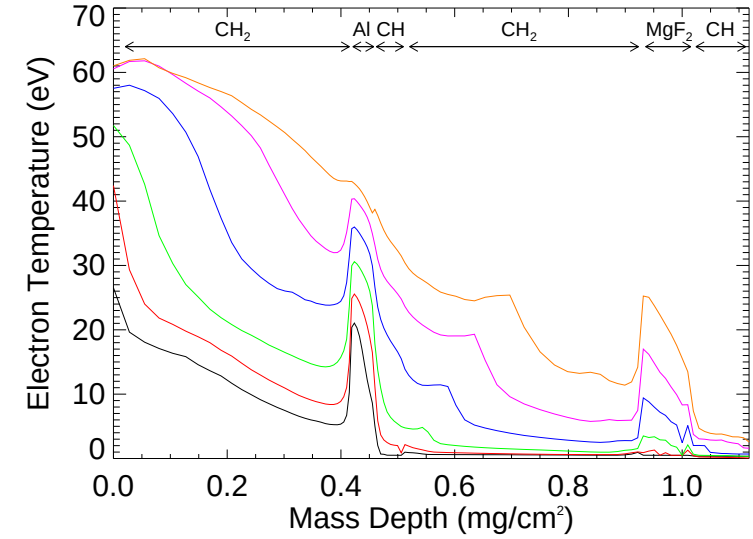

(a)

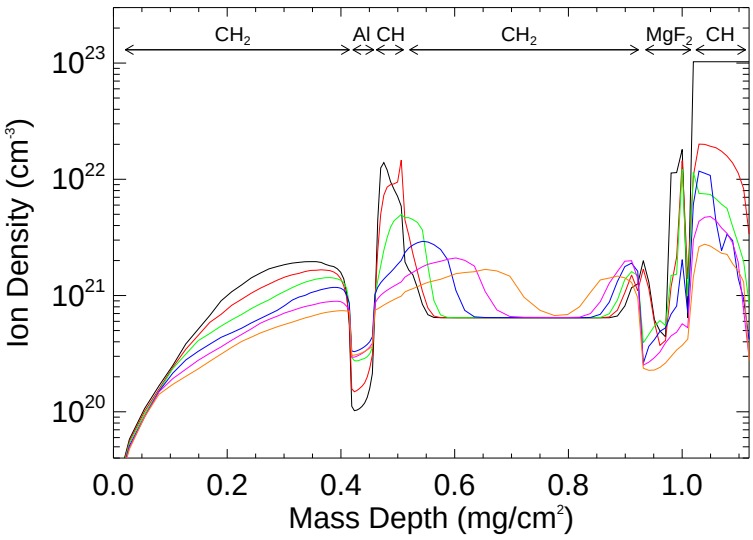

(b)

Figure 6.26: **(a)** Electron temperature and **(b)** ion density profiles in the experimental sample on shot z874 as calculated by BUCKY for times of 92ns (black), 94ns (red), 96ns (green), 98ns (blue), 100ns (purple), and 102ns (orange).

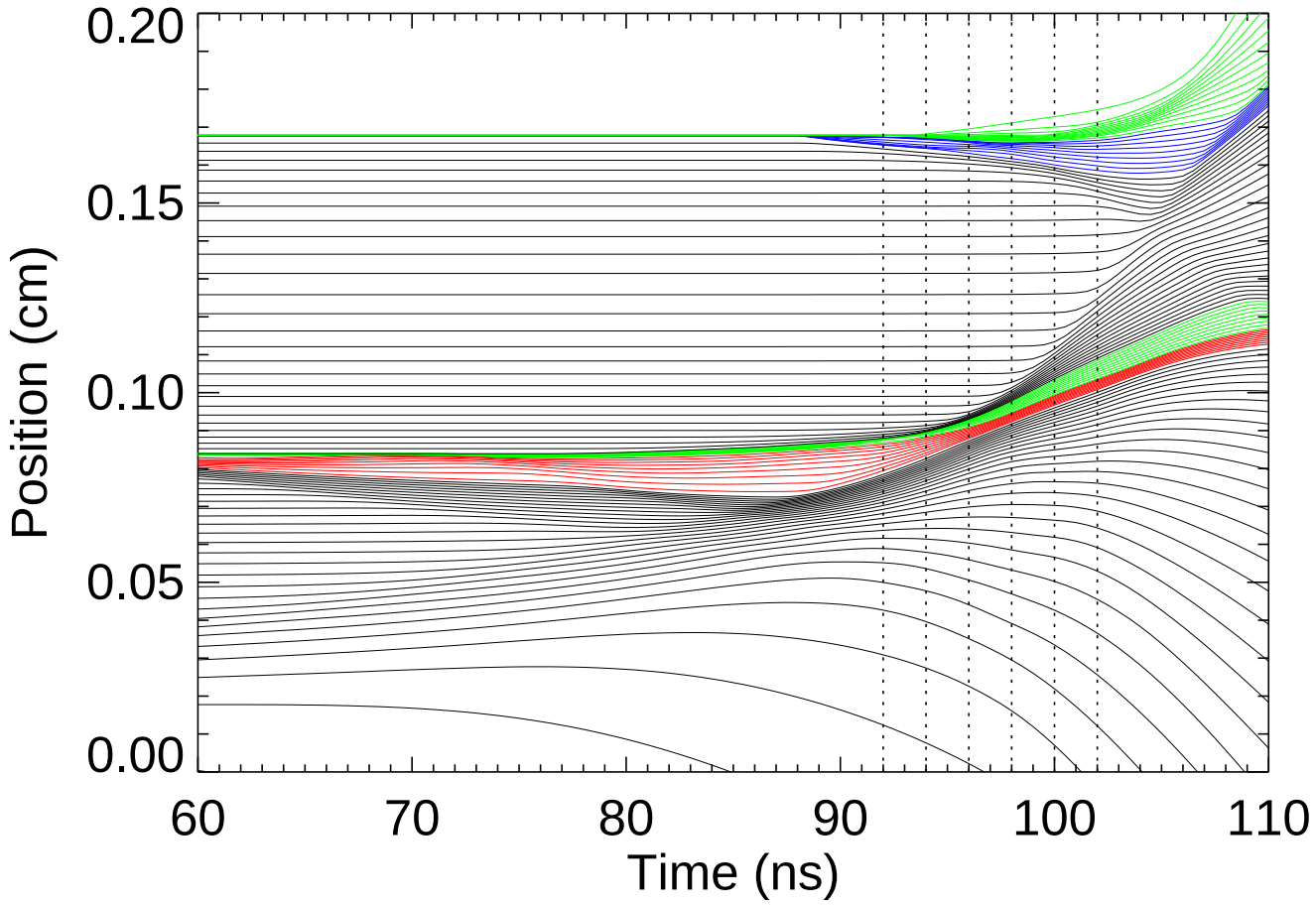

Figure 6.27: Mass contours (Lagrangian zone positions) for the CH_2 (black) foam, the Al tracer (red), the MgF_2 tracer (blue), and the CH substrates (green) as a function of time for a BUCKY calculation of the foam experiment on shot z817. The dotted lines correspond to the center of each frame in the time-resolved data.

Figure 6.28(b) shows the opacity of the CH_2 just in front of the Al and just in front of the MgF_2, as well as the Al and MgF_2 opacities at the front of each tracer. Finally, Figure 6.28(c) shows the frequency-dependent net radiation heating at the front of the Al and MgF_2 tracers.

As seen in Figure 6.28(a), the spectrum at the front boundary of the Al tracer is strongly peaked in the range $200eV < h\nu < 300eV$. As discussed in §6.1.3, these are the energies just below the carbon K-edge. The spectrum at the back of the Al tracer shows that a large fraction (over half) of the energy in this range is absorbed in the Al. The opacity plot in Figure 6.28(b) shows that this frequency range coincides with the high opacity of the Al L-shell bound-free absorption edge. This absorption is further clarified in Figure 6.28(c), which shows that the majority of the radiation heating in the Al tracer occurs in the range $200eV < h\nu < 300eV$. In contrast, the spectrum at the front of the MgF_2 tracer has a much lower fraction of the total energy below the carbon K-edge, and a majority of the energy in the range $800eV < h\nu < 2000eV$. However, Figure 6.28(c) shows that the majority of the radiation heating in the MgF_2 still occurs in the range $200eV < h\nu < 300eV$, corresponding to the bound-free opacity just above the L-shell of Mg. This implies that the heating in the MgF_2 is most sensitive to the opacity of the CH_2 in the region just below the carbon K-edge. As seen in Figure 6.28(b), the opacities of the CH_2 in this spectral range are different by a factor of 20-30 between the area in front of the Al tracer and that in front the MgF_2. This difference corresponds to the much lower temperature of the CH_2 toward the back of the sample compared to that at the location of the Al tracer. The fact that the temperatures calculated in both the Al and the the MgF_2 are in agreement with the experimental data suggests that the opacities over the range of temperatures occurring in the CH_2 are being adequately modeled (at least in the energy range $200eV < h\nu < 300eV$).

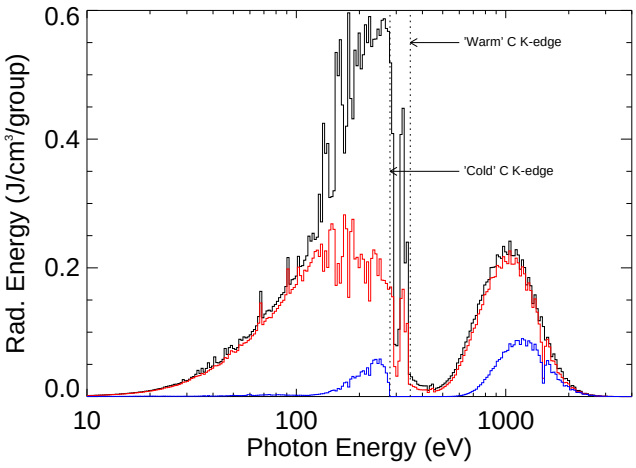

(a)

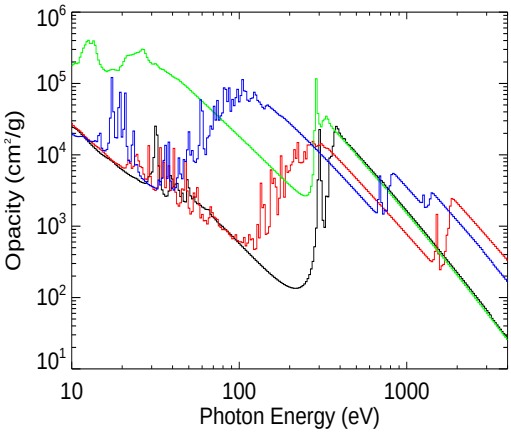

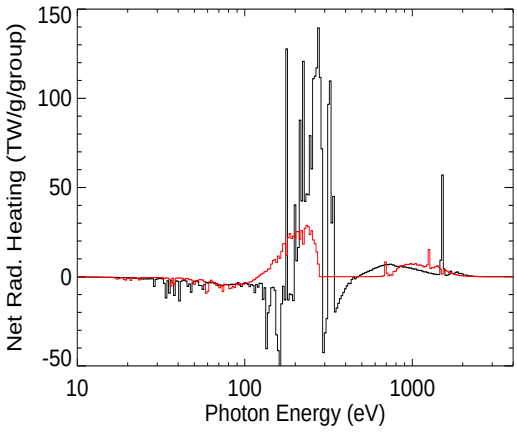

(b) **(c)**

Figure 6.28: Frequency-dependent features of the BUCKY rad-hydro model of the experiment on shot z874 at a time of $100ns$. **(a)** Multi-group radiation energy density at the front boundary of the Al tracer (black), the back boundary of the Al tracer (red), and the front boundary of the MgF_2 tracer (blue). **(b)** Multi-group CH_2 opacity just in front of the Al (black) and just in front of the MgF_2 (green) along with the Al (red) and MgF_2 (blue) opacities at the front of each tracer. **(c)** Multi-group net radiation heating at the front of the Al (black) and MgF_2 (red) tracers.

As a final check on the comparison between the calculated Al and MgF_2 conditions and those recorded in the experiment, Figure 6.29 shows the time-resolved absorption spectra on shot z874 overlaid by the spectra calculated from the radiation-hydrodynamics model assuming a 10% increase in the z-pinch emission powers over the nominal values. The calculations are done with the SPECT3D spectral post-processing code using a detailed configuration analysis (DCA) of the Al and MgF_2 at the temperatures and densities dictated by the rad-hydro calculation. Each spectrum is calculated under an assumption of LTE, and is averaged over the times corresponding to the data as weighted by the time-dependent intensity of the backlighter and the micro-channel-plate pulse history.

First consider the Al K-α spectra. As seen in the figures, the measured and calculated spectra are in fair agreement. With the exception of frame 1, each spectrum is calculated to be within 1σ of the minimum χ^2 found in the SPECTROFIT analysis. Moreover, frames 2, 3, and 4 were found to have a χ^2 value that was less than the minimum. This is due to temperature and density gradients in the tracers that are accounted for in the rad-hydro model, but not in the SPECTROFIT analysis. The χ^2 between the calculated and measured spectra in frame 1 was found to be 2.18 compared to the minimum of 1.08. This is just outside the 1σ level, but is considered a reasonable fit given the low signal level and erratic 'absorption' features in that frame.

The comparison between the calculated and measured Mg K-α spectra is also quite good. The χ^2 between the spectra in each frame was calculated to be within 1σ of the minimum found in the SPECTROFIT analysis. In this case, both frames 5 and 6 were found to have a χ^2 that was less than the minimum. Again, this is due to gradients in the temperature and density in the MgF_2 tracer that are not accounted for in the SPECTROFIT analysis.

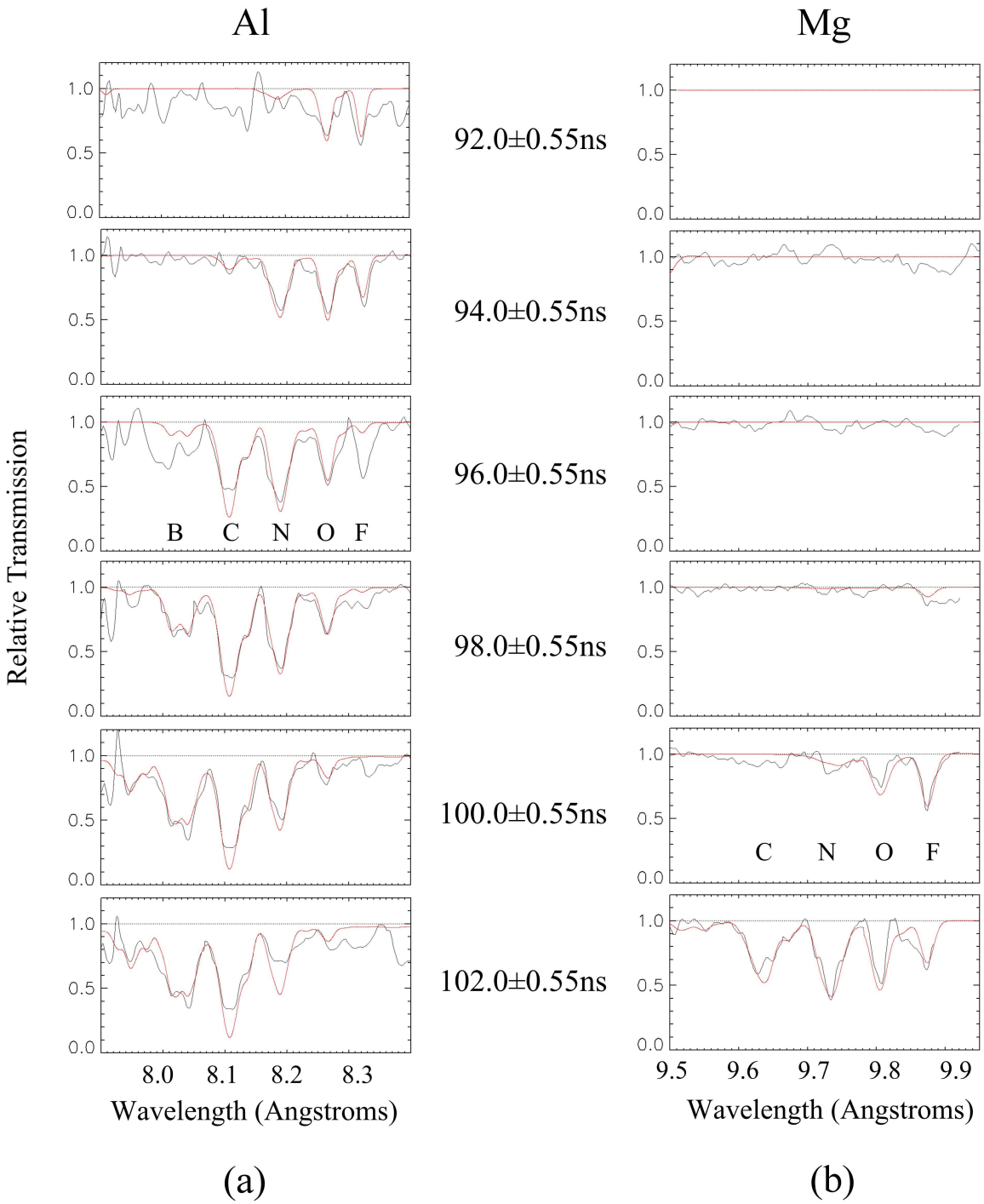

Figure 6.29: Comparison between the SPECT3D calculated relative transmission spectra (red) and the time-resolved data from shot z874 in the **(a)** Al and **(b)** MgF_2 tracers.

Therefore, given the uncertainties in the data and the calculations, the comparisons in Figures 6.22 and 6.13 demonstrate that the experimental data from shot z874 in both the Al and MgF_2 can be adequately reproduced by the computational methods and associated data tables as applied in this section.

6.3 Measurements of Multiple MgF_2 Tracers

6.3.1 Experiment Configuration

The third experiment on the radiative transfer in CH_2 foam measured the time-dependent absorption spectra of MgF_2 tracers at four different depths within three separate samples on shot z1122. Table 6.3 lists the important parameters of the experiment configuration for the quantities as defined in Figure 5.1, and Figure 6.30 shows a schematic of the foam samples. The three samples were composed of $5mg/cc$ CH_2 foam that were stepped with two different thicknesses. The steps were $8mm$ wide, $3mm$ tall, and separated by an optically thick steel bar that was $2mm$ tall. Each sample had one step that was $0.5mm$ thick ($\rho x = 0.25mg/cm^2$), and a second step that was different for each sample. This second step was $1.0mm$ thick ($\rho x = 0.5mg/cm^2$) on LOS 13/14, $1.5mm$ thick ($\rho x = 0.75mg/cm^2$) on LOS 21/22, and $2.0mm$ thick ($\rho x = 1.0mg/cm^2$) on LOS 1/2. MgF_2 tracer foils were placed on the back side of each step, and were composed of a 1010Å MgF_2 layer on the foam facing side of a $1.015\mu m$ CH substrate. The thicknesses of the tracer foils were verified by a profilometer, which was calibrated by a quartz gauge. An aperture was placed between the spectrometer and the sample to provide a $7.0mm$ wide by $10.0mm$ tall field-of-view about the center of the foam. In this case, the $4.5mm$ width of the REH in the primary hohlraum acted as the limiting aperture width.

The samples were constructed by mounting the MgF_2 tracers on a steel frame that was, $0.5mm$, $1.0mm$, or $1.5mm$ thick, and had two windows each $8mm$ wide and $3mm$ tall. The tracers were placed on the front of the bottom window and the back of the top window, each with the MgF_2 layer facing the front of the frame. A diamond-turned steel platform that was $0.5mm$ thick was used to space the foil frame from the front of a larger foam frame, and the foil frame was epoxied into place. The foam frame was then

Shot #	$r_p\,(mm)$	$h_p\,(mm)$	**Wire #**	**Wire Diam.**	$w_s\,(mm)$	$d\,(mm)$	$w_a\,(mm)$	$h_a\,(mm)$
z1122	20 outer 10 inner	12	240 outer 120 inner	$7.8\mu m$	4.8	48.0	7.0	10.0

Table 6.3: Geometric parameters and z-pinch configuration for the foam transport experiment on shot z1122. z1122 was a nested array tungsten z-pinch with a $2.5mm$ radius, $14mg/cc\ CH_2$ foam central target.

filled from the front with the $5mg/cc\ CH_2$ foam solution, which formed a stepped sample that had a differential thickness equal to the thickness of the steel foil frame. After the foam gelled and before it completely solidified, a flat scalpel was used to shear off the excess foam material to provide a flat surface along the front edge. Figure 6.31(a)-(c) show front- and back-lit pictures of the pinch facing surface of the foam sample from each LOS.

Absorption spectra through the MgF_2 tracer layers were taken by a space-resolved time-integrated convex crystal spectrometer (TIXTL) on each LOS. The spectrometers were fielded with a source-to-crystal distance of $455cm$, and a crystal-to-film distance of $7.1cm$. Each contained a potassium acid phlalate (KAP) crystal with a $2d$ spacing of 26.62Å, which were rotated to center the spectral range on a wavelength of 9.1Å. The crystals were bent to a $101.6mm$ radius on LOS 13/14 and LOS 21/22, and a $50.8mm$ radius on LOS 1/2, which provided a spectral resolution of ≈ 700 on LOS 1/2 and ≈ 850 on the other two LOS. Each was filtered between the crystal and film by $8.5\mu m$ of Be. In addition, each spectrometer had $300\mu m$ and $500\mu m$ space-resolving slits that were oriented for vertical resolution in order to provide distinct spectra from each step in the samples.

The z-pinch performance on these shots was measured by a suite of diagnostics looking through LOS other than that used by the experimental sample. The primary z-pinch

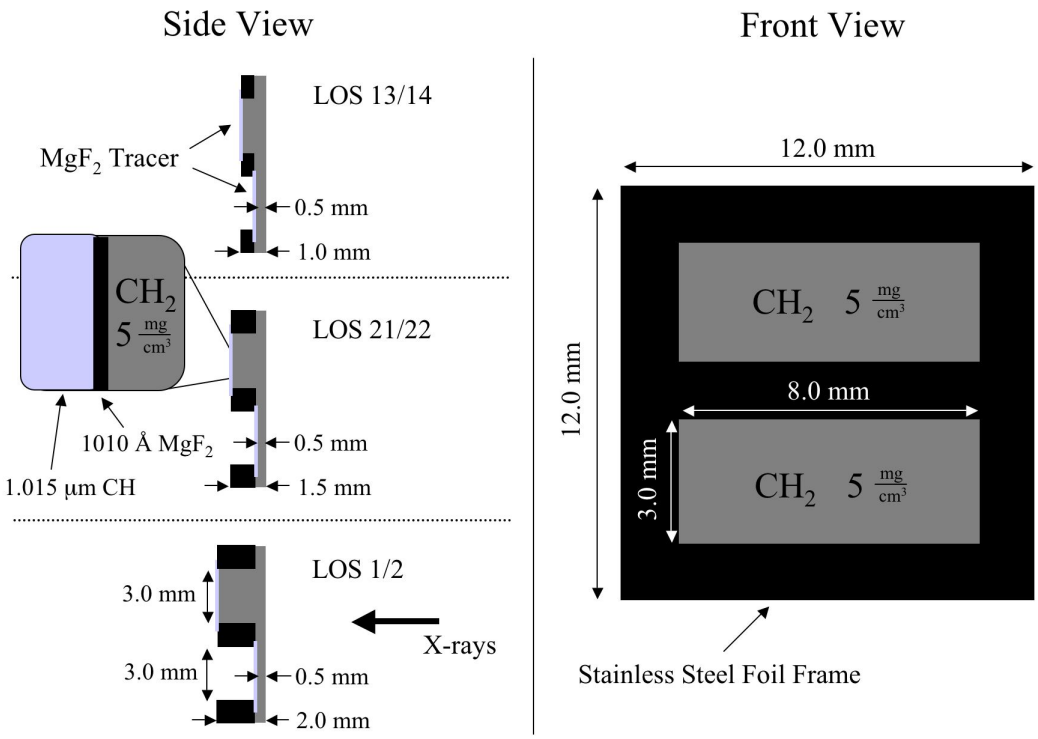

Figure 6.30: Schematic diagram of the foam sample geometry for the ride-along experiment on shot z1122.

diagnostic that was utilized for these experiments was an array of filtered x-ray diodes (XRDs), which provided the pinch power history when normalized by a bolometer viewing from the same angle on the same line-of-sight.

6.3.2 Experimental Data

Figure 6.32 shows the time-dependent z-pinch power, temperature, and radius from shot z1122 on the Z facility. The time-axis in this figure, and throughout the remainder of this section, has been shifted so that the peak of the x-ray emission power occurs at $100ns$. The powers are determined from filtered XRD measurements that have been normalized by bolometer data. According to this data, z1122 produced $745 \pm 149kJ$ in

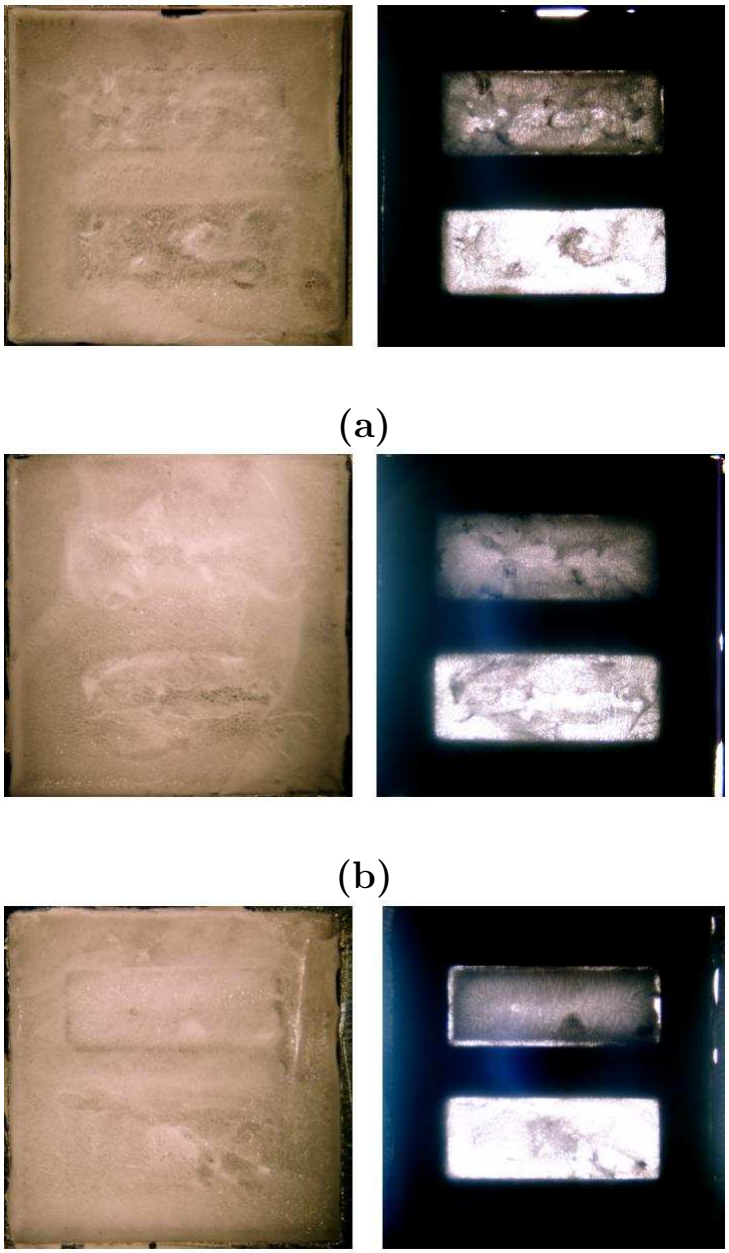

Figure 6.31: Front- and back-lit photographs of the pinch facing surface of the foams from shot z1122 on **(a)** LOS 13/14 (0.5mm step), **(b)** LOS 21/22 (1.0mm step), and **(c)** LOS 1/2 (1.5mm step).

a $3.9ns$ FWHM pulse peaked at $108 \pm 22TW$. This power pulse is very similar to that from shot z1031 discussed in Chapter 5, and the z-pinches had identical geometries and compositions. As in the case of shot z1031, the z-pinch radii from z1122 are determined from Screamer models of the implosion trajectory for times $< 93ns$, and from experimental data published by Sanford et al. [105] for similar z-pinches at times $\geq 92ns$. The temperatures were then determined from the pinch power and radius time histories by assuming that the z-pinch is a uniform cylindrical surface emitter. The backlighter time-history in the x-ray range $2.5\text{Å} < \lambda < 12.4\text{Å}$ is also shown in the figure. To illustrate the relative timing, the peak of this curve has been normalized to the peak of the total x-ray power, and indicates a backlighter time history of $100 \pm 1.5ns$.

Figure 6.33(a) and (b) show the raw film data and associated spectral lineouts as recorded by the space-resolved time-integrated convex crystal spectrometers (TIXTLs) on shot z1122. The data correspond to the foam samples on each of the three lines-of-sight. The lineouts have been processed by the EXRAY code (see Appendix A) to determine the wavelength scale, and to apply the appropriate corrections for the film response, filter transmission, crystal reflectivity (using the MDP reflectivity model), and the crystal geometry. In addition, the x-ray background has been subtracted from the data, where the background was determined by processing an unilluminated strip of the film in the same manner as the data.

As discussed above, each of the samples in this experiment contained a section that had $0.25mg/cm^2$ of $5mg/cc\ CH_2$ foam on the z-pinch facing side of the MgF_2 tracer. These served as a check on the relative radiation drive at each sample. If the samples are well manufactured and well positioned, and if the z-pinch emission power is azimuthally symmetric, then the absorption spectrum from each of these sections on each LOS should be statistically identical. The overlaid spectra from these sections of each

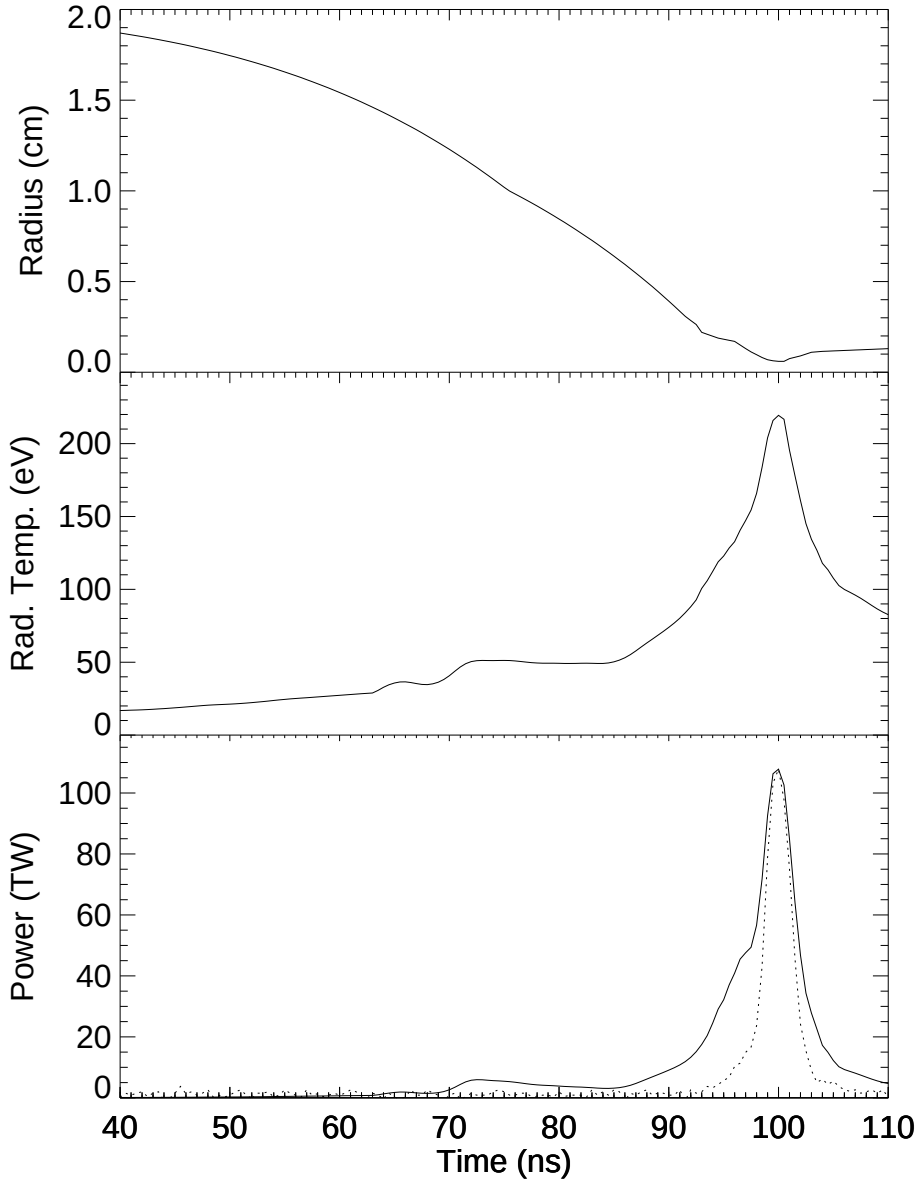

Figure 6.32: Z-pinch power, temperature, and radius profiles for shot z1122 on Z. The power is measured by a filtered XRD normalized to bolometer measurements of the total radiated energy. The radii are taken from calculations at times $< 93ns$, and from published data on similar z-pinches for times $\geq 93ns$. The temperature is calculated from the power and radius profiles assuming the z-pinch is a uniform cylindrical surface emitter. Also shown in this figure is the time-history of the x-ray emission in the spectral range $2.5\text{Å} < \lambda < 12.4\text{Å}$ as normalized to the peak of the total z-pinch power (dotted).

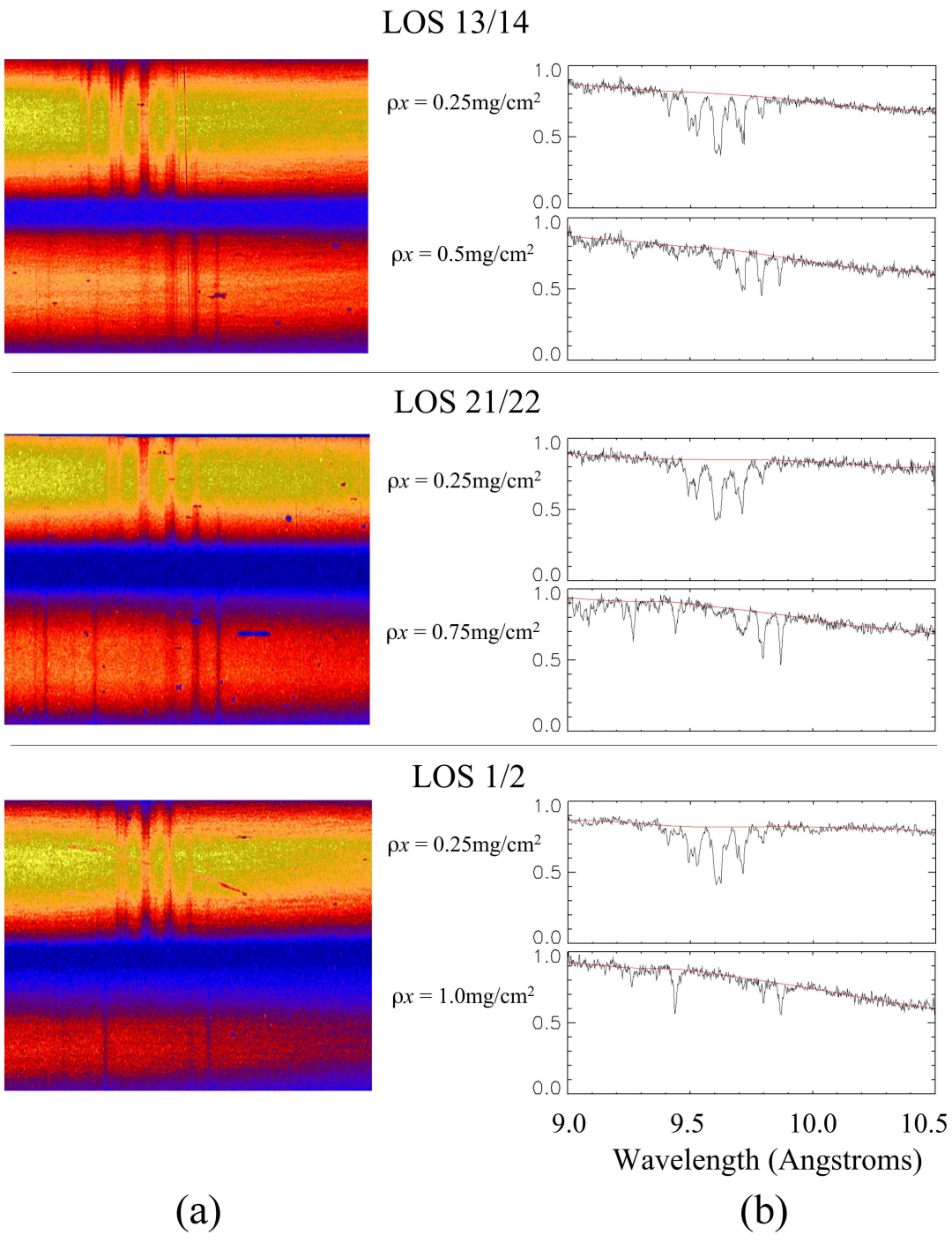

Figure 6.33: **(a)** Raw film data and **(b)** normalized spectral lineouts from the TIXTLs on shot z1122. The lineouts have been processed for the film response, filter transmission, crystal reflectivity, and the crystal geometry.

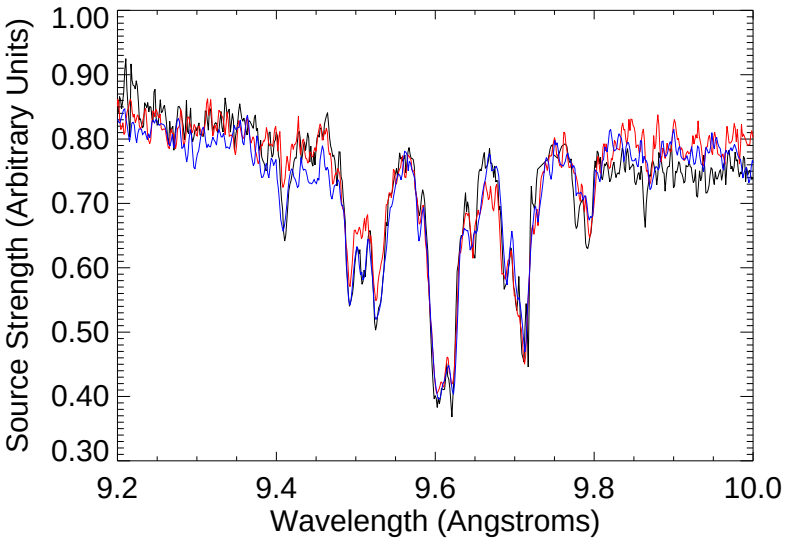

Figure 6.34: Comparison between the recorded Mg absorption spectra from LOS 13/14 (black), LOS 21/22 (red), and LOS 1/2 (blue) for the section of each foam sample that was $0.25 mg/cm^2$ thick.

sample are shown in Figure 6.34. Using the calibration data of the statistical uncertainty for RAR2497 film (as discussed in Appendix C), the maximum chi-squared value between these three spectra was determined to be 1.07. This indicates that, within the uncertainties imposed by the fluctuations in the data, these three spectra are indeed statistically identical, and the radiation drive on each sample can be assumed to be the same.

In order to compare to the calculations of the K-α absorption spectra, the data must be converted to a relative transmission by the division of an assumed continuum. For these spectra, that continuum was determined by removing the absorption features, and filtering the remaining signal by a 0.3Å boxcar filter. The resulting continuum is overlaid on the data in Figure 6.33. The relative transmission was then calculated by dividing the measured signal by this continuum, and is shown for each of the different foam thicknesses in Figure 6.35 (the data from the $0.25 mg/cm^2$ thick sample was taken from LOS 13/14). This is considered an acceptable procedure since the important information about the

sample conditions is contained in the relative intensities of the absorption features, which are relatively unchanged by the division of the continuum.

Through a statistical comparison between calculated Mg absorption spectra (in a MgF_2 plasma) and the relative transmission spectra in Figure 6.35, the possible combinations of temperature and density in the plasma at each depth of the foam can be determined by the SPECTROFIT code. Using this code, the weighted χ^2 between the unsmoothed transmission data and SPECT3D calculations was computed for 2220 combinations of temperature and density over the ranges $1eV \leq T_e \leq 60eV$ and $6 \times 10^{18} cm^{-3} \leq n_i \leq 6 \times 10^{23} cm^{-3}$. The statistical deviations in the intensity of each point in the data were determined from independent calibration experiments described in Appendix C. Each comparison was restricted to the spectral range of the K-α features and the Ne-like ($MgIII$) and F-like ($MgIV$) K-β lines[e]. During the χ^2 fitting procedure, the absolute depths of the measured absorption were allowed to uniformly vary by $\pm 10\%$ (see footnote (b) on page 122). The resulting χ^2 contour plots for each of the spectra in Figure 6.35 are shown in Figure 6.36(a)-(d), and the $+1\sigma$ contours from each are overlaid in Figure 6.37.

As one might expect, these contour plots show that the temperature of the MgF_2 tracer decreases as the amount of CH_2 foam between the tracer and the z-pinch increases. It is up to the computational models to describe how the conditions change as a function of depth.

[e]This is believed to be the first time the F-like and Ne-like K-β lines have been used as a diagnostic of the conditions in a Mg plasma.

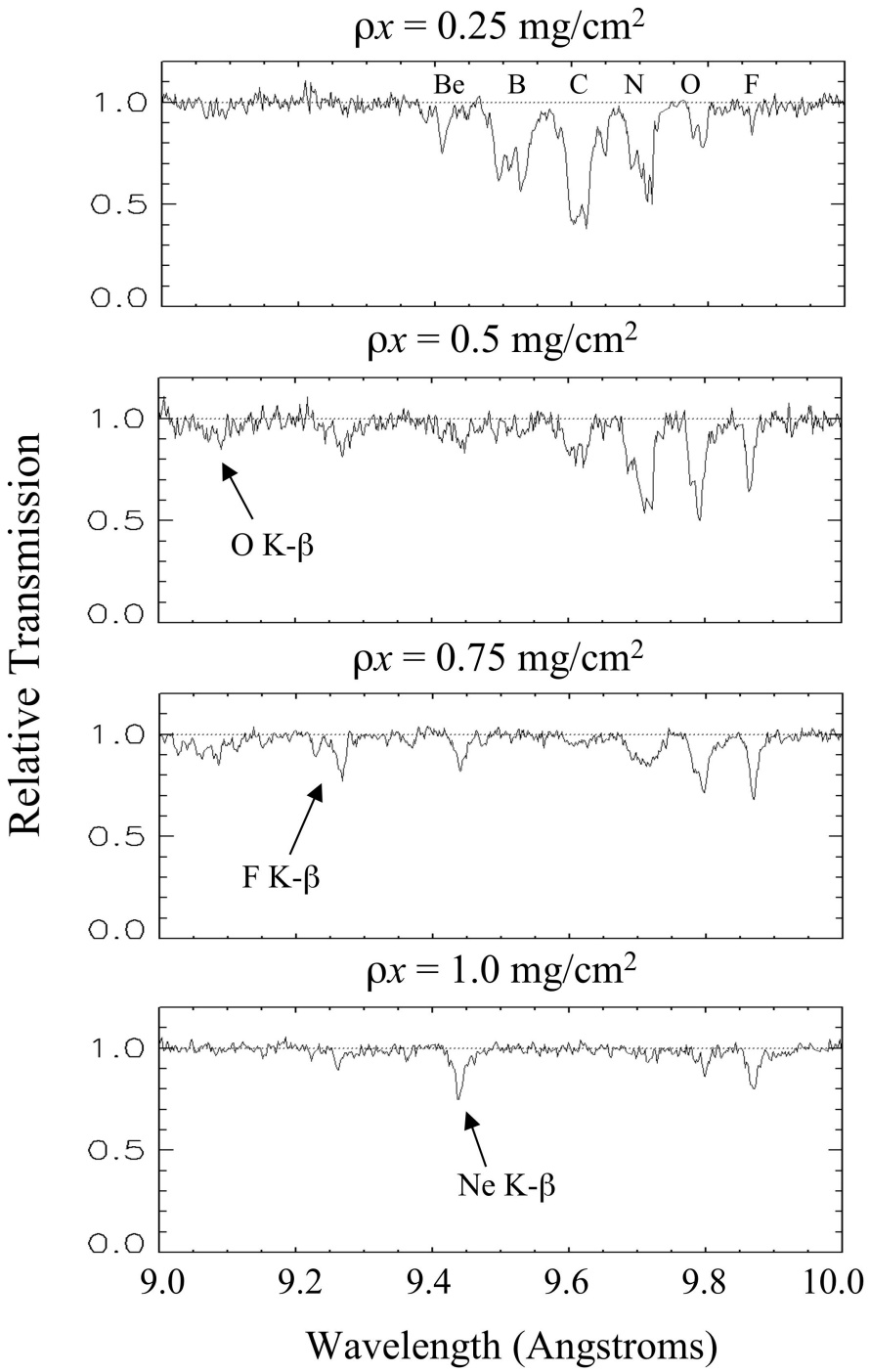

Figure 6.35: Relative transmission spectra of the Mg K-α and partial K-β series from the time-integrated convex crystal spectrometer data on shot z1122. This data is shown for foam thicknesses of $\rho x = 0.25 mg/cm^2$, $0.5 mg/cm^2$, $0.75 mg/cm^2$, and $1.0 mg/cm^2$.

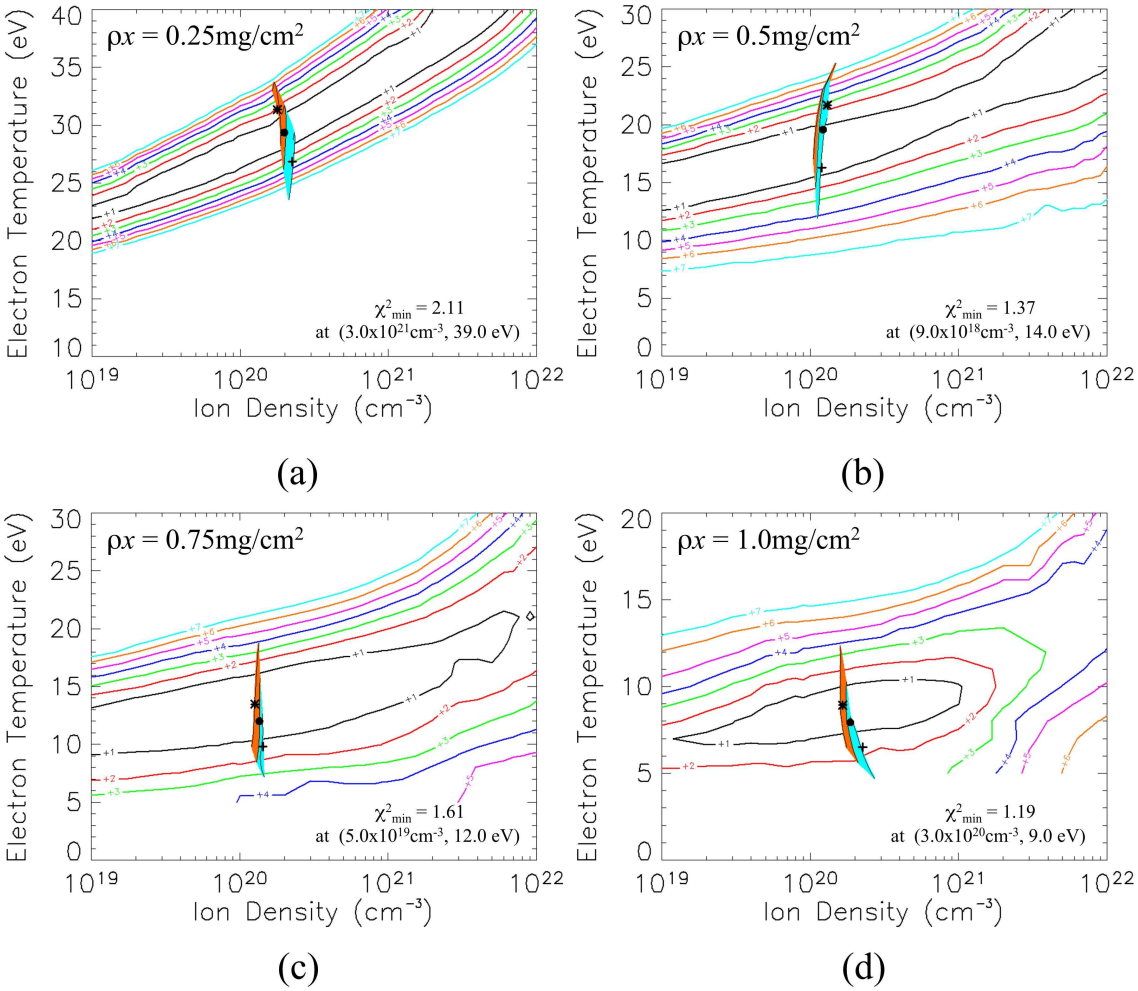

Figure 6.36: Contour plots from the SPECTROFIT χ^2 comparisons between the data from shot z1122 and calculations of the Mg K-α absorption features in a MgF_2 plasma behind a $5mg/cc\ CH_2$ foam of thickness **(a)** $0.25mg/cm^2$, **(b)** $0.5mg/cm^2$, **(c)** $0.75mg/cm^2$, and **(d)** $1.0mg/cm^2$. The shaded regions correspond to plasma conditions from BUCKY rad-hydro calculations assuming z-pinch emission powers of $80-100\%$ (blue) and $100-120\%$ (orange) of the measured value. The symbols correspond to simulated mass- and time-averaged conditions in the tracer assuming z-pinch emission powers of 80% (cross), 100% (dot), and 120% (star) of the measured value.

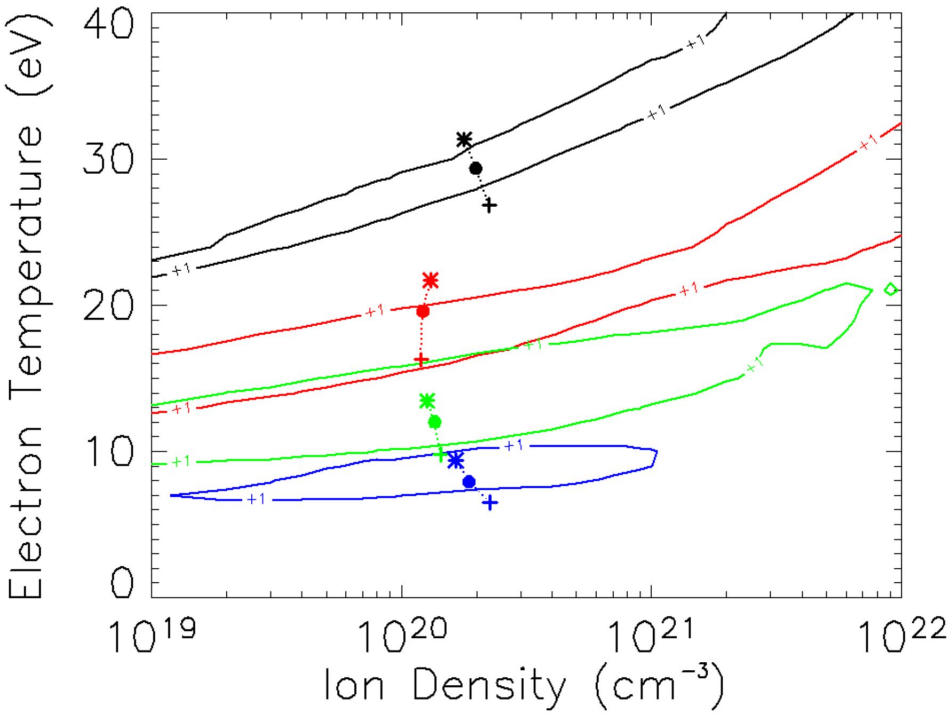

Figure 6.37: $+1\sigma$ contours from the SPECTROFIT χ^2 comparisons between the data from shot z1122 and calculations of the Mg K-α absorption features in a MgF_2 plasma behind a $5mg/cc$ CH_2 foam of thickness $0.25mg/cm^2$ (black), $0.5mg/cm^2$ (red), $0.75mg/cm^2$ (green), and $1.0mg/cm^2$ (blue). The points correspond to mass- and time-averaged plasma conditions from BUCKY rad-hydro calculations assuming z-pinch emission powers of 80% (cross), 100% (dot), and 120% (star) of the measured value.

6.3.3 Experiment Modeling

The experiment described in §6.3.1-6.3.2 was modeled using the procedure described in Chapter 4. As described in that chapter, the first step in simulating the dynamics of the experiment requires a calculation of the time- and frequency-dependent radiation drive on the sample surface. These calculations were done using the VISRAD view-factor code. An example of the 3-D VISRAD grid for the geometry described in §6.3.1 is shown in Figure 6.38. Note that there are two different samples in this grid corresponding to the two sections of each foam as described in Figure 6.30. In this model, the z-pinch radius

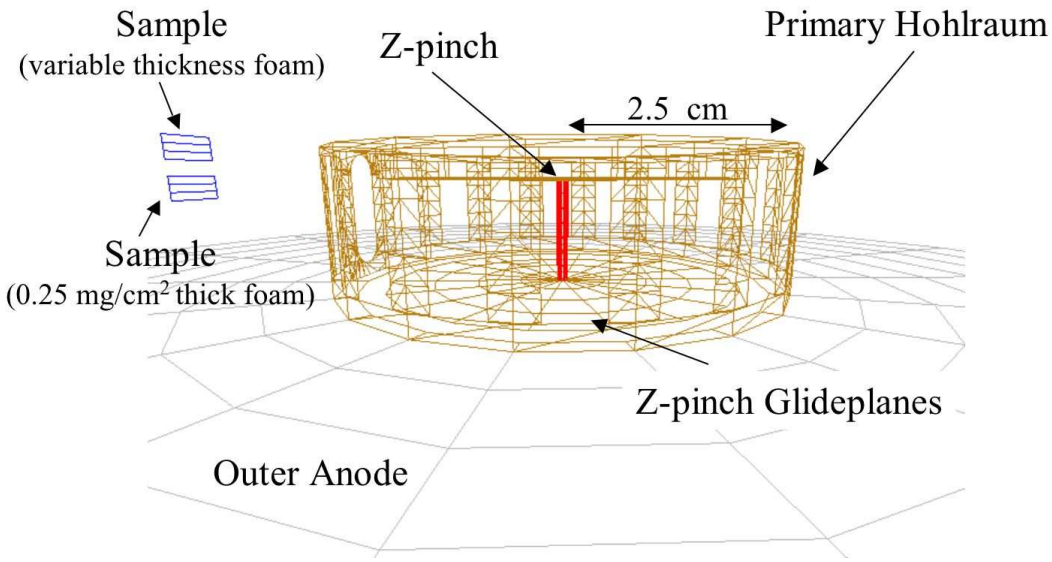

Figure 6.38: Calculational grid for the VISRAD view-factor model of shot z1122 at the time of peak z-pinch power.

and power histories from Figure 6.32 were input as the power source (shown in red on Figure 6.38), and an independent view-factor calculation was conducted for 69 time-steps over the range $0ns \leq t \leq 110ns$. It took 5 iterations on these view-factor calculations for the albedos to stabilize, and the resulting drive power on the two samples to converge within 1% on 2 successive iterations (as described in §4.1).

The resulting albedos of the the outer anode, z-pinch glideplanes, and the primary hohlraum (as labeled in Figure 6.38) are shown in Figure 6.39(a), and the final drive power on each sample surface is shown in Figure 6.39(b). This drive history was calculated for the nominal (measured) z-pinch power, and reaches a peak radiation power of $0.57TW$ on the lower sample and $0.55TW$ on the upper sample. At the time of peak z-pinch emission ($t = 100ns$), the driving radiation spectrum on each sample peaks at $290eV$, and has an average energy of $662eV$ on the lower sample and $660eV$ on the upper sample. At this time, the contributions to the drive flux on the lower sample from each of the

major objects in the view-factor grid were calculated to be; 68% from the z-pinch, 17% from the bottom glide-plane, 10% from the primary hohlraum wall, and 5% from the outer anode. The upper sample sees about 1% less from the z-pinch, and about 1% more from the lower glideplane. These calculated drive histories are assumed to be the same for each of the three foam assemblies fielded on shot z1122 (as justified in §6.3.2).

The drive histories from Figure 6.39(b) were applied as a time- and frequency-dependent radiation boundary condition in radiation-hydrodynamics calculations of the sample response. The higher drive pulse was applied to the sample that had a foam thickness of $0.25 mg/cm^2$, and the lower drive pulse was applied to the samples that had thicknesses of $0.5 mg/cm^2, 0.75 mg/cm^2$ and $1.0 mg/cm^2$. These different drive pulses were used to account for the small gradient that the view-factor model calculated to exist between the top and bottom sections of each foam assembly (the foam of variable thickness was in the top section of each assembly). These simulations were done with the BUCKY 1-D Lagrangian rad-hydro code using multi-angle short-characteristics radiation transport for 500 log-spaced photon energy groups from $0.1 - 10^4 eV$. The opacities of each material were calculated from PROPACEOS tables that contained 39 temperature points from $0.1 - 100 eV$, and 41 log-spaced density points from $10^{19} - 10^{23} cm^{-3}$. The equation-of-state for the CH_2 and CH materials were taken from the SESAME EOS tables and those for the MgF_2 were taken from QEOS calculations. The rad-hydro models were begun at $t = 0 ns$, and ended at a time of $110 ns$ using a quiet-start vaporization model set at a temperature of $0.4 eV$. These calculations (including the view-factor simulations) were then repeated for each sample assuming the z-pinch power was 20% lower and then 20% higher than the measured value. This was done to account for the uncertainty in the z-pinch power measurements, which were shown in §4.1 to be the dominant uncertainty in the calculated radiation drive.

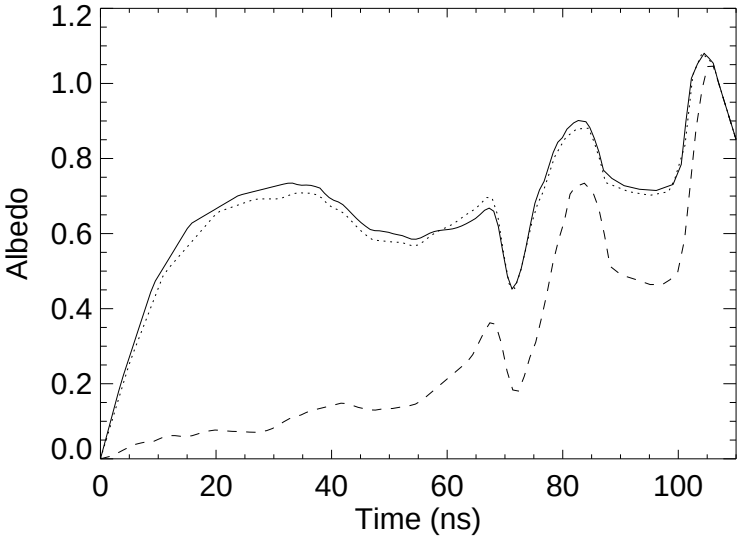

(a)

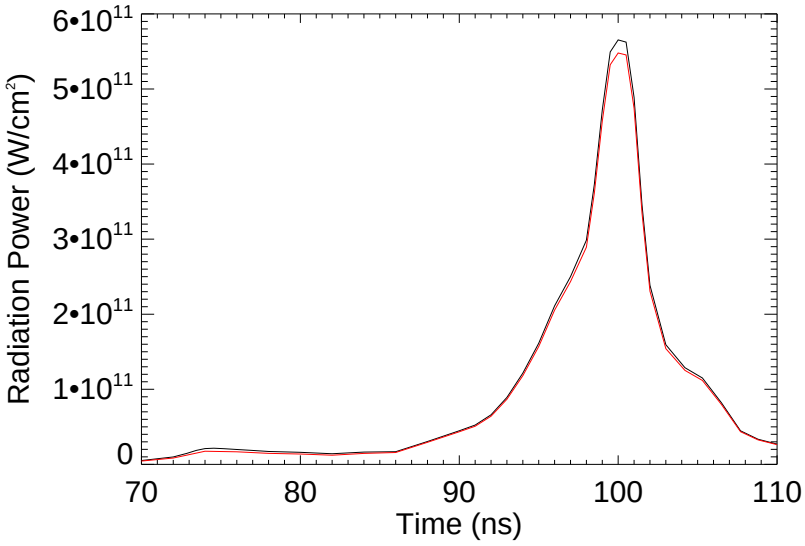

(b)

Figure 6.39: **(a)** BUCKY calculated albedo histories used for the final view factor calculations of shot z1122. The albedos are shown for the pinch glideplanes (solid), the primary hohlraum (dotted), and the outer anode (dashed). **(b)** VISRAD modeled radiation power history on the surface of the lower (black) and upper (red) foam samples on shot z1122.

The mass-averaged temperature-density phase space of the calculated conditions in the MgF_2 foils are shown on the χ^2 contour plots in Figures 6.36(a)-(d) over the times corresponding to the width of the backlighter time-history ($100.5 \pm 1.5ns$). These calculations are shown as a blue shaded region corresponding to the calculated conditions assuming the pinch power ranged from $80-100\%$ of the nominal value, and as an orange shaded region for the calculated conditions assuming the power ranged from $100-120\%$ of the nominal value. The lines in each shaded region correspond to the calculated mass-averaged conditions in the MgF_2 over the backlighter time (time follows along each line). The calculations are shown in this way because it provides a quick visual way to compare to the data. If the calculated conditions are going to be a good approximation to those observed in the experiment, then part of the shaded region must fall within the $+1\sigma$ contours. This can be further constrained by calculating the time-averaged conditions in the foils weighted by the backlighter pulse history shown in Figure 6.32. These points are over-plotted on each contour plot in Figure 6.36 and on the $+1\sigma$ contours in Figure 6.37 as a large symbol corresponding to assumed pinch powers of; 80%, 100%, and 120% of the nominal value. Since the data recorded on the time-integrated spectrometers are truly a measure of the mass- and time-averaged conditions in the foils, then these points are the best diagnostic of the comparison between the data and the rad-hydro models.

As seen in Figure 6.37, the calculated conditions in the MgF_2 tracers are in excellent agreement with the experimental data for each of the different foam thicknesses. At the nominal z-pinch power, the calculated conditions are all within 1σ of the experimental data. This implies that, over the peak of the main drive pulse at $t = 100.5 \pm 1.5ns$, the rad-hydro calculations can reproduce the conditions in the MgF_2 tracers at 4 different depths throughout the CH_2 foam. These constraints provide confidence in the calculations, which can then be used to investigate the dynamics in the sample.

Figure 6.40(a) and (b) show the time history of the average temperature[f] and density in the MgF_2 layers as calculated by BUCKY assuming the nominal pinch emission power at all times. As one might expect, the temperature of the tracer at any given time decreases as the depth into the foam increases. Early in time ($t < 90ns$) the density of each tracer also decreases as a function of depth. At a time of $100ns$, the average temperature in each tracer is calculated to be about 30, 20, 12, and $8eV$ as a function of increasing depth. The density of each tracer at this time is calculated to be about 2, 1.2, 1.4, and $1.8 \times 10^{20} cm^{-3}$. The 'bump' at $t \approx 102 - 104ns$ on the temperature history of the tracer at a depth of $0.5mg/cm^2$ is due to shock heating from the ablatively driven shock. This shock is also evident in the density histories, and shows up as a slow re-compression of the first tracer at $t \approx 93ns$, and a quick re-compression of the second tracer at $t \approx 102ns$. The compression of the second tracer is much quicker and stronger because it more closely coincides with the peak of the radiation pulse, which drives the shock. The third tracer shows a small influence from this shock very late in time ($t \approx 108ns$), and the fourth tracer shows no interaction with the shock up to the end of the simulation history ($t = 110ns$).

The hydrodynamics in each sample are better visualized through a plot of the mass contours as a function of time. These are shown for each sample in Figures 6.41(a)-(d). Each tracer is seen to expand forward into the lower density CH_2 foam during the foot pulse of the driving radiation ($t < 95ns$). The tracer at $\rho x = 0.25mg/cm^2$ interacts with the ablatively driven shock front early in time, and is significantly displaced by the time the data has been taken. The tracer at $0.5mg/cm^2$ is impacted by the shock front at the end of the data frame, but otherwise remains relatively stagnant. The other two tracers remain at a fairly constant density throughout the data frame, and only are impacted by

[f]The electron and ion temperatures were calculated to be close equilibrium.

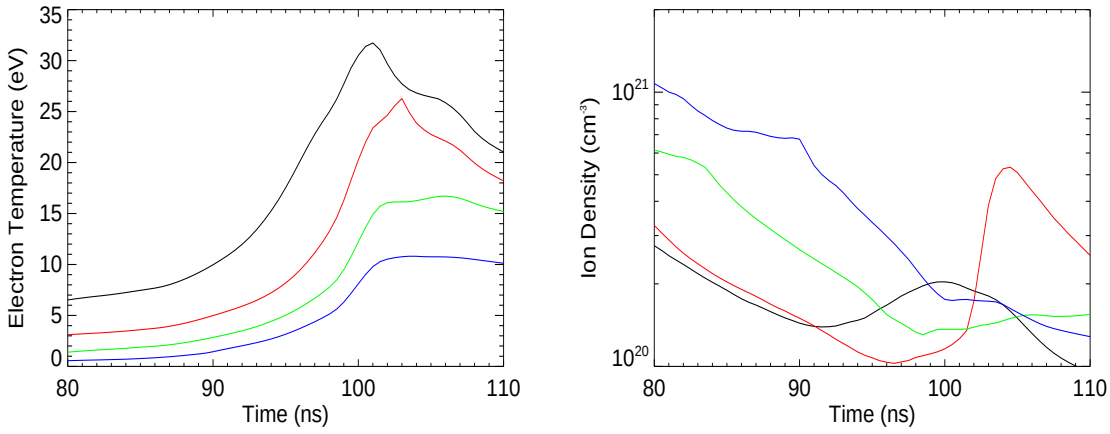

(a) **(b)**

Figure 6.40: BUCKY calculated mass averaged **(a)** temperature and **(b)** density conditions on shot z1122 in the MgF_2 tracers at depths in CH_2 foam of $\rho x = 0.25 mg/cm^2$ (black), $0.5 mg/cm^2$ (red), $0.75 mg/cm^2$ (green), and $1.0 mg/cm^2$ (blue).

the shock late in time.

To further investigate the details of the calculated dynamics in the CH_2 foam and each of the tracers, Figures 6.42(a) and (b) show the spatial profiles of the electron temperature and ion density in each sample. These curves are averaged over time as weighted by the backlighter pulse. As expected, the temperatures and densities in each sample are approximately the same near the front of the CH_2 ($\rho x \leq 0.15 mg/cm^2$). However, the conditions of the CH_2 are altered near the tracers. Namely, the density and temperature of the CH_2 are higher near the tracer than in the equivalent position with the tracer further back. This is due to the propagation of a shock wave that is launched in the CH_2 by the expansion of the MgF_2 tracer, which is radiatively heated to a higher temperature than the surrounding materials. The one exception to this is in the density of the CH_2 near the first tracer. The ablatively driven shock from the front of the sample has already passed through this tracer, which has expanded out the back

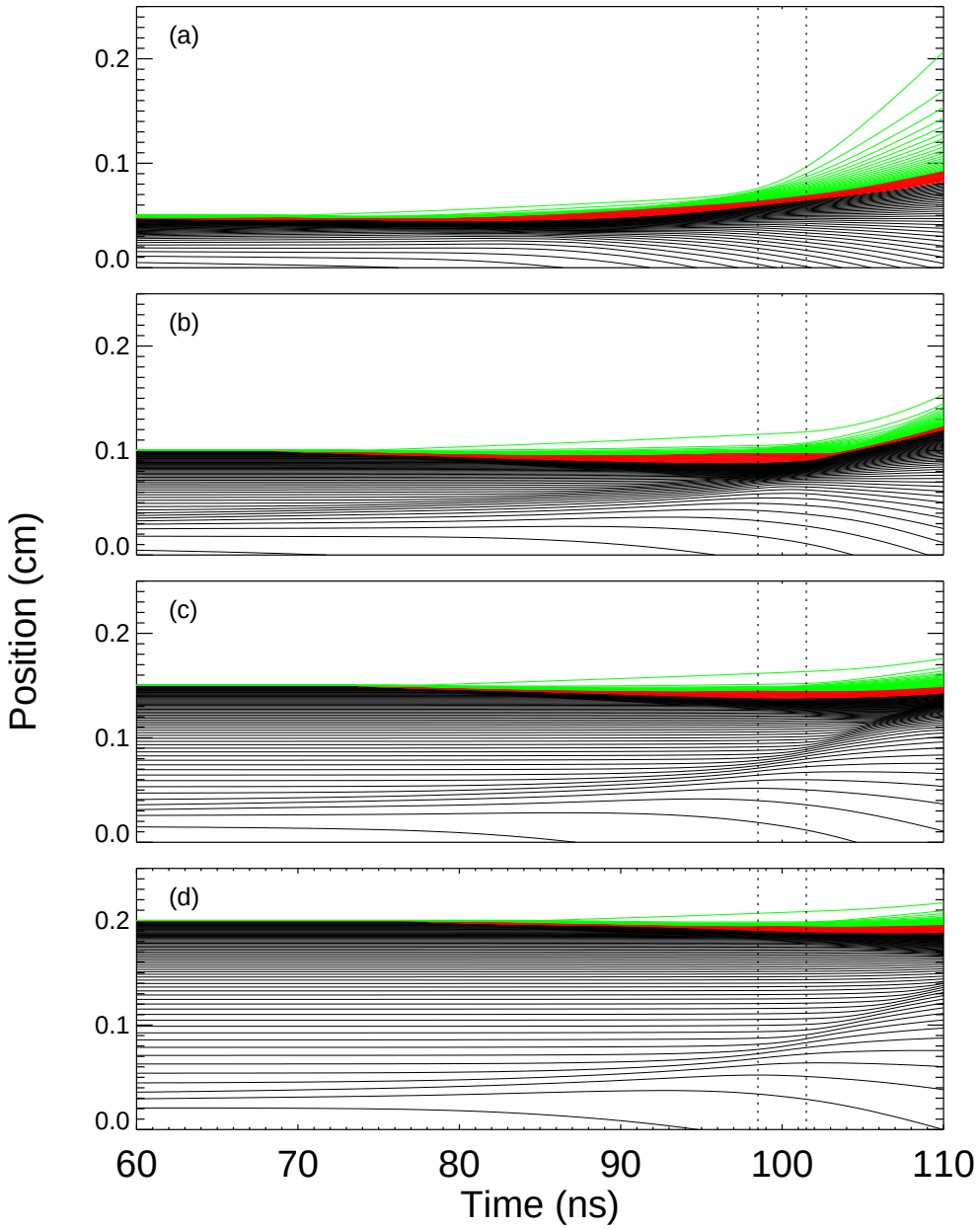

Figure 6.41: Mass contours (Lagrangian zone positions) for the CH_2 foam (black), the MgF_2 tracers (red), and the CH substrates (green) as a function of time for BUCKY calculations of the foam experiments on shot z1122. The figures are shown for total foam thicknesses of $\rho x = 0.25 mg/cm^2$ (a), $0.5 mg/cm^2$ (b), $0.75 mg/cm^2$ (c), and $1.0 mg/cm^2$ (d). The dotted lines correspond to the positions of the half-width-at-half-max of the backlighter pulse at $t = 100 \pm 1.5 ns$.

of the sample.

As in each of the experiments analyzed in this thesis, the frequency-dependent heating of the materials play a dominant role in determining the time-dependent temperature and density of the conditions in both the CH_2 foam and the MgF_2 tracers. However, the details are slightly different in this experiment than those described in §6.1 and §6.2. The VISRAD calculations of the radiation drive on this experiment (shot z1122) determined an average spectral energy at peak emission of about $660eV$, roughly $120eV$ higher than that calculated for shots z817 and z874. This puts quite a bit more energy in the photon range above the carbon K-edge. To illustrate, Figure 6.43(a) shows the radiation spectrum at peak z-pinch emission calculated by BUCKY at the front of each tracer. The figure demonstrates how there is a significant amount of energy in the spectral range $700eV < h\nu < 2000eV$ at each of the locations. In addition, the fraction of the total energy contained in this range increases with increasing depth into the foam. Not surprisingly, the details of these spectra have an effect on the heating in each of the MgF_2 tracer layers. Figure 6.43(b) shows the frequency-dependent net radiation heating in each of the tracers. As one might expect, the percentage of the total radiation heating that occurs in the range $700eV < h\nu < 2000eV$ increases with increasing depth. However, with the exception of the tracer at $\rho r = 1.0mg/cm^2$, the majority of the heating still occurs in the range below the carbon K-edge at energies of $100eV < h\nu < 300eV$. In the last tracer, there is a comparable amount of heating above and below the carbon K-edge even though the radiation spectrum is strongly weighted in the range above. This is due to the very high photo-ionization cross-section of the Mg L-shell.

Figures 6.44(a) and (b) show the opacities of the CH_2 and MgF_2 plasmas for the conditions calculated by BUCKY at $t = 100ns$ on either side of the front boundary of each tracer. The CH_2 opacities at each position are equivalent in the range $h\nu > 400eV$,

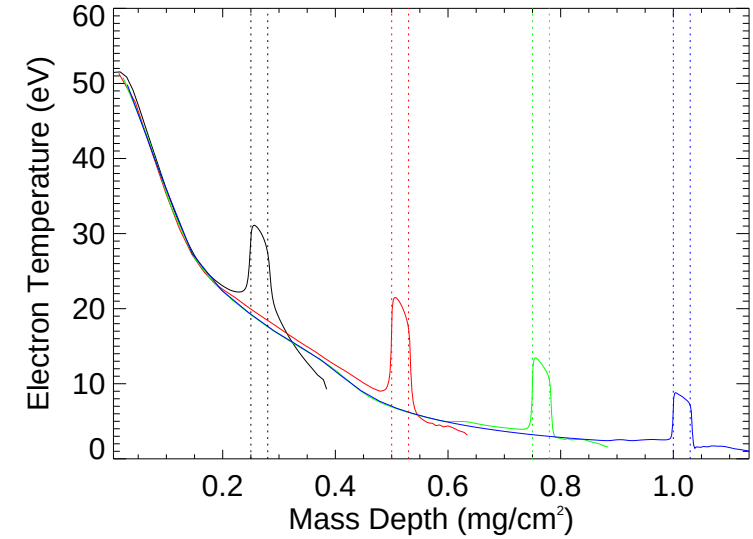

(a)

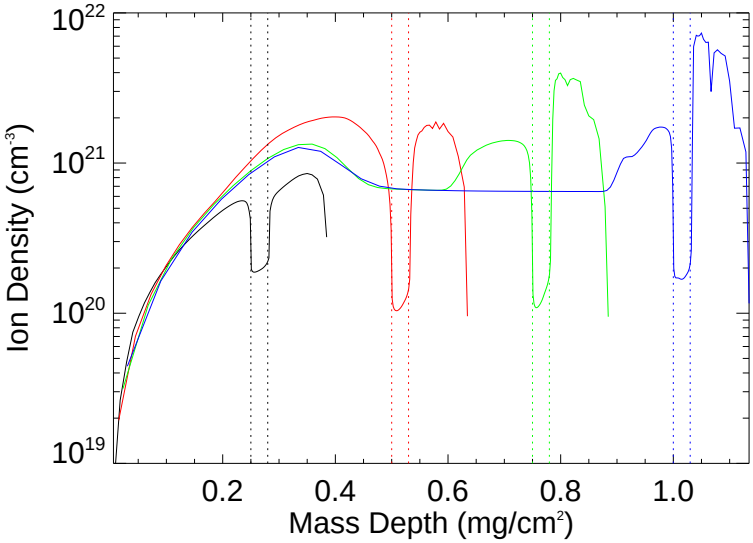

(b)

Figure 6.42: BUCKY calculated **(a)** temperature and **(b)** density profiles in the foam samples on shot z1122 for the MgF_2 tracers at a depth of $\rho x = 0.25 mg/cm^2$ (black), $0.5 mg/cm^2$ (red), $0.75 mg/cm^2$ (green), and $1.0 mg/cm^2$ (blue). The curves are averaged over the backlighter time-history, and the dotted lines mark the front and back positions of each MgF_2 tracer.

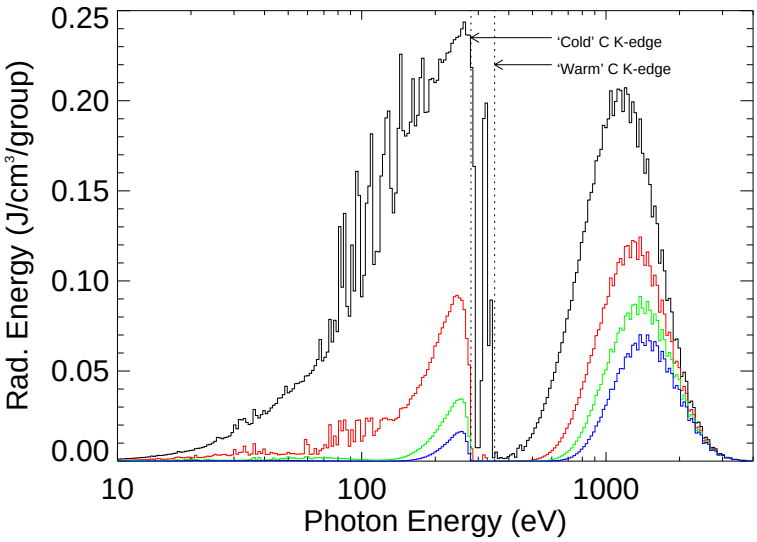

(a)

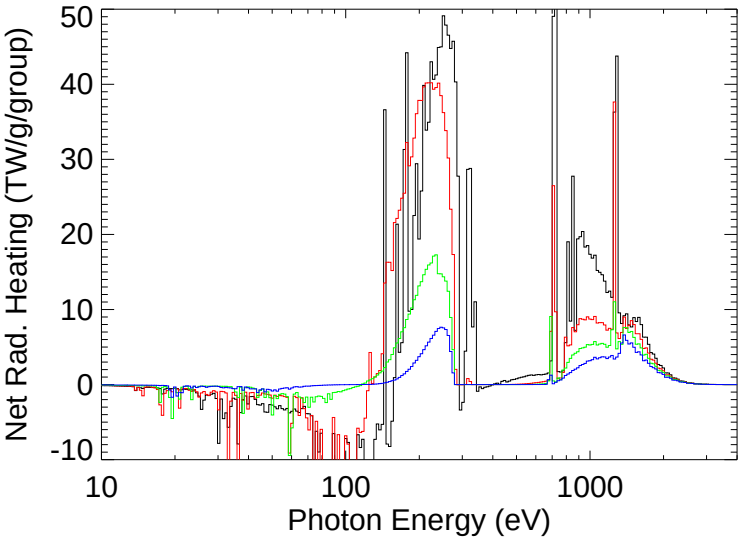

(b)

Figure 6.43: BUCKY calculated **(a)** radiation energy density and **(b)** net radiation-heating in the MgF_2 at a depth into the CH_2 foam samples of $\rho x = 0.25 mg/cm^2$ (black), $0.5 mg/cm^2$ (red), $0.75 mg/cm^2$ (green), and $1.0 mg/cm^2$ (blue). Each curve is shown at a time of $100 ns$ for the simulations of the foam samples on shot z1122.

but are very different at energies below that. These differences are due to the ionization states of the carbon. Near the front of the CH_2, the plasma is at a higher temperature and a correspondingly higher ionization state than that near the back. As the ionization state increases, there are fewer electrons in the $n = 2$ state, which leads to a lower photo-ionization cross-section in the range $20eV < h\nu < 300eV$. However, none of the CH_2 plasma is at a high enough temperature for the carbon to be completely ionized out of the $n = 1$ state, and the photo-ionization cross-sections in the range $h\nu > 400eV$ are approximately equivalent. It is easy to see how this opacity structure can lead to the radiation spectra shown in Figure 6.43(a).

The opacity of the MgF_2 shows a very similar dynamic (although there is more structure because the mixture has multiple elements at a higher atomic number than carbon). In every case, however, the opacity of the MgF_2 plasma is higher in the range below the carbon K-edge ($h\nu < 300eV$) than that above $400eV$. Therefore, the radiation in the range $< 300eV$ couples better to the MgF_2. This leads to the radiation heating profiles that were seen in Figure 6.43(b). The interesting thing about these dynamics is that, because the resulting temperature and density in the MgF_2 tracers are all in good agreement with the experimental data, then the opacities of each material and the driving radiation spectra must be well modeled.

As a final check on the comparison between the calculated MgF_2 conditions and those recorded in the experiment, Figure 6.45 shows the Mg absorption spectra on shot z1122 overlaid by the spectra calculated from the radiation-hydrodynamics model assuming the nominal z-pinch emission powers. The calculations are done with the SPECT3D spectral post-processing code using a detailed configuration analysis (DCA) of the MgF_2 at the temperatures and densities dictated by the rad-hydro calculation. Each spectrum is calculated under an assumption of LTE, and is averaged over the time-dependent intensity

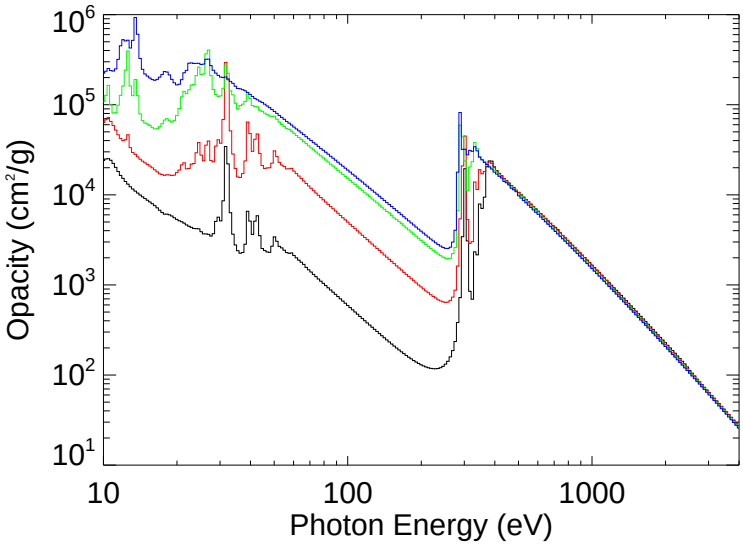

(a)

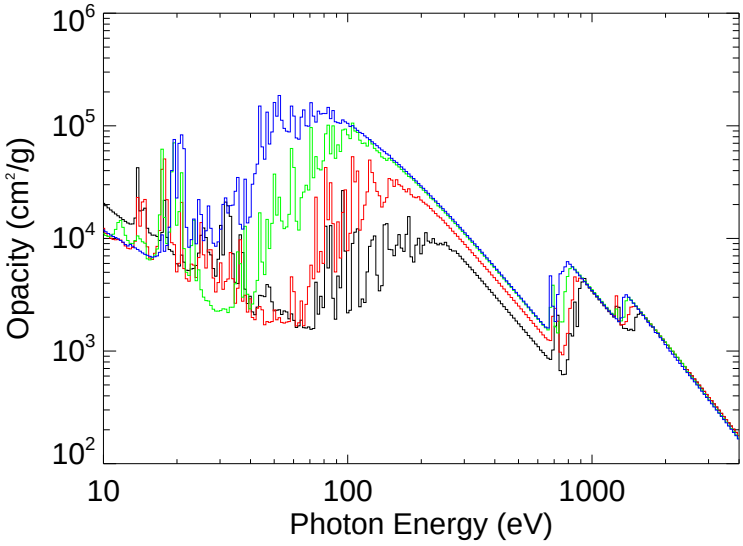

(b)

Figure 6.44: Opacities of the **(a)** CH_2 and **(b)** MgF_2 on either side of the front boundary of the tracers at $\rho x = 0.25 mg/cm^2$ (black), $0.5 mg/cm^2$ (red), $0.75 mg/cm^2$ (green), and $1.0 mg/cm^2$ (blue). Each curve is shown at a time of $100 ns$ for the BUCKY simulated conditions of the foam samples on shot z1122.

of the backlighter pulse. As seen in the figures, the measured and calculated spectra are in fair agreement. Each spectrum is calculated to be within 1σ of the minimum χ^2 found in the SPECTROFIT analysis. Moreover, the spectrum at $\rho x = 0.75 mg/cm^2$ was found to have a χ^2 value that was less than the minimum. This is due to temperature and density gradients in the tracers that are accounted for in the rad-hydro model, but not in the SPECTROFIT analysis. The χ^2 of the tracers at $\rho x = 0.5 mg/cm^2$ and $1.0 mg/cm^2$ were calculated to be very close to (but inside) the 1σ level. In the former, this is due to a slightly higher distribution of ionization states in the calculation than the data. In the latter, it is due primarily to the difference in the measured and calculated F-like K-β lines, which are seen to be slightly overestimated in the calculations. However, the χ^2 analysis suggests that each of these calculations are statistically equivalent to the data.

Therefore, given the uncertainties in the data and the calculations, the comparisons in Figures 6.37 and 6.45 demonstrate that the experimental data of the conditions inside each of the MgF_2 tracers on shot z1122 can be adequately reproduced by the computational methods and associated data tables as applied in this section.

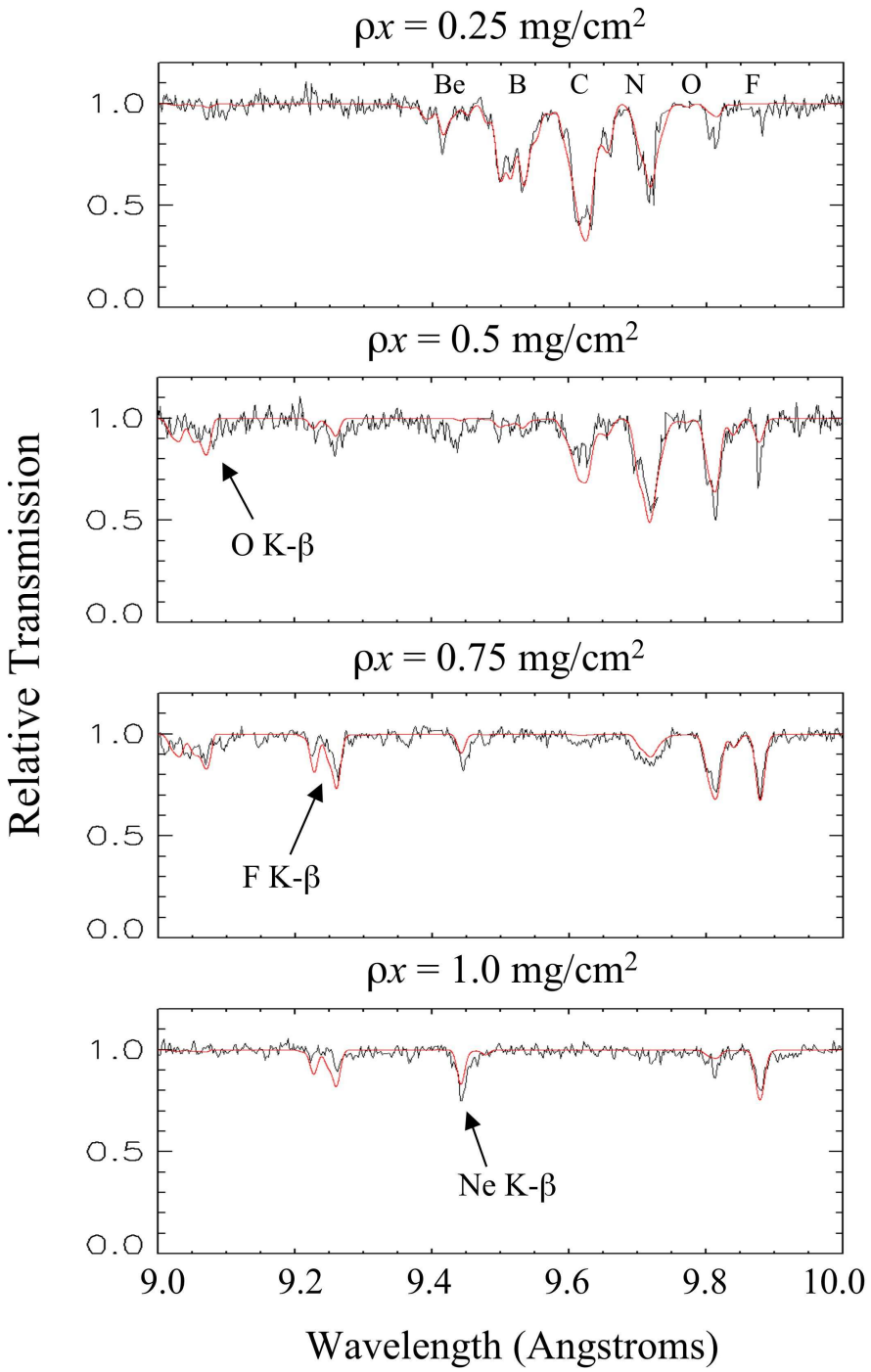

Figure 6.45: Comparison between the SPECT3D calculated relative transmission spectra (red) and the spectral data from shot z1122 in the MgF_2 tracers.

6.4 Summary and Discussion of the Radiative Transfer in CH_2 Foam

The experiments discussed in §6.1-§6.3 were each shown to be well modeled by the calculational methods defined in Chapter 4. Each of these calculations used a very specific set of computational models and data tables. Namely, these simulations were conducted with the BUCKY 1-D Lagrangian rad-hydro code using multi-angle short-characteristics radiation transport for 500 log-spaced photon energy groups from $0.1 - 10^4 eV$. The opacities of each material were calculated from PROPACEOS tables that contained 39 temperature points from $0.1 - 100eV$, and 41 log-spaced density points from $10^{19} - 10^{23} cm^{-3}$. The equation-of-state for the CH_2, CH, and Al materials were taken from the SESAME EOS tables and those for the MgF_2 were taken from QEOS calculations[g]. The ability to reproduce the spectral data from each of these experiments using this same set of models provides confidence in their accuracy. The different amplitudes and distributions of the radiation drives utilized in these experiments further support this claim.

To illustrate the differences in the radiation drives, Figures 6.46(a) and (b) show the VISRAD calculated drive power and average spectral energy on the surface of the foam samples from shots z817, z874, and z1122. The powers from shots z817 and z874 are seen to be very similar up to about $96ns$, at which time the drive on z874 increases to a peak that is roughly 20% higher. The average energy of the drive spectrum on shot z817 is about $50eV$ higher than that on z874 for $90ns < t < 96ns$, but approximately equivalent at the peak.

The drive power from shot z1122 has a drastically different shape and amplitude than both z817 and z874. The peak power on shot z1122 is a factor of 2 less than that from

[g]The SESAME tables were not used for the MgF_2 because no tables exist for that material.

shot z874, and about 80% less than that on z817. However, the average spectral energy at the peak drive on shot z1122 is over $100eV$ higher than that on both z817 and z874. Given these differences in the characteristics of the radiation drive, the ability to model the conditions in the tracers on each of these experiments provides another degree of confidence in the calculational models.

With this confidence, the experiments described in this chapter can be used to investigate the validity of other models. This is an important study because the models applied in §6.1-§6.3 are very detailed, and not always practical for large multi-dimensional simulations. In other words, it is important to determine 'what we can get away with' in order to maintain an approximately correct solution with the minimum amount of computational work. From a more academic standpoint, it is also important to determine the differences in the calculational models in order to reveal places where those models may have deficiencies. If such deficiencies can be addressed, than the model can be considered a better representation of reality.

As discussed at length in §3.1, the important factors that need to be considered for the types of simulations discussed in this thesis are; incident radiation spectra, radiation group structure, plasma opacity, radiation transport, and equation of state. In the following sections, different models of each factor are compared to the data from shot z1122, and each are contrasted to the 'baseline' models that were used in §6.3.3 to simulate that experiment. The experiment from shot z1122 was selected for this comparison for a few reasons. First, the spectral data acquired on that shot was of very high quality. Second, the intensity-dependent statistical fluctuations in the x-ray film exposure have been independently measured near the wavelengths of the Mg K-α lines. These measurements provide a degree of confidence in the statistical weights required for an accurate χ^2 analysis between the calculated and measured absorption spectra. This translates to a high

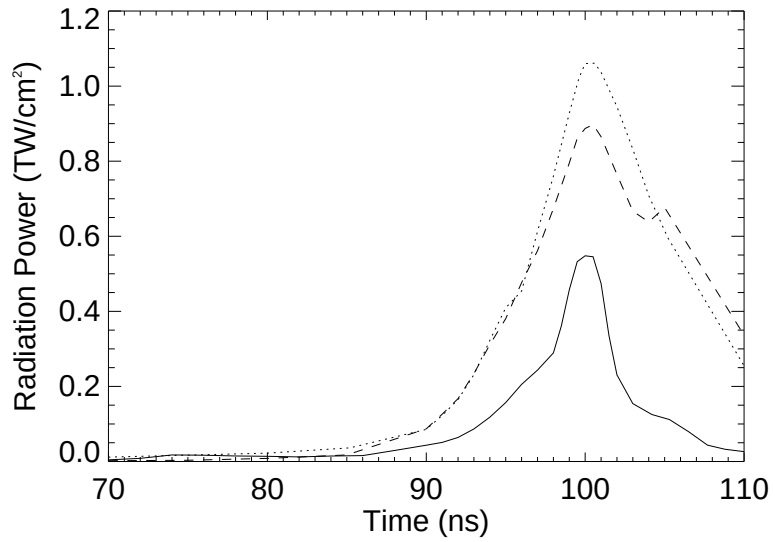

(a)

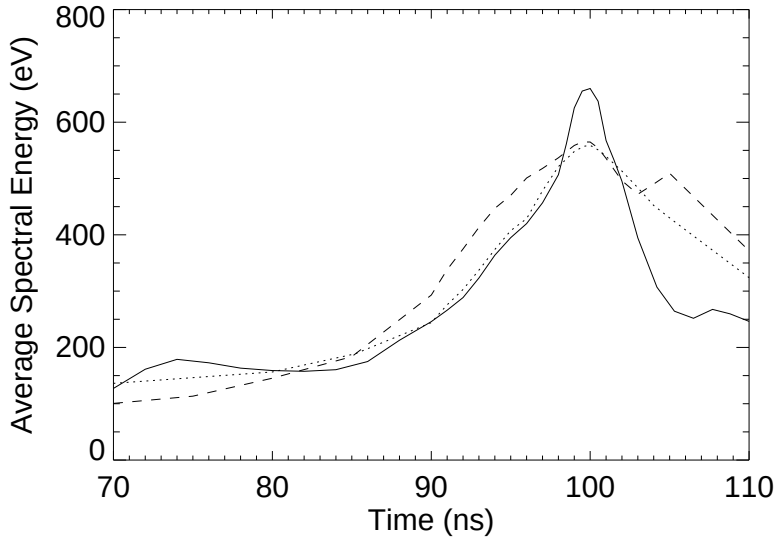

(b)

Figure 6.46: VISRAD calculated **(a)** radiation power and **(b)** average spectral energy on the surface of the foam samples on shots z1122 (solid), z874 (dotted), and z817 (dashed).

degree of confidence in the 1σ contours of the temperature and density conditions in each tracer. Third, of the three foam experiments described in this thesis, the experiment of shot z1122 holds the tightest constraints on the computational models. This experiment simultaneously measured the conditions of a MgF_2 tracer at 4 different depths throughout the foam sample. These conditions can only be reproduced by models that provide an adequate representation of the foam conditions and associated opacities over the full range of conditions on that experiment.

6.4.1 Incident Spectra

In §3.1, it was shown that the incident drive spectra can have a significant impact on the characteristics of the penetrating radiation field. In each of the experiments described in this thesis, the incident radiation spectra that successfully reproduced the data were calculated by the VISRAD view-factor code in the specific geometry of the experiment. It was shown in §4.1 that, in these view-factor calculations, uncertainties in the z-pinch power dominate the uncertainties in both the amplitude and average energy of the drive spectra. Thus, the uncertainty in the z-pinch power was included in the analysis of each foam experiment. However, it was also shown in §4.1 that a 20% difference in the z-pinch radii can lead to a 5% difference in the average energy of the drive spectra. This is not very much, but if the assumed radii were off by a factor of 2, then the average drive energy could be off by 25%. In addition, it was shown in §3.3 that the spectral distribution from a tungsten z-pinch has a high-energy, non-thermal tail at $h\nu > 2000eV$. This non-thermal component to the z-pinch spectra was not considered in any of the view-factor calculations. Since each of the power measurements used in this thesis were based on normalizations of XRD traces to energy-integrated bolometer data, the assumed thermal z-pinch power could be too high by the fraction of the total energy that exists in the non-

thermal tail. This extra energy would still reach the sample, but it would be distributed at much higher photon energies than the average energy of the VISRAD calculated drive spectra.

To explore the effects of changes in the distribution of the drive spectra, Figure 6.47 shows the 1σ contours of the tracer conditions on shot z1122 overlaid by BUCKY calculations of the tracer conditions assuming four variations on the drive spectra. In each calculation, every other parameter was held the same as in the baseline calculation[h] with the exception of the assumed z-pinch power. The pinch power was varied to put the calculated conditions of the first tracer within 1σ of the experimental data. The first case is the baseline calculation assuming the VISRAD drive spectra (shown at 100% of the measured z-pinch power). The second case is the VISRAD calculated drive power with a blackbody distribution at the temperature of the z-pinch (shown at 120% of the measured z-pinch power). The third case is the VISRAD calculated drive power with a blackbody distribution at the flux-equivalent radiation temperature of the drive power (shown at 80% of the measured z-pinch power). The final case is the VISRAD calculated drive spectra with an additional 10% of the drive energy added in the range $2000eV \leq h\nu \leq 3100eV$ (shown at 90% of the measured z-pinch power). This last drive spectra was constructed assuming that there is 10% of the calculated drive power in a non-thermal tail corresponding to the range of the tungsten M-shell UTAs, which were shown in §3.3 to be in emission.

As can be seen in the figure, the only case that does not agree with the experimental data in every tracer is the one that assumes a blackbody distribution at the flux-equivalent radiation temperature of the drive power. At 80% of the measured z-pinch power, the

[h]The 'baseline calculation' here and throughout the rest of this chapter refers to the simulations of z1122 as described in §6.3.

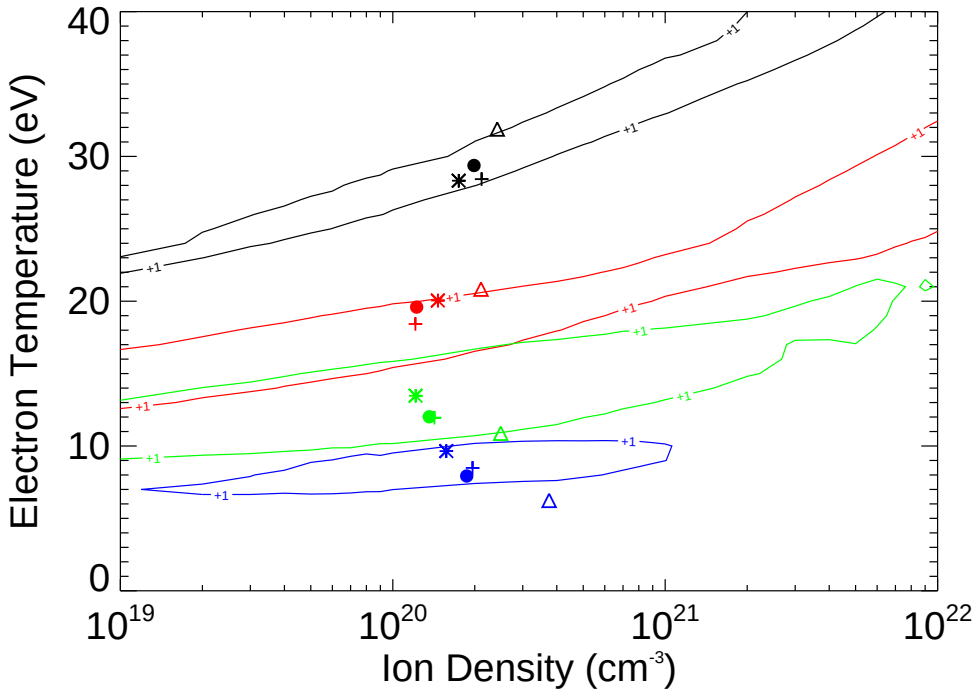

Figure 6.47: Effect of radiation drive spectra on the calculated tracer conditions. The $+1\sigma$ contours are as described in Figure 6.37. The symbols correspond to mass- and time-averaged plasma conditions in each tracer from BUCKY rad-hydro calculations assuming the following drive spectra; VISRAD spectra from the baseline calculation (dots), VISRAD drive power with a blackbody distribution at the temperature of the z-pinch (stars), VISRAD drive power with a blackbody distribution at the flux-equivalent radiation temperature of the drive power (triangles), and VISRAD drive spectra with an additional 10% of the drive energy in tungsten M-shell emission (crosses).

calculated conditions in this case are still just above the 1σ contour in the first tracer and below the 1σ contour in the last tracer. This implies that the distribution of radiation under the flux-equivalent blackbody spectra is at too steep of a gradient to reproduce the data. That is, lowering the drive power to put the calculations in better agreement with the first tracer would put the calculations in worse agreement with last tracer (and visa versa). This is not that surprising given the discussion of the tracer heating dynamics

in §6.3. As the depth of the tracer increases, the photon energies above $700eV$ become more important in the radiative heating. For this case, the low drive flux correlates to a low blackbody temperature, which is deficient in the high photon energies required to heat the last tracer.

One would not expect that the spectra of the radiation drive would be anything like the flux-equivalent blackbody. The dominant fraction of the total drive flux comes from the z-pinch ($\approx 70\%$ on this shot). Figure 6.47 shows that, even if the spectrum is modeled as a diluted blackbody distributed as the temperature of the z-pinch, the calculations can reproduce the conditions in each of the tracers. However, achieving this agreement requires assuming 120% of the measured z-pinch power because the carbon K-shell filters out more of the radiation at the resulting spectral energies.

The most interesting information in Figure 6.47 is the comparison between the baseline calculation and that assuming a 10% contribution from the tungsten M-shell. As seen in the figure, these two calculations are very similar, and each is driven by the same total energy. That is, the calculation assuming the M-shell contribution agrees with the data in each of the tracers assuming 90% of the measured z-pinch power. With the additional 10% of the energy from M-shell emission, this calculation has about the same total drive energy as the baseline calculation. Since this case is the most likely possible deviation from that assumed in the baseline calculation, it provides more confidence in the validity of the baseline models.

6.4.2 Radiation Group Structure

One fundamental issue that must always be addressed in calculating the dynamics of a radiatively heated sample is the treatment of the radiation field. Typically, that means choosing the number and distribution of frequency bins that are going to be included

in the calculation. If the plasma is expected to have a very high opacity across the entire spectrum at all times, or if the radiation field always has a planckian distribution at the temperature of the plasma, then a single-group (or Gray) approximation can be quite valid. However, for the experiments discussed in this thesis, it is clear that some frequency structure must be included in order to capture the penetrating radiation that heats the tracer layers. The question is how much detail is required.

Figure 6.48 shows the 1σ contours of the tracer conditions on shot z1122 overlaid by BUCKY simulations of the tracer conditions assuming five variations on the radiation group structure. In each simulation, every other parameter was held the same as in the baseline calculation, including the assumed z-pinch power. The simulations are shown for 500, 100, 40, and 20 photon energy groups, each evenly log spaced in the range $0.1eV \leq h\nu \leq 10^4eV$. The fifth simulation is shown for 40 unevenly spaced groups, which had 10 groups in the range $0.1eV \leq h\nu < 200eV$, 20 groups in the range $200eV \leq h\nu < 400eV$, and 10 groups in the range $400eV \leq h\nu \leq 10^4eV$.

As seen in the figure, only the 500 group and 40 unevenly grouped calculations lie entirely within the 1σ contours of each tracer. However, the 100 group calculation is only slightly below the contour of the last tracer. Given the uncertainties in the drive spectra analyzed above, the 100 group calculation is considered to be acceptable. The evenly spaced 40 group calculation shows marginal agreement, and the 20 group calculation is completely incorrect.

To demonstrate the differences in the resulting conditions of the CH_2 foam as a function of the radiation group structure, Figure 6.49 shows the temperature profile through the $1.0mg/cm^2$ thick foam sample for each of the group structures in Figure 6.48. This figure shows how, in the first $0.5mg/cm^2$, the calculated temperature gradient in the sample decreases as the number of groups decreases. The unevenly spaced 40 group

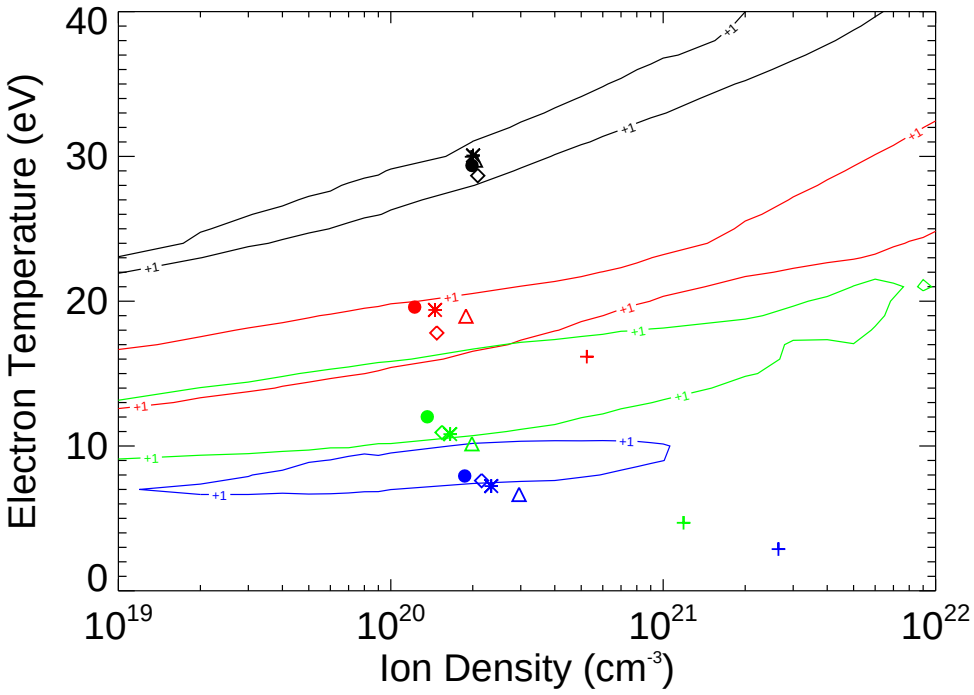

Figure 6.48: Effect of radiation group structure on the calculated tracer conditions. The $+1\sigma$ contours are as described in Figure 6.37. The symbols correspond to mass- and time-averaged plasma conditions in each tracer from BUCKY rad-hydro calculations using the following radiation group structures; 500 group (dots), 100 group (stars), 40 group (triangles), and 20 group (crosses) each evenly log spaced in the range $0.1eV \leq h\nu \leq 10^4 eV$. Also shown is an unevenly spaced 40 group calculation (diamonds) with 10 groups in the range $0.1eV \leq h\nu < 200eV$, 20 groups in the range $200eV \leq h\nu < 400eV$, and 10 groups in the range $400eV \leq h\nu \leq 10^4 eV$.

calculation is an exception. In this case, 20 frequency groups were devoted to resolving the carbon K-edge in the range $200eV \leq h\nu < 400eV$, and the resulting temperature profile tracks almost exactly along the 500 group calculation. This is an important result because the 40 group calculations take over a factor of 10 less time to compute than the 500 group. Clearly, choosing a group structure that resolves the carbon K-edge in some detail is paramount in properly computing the conditions in a CH_2 foam.

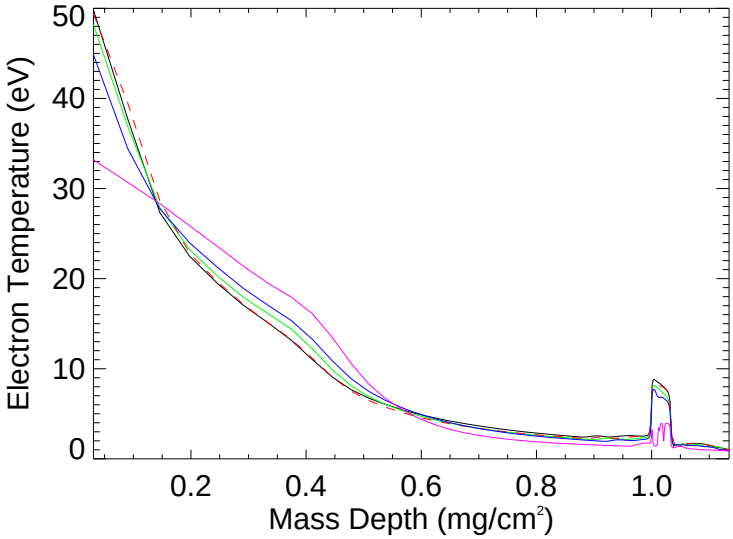

Figure 6.49: BUCKY calculated temperature profiles in the $1.0 mg/cm^2$ thick foam sample on shot z1122. The curves are averaged over the backlighter time history, and are shown for different BUCKY rad-hydro calculations using the following radiation group structure; 500 group (black), 100 group (green), 40 group (blue), and 20 group (purple) each evenly log spaced in the range $0.1eV \leq h\nu \leq 10^4 eV$. Also shown is an unevenly spaced 40 group calculation with 10 groups in the range $0.1eV \leq h\nu < 200eV$, 20 groups in the range $200eV \leq h\nu < 400eV$, and 10 groups in the range $400eV \leq h\nu \leq 10^4 eV$ (red dashed).

6.4.3 CH_2 Opacity

The changes in the calculated foam conditions as a function of the radiation group structure are due to the associated approximations that are made to the plasma opacities. That is, decreasing the number of energy groups requires making a more coarse approximation to the true material opacity. It stands to reason that, given a fixed group structure, different approximations in the calculations of the plasma opacities can also lead to differences in the calculated foam conditions.

Up to this point, the model that has been used to simulate the CH_2 plasma opacities is among the most complex and detailed models available. In particular, the PROPACEOS

opacities used in each of the simulations in this chapter were computed using Detailed Term Accounting (DTA) through multi-configuration Hartree-Fock calculations of the energy levels and atomic cross-sections. This model requires the calculation of the interaction between the many wave-functions (hundreds) associated with each atomic configuration. Even if these configurations and cross-sections are tabulated, statistical calculations of the configuration populations of the many available energy states are too slow to compute in-line with the radiation-hydrodynamics. For example, the PROPACEOS CH_2 opacities used in this thesis were calculated at LTE from DTA atomic data tables of all the available configurations for each ionization state. Such a calculation takes roughly 20 seconds on a $2.4GHz$ Pentium-4 to calculate the 500 group opacity of a plasma at $T = 30eV$ and $n_i = 1. \times 10^{20} cm^{-3}$. If a rad-hydro calculation has 1000 zones, each with a different temperature and density, doing this calculation in-line would take over 5.5 hours to complete a single time-step. This can be sped up considerably by ignoring some configurations or collapsing the fine structure into 'super configurations', but that means a loss of accuracy.

The usual approach taken with DTA opacity calculations is to build a table of opacities as a function of temperature, density, and radiation group energy. There are two problems with this approach. First, calculating the opacities in the absence of the rad-hydro results requires making an assumption on the distribution of the radiation field. Under some plasma conditions, the radiation field can have a significant effect on the ionization states and configuration populations through bound-free and bound-bound photo-absorption. Second, the size of the tabular opacity files can become quite large. For the opacity tables used in this thesis, a 39 by 41 by 500 point table takes up about $24Mb$ of memory. However, this table only covers a range from $0.1 - 100eV$ in temperature and $0.1 - 10^4 eV$ in photon energy. For simulations of experiments that cover a much larger range of

temperatures and photon energies, the size of these tables can grow by a factor of 10 - 100. Historically, these issues have been avoided by using a much simpler 'average atom' atomic model to calculate opacities in-line with the hydrodynamics.

To explore the effects of different opacity models on the radiative transfer, Figure 6.50 shows the 1σ contours of the tracer conditions on shot z1122 overlaid by BUCKY simulations of the tracer conditions assuming four different tabular opacities for the CH_2. In each calculation, every other parameter was held the same as in the baseline calculation with the exception of the assumed z-pinch power. The pinch power was varied to put the calculated conditions of the first tracer within 1σ of the experimental data. The first table was generated by the PROPACEOS DTA model from the baseline calculation (shown at 100% of the measured z-pinch power). The second table was generated by an XSN average atom model [108] (shown at 70% of the measured z-pinch power). The third table was generated by an EOSOPA DTA model (shown at 90% of the measured z-pinch power). The final table was generated by an EOSOPA UTA model (shown at 100% of the measured z-pinch power).

As seen in the figure, the calculations produce a different distribution of conditions in the MgF_2 tracers for each of the opacity tables. The XSN average atom model is seen to be much to 'transparent'. That is, the assumed z-pinch power had to be reduced by 70% to bring the calculated conditions within the 1σ error bar of the first tracer. Even at this low drive power the calculated temperatures in each of the other tracers are still much higher than indicated by the data. The EOSOPA DTA opacities suffer from a similar problem. The calculations using these opacities compare very well to the data in the first tracer, are marginal in the second and third tracer, and predict too high of a temperature in the fourth tracer. The EOSOPA UTA model is the only other model (besides the PROPACEOS DTA model used in the baseline calculation) that predicts

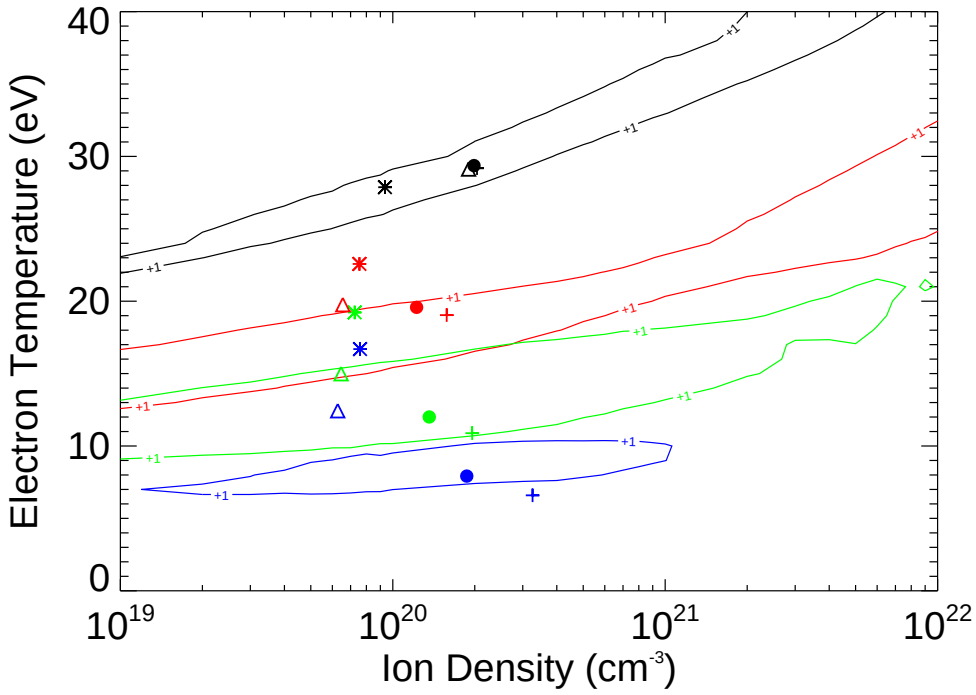

Figure 6.50: Effect of CH_2 opacity model on the calculated tracer conditions. The $+1\sigma$ contours are as described in Figure 6.37. The symbols correspond to mass- and time-averaged plasma conditions in each tracer from BUCKY rad-hydro calculations using tabular opacities from the following atomic models; PROPACEOS DTA (dots), XSN average-atom (stars), EOSOPA DTA (triangles), and EOSOPA UTA (crosses).

conditions that are close to being within 1σ of each tracer. This is somewhat surprising since the EOSOPA DTA model is expected to be much more complete and accurate than the UTA model.

To illustrate the differences in each of these opacities, Figure 6.51 shows the 500 group opacity of CH_2 at $6eV$ and $5mg/cc$ (corresponding to the conditions in the baseline calculation as shown in Figure 6.42 at $\rho x = 0.6mg/cm^2$) as calculated by each atomic model. These opacities are shown in the range $100eV \leq h\nu \leq 1000eV$ because this was

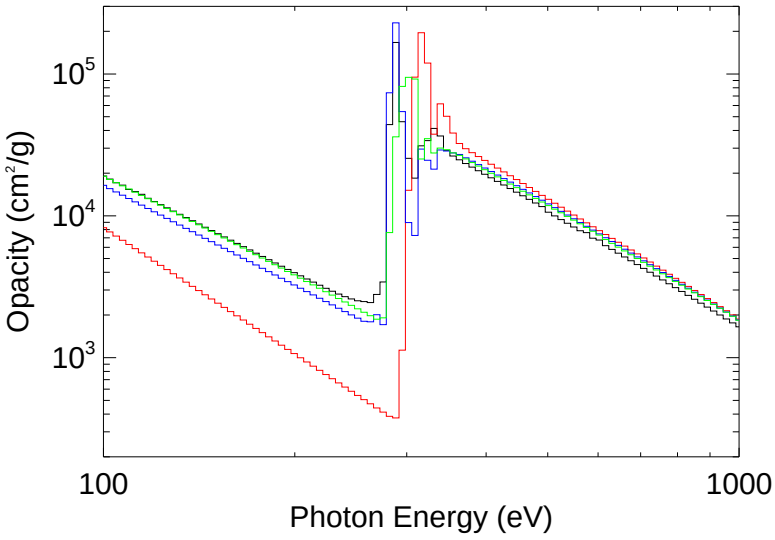

Figure 6.51: CH_2 opacities at $T_e = 6eV$ and $\rho = 5mg/cc$ as calculated by PROPACEOS DTA (black), XSN average-atom (red), EOSOPA DTA (blue), and EOSOPA UTA (green).

shown throughout this chapter to be the most important region for the transport of the penetrating radiation. Each model is seen to compute a different opacity throughout this range.

The XSN average atom model calculates a bound-free opacity below the carbon K-edge (ionization out of the L-shell) that is much lower than that computed by each of the other models. This represents a serious deficiency in the average atom approach. In this model, only a single average ionization state is considered to exist, with a fractional number of electrons in each level. No fine structure is included, and the energy levels are computed from the analytic hydrogenic formulas by assuming a screening potential. The lack of detail in the average atom approach produces opacities that are much too low to provide the correct radiative transfer characteristics at the conditions of the CH_2 foams studied in this thesis.

The EOSOPA DTA model also calculates bound-free opacities that are seemingly too low. As discussed in §4.3, there are two important differences between the DTA models in EOSOPA and PROPACEOS. First, PROPACEOS uses the Hummer-Mihalas partition function to compute occupation probabilities. EOSOPA uses the boltzmann partition function. Second, PROPACEOS uses tabulated Hartree-Fock cross-sections to compute the bound-free opacities. EOSOPA uses fits to these cross-sections. Each of these have been shown to cause differences in the calculated opacities at low temperatures [109]. The formulism in PROPACEOS is more consistent with the data presented in this thesis.

Finally, the EOSOPA UTA model calculates opacities that are very similar to those in PROPACEOS. The largest difference is in the area directly at the K-edge, where the details of the atomic structure and associated occupations are the most important for computing the photo-ionization rates. The resulting CH_2 opacity in this region is critical for properly computing the magnitude and distribution of the the radiation that penetrates deep into a CH_2 foam.

Based on each of these comparisons, it is concluded that the calculated opacity using the PROPACEOS DTA atomic model is the most consistent with the experimental data. The XSN average atom model is completely incorrect, and should be avoided wherever possible. The differences between the PROPACEOS and EOSOPA DTA models are enough to invalidate the EOSOPA model at low temperatures, but is likely to be satisfactory for foam conditions at temperatures greater than about $30eV$. Finally, the EOSOPA UTA model is not as good as the PROPACEOS DTA model, but satisfactory across the range of conditions studied in this thesis.

6.4.4 Radiation Transport Model

As was discussed in detail in §1.4, there are a number of different approximations to the radiation transport equation that are commonly used in radiation-hydrodynamics codes. Each of the simulations in this chapter were conducted with short-characteristics. This approximation was used because, as demonstrated in Appendix B, it provides very accurate solutions in plasmas where scattering can be neglected and the radiation field can be considered as steady-state (dE/dt is very small). However, these statements are only true in 1-D. Multi-angle methods like short-characteristics and discrete ordinates are known to have problems in multiple dimensions (ex. ray effects). In addition, these methods typically require much more computation time than a simple model like diffusion. For these reasons, simulations in multi-dimensional plasmas most often use flux-limited diffusion, which was shown in Appendix B to be inaccurate for many types of problems. The question that needs to be answered is whether or not flux-limited diffusion is an adequate approximation for the radiation fields in the CH_2 foams studied in this thesis.

Figure 6.52 shows the 1σ contours of the tracer conditions on shot z1122 overlaid by BUCKY simulations of the tracer conditions assuming five approximations to the radiation transport equation. In each simulation, every other parameter was held the same as in the baseline calculation, including the assumed z-pinch power. The first approximation is multi-angle short-characteristics as used in the baseline calculation. The second approximation is diffusion with no flux-limiter. The third approximation is flux-limited diffusion using the Larsen (n=6) flux-limiter. The fourth and fifth approximations are time-dependent and time-independent flux-limited diffusion using the Levermore-Pomraning flux-limiter.

As seen in the figure, the simulated conditions assuming non-limited diffusion and

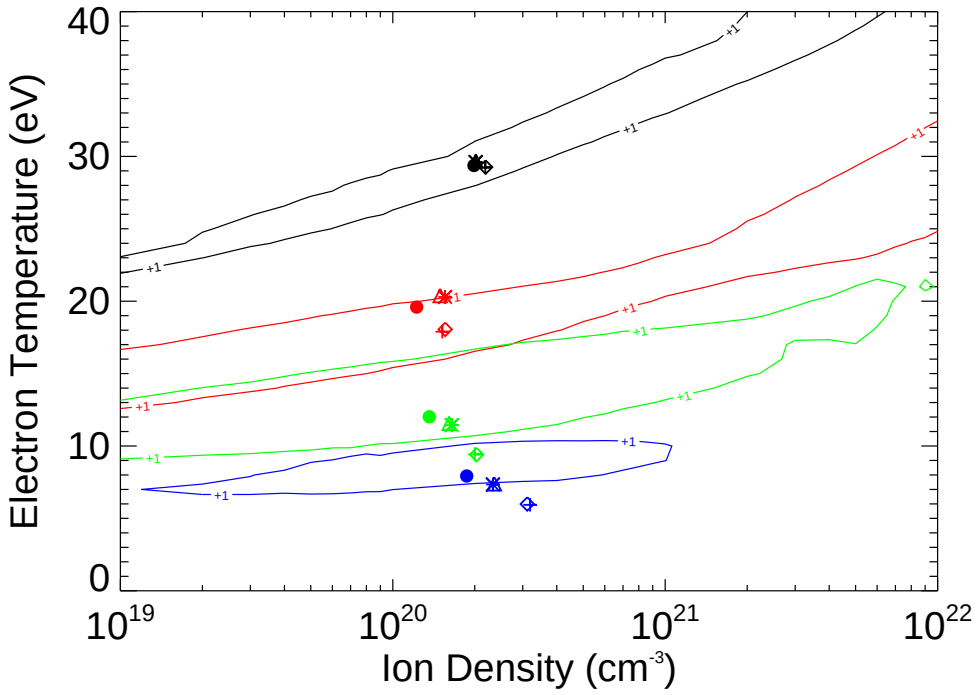

Figure 6.52: Effect of radiation transport model on the calculated tracer conditions. The $+1\sigma$ contours are as described in Figure 6.37. The symbols correspond to mass- and time-averaged plasma conditions in each tracer from BUCKY rad-hydro calculations using the following radiation transport approximations; multi-angle short-characteristics (dots), diffusion (stars), flux-limited diffusion with the Larsen (n=6) limiter (triangles), and flux-limited diffusion with the Levermore-Pomraning limiter assuming time-dependent (crosses) and time-independent (diamonds) forms of the diffusion equation.

flux-limited diffusion with the Larsen (n=6) flux-limiter are virtually identical. Each of these fall within 1σ of the experimental data in every tracer. However, the solution assuming the Levermore-Pomraning limiter predicts temperatures that are too low in the last two tracers. These results imply that, in the foam samples on z1122, the R-value (the scaled radiation energy gradient) as shown in Figure 1.17 is between about 1 and 2. As discussed in §2.1, this is a precarious position for flux-limited diffusion. When any two

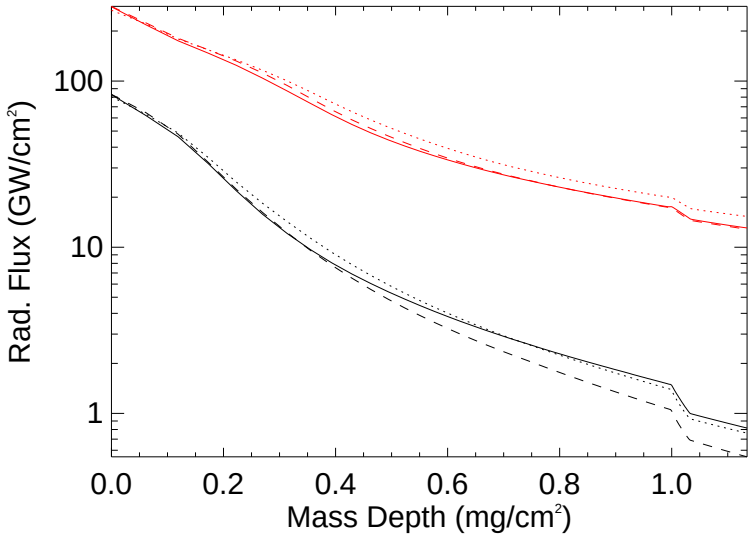

Figure 6.53: Radiation flux distribution in the $1.0 mg/cm^2$ foam sample on shot z1122 as calculated by BUCKY using short-characteristics (solid) and flux-limited diffusion with the Larsen (n=6) limiter (dotted) and the Levermore-Pomraning limiter (dashed). The profiles are shown at simulation times of $96ns$ (black) and $100ns$ (red).

flux-limiters predict two significantly different solutions, flux-limited diffusion in general is suspect. Figure 6.52 suggests that the less restrictive Larsen (n=6) flux-limiter provides a better solution throughout the sample than the Levermore-Pomraning limiter. However, this may only be true for this particular set of conditions. To illustrate, Figure 6.53 shows the radiation flux distribution throughout the $1.0 mg/cm^2$ thick sample calculated by short-characteristics and flux-limited diffusion for both the Larsen and Levermore-Pomraning limiters. These profiles are shown at times of $96ns$ and $100ns$. At $96ns$, the Larsen result follows very close to the short-characteristics result, and the Levermore-Pomraning result is too restrictive. In contrast, at $100ns$ the Levermore-Pomraning result follows very close to the short-characteristics result, and the Larsen result is not restrictive enough. The fact that the tracer conditions assuming the Larsen limiter are the most consistent with the data only implies that the *time-integrated* radiation field

at the location of each tracer is best modeled by the Larsen (n=6) limiter. This result could be different if the conditions of the radiation field and the CH_2 plasma were like that at $t = 100ns$ for a longer period of time.

It is of particular interest that the *time-independent* solution using the Levermore-Pomraning limiter agrees almost exactly with the time-dependent one. This implies that, over any given time-step, the radiation field is nearly steady-state. There is no real guarantee that this is true for any other transport approximation. However, it is reasonable to assume that, because the calculated conditions are similar between flux-limited diffusion and short-characteristics, the radiation field can be considered as steady-state for the short-characteristics solution as well. This is an important result. As demonstrated in Appendix B, short-characteristics predicts solutions that are very close to the true solution of the transport equation when the radiation field is steady-state and there is no scattering. This provides another degree of confidence in the baseline calculation, and justifies the use of short-characteristics as the standard against which to compare the diffusion solutions.

To further investigate the differences between the various transport approximations, Figure 6.54(a) shows the time-dependent radiation temperature at a depth of $1.0mg/cm^2$ (the front boundary of the last tracer) and the average electron temperature in the last tracer as calculated by short-characteristics and flux-limited diffusion. In addition, Figure 6.54(b) shows the percent difference (in temperature) between these approximations. The radiation temperature calculated using the Larsen limiter is within about 5% of the short-characteristics solution at all times, but the electron temperature differs by as much as 40%. The Levermore-Pomraning limiter differs from the short-characteristics solution by as much as about 15% in radiation temperature and 60% in electron temper-

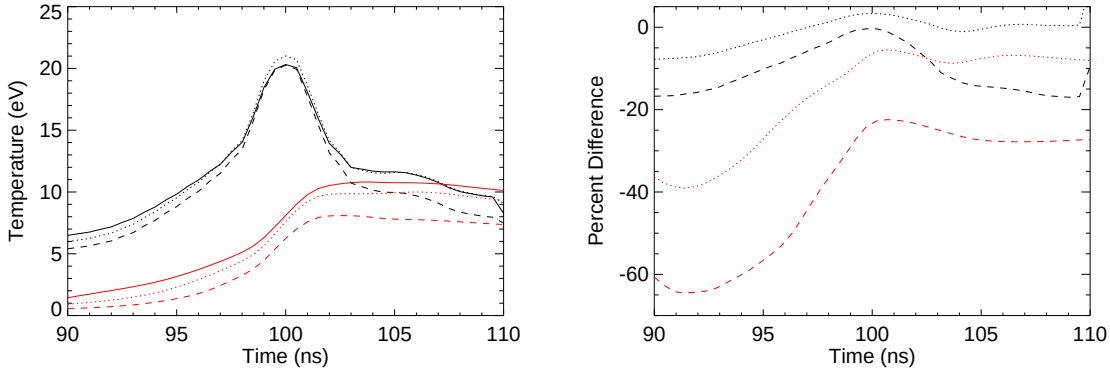

(a) **(b)**

Figure 6.54: **(a)** Radiation temperature (black) at the front boundary of the tracer at $\rho x = 1.0 mg/cm^2$ on z1122 and the average electron temperature in that tracer (red) as calculated by BUCKY. These calculations are shown assuming short-characteristics (solid) and flux-limited diffusion with the Larsen (n=6) (dotted) or Levermore-Pomraning limiters (dashed). **(b)** Percent deviation between the short-characteristics and flux-limited diffusion results in (a).

ature[i]. Based off this comparison, it is clear that flux-limited diffusion does have some shortfalls. However, the calculation at this depth is probably a worst case scenario. As the radiation field penetrates deeper into the foam, the transport becomes more directional (the Eddington factor approaches 1). This is evidenced by the non-equilibrium between the radiation and electron temperatures throughout the rising edge of the heating pulse. Toward the front of the foam samples, the radiation field is more isotropic and the flux-limited diffusion solutions are much better. The radiation field and the electron temperature in the first tracer (at $\rho x = 0.25 mg/cm^2$) as calculated by short-characteristics and each diffusion approximation agree within a few percent at all times.

It is therefore recommended that, for radiation distributions similar to those studied in this thesis, flux-limited diffusion only be used to determine the rough scaling of the

[i]The large variations in the temperature of the tracer demonstrates the sensitivity of the experimental method to the strength and distribution of the radiation field.

radiation conditions inside a $5mg/cc\ CH_2$ foam that is thicker than about $0.25mg/cm^2$. If the radiation field needs to be known to better than about 5% in temperature (20% in flux), then a more accurate non-diffusive solution must be employed.

6.4.5 Equation of State

The final physical model that needs to be considered in a calculation of the CH_2 foam dynamics is the equation-of-state (EOS). All of the calculations presented in this thesis used the SESAME tabulated EOS for CH_2 (table 7171). The SESAME tables tend to be the standard that most radiation-hydrodynamics codes use for the EOS. However, these tables only exist for a few select materials and are composed of a blending of different models. There is very little information available about which models were used for which materials and in which regimes. An obvious question to ask is how do different EOS models change the dynamics of the calculations.

Figure 6.55 shows the 1σ contours of the tracer conditions on shot z1122 overlaid by BUCKY simulations of the tracer conditions assuming four different EOS tables for the CH_2. In each simulation, every other parameter was held the same as in the baseline calculation, including the assumed z-pinch power. The first table was taken from the SESAME library as used in the baseline calculation. The second table was calculated with QEOS [106]. The third table was calculated with PROPACEOS [91]. The final table was calculated assuming an ideal-gas EOS at all temperatures and densities.

As seen in the figure, the calculations using the ideal gas EOS table are the only ones that do not fall completely within 1σ of the tracer conditions at every depth. The other three tables all provide very similar solutions. The only place that these calculations differ by any significant amount is in the tracer at a depth of $0.5mg/cm^2$. As was shown in §6.3.3, this tracer is heavily influenced by the ablatively driven shock at the time the

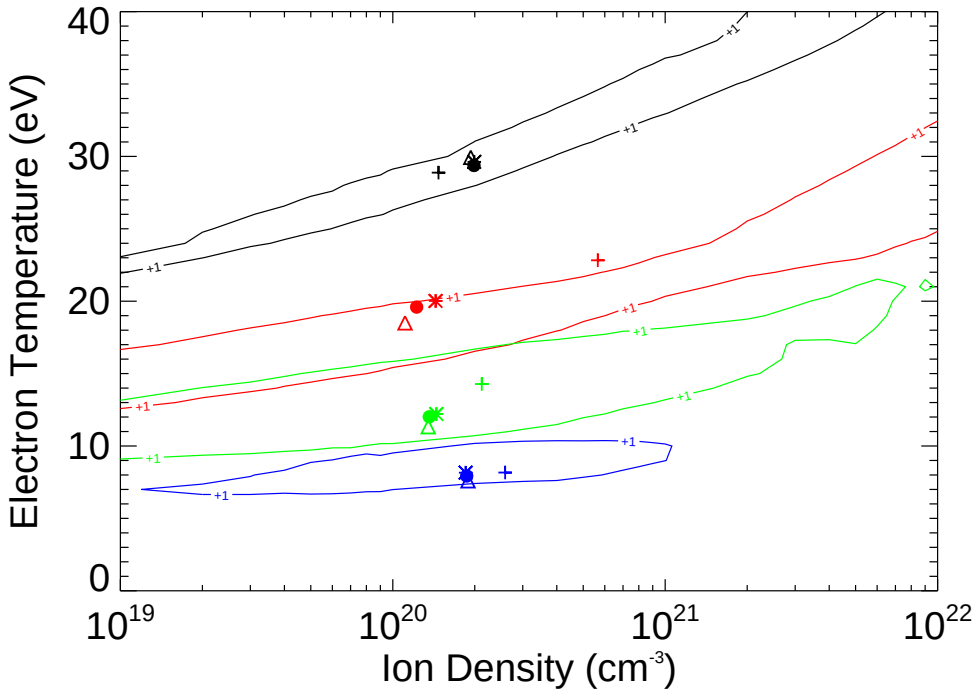

Figure 6.55: Effect of EOS model on the calculated tracer conditions. The $+1\sigma$ contours are as described in Figure 6.37. The symbols correspond to mass- and time-averaged plasma conditions in each tracer from BUCKY rad-hydro calculations using tabulated EOS data from the following sources; SESAME (dots), QEOS (stars), PROPACEOS (triangles), and Ideal-Gas (crosses).

data was taken. The location of a shock front is the place where differences in the EOS are most pronounced. In addition, this is the only tracer for which the calculations using the ideal gas EOS do not predict conditions within 1σ of the data. It is not surprising that the characteristics of a shock front calculated in an ideal gas are different from those calculated in a more physical model.

Given these comparisons, it is concluded that the calculations presented in this thesis are not sensitive to the EOS. This is an important conclusion for two reasons. First, the

insensitivity to the EOS places more importance on the other models in the calculation. Since the goals of this thesis are to study the radiative transfer properties in CH_2 foam, it is beneficial that the EOS is of little consequence. Second, it is unknown how the structure of the CH_2 foam affects the hydrodynamics. Since each EOS model provides a solution that is consistent with the data, there is evidence that, after the long foot pulse and during the main radiation drive, the CH_2 can be treated as a uniform vapor.

6.4.6 Future Work

Each of the conclusions drawn above were found to be consistent with the experimental data from shots z817 and z874. Although, the fewer constraints in these experiments provide less of a distinction between some of the models. For example, the foam on shot z817 had only a single tracer at a depth of $0.5 mg/cm^2$ that was calculated to quickly reach temperatures of $30 - 40 eV$. As shown in the comparison between the different opacity models in Figure 6.50, each opacity model can be reasonably made to fit the conditions at this temperature. This makes it difficult to distinguish between the models. The two tracers on shot z874 provide more of a constraint on the opacity model than shot z817, and were also found to be in agreement with the conclusions drawn above. However, the rear MgF_2 tracer on this experiment was 'looking through' the Al tracer, and it was shown in §6.1.3 that the Al tracer has a significant impact on the radiation field. Even though the calculated opacities of these tracers were found to be well modeled in the foil experiments in Chapter 5, it is difficult to isolate the CH_2 opacity effects in this experiment. The same is true for the radiation transport.

The confidence in the resulting error bars from the χ^2 analysis of the data on shots z817 and z874 could also be improved. A true statistical comparison between experimental measurements and a model requires a good understanding of the natural fluctuations

in the data (ie. the standard deviation). Since the data from each of these shots was taken using a micro-channel plate intensifier for which the statistical fluctuations are not well understood, the data was assumed to follow Poisson statistics as calibrated by a region of each spectra with no known features. Defects in the film, micro-channel plate, or crystal reflectivity across these regions could affect this analysis. The resulting best-fit in the χ^2 analysis is not likely to be affected, but the 1σ confidence level could be.

The experiment on shot z1122 is therefore the best one for studying the differences in computational models within the CH_2 foam. With the experimental and computational methods developed in this thesis, the conclusions drawn above could be greatly strengthened by repeating this experiment for different z-pinch configurations with correspondingly different pulse-shapes.

This is not to say that the experiment on z1122 could not be improved. As seen throughout this thesis, the degeneracy of the ionization states for different combinations of temperature and density leaves a very wide phase-space in the χ^2 analysis where the conditions of the tracer are within 1σ of the best-fit spectra. If the density of the tracer could be measured, then this phase-space could be limited to the error bars of the density measurement. Attempts were made in the course of this thesis to measure the density through Stark broadening of high-n transitions in sodium (Na). However, the mean free path of the CH_2 samples was too short at the ≈ 11Å wavelength of the Na transitions for a sufficient signal-to-noise in the spectra. The calculations of the tracer conditions suggest that, at the time data is taken, the density is too low for the shorter wavelength lines of a higher Z element to be broadened beyond the current spectral resolution of the spectrometers at the Z facility. More work needs to be done to verify that this is true, and/or improve the spectral resolution on these experiments.

Another common method for measuring the density of a planar sample is to image

the expansion. Assuming a constant ρx, the extent of the plasma dictates its density. In the experimental configuration presented in this thesis, measuring the tracer expansion would require a diagnostic utilizing a separate backlighter with sufficient strength to see through $\approx 1cm$ of CH_2 foam at a spatial resolution of $\approx 10\mu m$. This capability has recently become available on the Z facility using spherical crystal imaging and the Beamlet laser backlighter system [110]. This measurement should be made in order to verify the hydrodynamic calculations of the tracer response and put an additional constraint on the models.

One interesting possibility for the extension of this work is in the measurement of the plasma conditions within the foam itself. The method applied in this thesis was to measure the conditions in tracers, which were shown to be significantly out of thermal equilibrium with the CH_2. This was done as a measure of the radiation field propagated to the tracer location. However, the penetrating radiation only really depends on the spatially integrated conditions of the foam, and does not provide detailed information on the location of the thermal wave front in the CH_2. It would be interesting to measure the propagation of the thermal wave front in the foam samples by imaging the self-emission from a direction perpendicular to the propagation of the driving radiation. If this was done in conjunction with the backlit tracer spectroscopy, then one would have information on both the radiation that penetrates into the foam and that which is absorbed and propagated in the CH_2. This information could be crucial to understanding the integrated radiative transfer in the dynamic-hohlraum driven ICF program.

However, making this measurement in the geometry employed throughout this thesis would be difficult. A useful side-on measurement of the foam self-emission requires that the emission propagated from the edge of the plasma be a good representation of the temperature on the interior. At the tens of eV temperatures of the foams in the

present geometry, the optical depth of the CH_2 would require that the foam samples be very narrow in the direction perpendicular to the propagating radiation. If left unconstrained, the foams would expand in this perpendicular direction and the experiment could no longer by well modeled in 1-D. This negates a very important advantage of the present ride-along geometry. Thus, experiments that make this measurement would require constrained samples, which may require a great deal of development work to be successful.

Finally, consideration needs to be made on the applicability of the results in this thesis to the dynamic-hohlraum system on Z. As shown through the sensitivity studies in §6.4, these experiments primarily probe the opacity of CH_2 and the details of the radiation transport (group structure and transport approximation). Furthermore, the experiments are sensitive to these models for electron temperatures from $\approx 2 - 60eV$, and radiation energies from $\approx 100 - 2000eV$. The question is how does this relate to the conditions in the dynamic-hohlraum.

Figure 6.56 shows LASNEX simulated electron and radiation temperature histories at the center of a $5mg/cc$ CH_2 foam in the dynamic-hohlraum geometry defined in Figure 1.15. Also shown in this figure is the measured radiation temperature exiting the top of the foam cylinder. The time axis on this figure is shifted so that the peak of the capsule implosion occurs at $\approx 0ns$. Up to a time of $t \approx -8ns$, the electron temperature is in the range of the experiments studied in this thesis. Over the entire duration of this time period, the calculated radiation temperature is out of equilibrium with the electrons. This implies that radiation is propagated to the center of the foam that does not interact well with the CH_2 opacity. These photons are primarily in the low-opacity range below the carbon K-edge. Again, this is precisely the region where the experiments in this thesis were focused. The actual spectra that drive the foam is likely to be different

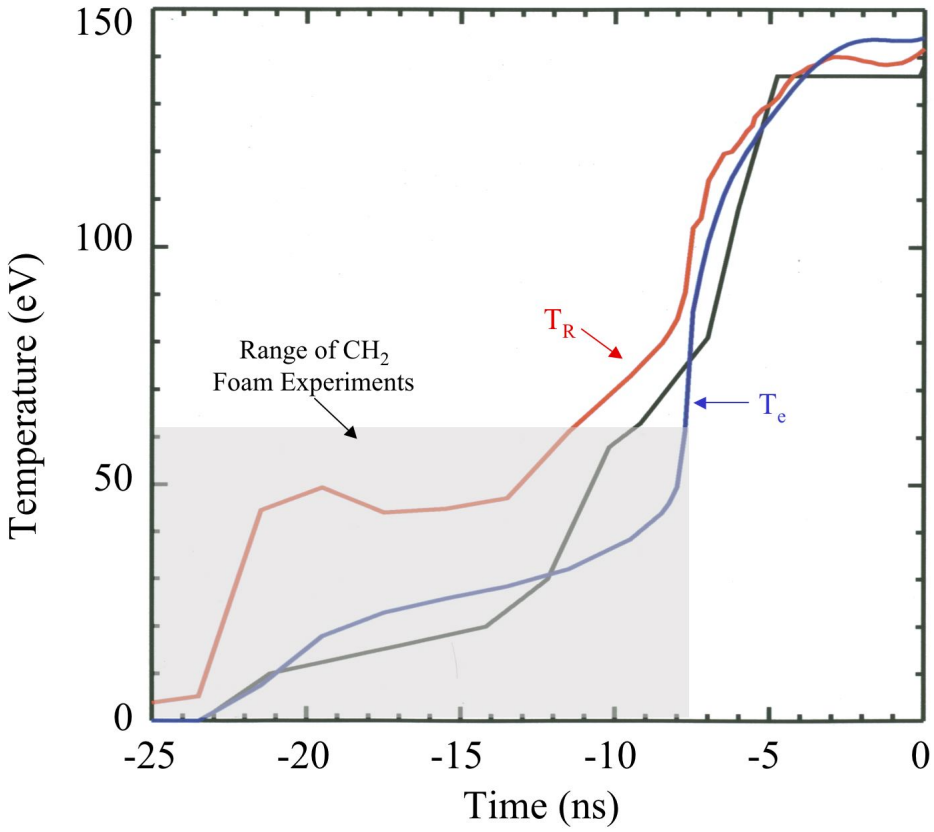

Figure 6.56: LASNEX simulated radiation (red) and electron (blue) temperature histories at the center of a $5mg/cc\ CH_2$ foam in the dynamic-hohlraum geometry shown in Figure 1.15. Also shown is the measured radiation temperature escaping out the top of the dynamic-hohlraum foam (black) [46].

from that used in this thesis, but the opacity and radiation-transport issues are the same. Therefore, the conclusions in this thesis are relevant to the dynamic-hohlraum system up to $\approx 8-10ns$ before the peak of the capsule implosion. This is the so called 'foot' of the radiation drive.

The experiments in this thesis have no relevance to the main drive-pulse. As seen in the figure, the foam temperature sharply increases to $> 100eV$ over about $1ns$ between -8 and $-7ns$. During this phase, the carbon in the CH_2 becomes fully stripped, the opacity of the foam rapidly drops, and the transport characteristics will be very different.

Experiments should be conducted that measure the radiative transfer in CH_2 under these conditions. However, these can not be done in the ride-along geometry employed throughout this thesis. To reach temperatures similar to that in the main drive-pulse will require dedicated experiments that use the radiation escaping from the top of dynamic-hohlraum during that phase. These should be done as an integral part of the dynamic-hohlraum driven ICF program plan.

Chapter 7

Conclusions

The first detailed experiments on the radiative transfer in $5mg/cc\ CH_2$ foam have been presented. Each of the experiments was conducted in a ride-along mode on Sandia National Laboratories Z facility, and used radiation emission from various z-pinch plasmas to drive the foam samples. These experiments measured the K-α absorption spectra from tracer layers buried in the foam, which serve as a diagnostic of the possible temperature and density conditions in the tracers. Calculations show that these conditions are sensitive to the amplitude and distribution of the penetrating radiation that propagates through the foam. A thorough χ^2 analysis between the measured absorption spectra and thousands of point calculations of the simulated K-α absorption features provided a statistical phase-space where the temperature and density of the tracer plasma are consistent with the observed spectra. This type of quantitative analysis is rarely done. While the application of spectroscopy to determine the conditions of a plasma is a well established diagnostic method, no examples of a full phase-space search of the plasma conditions corresponding to K-α absorption data could be found in the literature. This analysis was done with the SPECTROFIT χ^2 fitting code, which was developed for this

thesis.

In each of the foam experiments, the phase-space of possible temperature and density conditions in the tracer layers was used as a constraint on simulations of the foam dynamics. These simulations included a 3-D view-factor calculation of the radiation drive on the sample surface and a 1-D radiation-hydrodynamics calculation of the sample response and resulting tracer conditions. In each simulation, the tracer conditions were compared directly to the experimental phase-space and post-processed to determine the ionization states and associated spectral features. The synthetic spectra were then compared to the original experimental spectra to verify the consistency of the calculated results. Using a specific set of computational models, the simulations were shown to compare well with the experimental data.

Under the constraints of the experiments, these models provide insight into the radiative transfer process in $5mg/cc\ CH_2$ foam and lead to the following conclusions:

- For the plasma temperatures and z-pinch drive spectra as studied in this thesis, the opacity around the carbon K-edge in the spectral range $100eV < h\nu < 400eV$ is the most important factor that determines the amplitude and distribution of radiation that penetrates deep into a CH_2 plasma. The opacity of CH_2 in this spectral range was shown to have a very strong dependence on the temperature of the plasma. In the analysis of the foam experiment on shot z1122 in §6.3, this opacity was shown to drop by over a factor of 30 as the temperature increased from $\approx 2eV$ to $22eV$. Properly computing the radiative transfer in CH_2 foam under these conditions requires resolving the carbon K-edge with a suitable number of radiation groups. The best comparison to the experimental data was found using 500 logarithmically spaced energy groups in the range $0.1eV \leq h\nu \leq 10^4eV$. These calculations are well approximated by 40 unevenly spaced groups distributed with 10 groups in the

range $0.1eV \leq h\nu < 200eV$, 20 groups in the range $200eV \leq h\nu < 400eV$, and 10 groups in the range $400eV \leq h\nu \leq 10^4 eV$.

- The comparison of the tracer conditions to the experimental data is very sensitive to the CH_2 opacity model. The PROPACEOS DTA atomic model and associated tabular LTE opacity data for CH_2 were shown to provide solutions that are the most consistent with the experimental data. The EOSOPA DTA model was shown to be inconsistent with the experimental data at low temperatures. The primary differences between these models are in the assumed form of the statistical partition function and the handling of bound-free cross-section data. PROPACEOS assumes the Hummer-Mihalas partition function to compute the occupation probabilities and interpolates on tabulated Hartree-Fock cross-sections to compute the bound-free opacities. EOSOPA assumes the Boltzmann partition function and uses analytic fits to the bound-free cross-sections. The PROPACEOS model appears to be more correct.

- Throughout the range of temperatures and densities studied in this thesis, the XSN average-atom model predicts CH_2 opacities that are much too low in the range $100eV < h\nu < 300eV$. This model should be avoided wherever possible.

- Flux-limited diffusion is only an adequate transport approximation for making rough calculations of the radiation propagation into a CH_2 foam. For the conditions of the plasma and drive spectra in these experiments, the Larsen (n=6) flux-limiter agrees better with the data than the Levermore-Pomraning limiter. However, this may not be true for any other set of conditions. No conclusions can be drawn about which limiter is better in general. In addition, the simulations of the foam experiment on shot z1122 show as much as a 15% discrepency in the

calculated radiation temperature between flux-limited diffusion and the more accurate short-characteristics approximation. For the very stringent requirements of the radiation timing in ICF, one can not expect flux-limited diffusion to adequately predict the radiation transport.

- It has been speculated that, in a z-pinch driven system, high energy photons early in time may preheat a low-density low-Z foam ahead of the main radiation drive. This pre-heating would vaporize the solid strands and cause the foam material to homogenize so that it can be well modeled as an initially uniform density vapor. The data and calculations presented in this thesis are consistent with that speculation. However, no conclusion can be drawn as to whether this is true in the absence of the long radiation foot-pulse that preceded the main drive pulse in these experiments.
- The calculations of the CH_2 foam dynamics were found to be insensitive to the equation-of-state model. The SESAME, QEOS, and PROPACEOS equation-of-state models all predict conditions that are consistent with the data.
- The experiments presented in this thesis are relevant to the *foot pulse* of the dynamic-hohlraum ICF radiation drive in $5mg/cc$ CH_2 foam converters (up to $\approx 10ns$ before the peak of the capsule implosion). The stringent timing requirements of the radiation drive for successful ICF require that this phase of the dynamic-hohlraum be very well modeled. Using the experimental and computational methods presented in this thesis, more experiments should be done with differing radiation pulse shapes to further strengthen the conclusions drawn above. In addition, dedicated experiments on the Z facility should be conducted to extend the range of this work to temperatures $> 200eV$, which will be required to study the transfer dynamics during the main-pulse of the radiation drive.

References

[1] *President's Committee of Science Advisors on Science and Technology (PCAST) Panel on the U.S. Fusion Energy R&D Program*, (1995) (unpublished).

[2] J.L. Tuck, "Thermonuclear Reaction Rates," Los Alamos National Laboratory Report,LAMS-1640, (1954).

[3] C. Angulo et al. "A compilation of charged-particle induced thermonuclear reaction rates," Nuclear Physics A, **A656** No.1, p. 3 (1999).

[4] K. S. Krane, *Introductory Nuclear Physics*, (Wiley, New York, 1988).

[5] J. J. Duderstadt and G.A. Moses, *Inertial Confinement Fusion*, (Wiley, New York,1982).

[6] J. H. Nuckolls, L. Wood, A. Thiessen, and G.B. Zimmerman, "Laser compresssion of matter to super-high densities: thermonuclear (CTR) applications," Nature **239** No. 5368, p. 139 (1972).

[7] K. A. Brueckner and S. Jorna, "Laser-driven fusion," Rev. Mod. Phys., **46** No. 2, p. 325 (1974).

[8] T. R. Dittrich, S. W. Haan, M. M. Marinak, S. M. Pollaine, and R. McEachern, "Reduced scale National Ignition Facility capsule design," Physics of Plasmas, **5** No. 10, p. 3708 (1998).

[9] *Inertial Fusion Energy: Opportunity for Fusion Innovation*, UCRL-MI-125743 (Lawrence Livermore National Laboratory, 1997).

[10] J. D. Lindl, *Inertial Confinement Fusion: The Quest for Ignition and Energy Gain Using Indirect Drive*, (Springer-Verlag New York Inc., New York, 1998).

[11] J. J. MacFarlane, G. A. Moses, R. R. Peterson, "BUCKY-1 - A 1-D Radiation Hydrodynamics Code for Simulating Inertial Confinement Fusion High Energy Density Plasmas," UWFDM-984 (University of Wisconsin Fusion Technology Institute, 1995).

[12] W. J. Hogan, et al., "The National Ignition Facility," Nucl. Fusion, **41** No. 5, p. 567 (2001).

[13] J. A. Paisner, E. M. Campbell, and W. J. Hogan, "The National Ignition Facility protect," Fusion Technology, **26** No. 3, p. 755 (1994).

[14] G.S. Fraley, E.J. Linnebur, R.J. Mason, and R.L. Morse, "Thermonuclear burn characteristics of compressed deuterium-tritium microspheres," Phys. Fluids, **17**, p. 474 (1974)

[15] C. Kittel and H. Kroemer, *Thermal Physics*, (W.H. Freeman and Co., New York, 1980)

[16] R.E. Olson, private communication

[17] J. H. Nuckolls, "Laser-induced implosion and thermonuclear burn," Laser Interaction and Related Plasma Phenomena, Vol. **3B**, pp. 399-425 (Plenum, New York, 1994).

[18] *Inertial Confinement Fusion*, edited by K. A. Brueckner, (American Institute of Physics, New York, 1992).

[19] S. Eliezer and H. Hora, "The physics of directly driven targets," Nuclear Fusion by Inertial Confinement: A Comprehensive Treatise, p. 43, (CRC Press, Inc., Boca Raton, 1993).

[20] D. Cook et al., "Light ion driven inertial confinement fusion," Plasma Physics and Controlled Nuclear Fusion Research 1992, Vol. **3**, pp. 63-71 (International Atomic Energy Agency, Vienna, 1993).

[21] J. E. Rothenberg, "Polarization beam smoothing for inertial confinement fusion," Journal of Applied Physics, **87** No. 8, 3654 (2000).

[22] L. Phillips et al., "New Target Designs for Direct-Drive ICF," Laser and Particle Beams, **17** No.2, p. 225 (1999).

[23] Haan, S. M. Pollaine, J. D. Lindl et al.,"Design and modeling of ignition targets for the National Ignition Facility," Phys. Plasmas **2** No. 6, p. 2480 (1995).

[24] L. Suter et al., "Exploring the limits of the National Ignition Facilitys capsule coupling," Phys. Plasmas, **7** No. 5, p. 2092 (2000).

[25] S. P. Lyon and J. D. Johnson, "Sesame: The Los Alamos National Laboratory Equation of State Database," Los Alamos National Laboratory Report, LA-UR-92-3407 (1992).

[26] R. E. Kidder, "Theory of homogeneous isentropic compression and its application to laser fusion," Nuclear Fusion, **14** No. 1, p. 53 (1974).

[27] R. E. Kidder, "Laser compression of matter: optical power and energy requirements," Nuclear Fusion, **14** No. 4, p. 797 (1974).

[28] R. E. Kidder, "Laser-driven compression of hollow shells: power requirements and stability limitations," Nuclear Fusion, **16** No. 1, p. 3 (1976).

[29] R. E. Kidder, "Energy gain of laser-compressed pellets: a simple model calculation," Nuclear Fusion, **16** No. 3, p. 405 (1976).

[30] R. E. Kidder, "Laser-driven isentropic hollow-shell implosions: the problem of ignition," Nuclear Fusion, **19** No. 2, p. 223 (1979).

[31] Ya. B. Zeldovich and Yu. P. Raizer, *Physics of Shock Waves and High-Temperature Hydrodynamic Phenomena*, (Academic Press, New York, 1966).

[32] G.B. Zimmerman and W.L. Kruer, "Nuclear simulation of laser-initiated fusion," Comm. Plasma Phys. Controlled Nuc. Fusion, **2** No. 2, p. 51 (1975).

[33] R. E. Olson, "Shock Timing and Yield Sensitivity studies for NIF Ignition Capsules," Fusion Technology, **38**, p. 6, (2000).

[34] J.D. Kilkenny et al., "Lawrence Livermore National Laboratory's activites to achieve ignition by X-ray drive on the National Ignition Facility," Laser Particle Beams, **17** No. 2, p. 159 (1999).

[35] W.J. Krauser et al., "Ignition target design and robustness studies for the National Ignition Facility, " Phys. Plasmas, **3** No. 5, p. 2084 (1996).

[36] W. H. Bennett, "Magnetically self-focussing streams," Phys. Rev., **45**, p. 890, (1934).

[37] L. Tonks, "Theory of magnetic effects in the plasma of an arc," Phys. Rev., **56**, p. 360, (1939).

[38] C. W. Hartman, J.L. Eddleman, A.A. Newton, L.J. Perkins, and U. Shumlak, "Magnetic confinement fusion and the continuous-flow pinch," Comments on Plasma Physics and Controlled Fusion., **17** No.5, p. 267 (1996).

[39] D. D. Ryutov, M. S. Derzon, and M. K. Matzen, *The Physics of Fast Z Pinches*, SANDIA report, SAND98-1632, (1998).

[40] D. L. Peterson et al., "Characterization of energy flow and instability development in two-dimensional simulations of hollow z-pinches," Physics of Plasmas, **5** No. 9, p. 3302 (1998).

[41] R. B. Spielman et al., "PBFA II-Z: A 20-MA driver for Z-pinch experiments," Tenth IEEE International Pulsed Power Conference, 1, p. 396, (1995).

[42] R. B. Spielman et al., "Wire-array z-pinches as intense x-ray sources for inertial confinement fusion," Plasma Phys. Control. Fusion, **42**, p. B157 (2000).

[43] R. J. Leeper et al., "Z-pinch driven inertial confinement fusion target physics research at Sandia National Laboratories," Nuclear Fusion, **39** No. 9Y, p. 1283 (1999).

[44] B. Schwarzschild, "Inertial-Confinement Fusion Driven by Pulsed Power Yields Thermonuclear Neutrons," Phys. Today, July, p. 19 (2003).

[45] J. H. Brownell, R. L. Bowers, K. D. McLenithan, and D. L. Peterson, "Radiation environments produced by plasma z-pinch stagnation on central targets," Physics of Plasmas, **5** No. 5, p. 2071 (1998).

[46] J.E. Bailey et al., "X-Ray imaging measurements of capsule implosions driven by a Z-pinch dynamic hohlraum," Phys. Rev. Letters, **89** No. 9, p. 95004-1 (2002).

[47] S.A. Slutz, Personal Communication

[48] S.A. Slutz et al., "Dynamic hohlraum driven inertial fusion capsules," Phys. of Plasmas, **10** No. 5, p. 1875 (2003).

[49] J.E. Bailey et al., "Spectroscopy of argon-doped capsule implosions driven by a Z-pinch dynamic hohlraum," Radiative Properties of Hot Dense Matter, St. Malo, France (2002).

[50] E. E. Lewis and W.F. Miller Jr., *Computational Methods of Neutron Transport*, (American Nuclear Society, La Grange Park, IL, 1993).

[51] J. J. Duderstadt and L. J. Hamilton, *Nuclear Reactor Analysis*, (Wiley, New York, 1976).

[52] J. R. Lamarsh, *Introduction to Nuclear Engineering*, (Addison-Wesley Inc., Reading, MA, 1983).

[53] D. Mihalas, *Stellar Atmospheres*, (W. H. Freeman and Co., San Francisco, 1978).

[54] G. B. Rybicki and A. P. Lightman, *Radiative Processes in Astrophysics*, (Wiley, New York, 1979).

[55] T.A. Brunner, private communication

[56] C.D. Levermore and G.C. Pomraning, "A Flux-Limited Diffusion Theory," Astrophys. J., **248**,p. 321 (1979).

[57] G. L. Olson, L. H. Auer, and M. L. Hall, "Diffusion, P1, and other approximate forms of radiation transport," J. Quant. Spectrosc. Radiat. Transfer, **64**, p. 619 (2000).

[58] C.D. Levermore, " A Champman-Enskog Approach to Flux-Limited Diffusion Theory," Lawrence Livermore National Laboratory Report, Livermore, CA, UCID-18229 (1979).

[59] G. A. Moses, private communication

[60] G.L. Olson and P. B. Kunasz, "Short characteristic solution of the non-LTE line transfer problem by operator perturbation-I. The one-dimensional planar slab," J. Quant. Spectrosc. Radiat. Transfer, **38** No. 5, p. 325 (1987).

[61] P. B. Kunasz and G. L. Olson, "Short characteristic solution of the non-LTE line transfer problem by operator perturbation-II. The two-dimensional planar slab," J. Quant. Spectrosc. Radiat. Transfer, **39** No. 1, p. 1 (1988).

[62] K.E. Olson and D.L. Henderson, "Time dependent radiation transport in hohlraums using integral transport methods," Fusion Tech., **34** No.3, p.848 (1998).

[63] A.K. Prinja and G.L. Olson, "Radiative transfer in stochastic media with material temperature coupling," Transactions of the American Nuclear Society, **87**, p.135 (2002).

[64] Bingjing Su and G.L. Olson, "Non-grey benchmark results for two temperature non-equilibrium radiative transfer," J. Quant. Spectrosc. Radiat. Transfer, **62** No. 3, p. 279 (1999).

[65] T.A. Brunner, "Forms of approximate radiation transport - comparisons of the common methods," ANS M and C Conference, April, 2003.

[66] O. Willi et al., "Inertial confinement fusion and fast ignitor studies," Nuclear Fusion, **40** spec. issue, p. 537 (2000).

[67] D. G. Colombant, S. E. Bodner et al., "Effect of radiation on direct-drive laser fusion targets," Physics of Plasmas, **7** No. 5, p. 2046 (2000).

[68] O. Willi et al., "Inertial confinement fusion research using the VULCAN high power laser system," Plasma Physics and Controlled Nuclear Fusion Research 1994, **3**, p. 27 (1995).

[69] S. Yu. Gus'kov et al., "Scattering of laser radiation at the heating of low density foam targets," Laser and Particle Beams, **17** No. 2, p. 287 (1999).

[70] D. Hoarty, A. Iwase, C. Meyer, J. Edwards, and O. Willi, "Characterization of laser driven shocks in low density foam targets," Phys. Rev. Let, **78** No. 17, p. 3322 (1997).

[71] C. A. Back et al., "Diffusive, supersonic X-ray transport in radiatively heated foam cylinders," Physics of Plasmas, **7** No. 5, p. 2126 (2000).

[72] C. A. Back et al., "Detailed measurements of a diffusive supersonic wave in a radiatively heated foam," Phys. Rev. Let, **84** No. 2, p. 274 (2000).

[73] T. Afshar-Rad et al., "Supersonic propagation of an ionization front in low density foam targets driven by thermal radiation," Phys. Rev. Let, **73** No. 1, p. 74 (1994).

[74] D. Hoarty, O. Willi, L. Barringer, C. Vickers, R. Watt, and W. Nazarov, "Observation of ionization fronts in low density foam targets," Physics of Plasmas, **6** No. 5, p. 2171 (1999).

[75] D. Hoarty, L. Barringer, C. Vickers, O. Willi, and W. Nazarov, "Observation of transonic ionization fronts in low-density foam targets," Phys. Rev. Let, **82** No. 15, p. 3070 (1999).

[76] M. Lebedev et al., "Supersonic heat wave in low density foams generated by soft X-radiation from a Z-pinch plasma," Phys. Let A, **240** No. 1-2, p. 73 (1998)

[77] O. Willi, L. Barringer, C. Vickers, and D. Hoarty, "Study of super- and subsonic ionization fronts in low-density, soft X-ray-irradiated foam targets," Astrophysical Journal Supplement Series, **127** No. 2, p. 527 (2000).

[78] J. Massen et al., "Supersonic radiative heat waves in low-density high-Z material," Phys. Rev. E, **50** No. 6, p. 5130 (1994).

[79] J. Aubrey, R. L. Bowers, D. L. Peterson, G. A. Chandler, M. S. Derzon, T. J. Nash, and D. L. Fehl, "Radiation history and energy coupling to cylindrical target on the Z machine," Abstracts: 1999 IEEE International Conference on Plasma Science, p. 122 (1999).

[80] J. J. MacFarlane, M. S. Derzon, T. J. Nash, G. A. Chandler, and D. L. Peterson, "On the transparency of foam in low-density foam Z-pinch experiments," Rev. Sci. Inst., **70** No. 1, p. 323 (1999).

[81] D. Schroen, private communication.

[82] T. S. Perry et al., "Opacity measurements in a hot dense medium," Phys. Rev. Lett., **67** No.27, p.3784 (1991).

[83] T. S. Perry et al., "Quantitative measurement of mid-z opacities," J. Quant. Spectrosc. Radiat. Transf. **54**, p.317 (1995)

[84] P. T. Springer et al., "Spectroscopic absorption measurements of an iron plasma," Phys. Rev. Lett. **69**, p.3735 (1992).

[85] C. Chenais-Popovics et al., "Radiative heating of B, Al and Ni thin foils at 15-25 eV temperatures," J. Quant. Spectrosc. Radiat. Transf. **65**, p.117 (2000).

[86] T.J. Nash et al., "Diagnostics on Z," Rev. Sci. Instr., **72** No.1,p.1167 (2001).

[87] G.A. Chandler, et al., "Filtered X-ray diode diagnostics fielded on the Z accelerator for source power measurements," Rev. Sci. Inst. **70** No.1, pt.1-2, p.561 (1999).

[88] R.B. Spielman et al., "Fielding and calibration issues for diamond photoconducting detectors," Rev. Sci. Instr., **68** No.1, p.782 (1997).

[89] L.E. Ruggles et al., "Calibration of a time-resolving spectrometer in the 100-800 eV spectral region," Rev. Sci. Instr., **68** No., p.1063 (1997).

[90] M.E. Cuneo et al., "Characterization of z-pinch soft x-ray sources on the Z accelerator and applications to z-pinch-driven photoionization experiments," 4th Conference on High Energy Density Laboratory Astrophysics, Ann Arbor, MI, Feb. (2002).

[91] P. Wang, "EOSOPC - A Code for Computing the Equations of State and Opacities of High Temperature Plasma with Detailed Atomic Models," UWFDM-933, (University of Wisconsin Fusion Technology Institute, 1993).

[92] J. J. MacFarlane, "VISRAD: A 3-D view factor code and design tool for high energy density physics experiments," PCS-R-039,(Prism Computational Sciences, 2003).

[93] J. J. MacFarlane, private communication.

[94] A. R. Thomas-Cramer and K. A. Park, "Spect3D Imaging and Spectral Analysis Suite," PCS-R-003, (Prism Computation Sciences, Madison, WI, 2000).

[95] P. Wang, "Computation and Application of Atomic Data for Inertial Confinement Fusion Plasmas," UWFDM-855, (University of Wisconsin Fusion Technology Institute, 1991).

[96] J. J. MacFarlane, J. E. Bailey, T. A. Mehlhorn, G. A. Chandler, T. J. Nash, C. Deeney, and M. R. Douglas, "Simulating the radiation environment in Z experiments using a 3D view factor code with 1D radiation-hydrodynamics emission modeling," Rev. Sci. Instr., **72** No. 1, p. 1228 (2001).

[97] D.G. Hummer and D. Mihalas, "The equation of state for stellar envelopes. I. An occupation probability formalism for the truncation of internal partition functions," Astrophys. J., **331** No. 2, p. 794 (1988).

[98] B. Su and G.L. Olson, "Benchmark results for the non-equilibrium marshak diffusion problem," J. Quant. Spectrosc. Radiat. Transfer, **56** No. 3, p. 337 (1996).

[99] B. Su and G.L. Olson, "An analytical benchmark for non-equilibrium radiative transfer in an isotropically scattering medium," Ann. Nucl. Energy, **24** No. 13, p. 1035 (1997).

[100] J. Yuan, G.A. Moses, and G.A. Rochau, "A Graphical Tool for Computing Opacities for ICF Applications," International Journal of Modeling and Simulation, **23** No. 4, p. 218 (2003).

[101] M.E. Cuneo, et al., "Development and characterization of a Z-pinch-driven hohlraum high-yield inertial confinement fusion target concept," Phys. Plasmas, **8** No. 5, p.2257 (2001).

[102] G.A. Chandler, et al., "Z-pinch radial behavior using 1D visible and X-ray streak measurements on the Z-accelerator," 13th IEEE International Pulsed Power Conference, Las Vegas, NV, June (2001).

[103] M. L. Kiefer and M. M. Widner, "SCREAMER," 5th Institute of Electrical and Electronics Engineers (IEEE) Pulsed Power Conference, Arlington, VA (1995).

[104] M.E. Cuneo, private communication.

[105] T.W. Sanford, et al., "Dynamics and characteristics of a 215-eV dynamic-hohlraum X-ray source on Z," Phys. Plasmas, **9** No. 8, p. 3573, (2002).

[106] R.M. More, K.H. Warren, D.A. Young, and G.B. Zimmerman, "A new quotidian equation of state (QEOS) for hot dense matter," Physics of Fluids, **31** No.10, p.3059 (1988)

[107] J. J. MacFarlane, J. E. Bailey, et al., "X-ray absorption spectroscopy measurements of thin foil heating by Z-pinch radiation," Phys. Rev. E, **66** No.4, p. 46416-1-10, (2002).

[108] G. Pollak, "Detailed physics of the XSN-U opacity package," Lawrence Livermore National Laboratory report, LA-UR-90-2423, (1980?).

[109] J. J. MacFarlane, private communication.

[110] D.B. Sinars, et al., "Monochromatic x-ray backlighting of wire-array z-pinch plasmas using spherically bent quartz crystals," Rev. Sci. Instr., **74** No. 3, p. 2205, (2003).

Appendix A

EXRAY

Before the calculations described in Chapter 4 can be compared to the experimental data, this data must be reduced from the raw form in which it is generated to a form that is synergistic with the calculated values. In the case of a film-based spectrometer, the raw data is in the form of a spatially variant film exposure. This may be x-ray or optical film, but in either case the raw data must be corrected for film efficiency, converted from spacial to wavelength coordinates, and then corrected for the efficiency of the crystal reflectivity and geometry. Finally, the data must be adjusted by the transmission of any filters in the spectrometer and the quantum efficiency of the micro-channel plate intensifier (if one was used). For the purpose of increasing the consistency and accuracy of this data reduction process, a code called EXRAY was developed to quickly and consistently apply each of the corrections listed above. This code is specialized to the spectrometer configurations on Sandia's Z machine (see §1.3), and therefore contains ray-tracing capabilities for both elliptical and convex geometries.

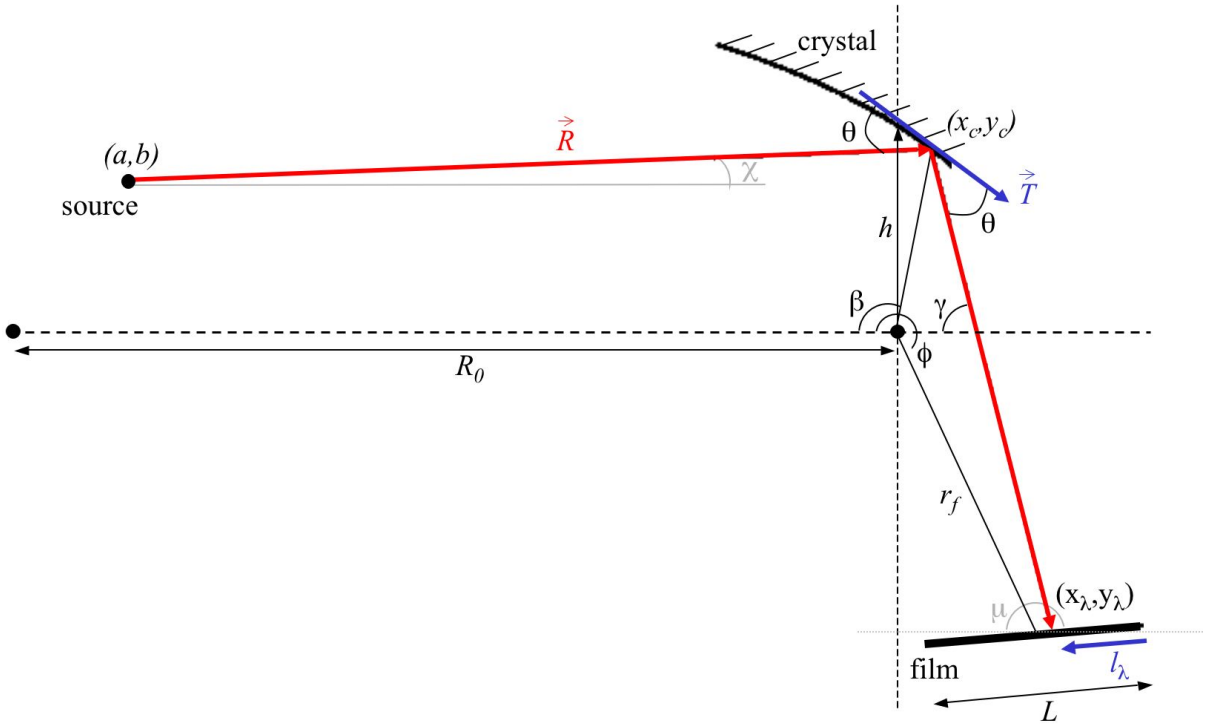

Figure A.1: Geometry of the elliptically curved crystal spectrometer.

A.1 Elliptical Ray-Tracing

The geometry of an elliptically bent crystal spectrometer is defined in Figure A.1 for an elliptical surface of eccentricity, ϵ, defined by:

$$\epsilon = \sqrt{1 + (h/R_0)^2} - h/R_0, \tag{A.1}$$

where h is the distance from a focus to the ellipse surface along a path perpendicular to the elliptical axis, and R_0 is the separation between the two ellipse focii (referred to as the spectrometer focal length). In the elliptical coordinate system defined by Figure A.1, the surface of the ellipse can be described by:

$$\left(x + \frac{R_0}{2}\right)^2 \left(1 - \epsilon^2\right) + y^2 - \frac{h^2}{1 - \epsilon^2} = 0, \tag{A.2}$$

so that the tangent vector to the ellipse surface, $\vec{T} = \hat{x} + \frac{dy}{dx}\hat{y}$, is derived as:

$$\vec{T} = \hat{x} - \frac{\left(x + \frac{R_0}{2}\right)(1-\epsilon^2)}{y}\hat{y}. \tag{A.3}$$

The intersection angle between the tangent vector and a ray originating from source point (a, b), $\vec{R} = (x-a)\hat{x} + (y-b)\hat{y}$, can be derived by the dot-product, $\vec{R}\cdot\vec{T} = |R||T|\cos\theta = R_x T_x + R_y T_y$, to give:

$$\begin{aligned}\left[(x-a)^2 + (y-b)^2\right]^{1/2}&\left[1 + \left(\frac{-\left(x + \frac{R_0}{2}\right)(1-\epsilon^2)}{y}\right)^2\right]^{1/2}\cos\theta \\ &= (x-a) + (y-b)\left[\frac{-\left(x + \frac{R_0}{2}\right)(1-\epsilon^2)}{y}\right].\end{aligned} \tag{A.4}$$

Assuming that θ is the Bragg angle defined by:

$$n\lambda = 2d\sin\theta, \tag{A.5}$$

for n the diffraction order and d the crystal lattice spacing, then Eq. A.4 defines which wavelength will diffract off the elliptical crystal at point (x, y).

For practicality, EXRAY uses the polar β coordinate rather than the Cartesian coordinates listed above. These coordinate systems are related in terms of the ellipse eccentricity as:

$$\begin{aligned}x &= \frac{-h\cos\beta}{1-\epsilon\cos\beta} \\ y &= \frac{h\sin\beta}{1-\epsilon\cos\beta},\end{aligned}$$

so that Eq. A.4 can be recast into the polar coordinate system as:

$$\begin{aligned}\left[1 + \left(\frac{\epsilon - \cos\beta}{\sin\beta}\right)^2\right]^{1/2}&\left[\left(\frac{-h\cos\beta}{1-\epsilon\cos\beta} - a\right)^2 + \left(\frac{h\sin\beta}{1-\epsilon\cos\beta} - b\right)^2\right]^{1/2}\cos\theta \\ &= \left(\frac{-h\cos\beta}{1-\epsilon\cos\beta} - a\right) - \left(\frac{h\sin\beta}{1-\epsilon\cos\beta} - b\right)\frac{\epsilon - \cos\beta}{\sin\beta}.\end{aligned} \tag{A.6}$$

This equation is highly non-linear in β, and must therefore be solved numerically for any given value of λ (i.e. a given θ) [a]. In EXRAY, this equation is solved by a secant iterative solver [1, 2] for a user defined grid of x-ray wavelengths. Note that, because of the general definition of the source point at (a, b), Eq. A.6 places no restrictions on the source location and will therefore provide the position and direction of the diffracted ray for a source located anywhere in space. Furthermore, in the case that the source is located at the ellipse focus, $(R_0, 0)$, then it can be shown that Eq. A.6 reduces to:

$$\beta = \theta + \cos^{-1}\left(\frac{\cos\theta}{\epsilon}\right), \tag{A.7}$$

which is the form given by Henke et al. [3].

Once the diffraction vector has been determined, then the x-ray wavelength can be related to a position on the film by determining the point where the diffracted ray intersects the film plane. The equation for the vertical position of the diffracted ray, $y_r(x)$, can be written as:

$$y_r(x) = y_c - (x - x_c)\tan\gamma, \tag{A.8}$$

where (x_c, y_c) are the coordinates (along the crystal surface) from which the diffracted ray originates and γ is the angle between the diffracted ray and the elliptical axis $\left(\gamma = 2\theta = \tan^{-1}\left[\frac{y_c - b}{x_c - a}\right]\right)$. In addition, the equation for the vertical position of the film plane, $y_f(x)$, can be written as:

$$y_f(x) = r_f \sin\phi - (x + r_f\cos\phi)\tan\mu, \tag{A.9}$$

where r_f and ϕ define the polar coordinates of the film center and μ defines the pitch angle of the film plane. Therefore, equating Eq. A.8 and A.9 provides the coordinates of

[a] On the other hand, the equation is linear in θ, and can be easily solved directly for a given value of β.

the intersection, (x_λ, y_λ), as:

$$\begin{aligned} x_\lambda &= \frac{(r_f \sin\phi - y_c) + r_f \cos\phi \tan\mu - x_c \tan\gamma}{\tan\mu - \tan\gamma} \\ y_\lambda &= y_r(x) = y_c - (x - x_c)\tan\gamma. \end{aligned} \tag{A.10}$$

These coordinates can then be transformed into the reference frame of the film plane by the equation:

$$l_\lambda = \frac{r_f \sin\phi + \frac{L}{2}\sin\mu - y_\lambda}{\sin\mu}, \tag{A.11}$$

where L is the film length and l_λ is measured from the short-wavelength side of the film. Once this term has been calculated for a distribution of wavelengths, then the identification of a single line in the experimental spectrum indexes the real film positioning to the calculation, and the film position coordinates can be transformed into x-ray wavelength.

A.2 Convex Ray-Tracing

The geometry of a convex crystal spectrometer is shown in Figure A.2 for a crystal of radius r_c, and a linear film plane of length L placed a distance r_f from the intersection of the crystal surface and the $\hat{y}$ axis. By inspection of the angular geometry, it can be derived that the polar angle of diffraction, β, can be expressed as:

$$\beta = \pi + \tan^{-1}\left(\frac{b}{|a|}\right) - 2\theta - \omega, \tag{A.12}$$

where θ is again given by Eq. A.5 and the angle ω is given by:

$$\omega = \sin^{-1}\left(\frac{r_c \sin\left(\frac{\pi}{2} - \theta\right)}{\sqrt{a^2 + b^2}}\right). \tag{A.13}$$

In contrast to the elliptical diffraction angle given by Eq. A.6, Eq. A.12 can be solved directly for a given value of λ (θ). However, the equation is non-linear in θ, and must therefore be solved numerically for any given value of β.

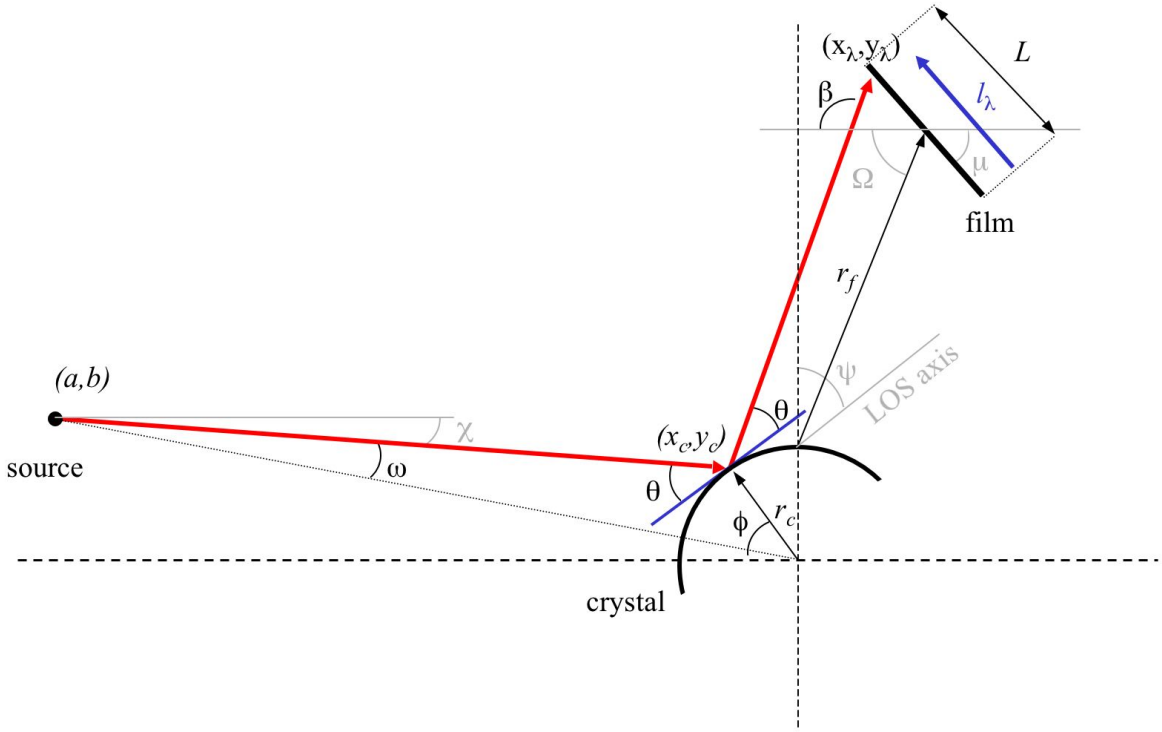

Figure A.2: Geometry of the convex curved crystal spectrometer.

As done in §A.1, the coordinates of the intersection point between the diffracted ray and the film plane can be derived from the equations for the ray, y_r, and the film, y_f, given by:

$$y_r = (x_c - x)\tan\beta + y_c \tag{A.14}$$

$$y_f = (r_f\cos\Omega - x)\tan\mu + r_f\sin\Omega + r_c, \tag{A.15}$$

where the diffraction coordinates (x_c, y_c) can be expressed as:

$$x_c = -r_c\cos\left(\frac{\pi}{2} - \theta - \omega + \tan^{-1}\left(\frac{b}{|a|}\right)\right)$$
$$y_c = r_c\sin\left(\frac{\pi}{2} - \theta - \omega + \tan^{-1}\left(\frac{b}{|a|}\right)\right).$$

Equating Eq. A.14 and A.15 then gives the intersection coordinates as:

$$x_\lambda = \frac{x_c \tan\beta - r_f \cos\Omega \tan\mu + y_c - r_f \sin\Omega - r_c}{\tan\beta - \tan\mu} \tag{A.16}$$

$$y_\lambda = r_f \sin\Omega + (r_f \cos\Omega - x_\lambda)\tan\mu, \tag{A.17}$$

which can be transformed into film coordinates to give:

$$l_\lambda = \frac{y_\lambda + \frac{L}{2}\sin\mu - r_f \sin\Omega - r_c}{\sin\mu}. \tag{A.18}$$

If the film plane is instead curved to a constant radius, r_f, then the equation for the film is given by:

$$y_f = \sqrt{r_f^2 - x^2} + r_c, \tag{A.19}$$

and the equation for the intersection point in film coordinates is given by:

$$l_\lambda = r_f \tan^{-1}\left(\frac{y_\lambda - r_c}{x_\lambda}\right), \tag{A.20}$$

where the point (x_λ, y_λ) must be determined by equating Eq. A.14 and A.19.

The coordinate axes in Figure A.2 are given in the crystal reference frame. In the convex spectrometer geometry, the spectral range is selected by rotating this reference frame by an angle ψ with respect to the spectrometer line-of-sight. Typically this rotation angle is chosen as the bragg angle of the median wavelength in the desired range. If the film plane is then placed at an angle of $\Omega = 2\psi$, then the median wavelength will diffract off the crystal at $(0, r_c)$, and intersect the film at a distance of $l_\lambda = L/2$. In EXRAY, the coordinates of the source and the location of the film plane are specified in the spectrometer reference frame. Therefore, they must be transformed into the reference frame of the crystal to be applicable to the equations derived above. These coordinate transformations are given by:

$$a = \sqrt{a'^2 + (r_c - b')^2}\sin\left[\tan^{-1}\left(\frac{a'}{r_c - b'}\right) + \psi\right] \tag{A.21}$$

$$b = -\sqrt{a'^2 + (r_c - b')^2}\cos\left[\tan^{-1}\left(\frac{a'}{r_c - b'}\right) + \psi\right] + r_c \tag{A.22}$$

$$\Omega = \Omega' - \psi, \tag{A.23}$$

where (a', b') and Ω' are the source coordinates and film angle in the line-of-sight reference frame.

A.3 Spectrometer Efficiency Corrections

Once a wavelength scale has been applied in one of the geometries listed above, EXRAY can correct the data for film response (on x-ray film), filter transmission, and crystal reflectivity.

A.3.1 X-ray Film Corrections

There are essentially 2 different x-ray film types in common use on Sandia's Z machine. These are Kodak RAR2497, and DEF. Each of these has been calibrated by Henke et al. [4–6] for energies in the range $1000eV \leq E \leq 10000eV$. In the case of the RAR film, the incident photon intensity, I, can be related to the film density, D, by a semi-empirical formula which is expressed as:

$$I = \frac{e^{\alpha D/a} - 1}{b\beta\left(1 - e^{-\mu' T/\sin\eta} e^{\alpha D/a}\right)}, \tag{A.24}$$

where a and b are parameters fit to the calibration data, T is the thickness of the film emulsion ($AgBr$ in a gelatin base), μ' is a heterogeneous absorption coefficient given by:

$$\mu' = \mu_0 - (1/d_g)\ln\left[1 - V\left(1 - e^{-(\mu_1 - \mu_0)d_g}\right)\right], \tag{A.25}$$

for μ_0 and μ_1 the absorption coefficients of the gelatin and $AgBr$ respectively, d_g the grain size of the $AgBr$, and V the volume fraction of the $AgBr$ in the emulsion. The

coefficients α and β in Eq. A.24 are related to the path length of the x-rays in the emulsion layer, and can be expressed as:

$$\alpha = \mu' / \sin\eta \tag{A.26}$$

$$\beta = \left(1 - e^{-\mu_1 d_g}\right) e^{-\mu_0 t / \sin\eta}, \tag{A.27}$$

for η the angle between the incident radiation and the film plane. In contrast to RAR film types, the DEF film has a second emulsion on the back of the film which must be included in the film intensity conversion. In this case, Henke et.al. derive the relation between the film density and intensity to be:

$$D = \frac{a}{\alpha} \ln \left[\left(\frac{1 + b\beta I}{1 + b\beta I e^{-\mu' T / \sin\eta}} \right) \left(\frac{1 + b\beta I e^{(-\mu_b t_b - \mu' T)/\sin\eta}}{1 + b\beta I e^{(-\mu_b t_b - 2\mu' T)/\sin\eta}} \right) \right], \tag{A.28}$$

where μ_b and t_b are the linear absorption coefficient and thickness of the polyester film base.

Given that the absorption coefficients are a function of the x-ray wavelength, then Eq. A.24 and A.28 must be solved for each value of λ in the experimental spectrum. In EXRAY, a cubic spline is fit to the tabulated absorption data for μ_0, μ_1, and μ_b, with the option of using a linear fit across photo-ionization edges. So, depending on the film type used in the experiment, Eq. A.24 or A.28 can be applied in EXRAY to convert the film density data to incident photon intensity.

A.3.2 Spectrometer Geometry Corrections

In the authoritative paper on pulsed plasma spectroscopy [3], Henke et al. derive a general equation for the diffraction efficiency of a curved crystal spectrometer as:

$$\frac{dN}{dA} = \frac{S_0}{r_f L_r} \left(\frac{d\chi}{d\theta} \right) \left(\frac{d\theta}{d\beta} \right) \left(\frac{dE}{d\theta} \right) R, \tag{A.29}$$

where S_0 is the source intensity (in $photons/steradian/s/eV$), L_r is the total path length of the ray, R is the (energy dependent) crystal reflectivity, and χ is the angle between the incident ray and the $\hat{x}$ axis (see Figure A.1). Solving this for the source intensity and converting to units of $J/sr/A$ gives:

$$S_0 = \left[\frac{(1.602 \times 10^{-19}) r_f L_r (hc) \tan\theta}{-\left(\frac{d\chi}{d\theta}\right)\left(\frac{d\theta}{d\beta}\right)\lambda^2 R} \right] \frac{dN}{dA}. \tag{A.30}$$

After correcting for the film response, the experimental data is directly proportional to $\frac{dN}{dA}$ (in units of $photons/cm^2$), so that Eq. A.30 provides a general expression for the correction of the diffraction efficiency of any crystal geometry. In EXRAY, the differential terms $\frac{d\chi}{d\theta}$ and $\frac{d\theta}{d\beta}$ are easily calculated in the elliptical geometry when the source is located near the focal length of the crystal ($a \approx R_0$), and Eq. A.30 can be directly applied to experimental data acquired on an elliptical crystal spectrometer.

In Henke's derivation, the film radius, r_f, and the polar diffraction angle, β, are given with respect to the ellipse focus. This is convenient for the elliptical geometry because the focus is a real crossover point, and fixed for x-rays of all wavelengths. However, there is no real crossover in the convex geometry, so that β and r_f are functions of the x-ray wavelength as they appear in Eq. A.29. Brown and Fatemi [11] analyzed the efficiency of the convex geometry, where they derived the differential diffraction relation:

$$\frac{d\chi}{d\theta} = -\left[1 - \left(1 + \frac{a^2}{r_c^2 \sin^2\theta}\right)^{-1/2}\right] \frac{r_c}{s} \sin\theta, \tag{A.31}$$

for s the distance from the crystal axis to the source location ($s = \sqrt{a^2 + b^2}$). Then, realizing that $\frac{d\theta}{d\beta} = \frac{dE}{dl_\lambda}\frac{d\theta}{dE}\frac{dl_\lambda}{d\beta}$ and that $dl_\lambda \approx r_f d\beta$, Eq. A.30 can be written as:

$$S_0 = \left[\frac{(1.602 \times 10^{-19}) L_r s (hc)}{\left[1 - \left(1 + \frac{a^2}{r_c^2 \sin^2\theta}\right)^{-1/2}\right] r_c \lambda R \sin\theta} \left(\frac{dl_\lambda}{d\lambda}\right) \right] \frac{dN}{dA}, \tag{A.32}$$

where $\frac{dl_\lambda}{d\lambda}$ is the dispersion on the film plane. This is essentially the same form as derived by Brown and Fatemi, and is the equation used in EXRAY for correcting data acquired on a convex crystal spectrometer.

The crystal reflectivity, R, is the primary source of error in the crystal efficiency corrections. There are a few different models for the absorption and scattering coefficients in the crystals, but the data is fairly sparse. In EXRAY, the crystal reflectivity values are linearly interpolated from tables of calculations [7] that contain both the modified Darwin-Prins (MDP) [8], and mosaic models for multilayer reflection. It is up to the user decide which model should be applied for a particular crystal and diffraction order.

A.3.3 Filter and Photocathode Corrections

The final set of corrections that needs to be considered is the transmission fraction of any filter materials in the spectrometer, and the quantum efficiency of the photocathode (if one was used). In EXRAY, the correction for the transmission through a combination of N filters is calculated by:

$$I_0 = Ie^{\sum_{i=0}^{N} \mu_i \Delta t_i}, \tag{A.33}$$

where μ_i is the linear absorption coefficient of the i^{th} filter material (taken from the Biggs and Lighthill cold opacity tables [9]), I_0 and I are the incident and transmitted photon intensities, and Δt_i is the thickness of the i^{th} filter. Finally, the correction for the photocathode quantum efficiency can be written as:

$$I_0 = I/Q, \tag{A.34}$$

where Q is a wavelength dependent quantum efficiency term ($0 \leq Q \leq 1$). The only photocathodes considered in EXRAY are cesium-iodide and gold, where the quantum efficiencies are taken from tabulated data and calculations by Henke et al. [10].

A.4 References

[1] K. Cochrane, private communication.

[2] J.D. Hoffman, *Numerical Methods for Engineers and Scientists*, (McGraw-Hill, New York, 1992).

[3] B.L. Henke, et al., "Pulsed plasma source spectrometry in the 80-8000-eF x-ray region," Rev. Sci. Instr., **54** No. 10, p. 1311, (1983).

[4] B.L. Henke, et al., "Low-energy x-ray response of photographic films. I. Mathematical models," J. Opt. Soc. Am. B, **1** No. 6, p. 818, (1984).

[5] B.L. Henke, et al., "Low-energy x-ray response of photographic films. II. Experimental characterization," J. Opt. Soc. Am. B, **1** No. 6, p. 828, (1984).

[6] B.L. Henke, et al., "High-energy x-ray response of photographic films: models and measurements," J. Opt. Soc. Am. B, **3** No. 11, p. 1540, (1986).

[7] B.L. Henke, "The high-energy x-ray response of some useful crystal analyzers," technical note.

[8] B.L. Henke, et al., "Characterization of multilayer x-ray analyzers: models and measurements," Opt. Eng., **25** No. 8, p. 937, (1986).

[9] F. Biggs and R. Lighthill, "Analytical approximations for x-ray cross sections III," SANDIA report, SAND87-0070, (1987).

[10] B.L. Henke, "The characterization of x-ray photocathodes," technical note.

[11] D.B. Brown and M. Fatemi, "Diffraction efficiency of the curved-crystal spectrograph," J. Appl. Phys. **51** No. 5, p. 2540, (1980).

Appendix B

Verification and Analysis of Radiation Transport in BUCKY

In order to verify the implementation of the radiation transport approximations in BUCKY, it was necessary to design a verification test suite that assures the accuracy of the finite difference equations as they appear in the code. This verification is accomplished in essentially three parts: First, a few simple test problems are solved analytically by both time-independent transport and diffusion, and are compared to BUCKY calculations using both flux-limited diffusion and short-characteristics. Second, some analytic problems specific to the flux-limited diffusion equations are compared to BUCKY calculations to verify each of the terms specific to flux-limited diffusion (such as the flux-limiter). Third, two time-dependent benchmark problems, which are intended to verify both the radiation transport and the associated coupling between the radiation energy and the plasma energy, are compared to both flux-limited diffusion and short-characteristics.

Most of these problems are only applicable to planar geometries, and therefore the majority of the discussion takes place in Cartesian coordinates. However, because the

flux-limited diffusion equations are also implemented for cylindrical and spherical geometries, a few problems that are specific to diffusion are also tested in these coordinate systems.

After completion of this test suite, one can have confidence that the finite difference equations in each transport approximation are properly implemented to solve the equations for which they are intended. One should note, however, that this says nothing of the applicability of each transport approximation to a particular problem. This is a much more complicated issue, and must usually be addressed on a case-by-case basis.

B.1 Flux-Limited Diffusion in BUCKY

The diffusion approximation as given in Eq. 1.40, can be rewritten as:

$$\frac{\partial E}{\partial t} - \nabla c D \nabla E = -c\sigma_a E + 4\pi\sigma_e B_\nu + 4\pi S, \tag{B.1}$$

where $E = \frac{1}{c} I_0$ is the radiation energy density in units of J/cm^3, S is an external source term in units of $J/cm^3/s$, and the diffusion coefficient, D, can be limited by any of the flux-limiters disscused in §1.4.1. This is the form of flux-limited diffusion as it is implemented in BUCKY.

B.1.1 Diffusion Boundary Conditions

Obtaining a solution to Eq. B.1 requires a definition of E on each boundary. The boundary conditions for diffusion can be defined through the incoming and outgoing partial flux ($\vec{F} = (F_{in} + F_{out})\hat{r}$)as:

$$F_{in} = -\int_{-1}^{0} \mu I d\mu \tag{B.2}$$

$$F_{out} = \int_{0}^{1} \mu I d\mu. \tag{B.3}$$

Boundary Condition	$\mathcal{A}$	$\mathcal{B}$	$\mathcal{C}$
Dirichlet	1	0	E_0
Vacuum	$-1/2$	1	0
Source	$-1/2$	1	$-2\frac{1}{c}F_{\text{in}} = -\frac{2\pi}{c}B_\nu(T_{\text{source}})$
Reflection	0	1	0
Albedo	$\frac{1}{2}(\alpha-1)/(\alpha+1)$	1	0

Table B.1: Coefficients for the diffusion boundary conditions [2]. α is the fraction of radiation reflected by the albedo boundary.

These can be solved by applying the approximation [1]:

$$I(r,\mu,t) = \frac{1}{2}I_0 + \frac{3}{2}\mu I_1, \tag{B.4}$$

including the evaluation of I_1 from Eq. 1.37 to give:

$$\frac{1}{c}F_{in} = \frac{1}{4}E - (\vec{\hat{n}}\cdot\vec{\hat{r}})\frac{1}{2}D\frac{\partial E}{\partial r} \tag{B.5}$$

$$\frac{1}{c}F_{out} = \frac{1}{4}E + (\vec{\hat{n}}\cdot\vec{\hat{r}})\frac{1}{2}D\frac{\partial E}{\partial r}, \tag{B.6}$$

for $\vec{\hat{n}}$ the unit vector outward normal to the boundary surface.

There are many types of boundary conditions that are of interest in diffusion calculations. All can be prescribed by some combination of Eq. B.5 and Eq. B.6. To simplify this prescription, these equations can be generalized into a single expression that is valid for any boundary condition [2]:

$$\mathcal{A}E - (\vec{\hat{n}}\cdot\vec{\hat{r}})\mathcal{B}D\frac{\partial E}{\partial r} = \mathcal{C}. \tag{B.7}$$

Table B.1 lists the factors $\mathcal{A}$, $\mathcal{B}$, and $\mathcal{C}$ for Dirichlet, source, vacuum, and albedo boundary conditions.

B.1.2 Diffusion Finite Difference Equations

In order to solve Eq. B.1 in BUCKY, it must be converted to Lagrangian coordinates and written in finite-difference form. Lagrangian coordinates are, by definition, in the

reference frame of the fluid particle and must therefore automatically conserve mass. Thus, the conversion from Eulerian (observer) to Lagrangian (particle) coordinates can be written as:

$$dm = \rho(r) r^{\delta-1} dr, \tag{B.8}$$

where ρ is the fluid density and δ is a geometry-dependent factor which is 1 for planar geometry, 2 for cylindrical geometry, and 3 for spherical geometry.

Applying this conversion to Eq. B.1 and re-arranging terms gives:

$$V\frac{\partial E}{\partial t} = \frac{\partial}{\partial m}\left(r^{\delta-1} V c \frac{1}{3\sigma_t}\frac{\partial E}{\partial r}\right) - c\sigma_a E + 4\pi\sigma_e B_\nu + V 4\pi S, \tag{B.9}$$

where σ_t, σ_a, and σ_e have been converted to units of $\frac{cm^2}{g}$, and V is the specific volume given by:

$$V = \frac{1}{\rho}. \tag{B.10}$$

This description is precise for static fluids, but requires a correction to account for a time-dependent zone thickness in a Lagrangian description where no particles are allowed to cross a zone boundary. This correction is derived from the first law of thermodynamics in the particle reference frame [3]:

$$\frac{\partial e_r}{\partial t} + P_r \frac{\partial V}{\partial t} = \dot{Q}_r, \tag{B.11}$$

where e_r is the specific radiation energy in units of $\frac{J}{g}$, P_r is the radiation pressure in $\frac{J}{cm^3}$, and $\dot{Q}_r$ is the heating term equivalent to everything on the right hand side of Eq. B.9. Converting the specific radiation energy to the radiation energy density by $e_r = EV$ then gives:

$$V\frac{\partial E}{\partial t} + E\frac{\partial V}{\partial t} + P_r\frac{\partial V}{\partial t} = \dot{Q}_r. \tag{B.12}$$

Finally, inserting the classical form of the radiation pressure, $P_r = \frac{1}{3}E$, gives the full

Lagrangian description of the radiation diffusion equation:

$$V\frac{\partial E}{\partial t} = \dot{Q}_r - \frac{4}{3}E\frac{\partial V}{\partial t}, \tag{B.13}$$

or expanding $\dot{Q}_r$ from Eq. B.9:

$$V\frac{\partial E}{\partial t} = \frac{\partial}{\partial m}\left(r^{\delta-1}Vc\frac{1}{3\sigma_t}\frac{\partial E}{\partial r}\right) - \frac{4}{3}E\frac{\partial V}{\partial t} - c\sigma_a E + 4\pi\sigma_e B_\nu + V4\pi S. \tag{B.14}$$

As derived in the Lagrangian reference frame, this equation is applicable to planar, cylindrical, and spherical coordinates.

Solving Eq. B.14 in BUCKY requires binning the photon energies into groups. This means making some choice about how to weight the opacities. Typically, this weighting is done by assuming the plasma to be at near LTE so that the radiation field is well-modeled as a Planckian distribution. Under this assumption, the three opacities in Eq. B.14 can be binned into the Planck emission opacity:

$$\sigma^g_{P,e} = \frac{\int_{\nu_g}^{\nu_{g+1}} \sigma_e B_\nu d\nu}{\int_{\nu_g}^{\nu_{g+1}} B_\nu d\nu}, \tag{B.15}$$

the Planck absorption opacity:

$$\sigma^g_{P,a} = \frac{\int_{\nu_g}^{\nu_{g+1}} \sigma_a B_\nu d\nu}{\int_{\nu_g}^{\nu_{g+1}} B_\nu d\nu}, \tag{B.16}$$

and the Rosseland opacity:

$$\frac{1}{\sigma^g_R} = \frac{\int_{\nu_g}^{\nu_{g+1}} \frac{1}{\sigma_t} B_\nu d\nu}{\int_{\nu_g}^{\nu_{g+1}} B_\nu d\nu}, \tag{B.17}$$

where ν_g are the group boundaries (in eV) for G total radiation groups. Then, the multi-group radiation diffusion equation is written as:

$$V\frac{\partial E^g}{\partial t} = \frac{\partial}{\partial m}\left(r^{\delta-1}\kappa^g_R\frac{\partial E^g}{\partial r}\right) - E^g\frac{4}{3}\frac{\partial V}{\partial t} - c\sigma^g_{P,a}E^g + 4\pi\sigma^g_{P,e}B^g_\nu + V4\pi S^g, \tag{B.18}$$

where each term has been integrated from ν_g to ν_{g+1}, κ^g_R is the radiation conductivity given by:

$$\kappa^g_R = \frac{cV}{3\sigma^g_R} = cD^g, \tag{B.19}$$

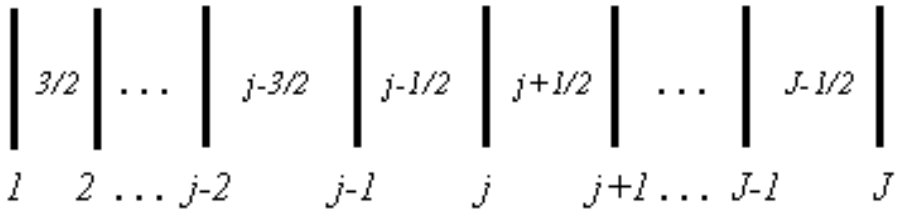

Figure B.1: Finite difference grid in BUCKY for $J-1$ zones with J boundaries.

and the multi-group diffusion coefficient, D^g, can be flux-limited by any one of the flux-limiters listed in §1.4.1.

In BUCKY, the radiation energy densities are stored as zone-centered values. Therefore, given the finite grid shown in Figure B.1, the finite difference form of Eq. B.18 can be written as:

$$\begin{aligned} V_{j-\frac{1}{2}}^{n+\frac{1}{2}} \frac{E_{j-\frac{1}{2}}^{g,n+1} - E_{j-\frac{1}{2}}^{g,n}}{\Delta t^{n+\frac{1}{2}}} &= \frac{1}{\Delta m_{j-\frac{1}{2}}} \left[\frac{{r_j^{\delta-1}}^{n+\frac{1}{2}} \kappa_{R,j}^{g,n+\frac{1}{2}}}{\Delta r_j^{n+\frac{1}{2}}} \left(E_{j+\frac{1}{2}}^{g,n+1} - E_{j-\frac{1}{2}}^{g,n+1} \right) \right] \\ &- \frac{1}{\Delta m_{j-\frac{1}{2}}} \left[\frac{{r_{j-1}^{\delta-1}}^{n+\frac{1}{2}} \kappa_{R,j-1}^{g,n+\frac{1}{2}}}{\Delta r_{j-1}^{n+\frac{1}{2}}} \left(E_{j-\frac{1}{2}}^{g,n+1} - E_{j-\frac{3}{2}}^{g,n+1} \right) \right] \\ &- E_{j-\frac{1}{2}}^{g,n+1} \frac{4}{3} \dot{V}_{j-\frac{1}{2}}^{n+\frac{1}{2}} - c\sigma_{P,a_{j-\frac{1}{2}}}^{g,n+\frac{1}{2}} E_{j-\frac{1}{2}}^{g,n+1} + 4\pi\sigma_{P,e_{j-\frac{1}{2}}}^{g,n+\frac{1}{2}} B_{\nu,j-\frac{1}{2}}^{g,n+\frac{1}{2}} \\ &+ V_{j-\frac{1}{2}}^{n+\frac{1}{2}} 4\pi S_{j-\frac{1}{2}}^{g,n+\frac{1}{2}}, \end{aligned} \tag{B.20}$$

where n is the time index, and the work term, $\dot{V}_{j-\frac{1}{2}}^{n+\frac{1}{2}}$, is given by:

$$\dot{V}_{j-\frac{1}{2}}^{n+\frac{1}{2}} = \frac{\left(r_j^{n+\frac{1}{2}}\right)^{\delta-1} u_j^{n+\frac{1}{2}} - \left(r_{j-1}^{n+\frac{1}{2}}\right)^{\delta-1} u_{j-1}^{n+\frac{1}{2}}}{\Delta m_{j-\frac{1}{2}}}, \tag{B.21}$$

for $u_j^{n+\frac{1}{2}}$ the fluid velocity evaluated at time $n+\frac{1}{2}$.

In addition, the radiation conductivity has a different implementation for each of the various forms of the flux-limiter. The finite-difference equations for each of these limiters

are given for the SUM-limiter:

$$\kappa_{R,j}^{g,n+\frac{1}{2}} = c\left[3\sigma_{R,j-\frac{1}{2}}^{g,n+\frac{1}{2}} V_{j-\frac{1}{2}}^{n+\frac{1}{2}} + 2\left(E_{j+\frac{1}{2}}^{g,n} + E_{j-\frac{1}{2}}^{g,n}\right)^{-1}\left|\frac{E_{j+\frac{1}{2}}^{g,n} - E_{j-\frac{1}{2}}^{g,n}}{\Delta r_j^{n+\frac{1}{2}}}\right|\right]^{-1} \tag{B.22}$$

the MAX-limiter:

$$\kappa_{R,j}^{g,n+\frac{1}{2}} = c\left[\max\left(3\sigma_{R,j-\frac{1}{2}}^{g,n+\frac{1}{2}} V_{j-\frac{1}{2}}^{n+\frac{1}{2}}, 2\left(E_{j+\frac{1}{2}}^{g,n} + E_{j-\frac{1}{2}}^{g,n}\right)^{-1}\left|\frac{E_{j+\frac{1}{2}}^{g,n} - E_{j-\frac{1}{2}}^{g,n}}{\Delta r_j^{n+\frac{1}{2}}}\right|\right)\right]^{-1} \tag{B.23}$$

the Larsen-limiter:

$$\kappa_{R,j}^{g,n+\frac{1}{2}} = c\left[\left(3\sigma_{R,j-\frac{1}{2}}^{g,n+\frac{1}{2}} V_{j-\frac{1}{2}}^{n+\frac{1}{2}}\right)^{n'} + \left(2\left(E_{j+\frac{1}{2}}^{g,n} + E_{j-\frac{1}{2}}^{g,n}\right)^{-1}\left|\frac{E_{j+\frac{1}{2}}^{g,n} - E_{j-\frac{1}{2}}^{g,n}}{\Delta r_j^{n+\frac{1}{2}}}\right|\right)^{n'}\right]^{-\frac{1}{n'}} \tag{B.24}$$

and the approximate simplified Levermore-Pomraning-limiter:

$$\begin{aligned}\kappa_{R,j}^{g,n+\frac{1}{2}} =& c\frac{2 + R_j^{g,n+\frac{1}{2}}}{\sigma_{R,j-\frac{1}{2}}^{g,n+\frac{1}{2}} V_{j-\frac{1}{2}}^{n+\frac{1}{2}}\left[6 + 3R_j^{g,n+\frac{1}{2}} + \left(R_j^{g,n+\frac{1}{2}}\right)^2\right]} \\ \text{for} \qquad & R_j^{g,n+\frac{1}{2}} = 2\left[\sigma_{R,j-\frac{1}{2}}^{g,n+\frac{1}{2}} V_{j-\frac{1}{2}}^{n+\frac{1}{2}}\left(E_{j+\frac{1}{2}}^{g,n} + E_{j-\frac{1}{2}}^{g,n}\right)\right]^{-1}\left|\frac{E_{j+\frac{1}{2}}^{g,n} - E_{j-\frac{1}{2}}^{g,n}}{\Delta r_j^{n+\frac{1}{2}}}\right|.\end{aligned} \tag{B.25}$$

For convenience, Eq. B.20 can be reduced to [4]:

$$\begin{aligned}\alpha_{j-\frac{1}{2}}^{n+\frac{1}{2}}\left(E_{j-\frac{1}{2}}^{g,n+1} - E_{j-\frac{1}{2}}^{g,n}\right) =& a_j^{g,n+\frac{1}{2}}\left(E_{j+\frac{1}{2}}^{g,n+1} - E_{j-\frac{1}{2}}^{g,n+1}\right) - a_{j-1}^{g,n+\frac{1}{2}}\left(E_{j-\frac{1}{2}}^{g,n+1} - E_{j-\frac{3}{2}}^{g,n+1}\right) \\ & - \gamma_{j-\frac{1}{2}}^{n+\frac{1}{2}} E_{j-\frac{1}{2}}^{g,n+1} - \omega_{j-\frac{1}{2}}^{g,n+\frac{1}{2}} E_{j-\frac{1}{2}}^{g,n+1} + \beta_{j-\frac{1}{2}}^{g,n+\frac{1}{2}},\end{aligned} \tag{B.26}$$

by definition of the coefficients:

$$\alpha_{j-\frac{1}{2}}^{n+\frac{1}{2}} = V_{j-\frac{1}{2}}^{n+\frac{1}{2}}\frac{\Delta m_{j-\frac{1}{2}}}{\Delta t^{n+\frac{1}{2}}} \tag{B.27}$$

$$a_j^{g,n+\frac{1}{2}} = r_j^{\delta-1^{n+\frac{1}{2}}}\frac{\kappa_{R,j}^{g,n+\frac{1}{2}}}{\Delta r_j^{n+\frac{1}{2}}} \tag{B.28}$$

$$\gamma_{j-\frac{1}{2}}^{n+\frac{1}{2}} = \frac{4}{3}\dot{V}_{j-\frac{1}{2}}^{n+\frac{1}{2}}\Delta m_{j-\frac{1}{2}} \tag{B.29}$$

$$\omega_{j-\frac{1}{2}}^{g,n+\frac{1}{2}} = c\sigma_{P,A_{j-\frac{1}{2}}}^{g,n+\frac{1}{2}} \Delta m_{j-\frac{1}{2}} \tag{B.30}$$

$$\beta_{j-\frac{1}{2}}^{g,n+\frac{1}{2}} = 4\pi\sigma_{P,e_{j-\frac{1}{2}}}^{g,n+\frac{1}{2}} B_{\nu,j-\frac{1}{2}}^{g,n+\frac{1}{2}} \Delta m_{j-\frac{1}{2}} + V_{j-\frac{1}{2}}^{n+\frac{1}{2}} 4\pi S_{j-\frac{1}{2}}^{g,n+1} \Delta m_{j-\frac{1}{2}}. \tag{B.31}$$

Finally, collecting terms in Eq. B.26 gives the tri-diagonal matrix equation for the radiation energy density at time $n+1$:

$$-A_{j-\frac{1}{2}}^{g,n+\frac{1}{2}} E_{j+\frac{1}{2}}^{g,n+1} + B_{j-\frac{1}{2}}^{g,n+\frac{1}{2}} E_{j-\frac{1}{2}}^{g,n+1} - C_{j-\frac{1}{2}}^{g,n+\frac{1}{2}} E_{j-\frac{3}{2}}^{g,n+1} = D_{j-\frac{1}{2}}^{g,n+\frac{1}{2}}, \tag{B.32}$$

where the matrix coefficients are given by:

$$A_{j-\frac{1}{2}}^{g,n+\frac{1}{2}} = a_j^{g,n+\frac{1}{2}} \tag{B.33}$$

$$B_{j-\frac{1}{2}}^{g,n+\frac{1}{2}} = \alpha_{j-\frac{1}{2}}^{n+\frac{1}{2}} + a_j^{g,n+\frac{1}{2}} + a_{j-1}^{g,n+\frac{1}{2}} + \gamma_{j-\frac{1}{2}}^{n+\frac{1}{2}} + \omega_{j-\frac{1}{2}}^{g,n+\frac{1}{2}} \tag{B.34}$$

$$C_{j-\frac{1}{2}}^{g,n+\frac{1}{2}} = a_{j-1}^{g,n+\frac{1}{2}} \tag{B.35}$$

$$D_{j-\frac{1}{2}}^{g,n+\frac{1}{2}} = \beta_{j-\frac{1}{2}}^{g,n+\frac{1}{2}} + \alpha_{j-\frac{1}{2}}^{n+\frac{1}{2}} E_{j-\frac{1}{2}}^{g,n}. \tag{B.36}$$

It should be noted that each of these matrix coefficients are listed as being evaluated at time $n+\frac{1}{2}$. In reality, these coefficients depend on the energy density, which is not yet known at time $n+\frac{1}{2}$, so that they are actually evaluated based on the energy density at time n. This solution to the diffusion equation is therefore semi-implicit. In some instances, the solution can be made more implicit by iterating over a time step until these coefficients (or the radiation energy density itself) converge on the value at time $n+1$. However, there is no guarantee that the iteration will converge in every situation, and may occasionally lead to erroneous solutions. Additionally, because these equations are derived in a 1-D coordinate system, the constant lagrangian mass term, $\Delta m_{j-\frac{1}{2}}$, is given in units of $\frac{g}{cm^2} cm^{\delta-1}$. Thus, the formulation of the diffusion equation given in Eq. B.32 is applicable in planar, cylindrical, and spherical coordinates.

Because the radiation energy density, E, is a zone-centered quantity in BUCKY, then the matrix coefficients in Eq. B.32 are only good for $3 \leq j \leq J-1$. The matrix values

on the edges must therefore be evaluated using the boundary conditions from Eq. B.7. Discretizing the boundary condition at $j = 2$ and $j = J$ on the finite grid of Figure B.1 gives:

$$\mathcal{A}_l E_1^{g,n+1} + \mathcal{B}_l \frac{1}{c} \kappa_{R,1}^{g,n+\frac{1}{2}} \left(\frac{E_{\frac{3}{2}}^{g,n+1} - E_1^{g,n}}{\Delta r_1^{n+\frac{1}{2}}} \right) = \mathcal{C}_l^{n+1} \tag{B.37}$$

$$\mathcal{A}_r E_J^{g,n+1} - \mathcal{B}_r \frac{1}{c} \kappa_{R,J}^{g,n+\frac{1}{2}} \left(\frac{E_J^{g,n+1} - E_{J-\frac{1}{2}}^{g,n}}{\Delta r_J^{n+\frac{1}{2}}} \right) = \mathcal{C}_r^{n+1}, \tag{B.38}$$

where Eq. B.37 is applied on the left boundary ($j = 1$) and Eq. B.38 is applied on the right boundary ($j = J$). The radiation energy density on these boundaries (E_1 and E_J) are defined on the first and last node (not the zone centers) so that $\kappa_{R,(1,J)}$ and $\Delta r_{(1,J)}$ are defined for:

$$\Delta r_1^{n+\frac{1}{2}} = \frac{1}{2} \left(r_2^{n+\frac{1}{2}} - r_1^{n+\frac{1}{2}} \right) \tag{B.39}$$

$$\Delta r_J^{n+\frac{1}{2}} = \frac{1}{2} \left(r_J^{n+\frac{1}{2}} - r_{J-1}^{n+\frac{1}{2}} \right). \tag{B.40}$$

Then, solving for the boundary values and plugging into Eq. B.32 gives:

$$\begin{aligned} -A_{\frac{3}{2}}^{g,n+\frac{1}{2}} E_{\frac{5}{2}}^{g,n+1} + \left[B_{\frac{3}{2}}^{g,n+\frac{1}{2}} + a_1^{g,n+\frac{1}{2}} \frac{\mathcal{B}_l a_1^{g,n+\frac{1}{2}}}{c r_1^{\delta - 1^{n+\frac{1}{2}}} \mathcal{A}_l - \mathcal{B}_l a_1^{g,n+\frac{1}{2}}} \right] E_{\frac{3}{2}}^{g,n+1} \\ = D_{\frac{3}{2}}^{g,n+\frac{1}{2}} + a_1^{g,n+\frac{1}{2}} \frac{c r_1^{\delta - 1^{n+\frac{1}{2}}} \mathcal{C}_l^{n+1}}{r_1^{\delta - 1^{n+\frac{1}{2}}} c \mathcal{A}_l - \mathcal{B}_l a_1^{g,n+\frac{1}{2}}} \end{aligned} \tag{B.41}$$

$$\begin{aligned} \left[B_{J-\frac{1}{2}}^{g,n+\frac{1}{2}} + a_J^{g,n+\frac{1}{2}} \frac{\mathcal{B}_r a_J^{g,n+\frac{1}{2}}}{c r_J^{\delta - 1^{n+\frac{1}{2}}} \mathcal{A}_r - \mathcal{B}_r a_J^{g,n+\frac{1}{2}}} \right] E_{J-\frac{1}{2}}^{g,n+1} - C_{J-\frac{1}{2}}^{g,n+\frac{1}{2}} E_{J-\frac{3}{2}}^{g,n+1} \\ = D_{J-\frac{1}{2}}^{g,n+\frac{1}{2}} + a_J^{g,n+\frac{1}{2}} \frac{c r_J^{\delta - 1^{n+\frac{1}{2}}} \mathcal{C}_r^{n+1}}{c r_J^{\delta - 1^{n+\frac{1}{2}}} \mathcal{A}_r - \mathcal{B}_r a_J^{g,n+\frac{1}{2}}}, \end{aligned} \tag{B.42}$$

which implies that the matrix coefficients at $j = 2$ and $j = J$ are given by:

$$A_{\frac{3}{2}}^{g,n+\frac{1}{2}} = a_2^{g,n+\frac{1}{2}} \tag{B.43}$$

$$B_{\frac{3}{2}}^{g,n+\frac{1}{2}} = \alpha_{\frac{3}{2}}^{n+\frac{1}{2}} + a_2^{g,n+\frac{1}{2}} + a_1^{g,n+\frac{1}{2}} + \gamma_{\frac{3}{2}}^{n+\frac{1}{2}} + \omega_{\frac{3}{2}}^{g,n+\frac{1}{2}} + \frac{a_1^{g,n+\frac{1}{2}}\mathcal{B}_l a_1^{g,n+\frac{1}{2}}}{cr_1^{\delta-1^{n+\frac{1}{2}}}\mathcal{A}_l - \mathcal{B}_l a_1^{g,n+\frac{1}{2}}} \tag{B.44}$$

$$C_{\frac{3}{2}}^{g,n+\frac{1}{2}} = 0 \tag{B.45}$$

$$D_{\frac{3}{2}}^{g,n+\frac{1}{2}} = \beta_{\frac{3}{2}}^{g,n+\frac{1}{2}} + \alpha_{\frac{3}{2}}^{n+\frac{1}{2}} E_{\frac{3}{2}}^{g,n} + a_1^{g,n+\frac{1}{2}} \frac{cr_1^{\delta-1^{n+\frac{1}{2}}}\mathcal{C}_l^{n+1}}{cr_1^{\delta-1^{n+\frac{1}{2}}}\mathcal{A}_l - \mathcal{B}_l a_1^{g,n+\frac{1}{2}}} \tag{B.46}$$

and

$$A_{J-\frac{1}{2}}^{g,n+\frac{1}{2}} = 0 \tag{B.47}$$

$$B_{J-\frac{1}{2}}^{g,n+\frac{1}{2}} = \alpha_{J-\frac{1}{2}}^{n+\frac{1}{2}} + a_J^{g,n+\frac{1}{2}} + a_{J-1}^{g,n+\frac{1}{2}} + \gamma_{J-\frac{1}{2}}^{n+\frac{1}{2}} + \omega_{J-\frac{1}{2}}^{g,n+\frac{1}{2}} + \frac{a_J^{g,n+\frac{1}{2}}\mathcal{B}_r a_J^{g,n+\frac{1}{2}}}{cr_J^{\delta-1^{n+\frac{1}{2}}}\mathcal{A}_r - \mathcal{B}_r a_J^{g,n+\frac{1}{2}}} \tag{B.48}$$

$$C_{J-\frac{1}{2}}^{g,n+\frac{1}{2}} = a_{J-1}^{g,n+\frac{1}{2}} \tag{B.49}$$

$$D_{J-\frac{1}{2}}^{g,n+\frac{1}{2}} = \beta_{J-\frac{1}{2}}^{g,n+\frac{1}{2}} + \alpha_{J-\frac{1}{2}}^{n+\frac{1}{2}} E_{J-\frac{1}{2}}^{g,n} + a_J^{g,n+\frac{1}{2}} \frac{cr_J^{\delta-1^{n+\frac{1}{2}}}\mathcal{C}_r^{n+1}}{cr_J^{\delta-1^{n+\frac{1}{2}}}\mathcal{A}_r - \mathcal{B}_r a_J^{g,n+\frac{1}{2}}}. \tag{B.50}$$

The Thomas algorithm [5] can then be used to solve Eq. B.32 by defining the forward-elimination variables EE and FF as:

$$EE_{\frac{1}{2}}^{g,n+\frac{1}{2}} = FF_{\frac{1}{2}}^{g,n+\frac{1}{2}} = 0 \tag{B.51}$$

$$EE_{j-\frac{1}{2}}^{g,n+\frac{1}{2}} = \frac{A_{j-\frac{1}{2}}^{g,n+\frac{1}{2}}}{B_{J-\frac{1}{2}}^{g,n+\frac{1}{2}} - C_{j-\frac{1}{2}}^{g,n+\frac{1}{2}} EE_{j-\frac{3}{2}}^{g,n+\frac{1}{2}}} \quad \text{, for} \quad 2 \le j \le J \tag{B.52}$$

$$FF_{j-\frac{1}{2}}^{g,n+\frac{1}{2}} = \frac{D_{j-\frac{1}{2}}^{g,n+\frac{1}{2}} + C_{j-\frac{1}{2}}^{g,n+\frac{1}{2}} FF_{j-\frac{3}{2}}^{g,n+\frac{1}{2}}}{B_{J-\frac{1}{2}}^{g,n+\frac{1}{2}} - C_{j-\frac{1}{2}}^{g,n+\frac{1}{2}} EE_{j-\frac{3}{2}}^{g,n+\frac{1}{2}}} \quad \text{, for} \quad 2 \le j \le J, \tag{B.53}$$

and then back-substituting to solve for the radiation energy density at time $n+1$ using the equations:

$$E_{J-\frac{1}{2}}^{g,n+1} = FF_{J-\frac{1}{2}}^{g,n+\frac{1}{2}} \tag{B.54}$$

$$E_{j-\frac{1}{2}}^{g,n+1} = EE_{j-\frac{1}{2}}^{g,n+\frac{1}{2}} E_{j+\frac{1}{2}}^{g,n+1} + FF_{j-\frac{1}{2}}^{g,n+\frac{1}{2}} \quad \text{, for} \quad 2 \le j \le J-1. \tag{B.55}$$

The mapping of variable names in BUCKY to the various quantities listed throughout this section is shown in Table B.2. Additionally, a flow-chart of the diffusion subroutines in BUCKY are shown in Figure B.2, and are described in Table B.3.

Variable	Type	Dimensions	Units	Description
erfd2a	R*8	G_{max}, J_{max}	$\frac{J}{cm^3\,\text{group}}$	$E^{g,n+1}_{j-\frac{1}{2}}$
erfd2c	R*8	G_{max}, J_{max}	$\frac{J}{cm^3\,\text{group}}$	$E^{g,n}_{j-\frac{1}{2}}$
srfd2b	R*8	G_{max}, J_{max}	$\frac{J}{g\,s\,\text{group}}$	$4\pi\sigma^{g,n+\frac{1}{2}}_{P,e_{j-\frac{1}{2}}} B^{g,n+\frac{1}{2}}_{\nu,j-\frac{1}{2}}$
esfd2b	R*8	G_{max}, J_{max}	$\frac{J}{cm^3\,s\,\text{group}}$	$4\pi S^{g,n+\frac{1}{2}}_{j-\frac{1}{2}}$
sr2b	R*8	G_{max}, J_{max}	$\frac{cm^2}{g}$	$\sigma^{g,n+\frac{1}{2}}_{R,j-\frac{1}{2}}$
sp2b	R*8	G_{max}, J_{max}	$\frac{cm^2}{g}$	$\sigma^{g,n+\frac{1}{2}}_{P,a_{j-\frac{1}{2}}}$
spe2b	R*8	G_{max}, J_{max}	$\frac{cm^2}{g}$	$\sigma^{g,n+\frac{1}{2}}_{P,e_{j-\frac{1}{2}}}$
ss2b	R*8	G_{max}, J_{max}	$\frac{1}{cm}$	$\sigma^{g,n+\frac{1}{2}}_{x_{j-\frac{1}{2}}}$
hnu1	R*8	$G_{max}+1$	eV	ν_g
xkrp1b	R*8	$J_{max}+1$	$\frac{cm^2}{s}$	$\kappa^{g,n+\frac{1}{2}}_{R,j}$
xkrm1b	R*8	$J_{max}+1$	$\frac{cm^2}{s}$	$\kappa^{g,n+\frac{1}{2}}_{R,j-1}$
dmass2	R*8	J_{max}	$\frac{g}{cm^{3-\delta}}$	$\Delta m_{j-\frac{1}{2}}$
v2b	R*8	J_{max}	$\frac{cm^3}{g}$	$V^{n+\frac{1}{2}}_{j-\frac{1}{2}}$
vdot2b	R*8	J_{max}	$\frac{cm^3}{g\,s}$	$\dot{V}^{n+\frac{1}{2}}_{j-\frac{1}{2}}$
rs1b	R*8	$J_{max}+1$	$cm^{\delta-1}$	$\left(r_j^{n+\frac{1}{2}}\right)^{\delta-1}$
dr2b	R*8	J_{max}	cm	$\Delta r_j^{n+\frac{1}{2}}$
al222b	R*8	J_{max}	$\frac{cm^\delta}{s}$	$\alpha^{n+\frac{1}{2}}_{j-\frac{1}{2}}$
aa221b	R*8	$J_{max}+1$	$\frac{cm^\delta}{s}$	$a^{g,n+\frac{1}{2}}_{j}$
gm222b	R*8	J_{max}	$\frac{cm^\delta}{s}$	$\gamma^{n+\frac{1}{2}}_{j-\frac{1}{2}}$
om222b	R*8	J_{max}	$\frac{cm^\delta}{s}$	$\omega^{g,n+\frac{1}{2}}_{j-\frac{1}{2}}$
bet22b	R*8	J_{max}	$\frac{J}{cm^{3-\delta}\,s}$	$\beta^{g,n+\frac{1}{2}}_{j-\frac{1}{2}}$
a22r	R*8	J_{max}	$\frac{cm^\delta}{s}$	$A^{g,n+\frac{1}{2}}_{j-\frac{1}{2}}$
b22	R*8	J_{max}	$\frac{cm^\delta}{s}$	$B^{g,n+\frac{1}{2}}_{j-\frac{1}{2}}$
c22r	R*8	J_{max}	$\frac{cm^\delta}{s}$	$C^{g,n+\frac{1}{2}}_{j-\frac{1}{2}}$
d2	R*8	J_{max}	$\frac{J}{cm^{3-\delta}\,s}$	$D^{g,n+\frac{1}{2}}_{j-\frac{1}{2}}$
dtb	R*8	1	s	$\Delta t^{n+\frac{1}{2}}$

Table B.2: Radiation transport variables in BUCKY for flux-limited diffusion. J_{max} is the maximum allowed number of zones and G_{max} is the maximum allowed number of groups.

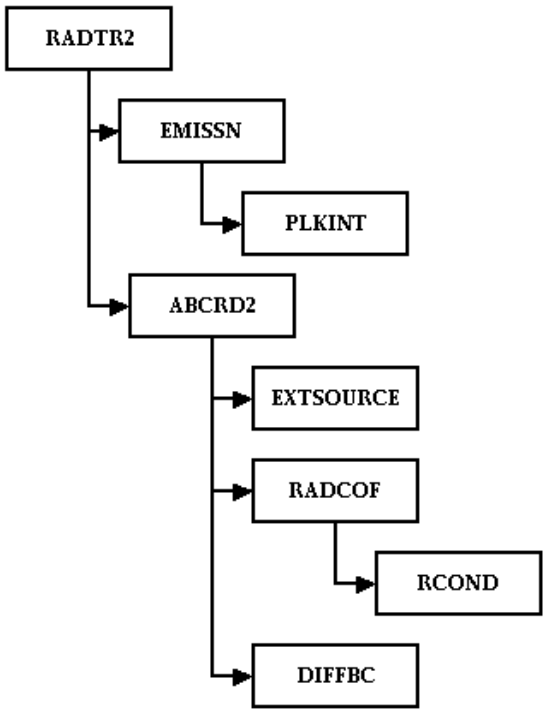

Figure B.2: Flow diagram for BUCKY flux-limited diffusion subroutines.

Subroutine	**Description**
radtr2	Outer frequency loop Thomas back-substitution Calculate $E_j^{g,n+1}$
emissn	Calculate $4\pi\sigma_{P,e_{j-\frac{1}{2}}}^{g,n+\frac{1}{2}} B_{\nu,j-\frac{1}{2}}^{g,n+\frac{1}{2}}$
plkint	Calculate $\int_{\nu_l}^{\nu_l+1} \frac{x^3}{e^x-1} dx$
abcrd2	Calculate $A_{j-\frac{1}{2}}^{g,n+\frac{1}{2}}$, $B_{j-\frac{1}{2}}^{g,n+\frac{1}{2}}$, $C_{j-\frac{1}{2}}^{g,n+\frac{1}{2}}$, and $D_{j-\frac{1}{2}}^{g,n+\frac{1}{2}}$ Thomas forward elimination
extsource	Calculate $4\pi S_{j-\frac{1}{2}}^{g,n+\frac{1}{2}}$
radcof	Calculate $\alpha_{j-\frac{1}{2}}^{n+\frac{1}{2}}$, $a_j^{g,n+\frac{1}{2}}$, $\gamma_{j-\frac{1}{2}}^{n+\frac{1}{2}}$, $\omega_{j-\frac{1}{2}}^{g,n+\frac{1}{2}}$, and $\beta_{j-\frac{1}{2}}^{g,n+\frac{1}{2}}$
rcond	Calculate $\kappa_{R,j}^{g,n+\frac{1}{2}}$
diffbc	Calculate $A_{j-\frac{1}{2}}^{g,n+\frac{1}{2}}$, $B_{j-\frac{1}{2}}^{g,n+\frac{1}{2}}$, $C_{j-\frac{1}{2}}^{g,n+\frac{1}{2}}$, and $D_{j-\frac{1}{2}}^{g,n+\frac{1}{2}}$ for j=(2,J)

Table B.3: Description of subroutines for BUCKY flux-limited diffusion.

	Source	Vacuum	Periodic	Albedo
$I_{bc,i}^{\pm g,n+1}$	$2\pi B_\nu^{g,n+\frac{1}{2}}(T_R)$	0	$I_{i,\,\frac{1}{K}}^{\mp g,n+1}$	$\frac{\alpha}{N}\sum_{i=1}^{N} I_{i,\,\frac{1}{K}}^{\mp g,n+1}$

Table B.4: Boundary conditions for the partial specific intensity in the finite difference equations for multi-angle short-characteristics. α is the albedo, and T_R is the radiation temperature specified on the boundary.

B.2 Short-Characteristics in BUCKY

The multi-angle method of short-characteristics as it is implemented in BUCKY follows closely to the solution given in §1.4.2. In BUCKY, the solution to Eq. 1.58 and 1.59 are written as a set of $(4J-2)$ finite difference equations given by:

$$I_{i,1}^{+g,n+1} = I_{bc,i}^{+g,n+1} \tag{B.56}$$

$$I_{i,K}^{-g,n+1} = I_{bc,i}^{-g,n+1} \tag{B.57}$$

$$I_{i,k}^{+g,n+1} = I_{i,k-1}^{+g,n+1} e^{-\Delta\tau_{i,k-1}^{g,n+\frac{1}{2}}} + \alpha_{i,k}^{+g,n+\frac{1}{2}} S_{T,k-1}^{g,n+\frac{1}{2}} + \beta_{i,k}^{+g,n+\frac{1}{2}} S_{T,k}^{g,n+\frac{1}{2}} + \gamma_{i,k}^{+g,n+\frac{1}{2}} S_{T,k+1}^{g,n+\frac{1}{2}} \tag{B.58}$$

$$I_{i,k}^{-g,n+1} = I_{i,k+1}^{-g,n+1} e^{-\Delta\tau_{i,k}^{g,n+\frac{1}{2}}} + \alpha_{i,k}^{-g,n+\frac{1}{2}} S_{T,k-1}^{g,n+\frac{1}{2}} + \beta_{i,k}^{-g,n+\frac{1}{2}} S_{T,k}^{g,n+\frac{1}{2}} + \gamma_{i,k}^{-g,n+\frac{1}{2}} S_{T,k+1}^{g,n+\frac{1}{2}}, \tag{B.59}$$

where K is the maximum grid index ($K = 2J-1$), and $I_{bc,i}^{\pm g,n+1}$ are the boundary conditions as listed in Table B.4.

Once the values of $I_{i,k}^{\pm g,n+1}$ are known at every value of i and k, then the radiation energy density can be computed at each zone center from Eq. 1.62 as:

$$E_{j-\frac{1}{2}}^{g,n+1} = \frac{1}{c}\sum_{i=1}^{N} w_i \left[I_{i,2j-2}^{+g,n+1} + I_{i,2j-2}^{-g,n+1} \right], \quad 2 \le j \le J. \tag{B.60}$$

Alternatively, in order to better conserve flux at the zone boundaries for significantly large values of $\Delta\tau$, the energy density can be computed by integrating Eq. 1.52 over μ using the calculated values of $I_i^{\pm}$ to evaluate the streaming term. Then, the finite

difference equations can be written on the Lagrangian grid in Figure B.1 as:

$$\begin{aligned} E_{j-\frac{1}{2}}^{g,n+1} =& \frac{4\pi}{c\sigma_{P,a_{j-\frac{1}{2}}}^{g,n+\frac{1}{2}}} \left(\sigma_{P,e_{j-\frac{1}{2}}}^{g,n+\frac{1}{2}} B_{\nu,j-\frac{1}{2}}^{g,n+\frac{1}{2}} + S_{j-\frac{1}{2}}^{g,n+\frac{1}{2}} \right) \\ & - \sum_{i=1}^{N} w_i \mu_i \left[\frac{\left(I_{i,2j-1}^{+g,n+1} - I_{i,2j-3}^{+g,n+1} \right) + \left(I_{i,2j-3}^{-g,n+1} - I_{i,2j-1}^{-g,n+1} \right)}{c \left(\tau_{2j-1}^{g,n+\frac{1}{2}} - \tau_{2j-3}^{g,n+\frac{1}{2}} \right)} \right], \qquad 2 \leq j \leq J. \end{aligned} \tag{B.61}$$

The mapping of variable names in BUCKY to the various quantities listed above is shown in Table B.5. Additionally, a flow chart of the short-characteristics subroutines in BUCKY is shown in Figure B.3, where a description of the calculations in each subroutine is listed in Table B.6.

Variable	Type	Dimensions	Units	Description
erfd2a	R*8	G_{max}, J_{max}	$\frac{J}{cm^3 \text{ group}}$	$E^{g,n+1}_{j-\frac{1}{2}}$
srfd2b	R*8	G_{max}, J_{max}	$\frac{J}{g\, s \text{ group}}$	$4\pi\sigma^{g,n+\frac{1}{2}}_{P,e_{j-\frac{1}{2}}} B^{g,n+\frac{1}{2}}_{\nu,j-\frac{1}{2}}$
esfd2b	R*8	G_{max}, J_{max}	$\frac{J}{cm^3\, s \text{ group}}$	$4\pi S^{g,n+\frac{1}{2}}_{j-\frac{1}{2}}$
sp2b	R*8	G_{max}, J_{max}	$\frac{cm^2}{g}$	$V^{n+\frac{1}{2}}_{j-\frac{1}{2}} \sigma^{g,n+\frac{1}{2}}_{P,a_{j-\frac{1}{2}}}$
spe2b	R*8	G_{max}, J_{max}	$\frac{cm^2}{g}$	$V^{n+\frac{1}{2}}_{j-\frac{1}{2}} \sigma^{g,n+\frac{1}{2}}_{P,e_{j-\frac{1}{2}}}$
ss2b	R*8	G_{max}, J_{max}	$\frac{1}{cm}$	$\sigma^{g,n+\frac{1}{2}}_{x_{j-\frac{1}{2}}}$
hnu1	R*8	$G_{max}+1$	eV	ν_g
sourcefn	R*8	$2J_{max}-1$	$\frac{J}{cm^2\, s\, sr \text{ group}}$	$\frac{1}{2\pi} S^{g,n+\frac{1}{2}}_{T_k}$
simins	R*8	$2J_{max}-1$	$\frac{J}{cm^2\, s\, sr \text{ group}}$	$\frac{1}{2\pi} I^{+g,n+1}_{i,k}$
siplus	R*8	$2J_{max}-1$	$\frac{J}{cm^2\, s\, sr \text{ group}}$	$\frac{1}{2\pi} I^{-g,n+1}_{i,k}$
dtau	R*8	$2J_{max}-2$	–	$\tau^{g,n+\frac{1}{2}}_{k} - \tau^{g,n+\frac{1}{2}}_{k-1}$
dtaumu	R*8	$2J_{max}-2$	–	$\Delta\tau^{g,n+\frac{1}{2}}_{i,k}$
alpham	R*8	$2J_{max}-1$	–	$\alpha^{+g,n+\frac{1}{2}}_{i,k}$
betam	R*8	$2J_{max}-1$	–	$\beta^{+g,n+\frac{1}{2}}_{i,k}$
gammam	R*8	$2J_{max}-1$	–	$\gamma^{+g,n+\frac{1}{2}}_{i,k}$
alphap	R*8	$2J_{max}-1$	–	$\alpha^{-g,n+\frac{1}{2}}_{i,k}$
betap	R*8	$2J_{max}-1$	–	$\beta^{-g,n+\frac{1}{2}}_{i,k}$
gammap	R*8	$2J_{max}-1$	–	$\gamma^{-g,n+\frac{1}{2}}_{i,k}$
wtangl	R*8	5	–	w_i
xmu	R*8	5	–	$\lvert\mu_i\rvert$
dr2b	R*8	J_{max}	cm	$r^{n+\frac{1}{2}}_{j} - r^{n+\frac{1}{2}}_{j-1}$

Table B.5: Radiation transport variables in BUCKY for multi-angle short-characteristics. J_{max} is the maximum allowed number of zones and G_{max} is the maximum allowed number of groups.

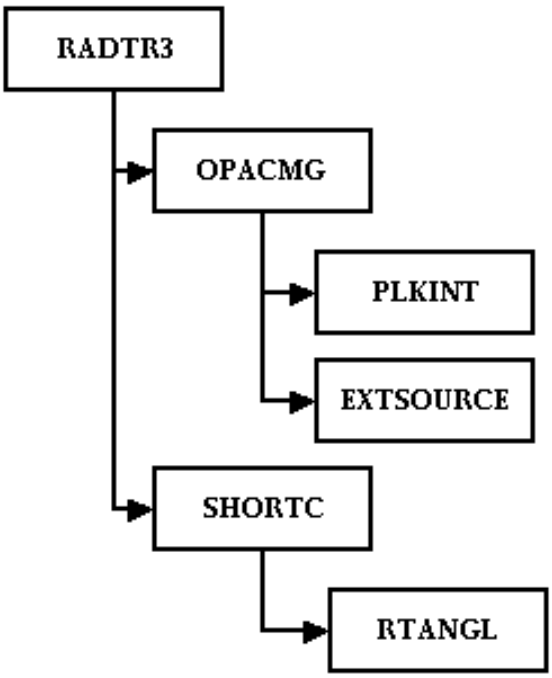

Figure B.3: Flow diagram for BUCKY multi-angle short-characteristics subroutines.

Subroutine	**Description**
radtr3	Outer frequency loop
opacmg	Set-up optical depth grid (Calculate $\tau_k^{g,n+\frac{1}{2}} - \tau_{k-1}^{g,n+\frac{1}{2}}$) Calculate $\frac{1}{2\pi} S_{T_k}^{g,n+\frac{1}{2}}$
plkint	Calculate $\int_{\nu_l}^{\nu_l+1} \frac{x^3}{e^x-1} dx$
extsource	Calculate $4\pi S_{j-\frac{1}{2}}^{g,n+\frac{1}{2}}$
shortc	Calculate $\frac{1}{2\pi} I_{i,k}^{\pm g,n+1}$ Calculate $E_{j-\frac{1}{2}}^{g,n+1}$
rtangl	Define w_i and $\lvert\mu_i\rvert$

Table B.6: Description of subroutines for BUCKY multi-angle short-characteristics.

B.3 Analytic Solutions for Transport and Diffusion

There are a few simple problems in cartesian coordinates where both the steady-state transport equation and the steady-state diffusion equation can be solved analytically. These problems are a good place to start in verifying the finite difference equations in BUCKY because they are also instructive in comparing diffusive solutions to true transport solutions.

All of the problems described in this section assume a purely absorbing cold (non-radiating) slab of thickness $x = X$ in 1-D cartesian coordinates. Under these circumstances, the steady-state mono-energetic transport equation can be simplified from Eq. 1.52 to give:

$$\frac{\partial}{\partial x}\left(I(x)e^{\frac{\sigma_a x}{\mu}}\right) = \frac{2\pi}{\mu}S(x)e^{\frac{\sigma_a x}{\mu}}. \tag{B.62}$$

Breaking the specific intensity into forward and backward propagating rays, and integrating over x gives:

$$0 < \mu \leq 1: \qquad I^{+}(x,\mu) = I^{+}(0,\mu)e^{\frac{-\sigma_a x}{\mu}} + \left[\frac{2\pi}{\mu}\int_0^x S(x')e^{\frac{\sigma_a x'}{\mu}}dx'\right]e^{\frac{-\sigma_a x}{\mu}} \tag{B.63}$$

$$-1 \leq \mu < 0: \qquad I^{-}(x,\mu) = I^{-}(X,\mu)e^{\frac{\sigma_a (X-x)}{\mu}} + \left[\frac{2\pi}{\mu}\int_X^x S(x')e^{\frac{\sigma_a x'}{\mu}}dx'\right]e^{\frac{-\sigma_a x}{\mu}}, \tag{B.64}$$

where it has been assumed that σ_a is constant throughout the slab. Furthermore, if it is assumed that the source function, S, can be described by an N^{th} order polynomial of the form:

$$S(x) = \sum_{i=0}^{N} c_{S,i}x^i, \tag{B.65}$$

then the integrals can be evaluated to give:

$$0 < \mu \leq 1: \qquad I^{+}(x,\mu) = I^{+}(0,\mu)e^{\frac{-\sigma_a x}{\mu}} + \frac{2\pi}{\sigma_a}\sum_{i=0}^{N} c_{S,i}\gamma_i^{+}(x,\mu) \tag{B.66}$$

$$-1 \leq \mu < 0: \qquad I^{-}(x,\mu) = I^{-}(X,\mu)e^{\frac{\sigma_a (X-x)}{\mu}} + \frac{2\pi}{\sigma_a}\sum_{i=0}^{N} c_{S,i}\gamma_i^{-}(x,\mu), \tag{B.67}$$

where the coefficients $\gamma_i^{\pm}$ are given by:

$$\begin{aligned}
\gamma_0^{+} &= [1 - e^{\frac{-\sigma_a x}{\mu}}] \\
\gamma_i^{+} &= [x^i - i\frac{\mu}{\sigma_a}\gamma_{i-1}^{+}] \\
\gamma_0^{-} &= [1 - e^{\frac{\sigma_a (X-x)}{\mu}}] \\
\gamma_i^{-} &= [x^i - X^i e^{\frac{\sigma_a (X-x)}{\mu}} - i\frac{\mu}{\sigma_a}\gamma_{i-1}^{-}].
\end{aligned} \tag{B.68}$$

Finally, if the boundary values, $I^{+}(0)$ and $I^{-}(X)$, are independent of μ, then integrating Eq. B.66 and Eq. B.67 over μ gives the radiation energy density as:

$$\begin{aligned}
E(x) &= \frac{1}{c}\left[\int_{-1}^{0} I^{-}(x,\mu)d\mu + \int_{0}^{+1} I^{+}(x,\mu)d\mu\right] \\
&= \frac{1}{c}\left[I^{+}(0)E_2(\sigma_a x) + I^{-}(X)E_2(\sigma_a(X-x))\right] \\
&\quad + \frac{2\pi}{c\sigma_a}\sum_{i=0}^{N} c_{S,i}\left[\epsilon_i^{+}(x) + \epsilon_i^{-}(x)\right],
\end{aligned} \tag{B.69}$$

where the coefficients $\epsilon_i^{\pm}$ are given by:

$$\begin{aligned}
\epsilon_i^{+} &= \sum_{n=0}^{i} \frac{i!}{(i-n)!}\frac{1}{\sigma_a^n}\frac{x^{i-n}}{n+1}(-1)^n + (-1)^{i+1}\frac{i!}{\sigma_a^i}E_{i+2}(\sigma_a x) \\
\epsilon_i^{-} &= \sum_{n=0}^{i} \frac{i!}{(i-n)!}\frac{1}{\sigma_a^n}\left[\frac{x^{i-n}}{n+1} - X^{i-n}E_{n+2}(\sigma_a(X-x))\right],
\end{aligned} \tag{B.70}$$

and the functions $E_n(\sigma_a x)$ and $E_n(\sigma_a(X-x))$ belong to the general family of functions called the exponential integrals given by:

$$E_n(x) = x^{n-1}\int_x^{\infty} \frac{1}{u^n}e^{-u}du. \tag{B.71}$$

If either of the boundary values depend on μ (as in the case of an albedo boundary condition), then the boundary terms in Eq. B.69 must be integrated independently. In

this case, the equation for the radiation energy density is given as:

$$\begin{aligned} E(x) =& \frac{1}{c}\left[\int_0^1 I^+(0,\mu')e^{\frac{-\sigma_a x}{\mu'}}d\mu' + \int_{-1}^0 I^-(X,\mu')e^{\frac{\sigma_a(X-x)}{\mu'}}d\mu'\right] \\ &+ \frac{2\pi}{c\sigma_a}\sum_{i=0}^{N} c_{S,i}\left[\epsilon_i^+(x) + \epsilon_i^-(x)\right]. \end{aligned} \tag{B.72}$$

Therefore, given the boundary conditions at $x = (0, X)$ and the spatial variation in the external source term, $S(x)$, then either Eq. B.69 or Eq. B.72 provides the general solution for the steady-state radiation energy density in a cold purely absorbing 1-D slab.

An analytic solution to this same problem can be defined for diffusion by simplifying Eq. B.1 to give:

$$\frac{\partial^2 E}{\partial x^2} - \frac{\sigma_a}{D}E = -\frac{4\pi}{cD}S. \tag{B.73}$$

If it is again assumed that the opacities are constant through the slab, and that the source function, S, can be described by an N^{th} order polynomial as in Eq. B.65, then Eq. B.73 can be solved by the superposition approach to give:

$$E(x) = ae^{\lambda x} + be^{-\lambda x} + \sum_{i=0}^{N} c_i x^i, \tag{B.74}$$

where λ is the inverse diffusion length, $\lambda = \sqrt{\frac{\sigma_a}{D}}$, and the coeffecients c_i are determined by:

$$\begin{aligned} c_N &= \frac{4\pi}{c\sigma_a}c_{S,N} \\ c_{N-1} &= \frac{4\pi}{c\sigma_a}c_{S,N-1} \\ c_i &= \frac{4\pi}{c\sigma_a}c_{S,i} + \frac{D}{\sigma_a}(i+2)(i+1)c_{i+2}, \qquad 0 \le i \le N-2. \end{aligned} \tag{B.75}$$

The coeffecients of the homogeneous solution (a and b) must be determined from the coupled set of boundary conditions defined in §B.1.1. Thus, plugging Eq. B.74 into Eq. B.7 gives:

$$a[\mathcal{A}_l + \mathcal{B}_l D\lambda] + b[\mathcal{A}_l - \mathcal{B}_l D\lambda] = \mathcal{C}_l - (\mathcal{A}_l c_0 + \mathcal{B}_l D c_1) \tag{B.76}$$

$$a[\mathcal{A}_r e^{\lambda X} - \mathcal{B}_r D\lambda e^{\lambda X}] + b[\mathcal{A}_r e^{-\lambda X} + \mathcal{B}_r D\lambda e^{-\lambda X}] = \mathcal{C}_r + \left[\sum_{i=1}^{N} (i\mathcal{B}_r D - \mathcal{A}_r X) c_i X^{i-1} - \mathcal{A}_r c_0\right], \tag{B.77}$$

where Eq. B.76 is applied at the left boundary ($x = 0$) and Eq. B.77 is applied at the right boundary ($x = X$). Then, solving these for the coefficients a and b gives:

$$a = \frac{\mathcal{C}_l - (\mathcal{A}_l c_0 + \mathcal{B}_l D c_1) - b[\mathcal{A}_l - \mathcal{B}_l D\lambda]}{\mathcal{A}_l + \mathcal{B}_l D\lambda} \tag{B.78}$$

$$b = \frac{\left[\mathcal{C}_r + \left(\sum_{i=1}^{N} (i\mathcal{B}_r D - \mathcal{A}_r X) c_i X^{i-1} - \mathcal{A}_r c_0\right)\right](\mathcal{A}_l + \mathcal{B}_l D\lambda)}{(\mathcal{A}_l + \mathcal{B}_l D\lambda)(\mathcal{A}_r + \mathcal{B}_r D\lambda) e^{-\lambda X} - (\mathcal{A}_l - \mathcal{B}_l D\lambda)(\mathcal{A}_r - \mathcal{B}_r D\lambda) e^{\lambda X}} - \frac{[\mathcal{C}_l - (\mathcal{A}_l c_0 + \mathcal{B}_l D c_1)](\mathcal{A}_r - \mathcal{B}_r D\lambda) e^{\lambda X}}{(\mathcal{A}_l + \mathcal{B}_l D\lambda)(\mathcal{A}_r + \mathcal{B}_r D\lambda) e^{-\lambda X} - (\mathcal{A}_l - \mathcal{B}_l D\lambda)(\mathcal{A}_r - \mathcal{B}_r D\lambda) e^{\lambda X}}. \tag{B.79}$$

Therefore, the analytic solution to the diffusion equation for the steady-state radiation energy density in a cold purely absorbing 1-D slab is given by Eq. B.74 where the coefficients are described by Eq. B.75, B.78, and B.79.

B.3.1 Source and Vacuum Boundaries with No External Sources

The simplest case to consider in solving the equations in §B.3 is a cold slab with no external sources, where a radiation temperature source is applied on one boundary and a vacuum condition on the other boundary. Under these conditions, Eq. B.69 reduces to:

$$E(x) = \frac{1}{c} I^{+}(0) E_2(\sigma_a x) = \frac{4\pi^5}{15h^3c^3} T_0^4 E_2(\sigma_a x), \tag{B.80}$$

where T_0 is the radiation temperature applied at the left boundary. Similarly for diffusion, Eq. B.74 can be reduced to:

$$E(x) = \frac{4\pi^5}{15h^3c^3} T_0^4 \frac{\left[\left(\frac{1}{2} - D\lambda\right) e^{\lambda(x-X)} - \left(\frac{1}{2} + D\lambda\right) e^{\lambda(X-x)}\right]}{\left(D\lambda - \frac{1}{2}\right)^2 e^{-\lambda X} - \left(D\lambda + \frac{1}{2}\right)^2 e^{\lambda X}}. \tag{B.81}$$

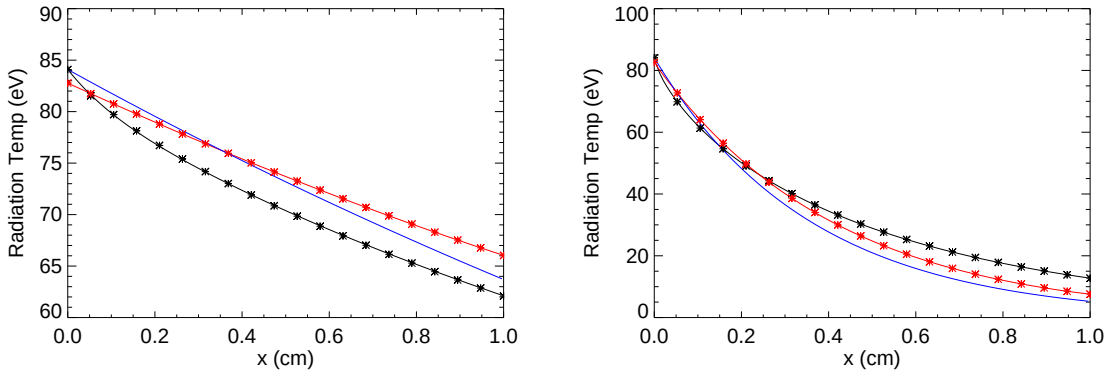

(a) (b)

Figure B.4: Comparison between the analytic transport (Eq. B.80) (black stars) and diffusion (Eq. B.81) (red stars) solutions to those calculated by BUCKY for short-characteristics (black line), diffusion (red line), and flux-limited diffusion (blue line). All calculations are done assuming no external sources, source and vacuum conditions on the left and right boundaries respectively, and an absorption opacity of (a) $0.5558cm^{-1}$ and (b) $5.558cm^{-1}$.

For convenience in comparison to BUCKY output, the radiation energy density can then be converted to an effective radiation temperature,T_r, by:

$$T_r(x) = \left(\frac{c}{4}\frac{E(x)}{\sigma_{SB}}\right)^{\frac{1}{4}}, \tag{B.82}$$

where σ_{SB} is the Stephan-Boltzmann constant.

Figure B.4 shows the solutions of Eq. B.80 and Eq. B.81 in comparison to that calculated by BUCKY for short-characteristics, diffusion, and flux-limited diffusion. The values for each of the variables in the equations are shown in Table B.7. This comparison is done for two different opacities. In Figure B.4(a), one mean free path is approximately 1.8 times the thickness of the slab. In this case, the distribution of radiation as calculated by the diffusion solution is significantly different than that calculated by the transport solution, and diffusion over-predicts the amount of radiation everywhere in the slab. This is not surprising since this problem violates most of the assumptions in the derivation

	X	T_0	σ_a	σ_t
Value	$1.0cm$	$100.0eV$	$0.5558cm^{-1}$ or $5.558cm^{-1}$	σ_a

Table B.7: Values used for each variable in comparing BUCKY short-characteristics and diffusion to the analytic equations.

of the diffusion equation. The average R value (as shown in Figure 1.17) throughout the slab is 2.17 (calculated from the transport solution). Under these conditions, one would expect the flux-limited diffusion solution to be a better approximation to the true transport characteristics (as evidenced by the figure).

In Figure B.4(b), one mean free path is approximately 0.18 times the thickness of the slab. In this case, the diffusion approximation does a much better job of capturing the true radiation distribution. The average R value for this radiation field is 1.35, which is only a modest difference from that in case (a). Surprisingly, Figure B.4(b) indicates that, for these conditions, the flux-limiter restricts the radiation too much, and actually looks less like the transport solution than pure diffusion. However, because this problem is calculated for a purely absorbing, non-radiating slab, it still violates the assumption in diffusion that requires the radiation field to be nearly isotropic. The primary points are that; the finite difference equations in BUCKY properly reproduce the analytic results, diffusion looks much more like transport when the optical depths are small compared to the size of the slab, and that flux-limited diffusion is not always better than pure diffusion.

B.3.2 Vacuum Boundaries With a Linear External Source

A slightly more complicated solution to the equations in §B.3 is to consider the case of a cold slab with vacuum boundaries, and a linearly dependent external source. If the

source term has the form:

$$S(x) = S_0(1 - \frac{x}{a}), \tag{B.83}$$

then, Eq. B.69 reduces to:

$$E(x) = \frac{1}{2c\sigma_a} S_0 \left[2\left(1 - \frac{x}{X}\right) - E_2(\sigma_a x) + \frac{1}{\sigma_a X}\left[E_3(\sigma_a(X-x)) - E_3(\sigma_a x)\right] \right], \tag{B.84}$$

and Eq. B.74 reduces to:

$$E(x) = ae^{\lambda x} + be^{-\lambda x} + \frac{4\pi}{c\sigma_a} S_0 \left(1 - \frac{x}{a}\right), \tag{B.85}$$

where the coefficients are given by:

$$a = -\frac{4\pi}{c\sigma_a} S_0 \frac{\left(\frac{D}{X} + \frac{1}{2}\right)\left(\frac{1}{2} - D\lambda)\right) e^{-\lambda X} + \frac{D}{X}\left(\frac{1}{2} + D\lambda\right)}{\left(D\lambda - \frac{1}{2}\right)^2 e^{-\lambda X} - \left(D\lambda + \frac{1}{2}\right)^2 e^{\lambda X}}$$

$$b = \frac{4\pi}{c\sigma_a} S_0 \frac{\left(\frac{D}{X} + \frac{1}{2}\right)\left(\frac{1}{2} + D\lambda)\right) e^{\lambda X} + \frac{D}{X}\left(\frac{1}{2} - D\lambda\right)}{\left(D\lambda - \frac{1}{2}\right)^2 e^{-\lambda X} - \left(D\lambda + \frac{1}{2}\right)^2 e^{\lambda X}}.$$

Assuming that the imposed external source function has a blackbody distribution, then S_0 in Eq. B.83 can be described by:

$$S_0 = \sigma_x \frac{2\pi^4}{15h^3c^2} T_0^4, \tag{B.86}$$

where σ_x is an artificial emission opacity [a].

The comparisons between BUCKY and the analytic results in Eq. B.84 and Eq. B.85 are shown in Figure B.5 for the same set of values listed in Table B.7. In each case, there is very good agreement between the BUCKY calculated results and the analytic solutions. In addition, Figure B.5(b) shows that diffusion is a good approximation to true transport when one mean free path is much less than the total thickness of the slab. This is not surprising since the external source function is isotropic, and meets the primary

[a] In BUCKY, this artificial emission opacity is assigned as a zone dependent value of the form: $\sigma_x = \sigma_a\left(1 - \frac{x}{X}\right)$, so that the external source function is conveniently defined as in Eq. B.83

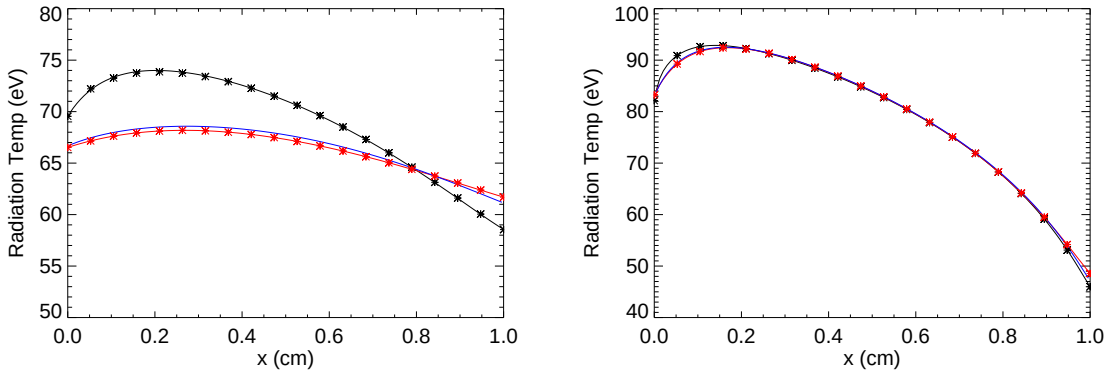

(a) (b)

Figure B.5: Comparison between the analytic transport (Eq. B.84) (black stars) and diffusion (Eq. B.85) (red stars) solutions to those calculated by BUCKY for short-characteristics (black line), diffusion (red line), and flux-limited diffusion (blue line). All calculations are done assuming a linear external source, vacuum conditions on both boundaries, and an absorption opacity of (a) $0.5558cm^{-1}$ and (b) $5.558cm^{-1}$.

criteria in the derivation of the diffusion equation (with the exception of the value near the boundary where radiation is allowed to escape). The agreement between diffusion and transport is not nearly as good in Figure B.5(a) where one mean free path is 2.2 times the thickness of the slab. Even though the external source function is isotropic, the low opacity allows the radiation to stream to the boundaries resulting in a significant non-isotropic component to the radiation flow. It is also worth noting that, in each of these cases, the flux-limiter provides no significant benefit over pure diffusion. The calculated R values for Figure B.5(a) and (b) are 2.3 and 0.1 respectively.

B.3.3 An External Source with a Source Boundary Condition

A more realistic case to consider in the comparison between transport and diffusion is that of a distributed external source function with a source boundary condition applied on one side. This may be thought of as a model for a sample that is being radiatively

heated by a nearby source. To identify a realistic source function, Eq. B.69 is iterated by initially assuming a cold material, and then fitting a polynomial to the resulting radiation distribution. This polynomial is then applied as the external source function for the next iteration, and the process is continued until a 'convergence' of the polynomial fit is achieved. The result is essentially modeling a sample that has come to equilibrium with the driving radiation source.

For the optically thin case ($\sigma_a = 0.5558cm^{-1}$), assuming a constant blackbody source on the left boundary at a temperature of $100eV$, the resulting external source function is represented by a 4^{th} order polynomial of the form:

$$S(x) = (12.617 - 8.4037x + 4.0473x^2 - 2.6986x^3 + 0.0047624x^4) * 1.e11 \qquad \frac{J}{cm^3\ s\ sr}.$$

Likewise for the optically thick case ($\sigma_a = 5.5558cm^{-1}$), the source function is represented by:

$$S(x) = (165.44 - 163.75x + 37.471x^2 - 22.651x^3 - 0.50728x^4) * 1.e11 \qquad \frac{J}{cm^3\ s\ sr}.$$

These polynomials are then interpolated onto the BUCKY finite difference grid (again using the artificial emission opacity to distribute the source), and calculated for short-characteristics, diffusion, and flux-limited diffusion. The results are shown in Figure B.6.

The first thing to notice about this figure is that the diffusion solution looks very much like true transport. This is especially true in Figure B.6(b) where one mean free path is much less than the thickness of the slab. This is a good illustration of why diffusion is such a popular way of computing the radiation transport. In plasmas driven by a steady state external radiation source, diffusion is a good approximation to true transport over a wide range of optical depths when the plasma temperature has enough time to equilibrate with the driving radiation source. The simple reason for this is that,

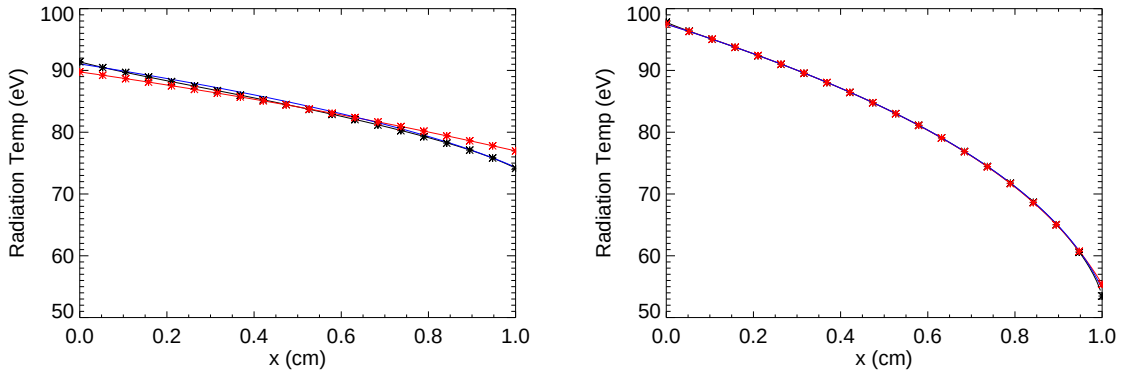

(a) (b)

Figure B.6: Comparison between the analytic transport (Eq. B.84) (black stars) and diffusion (Eq. B.85) (red stars) solutions to those calculated by BUCKY for short-characteristics (black line), diffusion (red line), and flux-limited diffusion (blue line). All calculations assume an external source function given by (a) Eq. B.3.3 and (b) Eq. B.3.3, source and vacuum conditions on the left and right boundaries respectively, and an absorption/emission opacity of (a) $0.5558cm^{-1}$ and (b) $5.558cm^{-1}$.

at any particular point in the slab, the plasma is isotropically radiating at the same intensity as the anisotropic component of the radiation field that is contributed from the source applied at the boundary. Thus, the total radiation field has only a weakly anisotropic component, and therefore satisfies the primary assumptions in the derivation of the diffusion equation.

B.3.4 A Boundary Source and an Albedo Boundary Condition

One final problem that can be applied to both short-characteristics and diffusion is intended to test the implementation of the albedo boundary condition. In this simple problem, a cold slab with no external source term has a source condition applied on the left boundary and an albedo condition applied to the right boundary.

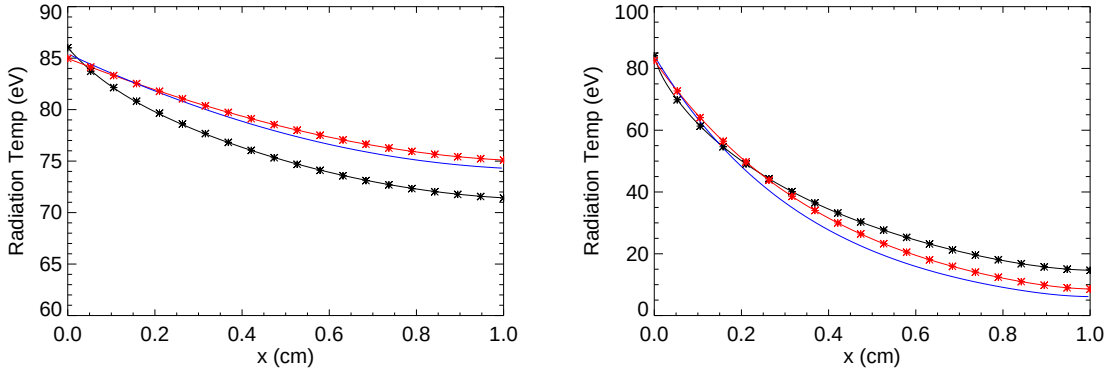

(a) (b)

Figure B.7: Comparison between the analytic transport (Eq. B.87) (black stars) and diffusion (Eq. B.88) (red stars) solutions to those calculated by BUCKY for short-characteristics (black line), diffusion (red line), and flux-limited diffusion (blue line). All calculations are done assuming no external sources, source and albedo ($\alpha = 0.75$) conditions on the left and right boundaries respectively, and an absorption opacity of (a) $0.5558 cm^{-1}$ and (b) $5.558 cm^{-1}$.

Under these circumstances, Eq. B.69 reduces to:

$$E(x) = \frac{4\pi^5}{15h^3c^3} T_0^4 \left[E_2(\sigma_a x) + \alpha E_2(\sigma_a X) E_2(\sigma_a (X - x)) \right] \tag{B.87}$$

where α is the albedo of the boundary at $x = X$. Similarly for diffusion, Eq. B.74 can be reduced to:

$$E(x) = ae^{\lambda x} + be^{-\lambda x}, \tag{B.88}$$

for the coefficients a and b given by:

$$a = \frac{b\left(D\lambda + \frac{1}{2}\right) - \frac{4\pi^5}{15h^3c^3} T_0^4}{\left(D\lambda - \frac{1}{2}\right)}$$

$$b = \frac{4\pi^5}{15h^3c^3} T_0^4 \frac{\left(\frac{1}{2}\frac{\alpha-1}{\alpha+1} - D\lambda\right) e^{\lambda X}}{\left(D\lambda - \frac{1}{2}\right)\left(D\lambda + \frac{1}{2}\frac{\alpha-1}{\alpha+1}\right) e^{-\lambda X} - \left(D\lambda + \frac{1}{2}\right)\left(D\lambda - \frac{1}{2}\frac{\alpha-1}{\alpha+1}\right) e^{\lambda X}}.$$

The comparison between these equations and the BUCKY calculated result is shown in Figure B.7 for the values in Table B.7 and an albedo of $\alpha = 0.75$. The results look

very much like those from §B.3.1 except that the radiation temperature is elevated due to the radiation energy that is reflected at the right boundary.

B.4 Solutions Specific to the Diffusion Equation

The problems in §B.3 provide nearly a complete benchmarking of the steady-state diffusion equations as implemented in BUCKY. However, because Eq. B.14 contains a term that is dependent on the coordinate system, the diffusion equations in BUCKY must also be verified in cylindrical and spherical coordinates.

B.4.1 Steady-State Diffusion in Cylindrical Coordinates

Assuming that there are no external source functions, Eq. B.73 can be rewritten in cylindrical coordinates as:

$$\rho\frac{\partial^2 E(\rho)}{\partial\rho^2}+\frac{\partial E(\rho)}{\partial\rho}=\rho\frac{\sigma_a}{D}E(\rho), \tag{B.89}$$

where ρ is the radial coordinate ($\rho=\sqrt{x^2+y^2}$). The solution to this equation is given by [6]:

$$E(\rho)=b'\,\mathrm{I}_0(\lambda\rho), \tag{B.90}$$

where I_0 is the modified Bessel function of the first kind. Plugging this into the general boundary condition in Eq. B.7 at $\rho=\rho_{\max}$ and solving for b' then gives:

$$E(\rho)=\frac{\mathcal{C}}{\mathcal{A}\,\mathrm{I}_0(\lambda\rho_{\max})-\mathcal{B}D\lambda\,\mathrm{I}_1(\lambda\rho_{\max})}\,\mathrm{I}_0(\lambda\rho). \tag{B.91}$$

In the case of a source boundary condition applied at $\rho=\rho_{\max}$, then Eq. B.91 can be written as:

$$E(\rho)=\frac{4\pi^5}{15h^3c^3}T_0^4\frac{\mathrm{I}_0(\lambda\rho)}{\frac{1}{2}\,\mathrm{I}_0(\lambda\rho_{\max})+D\lambda\,\mathrm{I}_1(\lambda\rho_{\max})}. \tag{B.92}$$

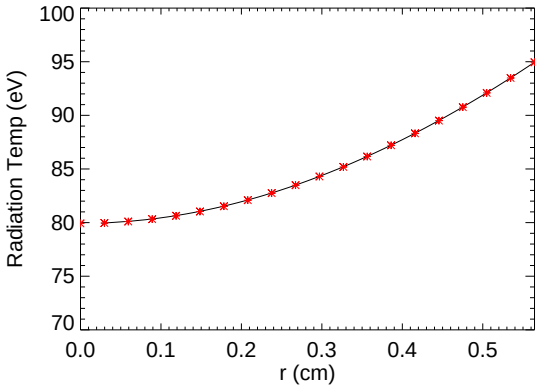

Figure B.8: Comparison between BUCKY calculated diffusion (solid line) and the steady state analytic result for cylindrical coordinates in Eq. B.92 (red stars) where the absorption and scattering opacities are given by $\sigma_a = 0.5558cm^{-1}$ and $\sigma_s = 5.558cm^{-1}$ respectively.

Figure B.8 shows the comparison between this analytic result and BUCKY calculated diffusion for a boundary temperature of $T_0 = 100eV$ applied at a maximum radius of $\rho_{\max} = 0.5643cm$. The material is assumed to both absorb and scatter radiation with opacities of $\sigma_a = 0.5558cm^{-1}$ and $\sigma_s = 5.558cm^{-1}$ respectively ($\sigma_t = \sigma_a + \sigma_s$). As evidenced by the figure, the BUCKY calculated result compares well with the analytic solution.

B.4.2 Steady-State Diffusion in Spherical Coordinates

Again assuming that there are no external source functions, Eq. B.73 can be rewritten in spherical coordinates as:

$$r^2 \frac{\partial^2 E(r)}{\partial r^2} + 2r \frac{\partial E(r)}{\partial r} = r^2 \frac{\sigma_a}{D} E(r), \tag{B.93}$$

where r is the radial coordinate ($r = \sqrt{x^2 + y^2 + z^2}$). The solution to this equation is given by [6]:

$$E(\rho) = b' \frac{\sinh(\lambda r)}{r}, \tag{B.94}$$

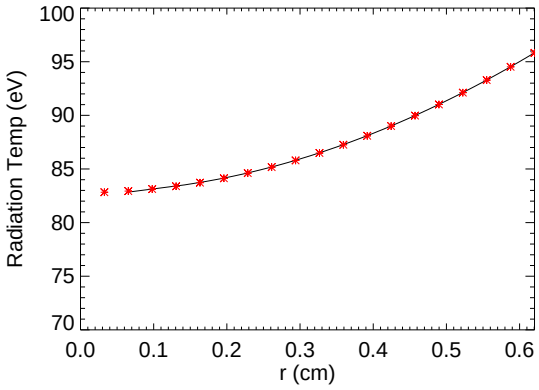

Figure B.9: Comparison between BUCKY calculated diffusion (solid line) and the steady state analytic result for spherical coordinates in Eq. B.96 (red stars) where the absorption and scattering opacities are given by $\sigma_a = 0.5558cm^{-1}$ and $\sigma_s = 5.558cm^{-1}$ respectively.

Plugging this into the general boundary condition in Eq. B.7 at $r = r_{\max}$ and solving for b' then gives:

$$E(r) = \left[\frac{\mathcal{C}r_{\max}}{\mathcal{A}\sinh(\lambda r_{\max}) - \mathcal{B}D\left[\lambda\cosh(\lambda r_{\max}) - \frac{\sinh(\lambda r_{\max})}{r_{\max}}\right]}\right]\frac{\sinh(\lambda r)}{r}. \tag{B.95}$$

In the case of a source boundary condition applied at $r = r_{\max}$, then Eq. B.95 can be written as:

$$E(\rho) = \frac{4\pi^5}{15h^3c^3}T_0^4\left[\frac{r_{\max}}{\frac{1}{2}\sinh(\lambda r_{\max})D\left[\lambda\cosh(\lambda r_{\max}) - \frac{\sinh(\lambda r_{\max})}{r_{\max}}\right]}\right]\frac{\sinh(\lambda r)}{r}. \tag{B.96}$$

Figure B.9 shows the comparison between this analytic result and BUCKY calculated diffusion for a boundary temperature of $T_0 = 100eV$ applied at a maximum radius of $r_{\max} = 0.6204cm$. The material is assumed to both absorb and scatter radiation with opacities of $\sigma_a = 0.5558cm^{-1}$ and $\sigma_s = 5.558cm^{-1}$ respectively ($\sigma_t = \sigma_a + \sigma_s$). As evidenced by the figure, the BUCKY calculated result again compares well with the analytic solution.

B.4.3 Flux-Limiters

As was demonstrated in §B.3, the flux-limiter in the diffusion coefficient can significantly alter the radiation profile calculated by diffusion. Thus, it is important to benchmark the implementation of each flux-limiter. However, because the flux-limiter makes the diffusion equation non-linear, this is somewhat difficult to accomplish by attempting a direct analytic solution to the flux-limited diffusion equation(s). Instead, one can manufacture a solution for the radiation energy density distribution, and then plug the solution into Eq. B.73 to determine the external source function that will produce that radiation distribution. This initial source function can then be input into BUCKY as an initial condition, and the resulting radiation energy density checked to verify the reproduction of the manufactured solution.

Assuming for simplicity that the test slab is cold, then the flux-limited diffusion equation can be written as:

$$\frac{\partial}{\partial x} D(x) \frac{\partial E(x)}{\partial x} = \sigma_a E(x) - \frac{4\pi}{c} S(x). \tag{B.97}$$

Furthermore, assuming that the solution for some source function $S(x)$ has a linear distribution of the form:

$$E(x) = ax + b, \tag{B.98}$$

then the coefficients a and b are dictated by the conditions of the radiation field at the boundaries. Thus, plugging Eq. B.98 into Eq. B.7 assuming Dirichlet conditions at the left and right boundary gives:

$$\begin{aligned} b &= \frac{4\pi}{c} B_\nu(T_L) \\ a &= \frac{1}{X} \frac{4\pi}{c} [B_\nu(T_R) - B_\nu(T_L)], \end{aligned} \tag{B.99}$$

where T_L and T_R are the radiation temperatures at the left and right boundaries respectively, and X is the total thickness of the slab.

Solving Eq. B.97 for each of the flux-limiters in §1.4.1 gives different source functions for:

the Sum Limiter:

$$S(x) = \left[\sigma_a(ax+b) - \frac{|a|a^2}{\left(3\sigma_t(ax+b)+|a|\right)^2}\right]\frac{c}{4\pi}, \tag{B.100}$$

the Max Limiter:

$$S(x) = \begin{array}{ll} \sigma_a(ax+b)\frac{c}{4\pi}, & 3\sigma_t > \frac{|a|}{ax+b} \\ \left[\sigma_a(ax+b) - \frac{a^2}{|a|}\right]\frac{c}{4\pi}, & 3\sigma_t < \frac{|a|}{ax+b} \end{array} \tag{B.101}$$

the Larsen Limiter:

$$S(x) = \left[\sigma_a(ax+b) - \frac{|a|^n a^2}{\left[(3\sigma_t)^n + \left(\frac{|a|}{ax+b}\right)^n\right]^{\frac{1}{n}+1}(ax+b)^{n+1}}\right]\frac{c}{4\pi}, \tag{B.102}$$

and the Simplified Levermore-Pomraning Limiter:

$$S(x) = \left[\sigma_a(ax+b) - \frac{a^4\left(a+4\sigma_t(ax+b)\right)}{\left(a^2+3\sigma_t a(ax+b)+6\sigma_t^2(ax+b)^2\right)^2}\right]\frac{c}{4\pi}. \tag{B.103}$$

Figure B.10(a) shows the range of R values throughout a $1.0cm$ thick slab for a total opacity of $0.5558cm^{-1}$, and a fixed temperature on the left and right boundaries of $100eV$ and $141.42eV$ respectively. According to Figure 1.17, this range is within the region where all the flux-limiters have a significant influence on the diffusion coefficient, and is therefore an acceptable place to test the implementation of the various flux-limiters. Figure B.10(b) shows the plots of the calculated source functions for each of these limiters. In addition to the parameters listed above, these calculations assume an absorption opacity of $5.558cm^{-1}$ (a factor of 10 higher than the total opacity) in order to keep the source function positive.

The relative errors between the BUCKY solutions and the linear radiation energy density in Eq. B.98 are shown in Figures B.11(a) and (b). In each case, the BUCKY

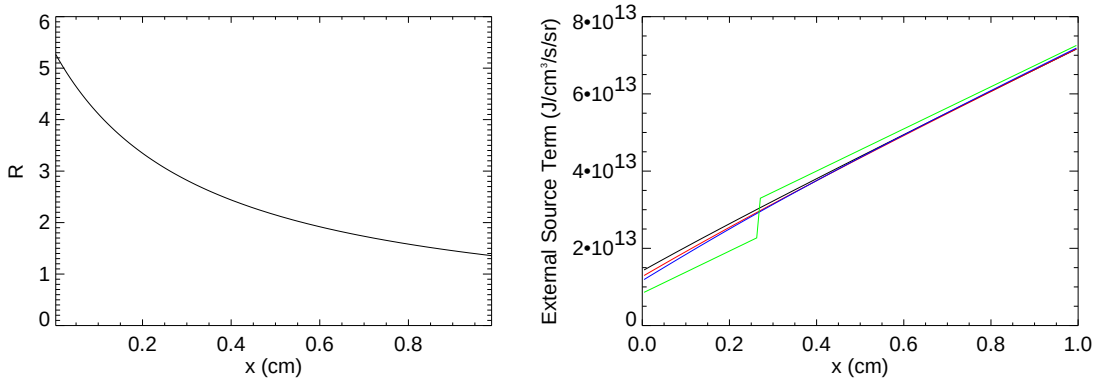

(a) (b)

Figure B.10: (a)Calculated R values for an assumed energy density of $E = B_\nu(100eV) + B_\nu(131.61eV)x$ and a total opacity of $0.5558cm^{-1}$. (b)External source functions for the SUM-limiter (black), the Levermore-Pomraning-limiter (red), the Larsen-limiter (blue), and the MAX-limiter (green).

calculated solution is taken after 100 cycles. The solutions using the SUM-, Larsen-, and Levermore-Pomraning-limiters as shown in B.11(a) all agree to better than 0.04%. However, the MAX-limiter shown in B.11(b) has maximum errors up to 1%. This is an artifact of the discontinuity that exists in the form of the MAX-limited diffusion coefficient, and is a good reason to avoid this form of the flux-limiter.

While BUCKY reproduces the expected solutions rather well, these cases only test the implementation of the numerics in the interior of the slab. Because the test cases assumed Dirichlet conditions on each boundary, the value of the radiation energy density on the left and right boundaries are well fixed and therefore not very demanding on the numerics. A more realistic case to consider would be that of a source condition on the left boundary of the slab and a vacuum condition on the right boundary. Solving Eq. B.7

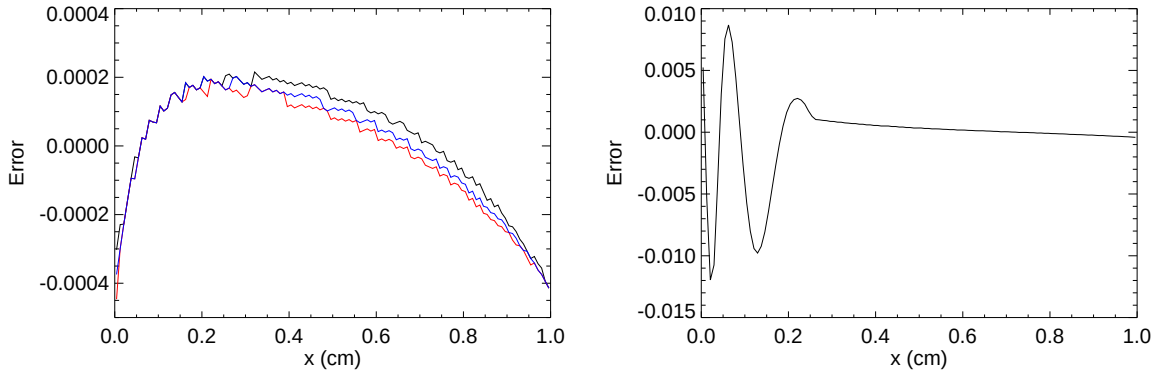

(a) (b)

Figure B.11: Relative errors between the assumed radiation energy density in Eq. B.98 and that calculated by BUCKY for the (a) SUM (black), Larsen n=2 (red), and Levermore-Pomraning-limiters (blue), and (b) that calculated for the MAX-limiter.

for these boundary conditions then gives the values of the coefficients in Eq. B.98 as:

$$\begin{aligned} b &= \frac{4\pi}{c} B_\nu(T_L) \frac{1+3\sigma_T X}{3(1+\sigma_T X)} \\ a &= -b/X. \end{aligned} \tag{B.104}$$

The comparison between the BUCKY calculated results (using the SUM-limiter) and the assumed form of the radiation energy density (using the coefficients in Eq. B.104) is shown in Figure B.12 (where $\sigma_a = \sigma_T = 0.5558 cm^{-1}$ and $T_L = 100eV$). In this case, the BUCKY calculation never settles on a single solution, but rather oscillates between 10 different distributions (5 of which are shown in the figure). This numerical periodicity occurs because the gradients at each edge are calculated based on the result of the calculation from the previous cycle. However, the boundary value of the energy density is calculated based on the gradient at each edge on the current cycle. Because the diffusion equation is elliptical, the values at each boundary effect the values throughout the entire sample thereby changing the gradient at each boundary (and thus the calculation of the boundary value). This leads to a periodic solution which, in this case, has a period of 10.

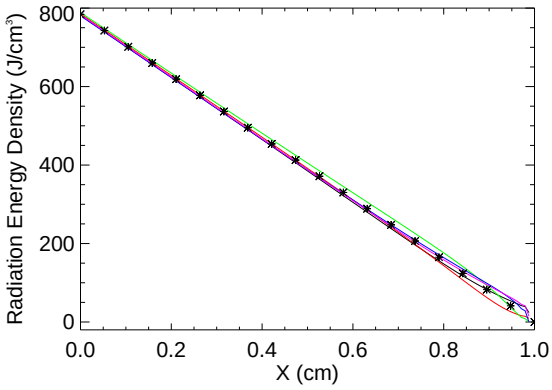

Figure B.12: Comparison between the BUCKY calculated radiation energy density for the SUM-limiter (solid lines) and the assumed value using the coefficients in Eq. B.104 (stars). The calculations assume a source condition on the left boundary and a vacuum condition on the right boundary.

According to Figure B.12, these solutions oscillate around the assumed solution, but have relative errors up to 35%. This is a problem inherent with the first order implementation of the finite-differencing scheme, and may only be fixed by using a higher order (nonlinear) solver.

B.4.4 Time Dependent Solutions

In addition to (all) the analytic steady state solutions presented up to this point, the implementation of the time-dependency of the diffusion equation in BUCKY also requires verification. Because of the difficulty in solving Eq. B.1 for real geometries, these solutions are all calculated for an infinite medium (thereby permitting the application of Fourier transform methods).

Planar Geometry

In the case of an infinitesimally thin, steady state planar source in a medium with constant opacities, the diffusion equation can be written as:

$$\frac{\partial E(x,t)}{\partial t} - \frac{c}{3\sigma_t}\frac{\partial^2 E(x,t)}{\partial x^2} = -\sigma_a E(x,t), \tag{B.105}$$

under the initial condition:

$$E(x,t_0) = E_0\delta(x-x_0), \tag{B.106}$$

where x_0 is the position of the radiation source, t_0 is the time when the source is turned on (and off), and E_0 is the total energy (in $\frac{J}{cm^2}$). Eq. B.105 can be solved in $E(k,s)$ space by taking the Laplace ($t \rightarrow s$) and Fourier ($x \rightarrow k$) transforms to give [6]:

$$E(k,s) = \frac{E_0}{\sqrt{2\pi}\left(s + \frac{ck^2}{3\sigma_t} + c\sigma_a\right)}. \tag{B.107}$$

The inverse transforms then yield the analytic, time-dependent radiation energy density distribution as:

$$E(x,t) = E_0\sqrt{\frac{3\sigma_t}{4\pi ct}}e^{-c\sigma_a(t-t_0)}e^{-\frac{3\sigma_t(x-x_0)^2}{4ct}}. \tag{B.108}$$

Figure B.13 shows the comparison between the BUCKY calculated results and the solution to Eq. B.108 at times of $1ps$, $10ps$, $20ps$, and $30ps$. Each calculation assumes $\sigma_a = \sigma_t = 5.558cm^{-1}$, $t_0 = 0s$, and $E_0 = 13751.9\frac{J}{cm^2}$. In BUCKY, the source is seeded with the analytical distribution at a time of $1ps$, and is centered on an initial source position of $x_0 = 50.0cm$. The source input is done this way to avoid complications associated with trying to model a delta function in time and space as a finite value in BUCKY. According to Figure B.13, the BUCKY calculation compares well to the analytic results at each time.

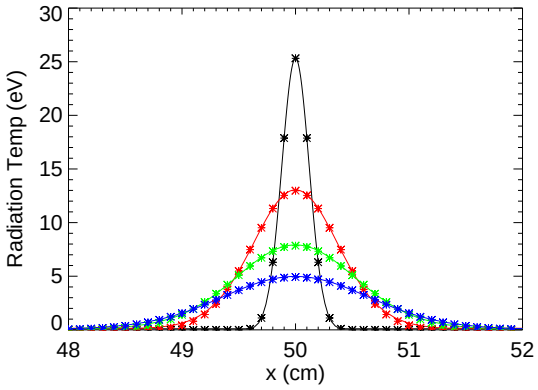

Figure B.13: Time-dependent radiation temperature in planar geometry as calculated by BUCKY (solid lines) and the analytic result in Eq. B.108 (stars) at times of $1ps$ (black), $10ps$ (red), $20ps$ (green), and $30ps$ (blue).

Spherical Geometry

Following the analysis by Brunner [6], the solution to the infinite planar source solution in Eq. B.108 can be transformed to a point source solution by:

$$E_{\text{point}}(r,t) = -\frac{1}{2\pi r}\frac{\partial E_{\text{plane}}}{\partial x}|_{x=r}. \tag{B.109}$$

The resulting equation for the time-dependent radiation energy density in spherical geometry can be written as:

$$E(r,t) = E_0\left[\frac{3\sigma_t}{4\pi ct}\right]^{3/2} e^{-c\sigma_a(t-t_0)}e^{-\frac{3\sigma_t r^2}{4ct}}, \tag{B.110}$$

where E_0 is now given in units of J, and it has been assumed that the initial source location is $r_0 = 0$.

Figure B.14 shows the comparison between the BUCKY calculated results and the solution to Eq. B.110 at times of $1ps$, $10ps$, $20ps$, and $30ps$. The BUCKY calculation is again seeded with the analytical energy density at a time of $1ps$, for a total initial energy of $E_0 = 13751.9J$.

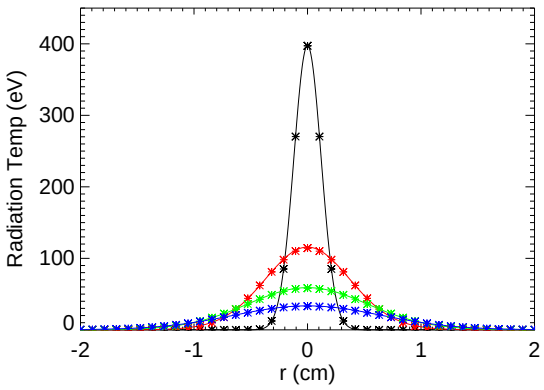

Figure B.14: Time-dependent radiation temperature in spherical geometry as calculated by BUCKY (solid lines) and the analytic result in Eq. B.110 (stars) at times of $1ps$ (black), $10ps$ (red), $20ps$ (green), and $30ps$ (blue).

Cylindrical Geometry

Finally, verifying the time-dependence in cylindrical geometry simply requires defining an infinite line source. This can be done by integrating Eq. B.110 over the line as:

$$E_{\text{line}}(\rho, t) = \int_{-\infty}^{\infty} E_{\text{point}}(\sqrt{\rho^2 + z^2}, t)dz. \tag{B.111}$$

Then, the solution for the case of an infinite line source in cylindrical geometry can be written as:

$$E(\rho, t) = E_0 \frac{3\sigma_t}{4\pi ct} e^{-c\sigma_a(t-t_0)} e^{-\frac{3\sigma_t \rho^2}{4ct}}, \tag{B.112}$$

for E_0 the total initial energy now given units of $\frac{J}{cm}$.

Figure B.15 shows the comparison between the BUCKY calculated results and the solution to Eq. B.112 at times of $1ps$, $10ps$, $20ps$, and $30ps$. The BUCKY calculation is again seeded with the analytical energy density at a time of $1ps$, for a total initial energy of $E_0 = 13751.9\frac{J}{cm}$. As in each of the comparisons above, the solutions calculated in BUCKY compare very well with the analytic results.

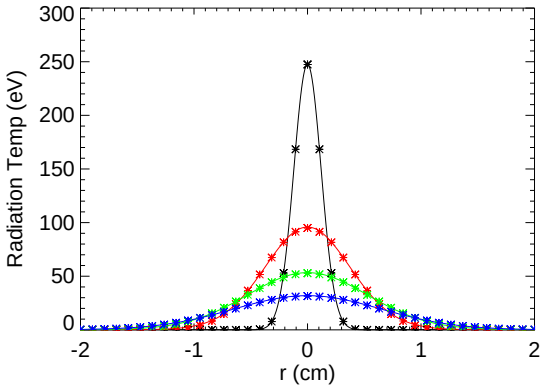

Figure B.15: Time-dependent radiation temperature in cylindrical geometry as calculated by BUCKY (solid lines) and the analytic result in Eq. B.112 (stars) at times of $1ps$ (black), $10ps$ (red), $20ps$ (green), and $30ps$ (blue).

B.5 Radiatively Heated Plasmas

One final class of problems which requires proper verification is the case of a radiatively heated plasma. Any transport code which is intended to model the radiation conditions inside a plasma with real temperature dependent material properties must include an energy conservation equation which couples the plasma conditions to the radiation field. This coupling is accomplished through the radiative emission and absorption terms that appear in each equation. In BUCKY, the conservation of energy is expressed as a temperature diffusion equation, and is written in Lagrangian coordinates as [4]:

$$c_v \frac{\partial T_p}{\partial t} = \frac{\partial}{\partial m}\left(r^{\delta-1}\kappa_p \frac{\partial T_p}{\partial r}\right) - \left[\frac{\partial E_p}{\partial V} + P\right]\frac{\partial V}{\partial t}T_p + A - J + S_p, \tag{B.113}$$

where T_p is the plasma temperature, c_v is the heat capacity, κ_p is the plasma thermal conductivity, P is the plasma pressure, S_p is an external source term, and A and J are the radiation absorption and emission terms respectively. As in the radiation transport equation, the radiation absorption and emission are given by:

$$A = c\sigma_{P,a}E \tag{B.114}$$

$$J = 4\pi\sigma_{P,e}\int_0^\infty B_\nu(T_p)d\nu. \tag{B.115}$$

In order to calculate an analytic solution to the coupled set of equations (between the radiation transport and the energy conservation equations), Eq. B.113 is typically simplified by assuming that thermal conductivity is negligible ($\kappa_p = 0$), the plasma is static ($\partial V/\partial t = 0$), and there are no external sources ($S_p = 0$). Then, if it is assumed that the heat capacity is proportional to the plasma temperature to the third power by:

$$c_v = \alpha T^3, \tag{B.116}$$

then Eq. B.113 can be written as:

$$\frac{\partial T_p(r,t)}{\partial t} = \frac{1}{\alpha T^3}\left(c\sigma_{P,a}E(r,t) - \sigma_{P,e}\sigma_{SB}T_p^4\right), \tag{B.117}$$

where σ_{SB} is the Stephan-Boltzmann constant ($= 1.02825{*}10^5 J/cm^2/s/eV^4$), and $E(r,t)$ is the radiation energy density given by either Eq. B.1 or Eq. B.61. These equations are solved by Su and Olson for both a Marshak wave in a semi-infinite slab [7] and a time-dependent finite source in an infinite slab [8].

B.5.1 The Marshak Wave Problem

The Marshak wave problem is a classic benchmark for radiation-hydrodynamics codes. The premise is very simple; An isotropic radiation source condition is placed on the boundary of an initially cold, semi-infinite slab. The radiation from the boundary source penetrates and heats the material, which itself radiates isotropically at the local plasma temperature. The result is two well-defined, propagating wavefronts corresponding to the penetrating radiation and thermal energy. These wavefronts eventually coalesce, and the total energy wave propagates deep into the plasma.

This problem has been solved analytically in the single group radiation diffusion approximation by Su and Olson [98]. Their solution is expressed as a function of 4 dimensionless variables given in the nomenclature of this document as:

$$x = \sqrt{3}\sigma' r \tag{B.118}$$

$$\tau = \left(\frac{16\sigma_{SB}\sigma'}{\alpha}\right) t \tag{B.119}$$

$$u(x,\tau) = \left(\frac{c}{4}\right)\left[\frac{E(r,t)}{\sigma_{SB}T_0^4}\right] \tag{B.120}$$

$$v(x,\tau) = \left[\frac{T_p}{T_0}\right]^4, \tag{B.121}$$

where $\sigma'/\rho = \sigma_R = \sigma_{P,e} = \sigma_{P,a}$, T_0 is the radiation temperature of the boundary source, and $E(r,t)$ is given by Eq. B.1. After a great deal of mathematics, their solutions for the dependent variables, u and v, are expressed as:

$$\begin{aligned} u(x,\tau) =& 1 - \frac{2\sqrt{3}}{\pi}\int_0^1 e^{-\tau\eta^2}\left[\frac{\sin[x\gamma_1(\eta)+\theta_1(\eta)]}{\eta\sqrt{3+4\gamma_1^2(\eta)}}\right]d\eta \\ &- \frac{\sqrt{3}}{\pi}e^{-\tau}\int_0^1 e^{-\tau/\epsilon\eta}\sqrt{\epsilon+\frac{1}{1-\eta^2}}\left[\frac{\sin[x\gamma_2(\eta)+\theta_2(\eta)]}{\eta(1+\epsilon\eta)\sqrt{3+4\gamma_2^2(\eta)}}\right]d\eta \end{aligned} \tag{B.122}$$

$$v(x,\tau) = \int_0^\tau e^{-(\tau-\tau')}u(x,\tau')d\tau', \tag{B.123}$$

where;

$$\gamma_1(\eta) = \eta\sqrt{\epsilon+\frac{1}{1-\eta^2}} \tag{B.124}$$

$$\gamma_2(\eta) = \sqrt{(1-\eta)\left(\epsilon+\frac{1}{\eta}\right)} \tag{B.125}$$

$$\theta_n(\eta) = \cos^{-1}\sqrt{\frac{3}{3+4\gamma_n^2(\eta)}}, n = 1,2 \tag{B.126}$$

for the transport parameter $\epsilon = 16\sigma_{SB}/\alpha c$. These integrals must then be solved numerically for some value of ϵ. Table B.8 lists the calculated values of Eq. B.122 and B.123 for $\epsilon = 0.1$, $(\alpha = 160\sigma_{SB}/c)$.

x	τ=0.01	0.1	1	10
0	0.23997	0.43876	055182	0.79720
0.1	0.17979	0.39240	0.51412	0.77644
0.25	0.11006	0.33075	0.46198	0.75004
0.5	0.04104	0.24629	0.38541	0.70679
0.75	0.01214	0.18087	0.32046	0.66458
1	0.00268	0.13089	0.26564	0.62353
2.5		0.01274	0.08147	0.40703
5			0.00961	0.17142
7.5			0.00097	0.06123
10				0.01909
15				0.00135

$u(x,\tau)$

x	τ=0.01	0.1	1	10
0	0.00170	0.03446	0.32030	0.78318
0.1	0.00110	0.02955	0.29429	0.76448
0.25	0.00055	0.02339	0.25915	0.73676
0.5	0.00012	0.01566	0.20925	0.69139
0.75		0.01030	0.16862	0.64730
1		0.00672	0.13563	0.60461
2.5		0.00035	0.03539	0.38320
5			0.00334	0.15285
7.5			0.00028	0.05166
10				0.01527
15				0.00098

$v(x,\tau)$

Table B.8: Analytic solutions to the Su and Olson Marshak wave problem for $\epsilon = 0.1$ [98]

Figure B.16(a) and (b) show the comparison between the analytic calculations and the conditions simulated by BUCKY. As evidenced by the figure, the BUCKY calculations compare very well to the analytic results at the plotted times of $\tau = 0.1, 1$, and 10.

B.5.2 Non-Equilibrium Transport in an Infinite Medium

Su and Olson have defined a second benchmark problem for non-equilibrium radiative transfer where they have constructed analytic solutions for both radiation diffusion and true transport [99]. In this problem, a finite radiation source in a region $-x_0 \leq x \leq x_0$ is active for a time $0 \leq \tau \leq \tau_0$ within an infinite slab. The solutions are expressed in the same dimensionless variables given in Eq. B.118-B.121 except that T_0 is now the temperature of the isotropic blackbody source. These problems are rather complex,

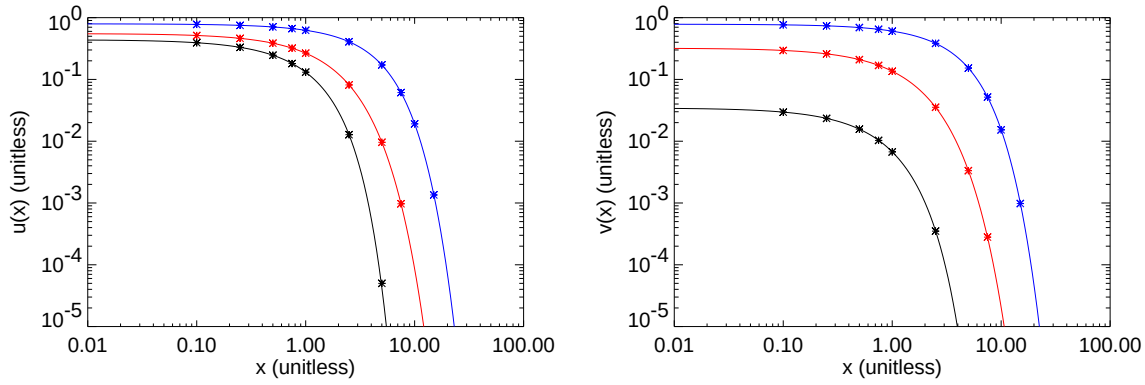

(a) (b)

Figure B.16: Comparison between a BUCKY simulation (lines) and the analytic calculations (stars) of the scaled (a) radiation energy, u, and (b) plasma energy, v, for the Su and Olson Marshak wave problem [98] at times of $\tau = 0.1$ (black), 1 (red), and 10 (blue).

and the reader is directed to the reference for the derivation and final expression of the solutions. Table B.9 and B.10 list the analytic evaluations of the diffusion and transport solutions respectively for a source with $\epsilon = 1$, $\tau_0 = 10$, and $x_0 = 0.5$.

The comparison between the analytic solutions and those calculated by BUCKY for the radiation diffusion case are shown in Figure B.17(a) and (b). As evidenced by the figure, BUCKY compares well at each time. Because Su and Olson have also provided solutions for the case of true radiation transport, this problem provides a unique opportunity to investigate the accuracy of flux-limited diffusion. Figure B.18(a) shows the comparison between the analytic solutions for the transport case, and those calculated by flux-limited diffusion (Levermore-Pomraning limiter). Figure B.18(b) shows the comparison between the analytic solution at a time of $\tau = 1.0$, and the flux-limited diffusion solution for each flux-limiter. Clearly, flux-limited diffusion does a decent job of approximating the analytic result. Also plotted in Figure B.18(b) is the short-characteristics solution to this problem at a time of $\tau = 1.0$. Under these circumstances, the short-

characteristics solution transports radiation far too quickly. This is not surprising since the Su and Olson benchmark is intentionally a time-dependent problem, and the implementation of short-characteristics in BUCKY is time-independent. However, this serves as a reminder that, although short-characteristics is a much better approximation to true transport in problems with slowly varying radiation fields, there are some instances when flux-limited diffusion will provide a more accurate result.

$u(x, \tau)$

x	τ=0.1	1	10	100
0.01000	0.09403	0.50359	1.86585	0.35365
0.10000	0.09326	0.49716	1.85424	0.35360
0.31623	0.08230	0.43743	1.74866	0.35309
0.50000	0.04766	0.33271	1.57237	0.35225
0.75000	0.00755	0.18879	1.29758	0.35051
1.00000	0.00064	0.10150	1.06011	0.34809
1.33352		0.04060	0.79696	0.34382
1.77828		0.01011	0.52980	0.33636
3.16228		0.00003	0.12187	0.30185
5.62341			0.00445	0.21453
10.0000				0.07351

$v(x, \tau)$

x	τ=0.1	1	10	100
0.01000	0.00466	0.21859	1.75359	0.35554
0.10000	0.00464	0.21565	1.74218	0.35548
0.31623	0.00424	0.18765	1.63837	0.35497
0.50000	0.00234	0.13590	1.46494	0.35411
0.75000	0.00023	0.06746	1.19584	0.35235
1.00000		0.03173	0.96571	0.34988
1.33352		0.01063	0.71412	0.34555
1.77828		0.00210	0.46369	0.33797
3.16228			0.09834	0.30294
5.62341			0.00306	0.21452
10.0000				0.07269

Table B.9: Analytic radiation diffusion solutions to the Su and Olson non-equilibrium transport problem in an infinite medium for $\epsilon = 1, \tau_0 = 10,$ and $x_0 = 0.5$ [99]

$u(x, \tau)$

x	τ=0.1	1	10	100
0.01000	0.09531	0.64308	2.23575	0.35720
0.10000	0.09531	0.63585	2.21944	0.35714
0.31623	0.09529	0.56187	2.06448	0.35664
0.50000	0.04765	0.35801	1.73178	0.35574
0.75000		0.11430	1.27398	0.35393
1.00000		0.03648	0.98782	0.35141
1.33352		0.00291	0.70822	0.34697
1.77828			0.45016	0.33924
3.16228			0.09673	0.30346
5.62341			0.00375	0.21382
10.0000				0.07200

$v(x, \tau)$

x	τ=0.1	1	10	100
0.01000	0.00468	0.27126	2.11186	0.35914
0.10000	0.00468	0.26839	2.09585	0.35908
0.31623	0.00468	0.23978	1.94365	0.35854
0.50000	0.00234	0.14187	1.61536	0.35766
0.75000		0.03014	1.16591	0.35581
1.00000		0.00625	0.88992	0.35326
1.33352		0.00017	0.62521	0.34875
1.77828			0.38688	0.34086
3.16228			0.07642	0.30517
5.62341			0.00253	0.21377
10.0000				0.07122

Table B.10: Analytic radiation transport solutions to the Su and Olson non-equilibrium transport problem in an infinite medium for $\epsilon = 1, \tau_0 = 10,$ and $x_0 = 0.5$

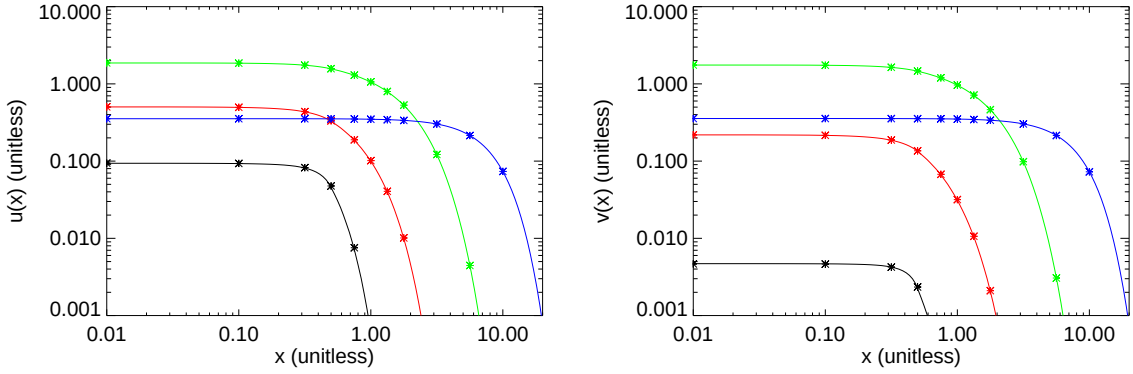

(a) (b)

Figure B.17: Comparison between a BUCKY simulation (lines) and the analytic calculations (stars) of the scaled (a) radiation energy, u, and (b) plasma energy, v, for the diffusion solution to the Su and Olson non-equilibrium transport problem at times of $\tau = 0.1$ (black), 1 (red),10 (green), and 100 (blue).

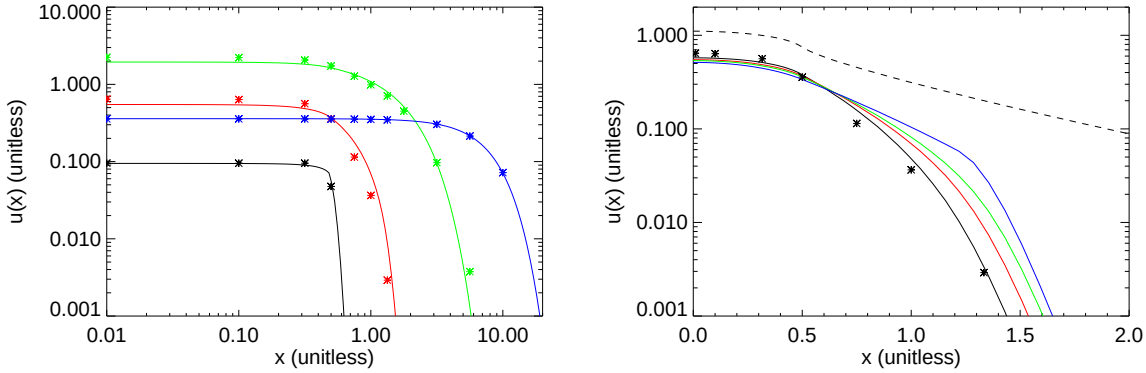

(a) (b)

Figure B.18: (a) Comparison between a BUCKY simulation using the Levermore-Pomraning version of flux-limited diffusion (lines) and the analytic calculations (stars) of the scaled radiation energy, u, for the transport solution to the Su and Olson non-equilibrium transport problem at times of $\tau = 0.1$ (black), 1 (red),10 (green), and 100 (blue). (b) Comparison between the analytic calculation (stars) and a BUCKY simulation using the (a) SUM-limiter, (b) Levermore-Pomraning-limiter, (c) Larsen-limiter (n=2), and (d) MAX-limiter at a time of $\tau = 1$. Also shown is a BUCKY calculation using short-characteristics (dashed).

B.6 References

[1] E.E. Lewis and W.F. Miller Jr., *Computational Methods of Neutron Transport*, (American Nuclear Society, La Grange Park, 1993).

[2] T.A. Brunner, "Forms of approximate radiation transport," SANDIA report, SAND2002-3739P, (2002).

[3] G.A. Moses, Private Communication.

[4] J.J. MacFarlane, G.A. Moses, and R.R. Peterson, 'BUCKY - A 1-D radiation hydrodynamics code for simulating inertial confinemnent fusion high energy density plasmas', UWFDM report, UWFDM-984.

[5] J.D. Hoffman, *Numerical Methods for Engineers and Scientists*, (McGraw-Hill, New York, 1992).

[6] T.A. Brunner, "Some analytic solutions to the diffusion equation," Internal Memo.

[7] B. Su and G.L. Olson, "Benchmark results for the non-equilibrium marshak diffusion problem," J. Quant. Spectrosc. Radiat. Transfer, **56** No. 3, p. 337 (1996).

[8] B. Su and G.L. Olson, "An analytical benchmark for non-equilibrium radiative transfer in an isotropically scattering medium," Ann. Nucl. Energy, **24** No. 13, p. 1035 (1997).

Appendix C

Counting Statistics on Kodak RAR2497 X-ray Film

Conducting a detailed χ^2 analysis between experimental data and a model fit to that data requires a good understanding of the statistical fluctuations (the standard deviation). That is, it is difficult to determine the quality of a fit without knowing the possible error in the data. In photon-counting, the statistical distribution of measured counts is represented to good approximation by the Poisson probability distribution [1], which is mathematically defined as:

$$P(x) = \frac{< x >^x e^{-<x>}}{x!}, \tag{C.1}$$

for x the number of counts recorded in any given measurement, and $< x >$ the average number of counts recorded over all measurements. It can be shown that the standard deviation in the recorded counts, σ, for the Poisson distribution is given by:

$$\sigma = \sqrt{< x >}. \tag{C.2}$$

Thus, if one can determine that a distribution of recorded counts follows a Poisson distribution, then the standard deviation can be determined directly from the mean value.

In x-ray spectroscopy, Kodak RAR2497 x-ray film is a standard detector for many time-integrated spectrometers (although it is no longer made). The active elements in the emulsion of RAR2497 film are grains of $AgBr$, and darkening on the film comes from 'activation' of these grains when they absorb a photon. How many grains are activated is sensitive to the absorption coefficient (the opacity) of the $AgBr$, and is therefore a function of the size of the grains, their packing fraction, the thickness of the emulsion, and the intensity and energy of the incident x-rays. As discussed in Appendix A, this film has been calibrated by Henke et al. [2–4] to relate film density to incident photon intensity (in $photons/\mu m^2$) as a function of x-ray energy. The mean number of incident photons can be found by multiplying the average corrected photon intensity by the observed area of the film. However, this is not the value that determines the statistical fluctuations in the recorded data. The observed fluctuations could be caused by any number of issues; the number of photons actually absorbed, random distributions in the packing fractions of the $AgBr$ grains, random processes that occur during film developing, and so on.

Conducting a rigorous statistical analysis of data recorded on RAR2497 film requires that the distribution function be *measured* as a function of the incident photon intensity (and perhaps the photon energy). If a number of measurements can be made at the same incident photon intensity, then a probability histogram that describes the observations can be constructed. If this recorded histogram has the same shape as a Poisson distribution, then a 'rescale factor' can be determined that quantifies the measured distribution and defines the associated uncertainty. This Appendix describes some basic experiments and the associated statistical analysis conducted to determine the rescale

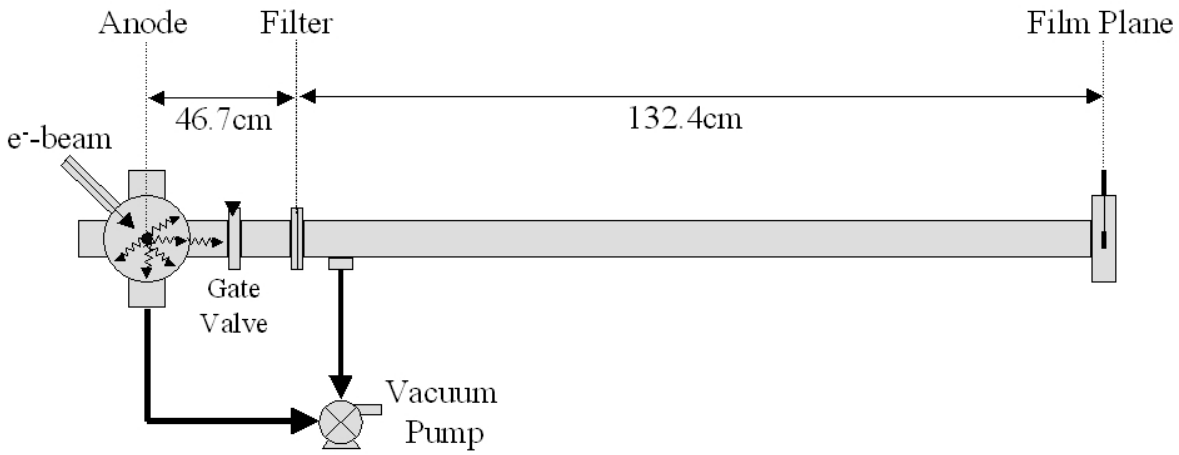

Figure C.1: Schematic of the experimental apparatus for the experiments on the statistical distribution of photon counting with RAR2497 x-ray film.

factors for RAR2497 film over a range of photon intensities.

C.1 Experimental Method

Figure C.1 shows a schematic diagram of the apparatus for these experiments. The x-rays come from a Manson source, an electron-beam device that excites or ionizes the various atoms in materials placed in the beam path (at the location of the anode). As these excited atoms decay, they give off isotropically distributed x-rays. These experiments used a magnesium-fluoride (MgF_2) anode, a beam energy of $\approx 8keV$, and a beam current of $\approx 3mA$. The spectral line of primary interest for these experiments is Mg K-α fluorescence at 9.890Å (1.2536keV). To block visible light and isolate this line from the other components of the anode emission, a 6μm thick aluminum filter was placed between the source and film plane at a distance of 132.4cm from the film. The film was placed at a distance of 179.1cm from the Manson source anode, and was exposed over a

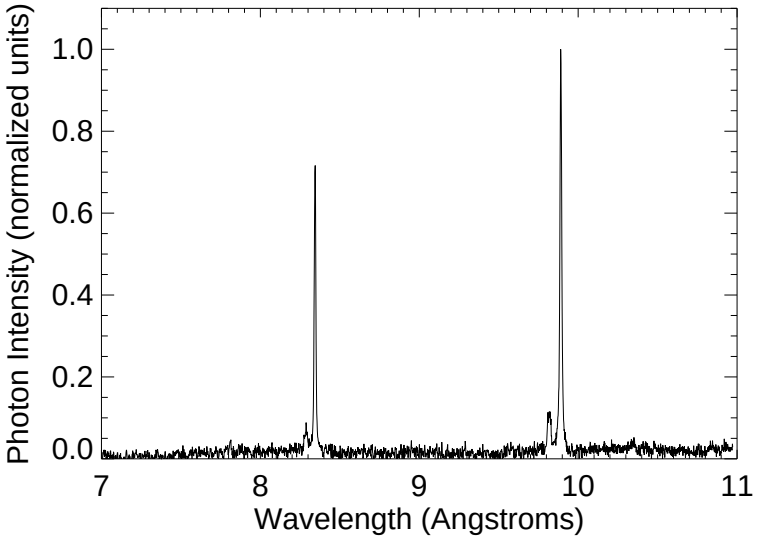

Figure C.2: X-ray spectrum at the location of the film plane with a MgF_2 anode and a $6.0\mu m$ Al filter.

$4cm \times 2.8cm$ area.

To measure the spectral distribution of the x-ray source hitting the film, a convex crystal spectrometer (with a $5.08cm$ radius potassium-acid-pthalate crystal) was placed at the film plane. Figure C.2 shows the recorded spectrum from a $3h$ exposure. There are 2 spectral features present. The most intense line is the Mg K-α fluorescence line at 9.890Å. The second line is from a contaminant on the MgF_2 anode. This line is likely to be from a first order reflection, which has a reflectivity that is over a factor of 30 higher than the second or third order. The 8.343Å wavelength is very close to that of the Al K-α fluorescence line, which lies at the peak of the Al filter transmission curve (above 4Å). The Henke density-to-intensity conversion factors for 8.34Å and 9.89Å are very similar so that, if this line is indeed from a first order reflection, it should have little bearing on the experiments.

The measurement procedure for the statistic calibration experiments was as follows:

Vacuum was pulled from both sides of the Al filter to a final pressure of $\approx 1 \times 10^{-5} Torr$. The Manson source voltage and emission current were turned up to their respective operating values to effectively 'turn-on' the x-ray emission. A $0.159cm$ thick Al cover slide was pulled from the front of the film to begin the exposure. At the end of the desired exposure time, the cover slide was moved back in front of the film, the Manson source current and voltage were turned off, and the system was vented. The film pack was then removed from the apparatus and brought to a dark-room for developing. The film was developed using the procedure outlined by Henke et al. [3] as used for the film density calibration experiments. This measurement procedure was repeated for exposure times of; $30s$, $60s$, $180s$, $300s$, $420s$, $600s$, $900s$, and $1800s$. At the beginning and end of each day of operation, a $\approx 3600s$ light-leak test was conducted by running through the entire procedure without turning on the x-ray source. After the exposures were all complete, the developed film was digitized on a Perkin-Elmer microdensitometer using a $14\mu m$ scan-box with a 0.1 numerical aperture for both the illumination and transmission beam cones.

C.2 Data and Analysis

As an example of the digitized exposures, Figures C.3(a) and (b) show the scanned image of the $300s$ exposure and a $250\mu m$ wide horizontal lineout across the image. As evidenced by the lineout, the exposure is quite uniform. The low exposure on the far right side of the image is from an area of the film that remained covered by the Al cover slide during the exposure. This part of the film is useful for determining the average chemical fog left on the film from the developing process. The fog must be subtracted from the measured film density to determine the net density required to apply the Henke intensity

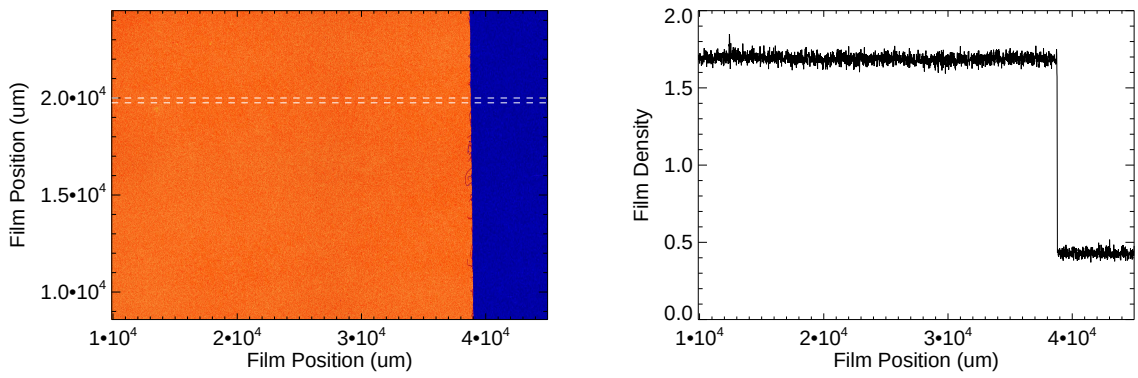

(a) **(b)**

Figure C.3: (a) Portion of the digitized film density from the $300s$ exposure test. **(b)** $250\mu m$ wide lineout of the exposure shown in (a).

corrections.

The analysis procedure for determining the probability distribution of each digitized exposure was as follows: A lineout was taken over the uniformly exposed portion of the digitized exposure. The mean density of the film fog was determined by averaging over a large area of the unexposed portion. The film fog was then subtracted from the lineout to determine the net film density. The net film density was then converted into photon intensity using the Henke correction tables for RAR2497 film assuming a photon wavelength of 9.890Å ($1253.6eV$). Table C.1 lists the resulting mean film density and intensity values determined for each exposure.

Each point in the corrected lineouts were considered as an independent measurement of the same incident photon intensity. These points were then binned into a histogram of the frequency of occurrence versus photon intensity. The histograms were constructed by 50 uniformly sized bins covering the range from the minimum to maximum photon intensity in the lineout. This procedure was repeated for each exposure using lineout widths of $14\mu m$ (1 pixel), $100\mu m$, $250\mu m$, $500\mu m$, $1000\mu m$, and $2000\mu m$. As an example

Exposure Time	**Film Fog**	**Mean Net Density**	**Mean Intensity** ($photons/\mu m^2$)
$30s$	0.493	0.223	1.02
$60s$	0.462	0.413	2.06
$180s$	0.442	0.940	6.10
$300s$	0.432	1.258	9.79
$420s$	0.438	1.466	12.9
$600s$	0.548	1.685	17.3
$900s$	0.442	1.958	24.6
$1800s$	0.440	2.284	37.8

Table C.1: Resulting film density and corresponding mean intensity from the uniform exposures on RAR2497 film.

of the resulting distribution, Figure C.4 shows the 50 point histogram from the single pixel ($14\mu m$) wide lineout of the $300s$ exposure shown in Figure C.3(a). The quality of the histogram indicates that the distribution is well sampled.

Once the distributions had been determined for all exposure times and lineout widths, an automated fitting routine was used to determine the rescale factor that produced the best fit between each histogram and an analytic probability distribution. In all but one case, the Gaussian distribution was used for this fit rather than the Poisson. This was done because each is a good approximation of the other at high mean count values, and the factorial in the Poisson distribution makes it difficult to compute at high counts. The Poisson distribution was only used in the case of the $14\mu m$ wide lineout of the $30s$ exposure. In this case, both the measured and rescaled count values were low enough to allow a complete solution of the Poisson distribution.

The best-fit rescale factor of each histogram was determined using the following procedure: The abscissa of the histogram (the recorded photon intensity) was multiplied by

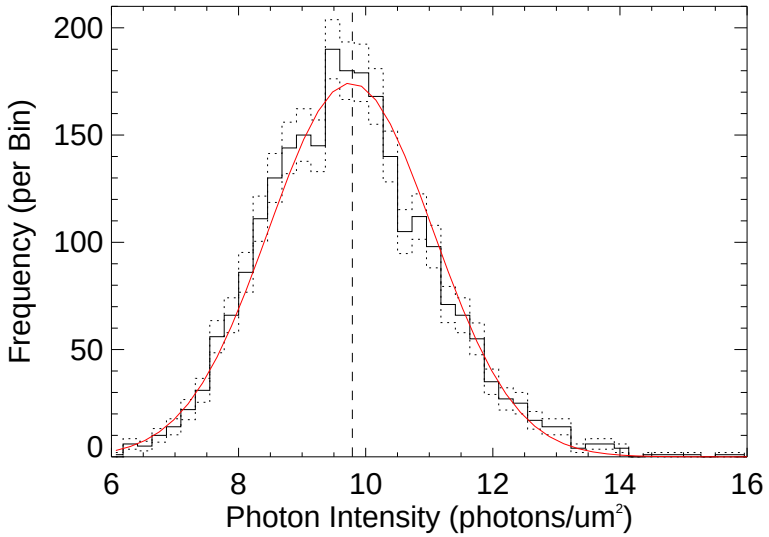

Figure C.4: Histogram of the distribution of photon intensities from a $14\mu m$ wide lineout taken on the $300s$ exposure shown in Figure C.3(a). Overlaid on the figure is the best-fit Gaussian distribution (red) at a rescale factor of 5.8. The χ^2 between these two distribution was determined to be 1.47.

a test rescale factor. The probability distribution was then computed using the average value of this 'rescaled' photon intensity. Since a probability distribution is a normalized function, the distribution was uniformly multiplied by the area under the rescaled histogram to put each distribution on the same axis. The χ^2 between the experimental histogram and the analytic probability distribution was then computed[a]. This procedure was then repeated for a large number of test rescale factors. Once a satisfactory range of χ^2 values was computed, a fifth order polynomial was fit to the χ^2 values as a function of rescale factor. The location of the minimum in this curve was considered as the best-fit rescale factor, and a final χ^2 and 1σ uncertainty between the histogram and the resulting distribution function was computed.

[a]To make this comparison, the data was assumed to follow Poisson statistics by defining the uncertainty in each bin height as the square root of the number of counts in the bin. If a fit can be found where the χ^2 is close to 1, then this prescribed uncertainty is at least consistent with the distribution.

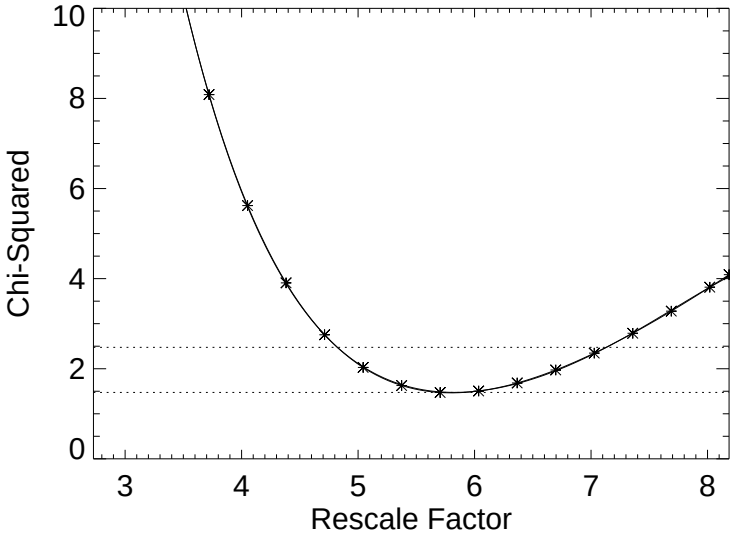

Figure C.5: χ^2 statistic as a function of test rescale factor between the data histogram and the Gaussian distribution function shown in Figure C.4. The symbols correspond to computed test points and the line is a fifth order polynomial fit to the symbols. The intersection of the solid line with the dotted lines marks the best-fit and 1σ confidence levels for the fit.

As an example, Figure C.5 shows the computed χ^2 as a function of rescale factor for the distribution of the $300s$ exposure shown in Figure C.4. The minimum χ^2 in this figure is 1.47 at a rescale factor of 5.8 with 1σ confidence levels at factors of 7.1 and 4.8. An overlay of the Gaussian distribution at the best-fit rescale factor is shown on the histogram in Figure C.4. The abscissa of the Gaussian has been divided by the rescale factor to put it on the same range as the data histogram. The standard deviation of the Gaussian is given by the square root of the average 'rescaled counts.' In the original units of the data, this standard deviation is given by:

$$\sigma = \frac{\sqrt{R < I >}}{R} = \sqrt{\frac{< I >}{R}}, \tag{C.3}$$

where R is the best-fit rescale factor and $< I >$ is the mean value of the data histogram (the photon intensity in $photons/\mu m^2$). Therefore, if the rescale factor is known for

some measured photon intensity, Eq. C.3 can be used to determine the uncertainty in the measurement.

Table C.2 shows the best-fit rescale factors as a function of the lineout width for each incident photon intensity recorded in the experiments. These rescale factors and the associated standard deviations in the incident photon intensity are plotted in Figure C.6 for the $14\mu m$ (single pixel) wide lineouts. The analysis suggests that there is a complex dependence of the statistical distribution on the incident photon intensity. At any given lineout width, the rescale factor increases for incident intensities between 1.02 and $2.05\mu m^{-2}$, and then decreases for $I \geq 6.1\mu m^{-2}$. The resulting standard deviation steadily increases as a function of incident photon intensity, but does not have a square root dependence. It is unclear what should cause such a complicated structure in the counting statistics. A few of the exposures were repeated and similar results were found. It is possible that the first two points in the data are below the linear region of the film response and the last point is above it. However, the rescale factors still show no constant dependence on the photon intensities in between. Regardless, the χ^2 between the histograms and analytic distribution functions were all very reasonable, which indicates that the measured distribution functions can be well represented by a Gaussian. Irrespective of what causes the complex relationship between the counting statistics and the incident intensity, the data in Table C.2 can be used to prescribe an uncertainty to the incident photon intensity for measurements made on RAR2497 film.

Mean Intensity		**Lineout Width**					
$(photons/\mu m^2)$		$14\mu m$	$100\mu m$	$250\mu m$	$500\mu m$	$1000\mu m$	$2000\mu m$
1.02	$R(I)$	$7.7^{+1.1}_{-1.5}$	$37.8^{+5.9}_{-7.8}$	$87.3^{+15.3}_{-20.6}$	$156.7^{+25.3}_{-33.9}$	$290.7^{+49.3}_{-67.8}$	$508.1^{+87.1}_{-117.8}$
	$\sigma(I)$	0.363 ± 0.030	0.164 ± 0.015	0.108 ± 0.011	0.081 ± 0.007	0.059 ± 0.006	0.045 ± 0.004
	χ^2	1.09	1.51	1.22	1.12	0.86	1.01
2.06	$R(I)$	$12.0^{+2.7}_{-2.0}$	$49.2^{+8.5}_{-6.7}$	$119.1^{+23.5}_{-17.6}$	$230.3^{+51.9}_{-37.9}$	$433.5^{+103.5}_{-75.9}$	$808.5^{+191.7}_{-140.3}$
	$\sigma(I)$	0.414 ± 0.040	0.204 ± 0.016	0.131 ± 0.011	0.094 ± 0.009	0.069 ± 0.007	0.050 ± 0.005
	χ^2	3.50	1.34	0.82	1.66	1.08	1.17
6.10	$R(I)$	$11.3^{+2.6}_{-1.9}$	$38.0^{+8.3}_{-6.3}$	$83.6^{+19.8}_{-14.1}$	$166.8^{+33.7}_{-25.7}$	$296.3^{+71.1}_{-53.0}$	$518.1^{+128.3}_{-93.1}$
	$\sigma(I)$	0.735 ± 0.073	0.401 ± 0.038	0.270 ± 0.027	0.191 ± 0.017	0.143 ± 0.015	0.108 ± 0.011
	χ^2	2.13	0.95	0.74	1.25	1.33	0.79
9.79	$R(I)$	$5.8^{+1.3}_{-1.0}$	$30.3^{+7.4}_{-5.3}$	$67.5^{+15.5}_{-11.1}$	$127.6^{+28.9}_{-21.9}$	$245.5^{+60.3}_{-44.1}$	$452.3^{+108.0}_{-79.6}$
	$\sigma(I)$	1.296 ± 0.127	0.569 ± 0.058	0.381 ± 0.037	0.277 ± 0.027	0.200 ± 0.021	0.147 ± 0.015
	χ^2	1.47	1.09	0.69	1.48	0.96	1.01

Table C.2: Rescale factors and associated standard deviations of the recorded photon intensity on RAR2497 film. The χ^2 values are listed for the comparison between the data histograms and the analytic distribution function at the best-fit rescale factors.

Mean Intensity		**Lineout Width**					
$(photons/\mu m^2)$		$14\mu m$	$100\mu m$	$250\mu m$	$500\mu m$	$1000\mu m$	$2000\mu m$
12.9	$R(I)$	$4.8\,^{+1.0}_{-0.8}$	$22.6\,^{+4.9}_{-3.7}$	$49.5\,^{+11.7}_{-8.6}$	$90.5\,^{+22.7}_{-16.4}$	$148.1\,^{+36.3}_{-25.6}$	$260.0\,^{+54.5}_{-42.7}$
	$\sigma(I)$	1.640 ± 0.147	0.756 ± 0.071	0.511 ± 0.052	0.378 ± 0.040	0.296 ± 0.030	0.223 ± 0.021
	χ^2	2.03	0.89	1.06	1.37	0.80	0.99
17.35	$R(I)$	$4.0\,^{+0.9}_{-0.7}$	$16.9\,^{+3.7}_{-2.8}$	$35.7\,^{+8.4}_{-6.0}$	$58.3\,^{+14.1}_{-10.1}$	$99.8\,^{+26.8}_{-19.2}$	$180.2\,^{+44.0}_{-32.0}$
	$\sigma(I)$	2.076 ± 0.207	1.014 ± 0.097	0.697 ± 0.069	0.545 ± 0.055	0.417 ± 0.047	0.310 ± 0.032
	χ^2	2.14	1.19	0.87	1.25	1.97	0.99
24.6	$R(I)$	$3.5\,^{+0.9}_{-0.7}$	$13.6\,^{+2.8}_{-2.0}$	$27.3\,^{+5.6}_{-4.4}$	$48.2\,^{+9.8}_{-7.4}$	$79.6\,^{+18.5}_{-14.1}$	$127.7\,^{+25.7}_{-19.6}$
	$\sigma(I)$	2.656 ± 0.301	1.347 ± 0.115	0.950 ± 0.086	0.714 ± 0.062	0.556 ± 0.056	0.439 ± 0.038
	χ^2	2.10	1.66	0.89	1.16	1.00	1.71
37.8	$R(I)$	$1.3\,^{+0.4}_{-0.3}$	$5.8\,^{+1.8}_{-1.2}$	$12.7\,^{+3.7}_{-2.6}$	$24.1\,^{+7.9}_{-5.4}$	$39.9\,^{+12.8}_{-9.0}$	$66.5\,^{+20.4}_{-14.5}$
	$\sigma(I)$	5.465 ± 0.774	2.558 ± 0.321	1.728 ± 0.209	1.252 ± 0.167	0.973 ± 0.130	0.754 ± 0.097
	χ^2	2.17	0.79	0.84	0.86	0.89	0.91

Table C.2: continued...

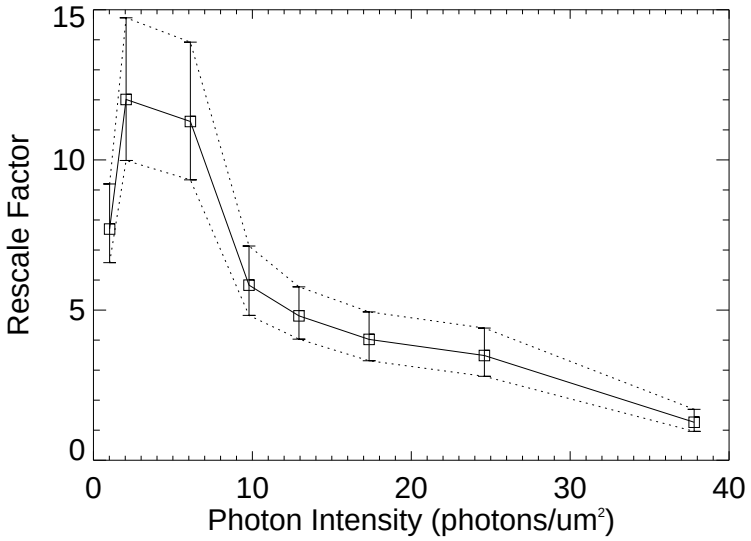

(a)

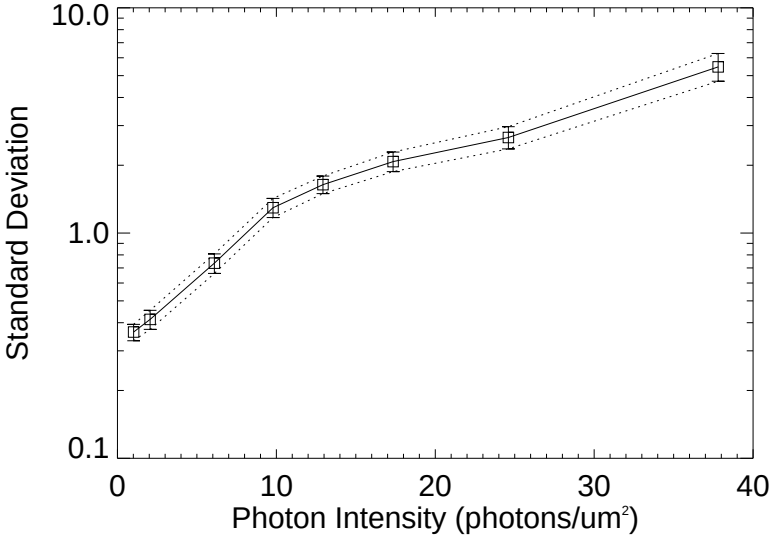

(b)

Figure C.6: (a) Rescale factors and **(b)** standard deviation for the statistical distribution of the recorded photon intensity on Kodak RAR2497 film. This data is shown for $14\mu m$ (single pixel) wide lineouts.

C.3 References

[1] G.F. Knoll, *Radiation Detection and Measurement*, (Wiley, New York, 1979).

[2] B.L. Henke, et al., "Low-energy x-ray response of photographic films. I. Mathematical models," J. Opt. Soc. Am. B, **1** No. 6, p. 818, (1984).

[3] B.L. Henke, et al., "Low-energy x-ray response of photographic films. II. Experimental characterization," J. Opt. Soc. Am. B, **1** No. 6, p. 828, (1984).

[4] B.L. Henke, et al., "High-energy x-ray response of photographic films: models and measurements," J. Opt. Soc. Am. B, **3** No. 11, p. 1540, (1986).